Remote sensing study of NO_x emissions from soils using space- and ground-based DOAS instruments

Dissertation

zur Erlangung des Grades

"Doktor der Naturwissenschaften"

am Fachbereich Physik, Mathematik und Informatik

der Johannes Gutenberg-Universität in Mainz

Jan Zörner

geb. in Halle (Saale)

Mainz, den 22.11.2016

Angefertigt am Max-Planck-Institut für Chemie, Mainz
Forschungsgruppe Satellitenfernerkundung

Abstract

Nitrogen oxides ($NO_x \equiv NO + NO_2$) are a group of toxic trace gases that degrade air quality and also play a key role in tropospheric chemistry by influencing ozone and nitrate aerosol formation. While fossil-fuel combustion from anthropogenic activity is the largest global source of NO_x, natural emissions also contribute to observed NO_2 concentrations. A large natural source of NO_x are microbial emissions from soils which constitute about 15 % of total NO_x emissions on a global scale. Comparisons between global chemistry models and satellite-derived estimates indicate that the knowledge on regional totals of soil emissions is still uncertain.

This thesis deepens the present understanding of soil emissions of NO_x by (i) improving the quantification of pulsed and seasonally enhanced soil emissions in semi-arid regions and (ii) exploring the contribution of soil emissions of NO_x in an agricultural region. This is achieved by investigating NO_2 column densities, as a proxy for NO_x, utilizing both space- and ground-based remote sensing instruments that capture scattered sunlight. NO_2 column densities are thereby retrieved through Differential Optical Absorption Spectroscopy (DOAS) which exploits the characteristic absorption features of trace gases in the ultra-violet and visible spectral ranges.

Pulsed soil emissions of NO_x, induced by the sudden rewetting of desiccated soils, are detected in this study as enhanced NO_2 vertical column densities (VCDs) at the beginning of the wet season in many semi-arid regions over the world including the Sahel, south-western Africa, Australia and parts of India. The findings suggest that the pulsing events can be subdivided into: (i) an intense, short-term enhancement over 1 to 3 days, (ii) moderate enhancements over the following 2 weeks, (iii) slightly enhanced emissions 1 to 2 days prior to the first precipitation and, (iv) seasonal background emissions which gradually increase at the onset of the wet season. It is found that such pulsed emissions contribute 21 % to 44 % to total soil NO_x emissions over the Sahel. A case study over Lake Chad indicates that intense soil pulsing events can dominate the local NO_x budget on these days.

In order to characterize NO_2 and HCHO levels in a region dominated by agricultural activity and to explore the role of soil emissions, an in-field measurement campaign was conducted in the Nördlinger Ries, Germany. In spite of the rural character of the study region, a relatively large anthropogenic contribution to NO_2 levels was found on a diurnal and weekly basis which mainly stems from road traffic as well as an industrial zone outside the Ries. While average NO_2 VCDs between June and September 2014 are at about 1.30 to 1.84×10^{15} molecules cm^{-2} during the working week, they are drastically reduced on Sundays to about 0.24 to 0.57×10^{15} molecules cm^{-2}. Laboratory analysis of soil samples suggests that soil emissions in the Nördlinger Ries play only a minor role during the working week, but may be the dominating source of NO_x on days with low anthropogenic contributions.

Zusammenfassung

Stickstoffoxide ($NO_x \equiv NO + NO_2$) gehören zu einer Gruppe gesundheitsschädlicher Spurengase, welche in Folge ihres chemischen Abbaus in der Troposphäre auch die Bildung von Nitrat-Aerosolen sowie Ozon beeinflussen. Die größte globale Quelle von NO_x ist die Verbrennung fossiler Brennstoffe im Verkehr sowie der Industrie. Bodenemissionen in Folge mikrobieller Prozesse sind eine der größten natürlichen Quellen von NO_x und stellen etwa 15 % der globalen Gesamtemissionen dar. Vergleichsstudien zwischen globalen Chemie-Modellen und satellitenbasierten Abschätzungen weisen jedoch auf Unsicherheiten in regionalen Gesamtsummen von Bodenemissionen hin.

Die vorliegende Doktorarbeit erweitert bisherige Erkentnisse zu Bodenemissionen von NO_x durch (a) eine verbesserte Quantifizierung kurzzeitig und saisonal erhöhter Bodenemissionen in semi-ariden Gebieten sowie (b) die Erforschung des Beitrages von Bodenemissionen von NO_x in einer stark landwirtschaftlich geprägten Region. Für diese Studien werden satellitengestützte sowie bodenbasierte Fernerkundungsinstrumente eingesetzt und NO_2 Säulendichten, stellvertretend für NO_x, mit der Differentiallen Optischen Absorptionsspektroskopie (DOAS) ausgewertet. Diese Technik nutzt die charakteristischen Absorptionsstrukturen von Spurengasen in den ultra-violetten und sichtbaren Wellenlenlängenbereichen.

Kurzzeitig erhöhte Bodenemissionen von NO_x, ausgelöst durch die Befeuchtung ausgetrockneter Böden, werden in dieser Studie als erhöhte vertikale Säulendichten (VCDs) von NO_2 gemessen. Solche Erhöhungen wurden zu Beginn der Regenzeit in vielen semiariden Gebieten der Welt gefunden - wie z.B. in der Sahel-Region, im Südwesten Afrikas, Australien und Teilen Indiens. Die Auswertungen deuten darauf hin, dass diese starken Emissionsereignisse aufgeteilt werden können: (1) in eine kurzzeitige Erhöhung über 1 bis 3 Tage, (2) eine leichte Erhöhung über die folgenden 2 Wochen, (3) einen leichten Anstieg der Emissionen bereits 1 bis 2 Tage for dem Regenereignis und (4) saisonale Hintergrundemissionen, welche zu Beginn der Regenzeit ansteigen. Diese von Niederschlag eingeleiteten, starken Emissionsereignisse tragen 21 bis 44 % zu den gesamten Bodenemissionen der Sahel bei. Eine Analyse für den Tschadsee zeigt, dass solche Ereignisse das lokale NO_x Budget an diesen Tagen bestimmen.

Zur Charakterisierung von NO_2 und HCHO Verteilungen sowie der Rolle von Bodenemission in einer von Landwirtschaft geprägten Region wurde eine Messkampagne im Nördlinger Ries in Deutschland durchgeführt. Dabei wurde eine erhebliche anthropogene Beeinflussung der täglichen und wöchentlichen Variationen in NO_2 Konzentrationen aufgrund von Straßenverkehr sowie einer Industriezone außerhalb des Ries festgestellt. Von Juni bis September 2014 betrugen die NO_2 VCDs werktags im Schnitt 1.30 bis 1.84×10^{15} Moleküle cm^{-2} und zeigten starke Reduzierungen an Sonntagen auf 0.24 bis 0.57×10^{15} Moleküle cm^{-2}. Laboruntersuchungen von Bodenproben weisen darauf hin, dass Bodenemissionen werktags zwar eine untergeordnete Rolle spielen, jedoch die stärkste Quelle an Tagen mit geringen anthropogenen Emissionen darstellen können.

Contents

Abstract i

Zusammenfassung iii

1 Introduction 1
- 1.1 Motivation . . . 1
- 1.2 Thesis objectives and structure . . . 3

2 Scientific background 5
- 2.1 Composition and structure of the atmosphere . . . 5
  - 2.1.1 Chemical composition . . . 5
  - 2.1.2 Vertical structure . . . 6
  - 2.1.3 Planetary boundary layer . . . 7
  - 2.1.4 Global circulation . . . 8
- 2.2 Chemistry of tropospheric NO_x . . . 10
  - 2.2.1 NO-NO_2 coupling . . . 10
  - 2.2.2 Sources of NO_x . . . 11
    - 2.2.2.1 Formation of NO at high temperatures . . . 11
    - 2.2.2.2 Soil emissions of NO_x . . . 12
  - 2.2.3 Sinks of NO_x . . . 17
  - 2.2.4 Impact on tropospheric ozone . . . 17
  - 2.2.5 Impact on aerosol formation . . . 18
- 2.3 The role of HCHO in the Troposphere . . . 19
  - 2.3.1 Sources of HCHO . . . 19
  - 2.3.2 Sinks of HCHO . . . 20
  - 2.3.3 Exchange with soils . . . 21
- 2.4 Remote sensing of trace gases in the UV/VIS . . . 22
  - 2.4.1 The concept of absorption spectroscopy . . . 22
  - 2.4.2 Differential Optical Absorption Spectroscopy (DOAS) . . . 22
  - 2.4.3 Ground-based approaches . . . 25
    - 2.4.3.1 Long-Path DOAS . . . 25
    - 2.4.3.2 Multi-Axis DOAS (MAX-DOAS) . . . 26
  - 2.4.4 Total columns and profiles from Multi-Axis DOAS . . . 28
  - 2.4.5 Space-based systems . . . 29
    - 2.4.5.1 Ozone Monitoring Instrument (OMI) . . . 31
    - 2.4.5.2 Global Ozone Monitoring Experiment 2 (GOME-2) . . . 33
    - 2.4.5.3 SCanning Imaging Absorption SpectroMeter for Atmospheric CHartographY (SCIAMACHY) . . . 34

3 Enhanced soil emissions of NO_x in semi-arid regions following precipitation 37
3.1 Research objectives and strategy . . . 37
3.2 Data . . . 38
3.2.1 Satellite-derived trace gas products . . . 38
3.2.2 Precipitation . . . 39
3.2.3 Soil moisture . . . 40
3.2.4 Other data sets . . . 40
3.3 Methodology . . . 42
3.4 Results . . . 44
3.4.1 Global Analysis . . . 44
3.4.2 Detailed analyses over the Sahel region . . . 46
3.4.2.1 Overview over the Sahel . . . 46
3.4.2.2 Seasonalities within the Sahel . . . 47
3.4.2.3 Daily variation in NO_2 VCDs after rewetting . . . 56
3.4.2.4 Land cover analysis . . . 58
3.4.2.5 Analysis for different soil temperatures . . . 60
3.4.2.6 Monthly maps of pulsed soil NO_x emissions in the Sahel 60
3.4.2.7 Influence from other sources on the NO_2 signal . . . 60
3.4.2.8 Enhanced emissions after Day0 . . . 64
3.4.3 Further study regions . . . 70
3.4.4 Sensitivity studies . . . 72
3.5 Discussion . . . 79
3.5.1 Estimated nitrogen emission fluxes from the emission pulse . . . 79
3.5.2 Seasonal soil nitrogen emissions in the Sahel . . . 80
3.5.3 Enhancements in NO_2 VCDs on Day-1 . . . 81
3.6 Conclusions . . . 82

4 Case study of pulsed soil emissions around Lake Chad 85
4.1 The study region . . . 85
4.2 Methodology . . . 87
4.3 Time series of precipitation and NO_2 VCDs . . . 88
4.4 Enhancement in OMI NO_2 VCDs . . . 92
4.4.1 Potential sources of the NO_2 enhancement . . . 92
4.4.2 Cloud fraction and AMF . . . 94
4.4.3 Lightning emissions of NO_x . . . 95
4.4.4 Fire emissions of NO_x . . . 97
4.5 Discussion on pulsed soil NO_x emissions . . . 100
4.6 Conclusions . . . 100

5 Measurement campaign on soil emissions in an agricultural region 103
5.1 Research objectives and strategy . . . 103
5.2 The study region . . . 104

5.3 Instrumental set-up . . . 107
5.3.1 The mini-MAX-DOAS instruments . . . 108
5.3.1.1 Castle Station . . . 110
5.3.1.2 Barn Station . . . 110
5.3.2 Long-Path DOAS . . . 111
5.3.3 Air quality monitoring station . . . 112
5.3.4 In-field weather stations . . . 113
5.3.5 Meteorological data from the DWD . . . 113
5.4 Trace gas and aerosol information from the MAX-DOAS instruments . . . 114
5.4.1 Correction of the raw spectra . . . 114
5.4.2 Spectral Retrieval . . . 115
5.4.2.1 DOAS fit examples for NO_2 . . . 116
5.4.2.2 DOAS fit examples for HCHO . . . 117
5.4.2.3 DOAS fit examples for O_4 . . . 118
5.4.3 Quality screening of the retrieved DSCDs . . . 121
5.4.4 Computation of trace gas profiles, mixing ratios and VCDs . . . 124
5.4.5 Cloud classification . . . 125
5.5 Meteorology in the Ries during the campaign . . . 126
5.6 Results . . . 127
5.6.1 Comparison of the measured to the simulated trace gas DSCDs . . . 127
5.6.2 Average trace gas and aerosol profiles . . . 128
5.6.3 Comparison of NO_2 VCDs to satellite observations . . . 130
5.6.4 Horizontal distribution of NO_2 and HCHO . . . 131
5.6.5 Temporal patterns of trace gas levels . . . 132
5.6.5.1 Diurnal cycle . . . 133
5.6.5.2 Weekly cycle . . . 134
5.6.5.3 Seasonal variation . . . 135
5.6.6 Trace gas VMRs under different sky conditions . . . 136
5.6.7 Dependence of near-surface trace gas VMRs on wind . . . 137
5.6.8 Multiple regression analysis: trace gas VMRs and environmental parameters . . . 140
5.6.9 Impact of sudden enhancements in soil moisture . . . 147
5.6.9.1 Daily environmental parameters and trace gases . . . 147
5.6.9.2 Days showing spikes in soil moisture and high trace gas VMRs . . . 150
5.7 Contribution of soil emissions to NO_2 VCDs . . . 156
5.8 Conclusions . . . 158

6 General conclusions and outlook 161

A Monthly averages of environmental parameters over Northern Africa 167
A.1 Monthly averages of GOME-2 NO_2 VCDs 167
A.2 Monthly averages of SCIAMACHY NO_2 VCDs 168
A.3 Monthly averages of daily fire counts 169
A.4 Monthly averages of daily lightning strikes 170
A.5 Albedo maps from the NO_2 products 171
A.5.1 OMI 171
A.5.2 GOME-2 172
A.5.3 SCIAMACHY 173

B Dependence of trace gas levels in the Nördlinger Ries on environmental parameters 175
B.1 Summary statistics for the independent variables 175
B.1.1 NO_2 175
B.1.2 HCHO 177
B.2 NO_2 VMRs shifted by one day 179
B.3 HCHO VMRs shifted by one day 181

Bibliography 183

List of abbreviations 201

List of figures 203

List of tables 215

CHAPTER 1

Introduction

1.1 Motivation

Air pollution poses an imminent threat to human health by causing a wide range of respiratory and cardiovascular diseases and has become the biggest environmental cause of premature death (OECD, 2014). Due to technological improvements and stringent environmental policies, emissions of many air pollutants have declined over the last decades (EEA, 2015a,b). However, concentrations of air pollutants are still on a high level in many places and the European Union (EU) limits for pollutants such as $PM_{2.5}$ (particulate matter with a diameter < 2.5 µm) and nitrogen oxides ($NO_x \equiv NO + NO_2$) are regularly exceeded at air quality monitoring stations in all member states (EEA, 2015a,b). Thus, air pollution is still one of the main environmental and social concerns, especially in urban areas where the population is exposed to highest concentrations.

Most problematic pollutants with respect to critically high concentrations and associated health risks are particulate matter (PM), NO_x as well as surface-level O_3 (EEA, 2015a,b). NO_x play a key role since they do not only affect human health directly but also influence the formation of aerosols, including $PM_{2.5}$, and O_3. During daytime, NO_x are mainly removed from the atmosphere by oxidation with OH producing nitric acid (HNO_3) (Jacob, 1999; Monks, 2005) which is an important component of acid deposition and contributes to the formation of nitrate aerosols (Bassett and Seinfeld, 1983). When ammonia (NH_3) is present in the air, NO_x react with HNO_3 to form ammonium nitrate (NH_4NO_3) aerosols which are a large contributor to $PM_{2.5}$ levels (e.g. Finlayson-Pitts and Pitts, 2000; Petetin et al., 2016).

Due to the variety of impacts of NO_x on the environment and human health, the knowledge and understanding of its emission sources is of high importance. While anthropogenic activity such as fossil fuel combustion is the largest source of NO_x, there are also important natural sources including biomass burning, lightning and microbial processes in soils.

Due to increased soil emissions of NO_x and NH_3 from cultivated (and strongly fertilized) soils, agriculture largely impacts $PM_{2.5}$ levels and, as Lelieveld et al. (2015) showed, even dominates mortality due to air pollution in Europe, Russia, Turkey, Korea, Japan and Eastern USA. Several studies point out that the reduction of precursor emissions such as NO_x leads to drastic decreases in ammonium nitrate and $PM_{2.5}$ levels (e.g. Hodan and Barnard, 2004; Blanchard and Hidy, 2005; Lelieveld et al., 2015; Pusede et al., 2016).

Although the total emissions of NO_x, for instance in Germany, decreased from 2885 kt in 1990 to 1223 kt in 2014 as reported by bottom-up inventories (Gniffke, 2016), the

observed NO_2 concentrations do not show such a drastic reduction and, furthermore, NO_x emissions from agricultural soils also showed no substantial change (135 kt in 1990 and 120 kt in 2014). In fact, emissions of NH_3 from agriculture substantially increased from 142 kt to 218 kt in the same time period raising the concerns for nitrate aerosol pollution in environments dominated by agriculture.

On a global basis, soil emissions of NO_x constitute an estimated fraction of $\sim 15\,\%$ of total NO_x emissions (Warneck and Williams, 2012; Hudman et al., 2012) and may dominate the local NO_x budget in non-industrialized remote tropical regions and agricultural areas (Yienger and Levy, 1995; Steinkamp et al., 2009). Bottom-up approaches using global chemistry models suggest global fluxes between 9 to 28 $\mathrm{Tg\,N\,yr^{-1}}$ with large uncertainties (e.g., Yienger and Levy, 1995; Steinkamp and Lawrence, 2011). Top-down approaches which constrain estimates based on space-based observations thereby hint at regional underestimations of soil emissions of NO_x by a factor of 2 or more indicating that that the nitrogen (N) mass balance is not captured accurately by the current models. (Jaeglé et al., 2004; Jaegle et al., 2005; Wang et al., 2007; Boersma et al., 2008; Stavrakou et al., 2008, 2013; Zhao and Wang, 2009; Hudman et al., 2012; Vinken et al., 2014).

Many studies investigated the sudden release of NO from soil after rewetting of desiccated soils and found pulsed emissions in situ and by laboratory measurements of soil samples (e.g., Williams et al., 1987; Johansson and Sanhueza, 1988; Williams et al., 1992; Levine et al., 1996; Scholes et al., 1997; Kim et al., 2012, and references therein). Soil emissions of NO_x occurring at the transition phase between the dry and wet season were also observed from space (Jaeglé et al., 2004; Bertram et al., 2005; Ghude et al., 2010; Hudman et al., 2012). Hudman et al. (2012) showed that these intense but short events of soil emissions, termed 'pulsed emissions', at the start of the wet season after a prolonged dry spell represent a large fraction of annual soil emissions in the Sahel region. However, Hudman et al. (2012) also point out that further research needs to be conducted to verify that the observed pulses are not biased by the retrieval algorithm.

As stated above, emissions of NO_x from natural and agricultural soils have adverse effects on the environment and human health. However, knowledge of the amount of NO_x from soils is still limited because (i) current studies on soil emissions of NO_x in humid climates only comprise point samples and laboratory measurements, (ii) global bottom-up approaches extrapolate field samples to vast geographic regions and (iii) global top-down estimates suffer from poor spatio-temporal resolution.

These limitations together with the raised awareness of health and environmental impacts of NO_x emissions from soils show the need for further research on this topic.

Specifically, open questions concern (i) the absolute amount of NO_x emitted during soil pulsing events in semi-arid areas (for single events and for seasonal averages), (ii) the question whether the so-far observed enhancements (from space) were biased by the retrieval algorithms, (iii) the contribution of soil emissions to the NO_x budget in agricultural regions in a humid climate and (iv) the question whether significant (precipitation-induced) soil pulsing events occur in the latter regions.

In addition, Veres et al. (2014) found in laboratory experiments that in addition of

NO_x, several volatile organic compounds (VOC) including formaldehyde (HCHO) exhibit pulsed emissions when dry soils are first wetted. However, there exist only few studies concerning soil emissions of HCHO and more research is needed to describe the magnitude of these emissions in semi-arid regions as well as agricultural environments.

1.2 Thesis objectives and structure

This thesis aims to deepen the present understanding of soil emissions of NO_x by investigating NO_2 column densities as a proxy for NO_x utilizing both space- and ground-based remote sensing instruments. The focus is on geographic regions most susceptible to soil emissions. These are, on the one hand, semi-arid areas which show strongest soil emissions at the start of the wet season and, on the other hand, regions dominated by agricultural activity which show enhanced soil emissions due to the intense use of fertilizer.

Thereby, the thesis mainly aims at (i) an improved quantification of pulsed and seasonally enhanced soil emissions in semi-arid regions and (ii) an exploration of the contribution of (pulsed) soil emissions of NO_x in an agricultural region.

Furthermore, one additional goal of this thesis is the investigation whether HCHO emitted from soils can be observed in these regions.

The above described general objectives are approached from different spatial scales (from global to regional and local) and involve the use of instruments that retrieve trace gases in the UV-VIS (ultra-violet and visible) spectral ranges using the Differential Optical Absorption Spectroscopy (DOAS, Platt and Stutz, 2008). The structure of the thesis is summarized in Table 1.1.

Table 1.1: Overview of the main study region and research approach per chapter.

Chapter	**Three**	**Four**	**Five**
Study region	Continents, The Sahel	Lake Chad	Nördlinger Ries
Spatial scale	Global and Regional	Regional to Local	Local
	10 000 to 100 km	100 to 10 km	10 km
Main approach	Space-based	Space-based	Ground-based
Trace gas	NO_2 & HCHO	NO_2	NO_2 & HCHO

Chapter 2 of the thesis provides a general overview over the scientific background relevant to the investigations, i.e. the structure of the atmosphere, chemical processes associated with the trace gases and inter-relations among the different species, the measurement technique as well as a detailed description of the used DOAS-type instruments and analysis principles.

Chapter 3, of which the main conclusions were published in Zörner et al. (2016), sheds light on precipitation-induced soil emission pulses of NO_x during the transition phase between the dry and wet season in semi-arid areas over the globe. It seeks to provide an improved quantification of short-term emission pulses (1–3 days) as well as their contribution to seasonal soil emissions in these regions. The primary focus is set on pulsed

soil emissions of NO_x as well as the seasonality in soil emissions in the Sahel region.

Chapter 4 presents an intense pulsing event of soil emissions of NO_x around Lake Chad in Central Africa. A detailed investigation is conducted to study the enhanced NO_2 VCDs on this particular day and to exclude other sources.

Chapter 5 studies soil emissions of NO_x from agricultural fields in a humid climate using ground-based DOAS measurements. A dedicated measurement campaign, involving several passive and active DOAS instruments, was organized in the Nördlinger Ries (Bavaria/Germany) within the framework of this PhD project.

Finally, Chapter 6 concludes by summarizing the keys findings for each chapter and provides recommendations for prospective research on soil NO_x emissions.

CHAPTER 2

Scientific background

2.1 Composition and structure of the atmosphere

Emissions of trace gases to Earth's atmosphere as well as their mixing are studied within this thesis. In order to provide a general overview over the atmosphere and its dynamics, the following section gives a concise description of its chemical composition, vertical structure and governing atmospheric motions. The section is mainly based on overviews from Wallace and Hobbs (2006) and Seinfeld and Pandis (2006).

2.1.1 Chemical composition

Compared to the radius of the Earth (6371 km), the atmosphere of the Earth is a relatively thin gaseous layer ($\sim$ 100 km) that protects life on the ground in a variety of ways, for example by absorbing harmful UV radiation from the Sun and keeping the Earth surface warm and relatively constant through its heat retention (Wallace and Hobbs, 2006). The atmosphere consists of a mixture of different gases whereby very few gases are responsible for more than 99 % of the total volume. These are for dry air: nitrogen (N_2) with a volume percentage of 78 %, oxygen (O_2) with 20.9 %, Argon (Ar) with 0.93 % and carbon dioxide (CO_2) with 0.04 %. The volume percentage of water vapour (H_2O) in air can range from almost 0 % to 5 % (Wallace and Hobbs, 2006) and shows a high spatio-temporal variability as it is mainly controlled by evaporation and precipitation.

The abundance of trace gases in the atmosphere is a result of the interplay between several processes such as the reactivity with other species, photochemistry or the rate at which they are produced (via direct emission or secondary formation processes) and destroyed (or deposited on surfaces). While N_2 and noble gases such as argon are chemically inert and exhibit quite constant mixing ratios, most chemical reactions in the atmosphere involve O_2 and trace gases. The latter are generally defined as gases that consume less than 1 % of the air volume and primarily comprise radicals such as OH, NO and NO_2 with relatively short lifetimes of seconds to hours. Despite their quite low abundance (in the order of parts per billion, ppb), they are very important in atmospheric chemistry because of their high reactivity with other gases and particles and are, thus, an important driver of local air quality and the climate.

The spatial variability of gases is primarily determined by their residence time in the atmosphere (Fig. 2.1). Thereby, longer-lived species such as N_2O, chlorofluorocarbon (CFC) or CO_2 with lifetimes beyond 100 years are well mixed in the entire atmosphere. In

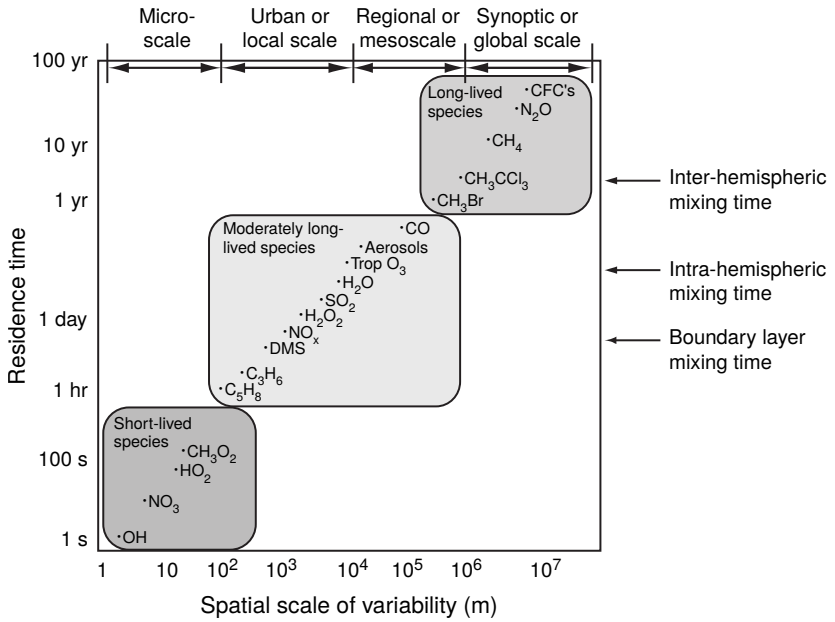

Figure 2.1: Spatial and temporal scales of variability for some atmospheric constituents from Wallace and Hobbs (2006).

contrast, shorter-lived species with residence times of less then a day mainly impact on the local scales where they were emitted.

In addition to gaseous species, the atmosphere also contains tiny solid and liquid particles ranging from nm to µm (and in rare cases to several mm) which are dispersed in the air (Seinfeld and Pandis, 2006). Prominent examples for such *aerosol particles* (in the following also referred to as *aerosols* for simplifcation) are water droplets, dust and soot particles as well as a wide range of biological aerosols, including fungi and pollen, that contain living organisms or were released from living organisms (Cox and Wathes, 1995). Many aerosols pose a hazard to human health (OECD, 2014) such, for instance, particulate matter with a diameter < 2.5 µm ($PM_{2.5}$) or with a diameter < 10 µm (PM_{10}). Moreover, aerosols can also influence the climate by scattering or absorbing incoming solar radiation and by serving as cloud condensation nuclei. Aerosols can be brought directly into the atmosphere through direct emissions, stirring up of dust from the surface and also indirectly from secondary formation processes in the atmosphere through the conversion of gases to particles (such as the nitrate aerosol formation described above).

2.1.2 Vertical structure

Earth's atmosphere is commonly subdivided into layers of similar thermodynamical properties, e.g. vertical gradients of temperature and pressure. Based on consistent alternations in the vertical temperature gradient, the atmosphere can be grouped into four distinct layers, i.e. the Troposphere, Stratosphere, Mesosphere and Thermosphere (Fig. 2.2).

The main focus of this thesis is on processes taking place in the Troposphere. This

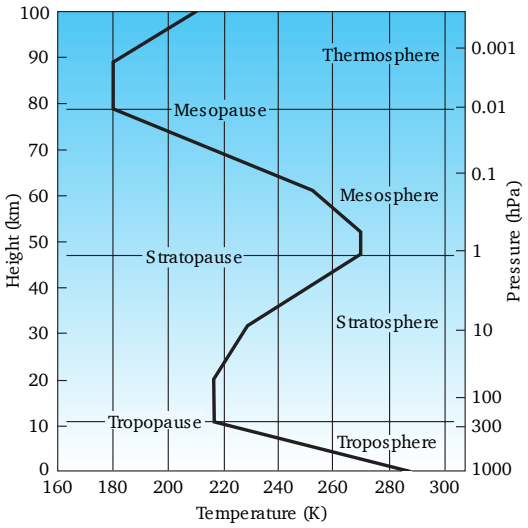

Figure 2.2: A typical mid-latitude vertical temperature profile (adapted from Wallace and Hobbs (2006)).

layer contains about 80 % of the atmosphere's mass including most atmospheric trace gases and aerosols. The air in the lowest part of the Troposphere is typically well mixed because of turbulent winds near the surface and convection processes. The latter enables warmer air masses from the surface to rise up. When this warm air cools down below the condensation point during the ascent, the water vapour in the air mass condenses and clouds are formed. The Troposphere extends to about 8 km at high latitudes and up to 18 km near the Equator in consequence of increased convective activity in warmer regions. In the stratosphere, the temperature gradient reverses and starts to increase with altitude due to enhanced ozone abundance absorbing solar UV radiation. In consequence, the positive temperature gradient leads to a stable layer with diminished vertical air motions. As a result, the Tropopause, which is the transition from the Troposphere to the Stratosphere, acts as a natural barrier for convective air masses.

2.1.3 Planetary boundary layer

The Troposphere, however, is not a uniform layer but consists, on the one hand, of the free Troposphere with low influence from Earth's surface and, on the other hand, of the planetary boundary layer (PBL) which directly interacts with the surface of the Earth through surface friction and other processes such as the direct exchange of gases and aerosols (Stull, 1988). Hence, the PBL is of primary interest when studying soil emissions of trace gases.

The diurnal cycle in the PBL shows a distinct day- and night-time behaviour whereby increased convection induced by solar heating and turbulences provoke increased mixing of gases during the day. As a consequence, the PBL extends much higher up in the atmosphere during the day (up to 3 km) compared to its diminished depth during the night. When the Sun sets, the surface cools down and a stable nocturnal surface layer develops. This layer extends several hundreds of meters at maximum and is characterized

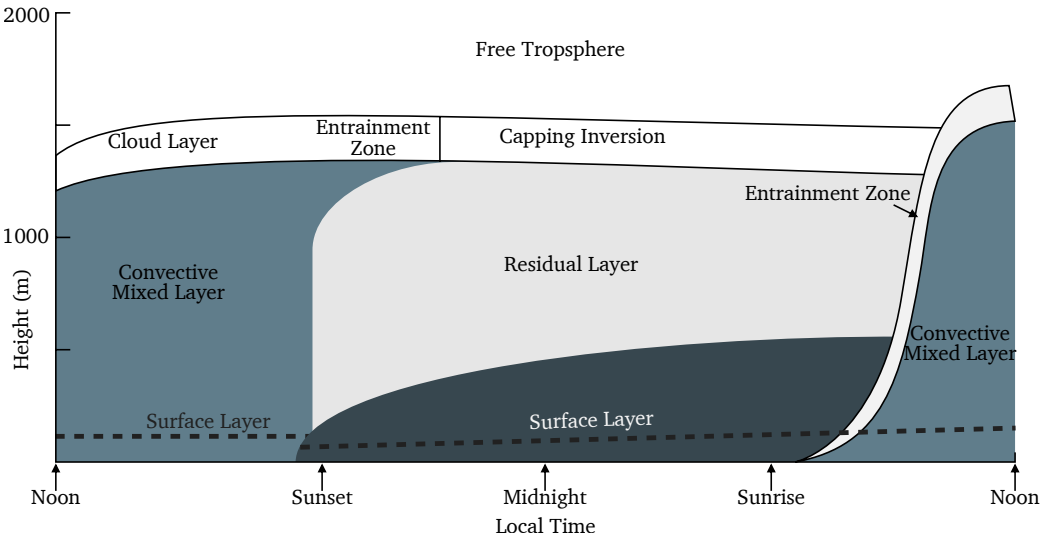

Figure 2.3: Day- and night-time behaviour of the planetary boundary layer (adapted from Stull (1988)).

by low turbulence. The residual region between this stable surface layer and the free Troposphere forms during the night and vanishes after sunrise. The border between the PBL and the free Troposphere is capped by a relatively stable inversion, i.e. an increase in temperature with altitude. This transition zone typically impedes air from further ascend and restricts the exchange of gases and particles between the two zones.

2.1.4 Global circulation

Within this thesis the primary study regions are located in the mid-latitudes and the sub-tropics. In order to understand the prevailing meteorology and wind conditions in specific, global atmospheric circulation patterns have to be considered.

The driving forces behind the global circulation are, on the one hand, the uneven solar heating of the Earth's surface which provokes pressure gradients between the Tropics and the Poles and, on the other hand, the rotation of the Earth which gives rise to the Coriolis force. The latter is the reason why the air cannot flow between the Equator and the poles undisturbed. In general, the global circulation can be approximated by three broad systems that govern the atmospheric motion: the Hadley, Ferrel and Polar cells.

High ground temperatures, induced by high insolation at the Equator, lead to consistent convection in this region. In turn, the ascending air causes a high pressure system at high altitudes. The air can only diverge away from the Equator in poleward direction and cools down on the way. At about 30° latitude, the air mass descends and causes a high pressure system close to the ground. Air that flows back to the Equator closes then the *Hadley cell*. In the Northern Hemisphere, these north-south winds are deflected by the Coriolis force to the west and are also-called *trade winds* (in the Southern Hemisphere the south-north winds are deflected to the east).

The winds in mid-latitudes are governed by the *Ferrel cell* (or: Fresnel cell) which is, in

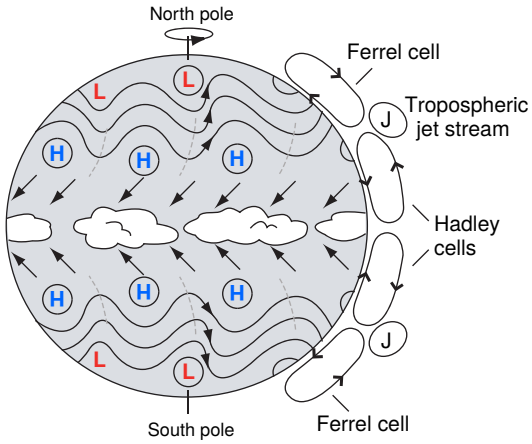

Figure 2.4: General global atmospheric circulation (adapted from Wallace and Hobbs (2006)).

part, driven by the circulation systems of the Hadley and Polar cell on either side. When the poleward moving air from the Hadley cell descends at about 30° latitude not all of it moves back to the Equator. The remaining air mass moves poleward and gets deflected by the Coriolis force in the Northern Hemisphere to the east, resulting in westerly winds (or: the 'West wind zone'), and in the Southern Hemisphere to the west.

Near the poles, solar heating of the surface is very small causing cold air masses to sink. The near-surface high pressure system then pushes the cold air masses in all directions. The cold polar air then moves into the direction of the Equator and encounters the warmer air coming from the south typically at about 60° latitude which causes the *Polar Front*. Subsequently, the warmer air mass rises up and diverges at high altitudes. One part moves to the poles, closing the *Polar cell*, and the other part moves southward, closing the *Ferrel cell*.

In order to understand the precipitation regime in Tropical and semi-arid regions near the Equator the concept of the Inter Tropical Convergence Zone (ITCZ) has to be introduced. The ITCZ is generally defined as the region where trade winds of the Northern and Southern Hemispheres converge, see Fig. 2.5. As the moist and warm surface air rises near the Equator, it expands and cools down releasing the accumulated moisture in a continuous series of precipitation systems and thunderstorms. The ITCZ can be observed from space-based instruments as a perpetual band of convective clouds encircling the Earth near the Equator. The location of the ITCZ varies seasonally within a few degrees around the Equator, moving northward in spring and southward in autumn. These seasonal shifts in latitude result in seasonal rainfall patterns in many equatorial regions. Long term changes in the ITCZ and the periodic rainfall events, hence, may result in extreme disturbances such as severe drought or flooding.

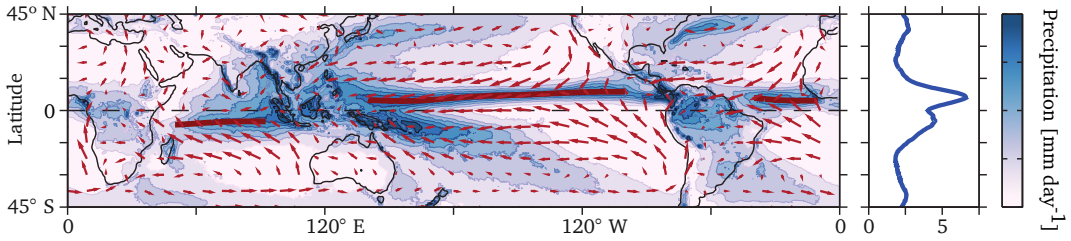

Figure 2.5: Illustration from Schneider et al. (2014): Global annual-mean precipitation and surface winds. The ITCZ over oceans (precipitation maximum) is marked by red lines. The right panel shows the zonal-mean precipitation. Precipitation data is taken from TRMM/TMPA for 1998–2012. The wind data are from ECMWF for the same years. The longest wind vector over the central Pacific corresponds to a wind speed of 8.1 m s^{-1}

.

2.2 Chemistry of tropospheric NO_x

As outlined in the introduction, nitrogen oxides (NO_x) play a central role in tropospheric chemistry and are a key driver of local and regional air quality. The following section gives a broad overview on their emission sources as well as chemical reactions in the atmosphere through their destruction processes. This section is based on overviews from Jacob (1999), Finlayson-Pitts and Pitts (2000) and Seinfeld and Pandis (2006).

2.2.1 NO-NO_2 coupling

Most NO_x emissions are released in the form of nitrogen oxide (NO) which is quickly converted to NO_2 in the atmosphere. The latter is driven by the availability of ambient O_3 which reacts with NO to form NO_2 and O_2 within minutes:

$$NO + O_3 \longrightarrow NO_2 + O_2 \tag{2.1}$$

When light is present, NO_2 is photolyzed (at wavelengths < 420 nm) back to NO and an oxygen radical is produced:

$$NO_2 + hv \xrightarrow{\lambda<420\ nm} NO + O \tag{2.2}$$

The oxygen radical then reacts with O_2 producing again an O_3 molecule:

$$O + O_2 + M \longrightarrow O_3 + M \tag{2.3}$$

This closed photochemical cycle works on short time-scales and tightly couples NO and NO_2 in tropospheric air. Thereby it is useful to introduce the "Leighton ratio" which gives the ratio between these two gases. This quantity depends on the photolysis rate of NO_2 (J), the abundance of O_3 and the rate constant of the reaction of O_3 with NO which is temperature-dependent (k):

$$LR = [NO]/[NO_2] = J(NO_2)/k[O_3] \tag{2.4}$$

While in near-surface air masses, most NO_x is present as NO_2 with a Leighton ration of about 0.3, at higher altitudes NO dominates in consequence of the lower temperatures (Eq. 2.2 diminishes) and higher photolysis rate (Eq. 2.1 becomes more important). At night-time, no photolysis takes place and most NO_x is present as NO_2 in consequence ($LR \rightarrow 0$).

2.2.2 Sources of NO_x

The majority of tropospheric NO_x is produced either via processes involving high temperatures such as combustion or lightning, or through microbial activity in soils. Thereby, direct emissions from anthropogenic sources such as traffic, heating and industrial activity account for about 22 to 35 $Tg\,N\,yr^{-1}$ (Denman et al., 2007; Stavrakou et al., 2013). The amount of natural emissions of NO_x is more difficult to asses but in the literature values of about 9 to 28 $Tg\,N\,yr^{-1}$ from soils are found (Yienger and Levy, 1995; Jaegle et al., 2005; Stavrakou et al., 2008; Steinkamp and Lawrence, 2011; Hudman et al., 2012; Stavrakou et al., 2013; Vinken et al., 2014), 3 to 16 $Tg\,N\,yr^{-1}$ from biomass burning (Jaegle et al., 2005; Jain et al., 2006; Denman et al., 2007; Stavrakou et al., 2013) and 2 to 8 $Tg\,N\,yr^{-1}$ from lightning (Schumann and Huntrieser, 2007; Murray et al., 2012; Stavrakou et al., 2013; Miyazaki et al., 2014). The inflow of stratospheric NO_2 to the Troposphere is a further, but marginal source of tropospheric NO_x. Combustion processes from anthropogenic activity and in specific from the transport and industrial sectors increased rapidly over the last decades and are thus the main emission source of NO_x on a global scale and concentrate especially in populated areas (Seinfeld and Pandis, 2006).

Due to the relatively short NO_x lifetime of a few hours, observed concentrations of NO_x give direct information on the source region of the emissions. This effect can be seen in average tropospheric NO_2 VCDs for the years 2005–2009, as observed by a spaceborne sensor in Fig. 2.6, that indicate that the main source regions of NO_x are urban and populated areas in China, Europe and the United States of America. Furthermore, regions with intense industrial activity, i.e. power plants, such as the Highveld in South Africa clearly stick out in the satellite imagery. In tropical and semi-arid regions NO_x levels are mainly controlled by emissions from biomass burning and soil emissions.

2.2.2.1 Formation of NO at high temperatures

As outlined above, the majority of NO_x emissions originate from combustion processes. The chemical production of NO occurs at temperatures above 2000 K and is known as the "Zel'dovic mechanism" following Zel'dovich (1946). At very high temperatures, molecular oxygen (O_2) starts to dissociate:

$$O_2 + M \rightleftharpoons O + O + M \tag{2.5}$$

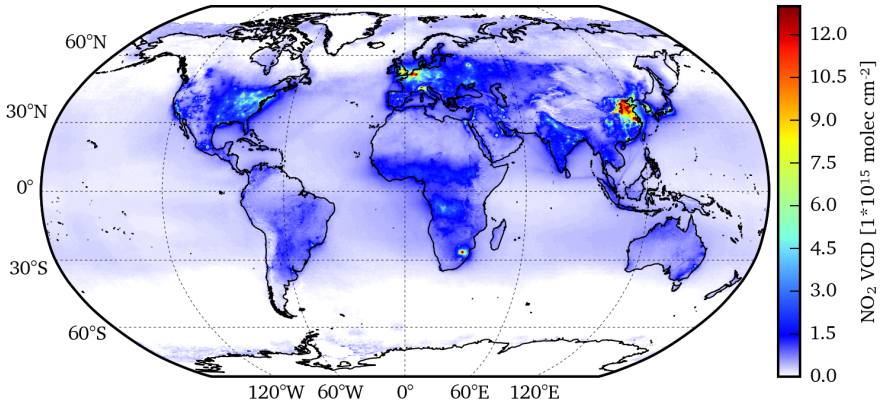

Figure 2.6: Tropospheric NO_2 VCDs averaged over the years 2005 to 2009 as observed by the OMI satellite sensor. Level-2 data taken from http://www.temis.nl

The resulting oxygen atoms then react with ambient nitrogen (N_2) to form NO and a nitrogen atom:

$$O + N_2 \rightleftharpoons NO + N \tag{2.6}$$

Subsequently, the nitrogen atom further reacts with ambient O_2 producing an NO molecule and an oxygen atom:

$$N + O_2 \rightleftharpoons NO + O \tag{2.7}$$

Thereby, the equilibria for equations 2.6 and 2.7 are biased towards the right hand side at high temperatures.

2.2.2.2 Soil emissions of NO_x

The main focus of this thesis is on NO_x emissions from soils (in the following: sNO_x). They constitute an estimated fraction of $\sim 15\,\%$ of total NO_x on a global basis (Warneck and Williams, 2012; Hudman et al., 2012; Vinken et al., 2014) and may dominate the local NO_x budget in non-industrialized regions like remote tropical and agricultural areas (Yienger and Levy, 1995; Steinkamp et al., 2009). Bottom-up approaches using global chemistry models suggest global fluxes between 4 to 15 $Tg\,N\,yr^{-1}$ with uncertainties of up to 5 to 10 $Tg\,N\,yr^{-1}$ (e.g. Yienger and Levy, 1995; Steinkamp and Lawrence, 2011; Hudman et al., 2012; Vinken et al., 2014, and references therein).

Steinkamp and Lawrence (2011) present global mean sNO_x emission rates [$ng\,N\,m^{-2}\,s^{-1}$] for the period from 1990 to 2000 (Fig. 2.7) which were calculated by an improved sNO_x model based on the well-established YL95 scheme (Yienger and Levy, 1995). Among the numerous improvements are, for instance the usage of a better resolved land cover classification, annually varying fertilization rates, the usage of volumetric soil moisture for dry/wet distinction, adjustment of an emission factor reproducing measured emissions (from literature) and an updated canopy reduction of released emissions. The latter is important as the effective NO_x fluxes from soils to the atmosphere are potentially offset by "canopy reduction" where nitrogen oxides are quickly deposited on available vege-

tation surfaces (Ganzeveld et al., 2002). Steinkamp and Lawrence (2011) found that the incorporated changes lead to a general increase of the global annual sNO_x emissions and indicate large discrepancies in regional soil emissions compared to previous works.

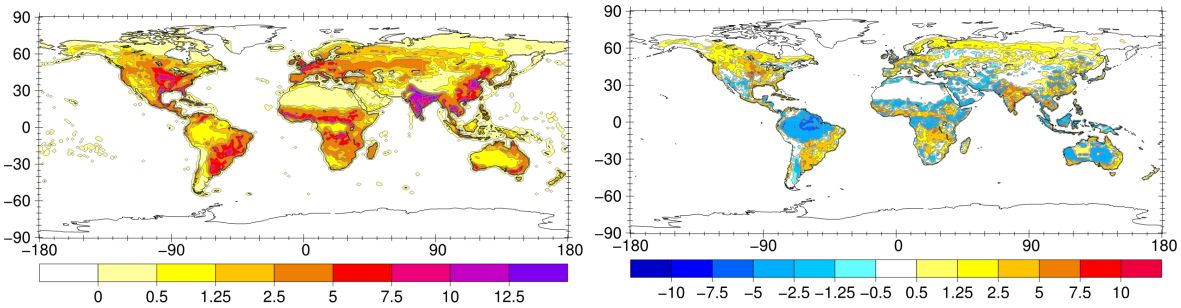

Figure 2.7: Left: global mean sNO_x emission rates [ng N m^{-2} s^{-1}] for the period from 1990 to 2000 calculated by an improved sNO_x model by Steinkamp and Lawrence (2011) based on the YL95 scheme (Yienger and Levy, 1995). Right: Difference between the updated and original model as implemented in the EMAC model.

Emissions of NO_x from natural and anthropogenically influenced soils are mainly driven by microbial activity within the top soil layer and associated chemical reactions (Conrad, 1996). Primarily, two important groups of micro-organisms, *nitrifiers* and *denitrifiers*, are involved in processes related to the turnover of nutrients in the soil as well as to the release of nitrogen containing gases from the soil (Pilegaard, 2013). NO is a gaseous by-product of such processes and once released reacts with ambient O_3, to form NO_2 within minutes (Eq. 2.1). In the following, three processes responsible for NO_x releases from soils are briefly described, based on knowledge from Conrad (1996) and Pilegaard (2013). Thereby, the amount of soil water controls the transport of oxygen into the soil and of gaseous nitrogen out of the soil.

Nitrification. Nitrification is the biological oxidation of nitrogen compounds and typically the oxidation of soil ammonium (NH_4^+) to nitrate (NO_3^-). Thereby, *Nitrosobacteria* are responsible for the first part of the processes requiring oxygen. The sequential mechanism leading to the production of NO is assumed to be:

$$NH_4^+ \longrightarrow NH_2OH \longrightarrow HNO \longrightarrow NO\uparrow \tag{2.8}$$

Nitrobacteria then oxidize nitrite to nitrate:

$$NO_2^- \longrightarrow NO_3^- \tag{2.9}$$

Under anoxic conditions, the same bacteria then reduce the NO_3^- to NO_2^- and further to NO. Both bacteria communities, *Nitrosobacteria* and *Nitrobacteria*, are autotrophic meaning that they are able to produce their own energy by transforming inorganic substances into organic substances. Heterotrophic nitrifiers also exist producing nitrate either through an

inorganic process chain

$$NH_4^+ \longrightarrow NH_2OH \longrightarrow NO_2^- \longrightarrow NO_3^- \tag{2.10}$$

or through an organic pathway

$$R{-}NH_2 \longrightarrow R{-}NHOH \longrightarrow R{-}NO \longrightarrow R{-}NO_2 \longrightarrow NO_3^- \tag{2.11}$$

Denitrification. The reduction of nitrogen compounds by microbes to gaseous products such as NO, N_2O and N_2 is called denitrification. Thereby, NO is released as a by-product:

$$NO_3^- \longrightarrow NO_2^- \longrightarrow NO\uparrow \longrightarrow N_2O\uparrow \longrightarrow N_2\uparrow \tag{2.12}$$

Chemodenitrification. Most soil emissions of NO, especially in semi-arid areas, are linked to microbial processes. However, some chemical (abiotic) formation processes of NO are known to exist which are more important for acidic soils with high nitrite (NO_2^-) concentrations (Davidson, 1992b). In this respect, chemodenitrification, which stands for the chemical decomposition of NO_2^-, can lead to NO production and release to the atmosphere.

Nitrate in soils is typically produced by microbes in the soil from ammonium (through nitrification) or from nitrate (through denitrification). Together with H^+ in water, which also originates from microbial activity, NO is produced during the process:

$$3\,NO_2^- + 2\,H^+ \longrightarrow 2\,NO\uparrow + NO_3^- + H_2O \tag{2.13}$$

Such soils are found in humid regions, i.e. the humid tropical belt and the northern temperate zone, where soil leaching removes alkaline material and associated salts from the soil profiles leading to pH values of less than 5.5 (Merry, 2009).

Findings from Su et al. (2011) and Oswald et al. (2013) suggest that gaseous nitrous acid (HONO), which is rapidly photolyzed to NO, is also emitted from soils:

$$NO_2^- + H^+ \rightleftharpoons HNO_2 \rightleftharpoons HONO\uparrow \tag{2.14}$$

Parameters controlling the release rate. The presence of nitrogen in the soil, as NH_4^+ or NO_3^-, is fundamental for NO-release as they are the starting point for both nitrification and denitrification processes. In consequence, emissions of nitrogen-containing gases, such as NO, N_2 and N_2O increase dramatically in soils with enhanced nitrogen availability due to the presence of N-fixing microbial species and plants (Virginia et al., 1982; van Groenigen et al., 2015) or through enhanced nitrogen input through nitrogen deposition or fertilization.

In semi-arid areas with sparse vegetation cover, surfaces are covered by a variety of communities of cyanobacteria, algae, lichens, mosses, microfungi, and other bacteria in differing proportions (Belnap and Lange, 2001; Barger et al., 2005). Associated organisms

within these biological crusted soils fix atmospheric N_2 and, thus, raise the nitrogen availability in the soil (Evans and Ehleringer, 1993). Recent findings from Weber et al. (2015) suggest that dryland emissions of reactive nitrogen are largely driven by biocrusts rather than the underlying soil and strongly depend on the soil water content, i.e. precipitation events. Throughout this thesis, all NO_x emissions from soils and biocrusts are referred to as sNO_x for simplicity.

Soil emissions of trace gases, furthermore, depend on a wide range of ambient environmental conditions such as soil type, soil moisture, temperature, pH value and nitrogen content (Conrad, 1996; Ludwig et al., 2001; Meixner and Yang, 2006; Oswald et al., 2013).

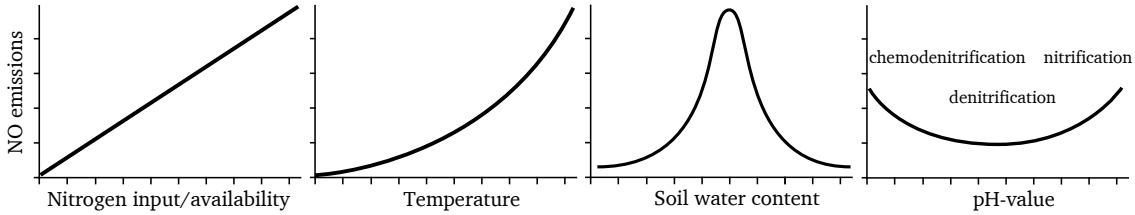

Figure 2.8: Overview of the schematic dependence of NO emission rates on several soil parameters: nitrogen availability, temperature, soil water content and pH value adapted from Pilegaard (2013).

Fig. 2.8 provides an overview over soil NO emission as function of several parameters following Pilegaard (2013). Generally, NO emissions depend linearly on the nitrogen input into the soil system whereby the slope also depends on the vegetation and input type.

Provided that other factors are not limiting NO emissions, higher temperatures stimulate microbial activity in the soil leading to higher emission rates.

The soil water content plays a crucial role in sNO_x by transporting NO_3^-, NH_4^+ as well as O_2 within the soil and thus regulates whether nitrification or denitrification dominates. While nitrification is the dominant process for NO-releases from dry, well-ventilated soils, denitrification dominates for wet soils (with a water-filled pore space of more than 60 %). sNO_x emission rates typically show a pronounced optimum at a distinct soil water content, which is, however, very variable for different soil types and properties (e.g. Schindlbacher et al., 2004; Meixner and Yang, 2006; Yu et al., 2008).

Although NO emissions depend on ambient pH values there is no clear relationship to the absolute amount of emissions. This is because the different sNO_x producing processes (nitrification, denitrification and chemodenitrification) dominate at different pH values.

In addition, agricultural management practices such as soil cultivation, fertilization and irrigation can also strongly affect the fluxes (Bouwman et al., 2002).

Enhanced emissions after rewetting / pulsing events. Many studies report an increased (or: pulsed) release of NO and other trace gases from desiccated soils after rewetting which is either controlled in laboratory or induced by natural precipitation (e.g., Anderson and Levine, 1987; Williams et al., 1987; Johansson and Sanhueza, 1988; Davidson et al., 1991; Williams et al., 1992; Valente and Thornton, 1993; Guenzi et al., 1994; Levine et al., 1996;

Scholes et al., 1997; Kirkman et al., 2001). This effect is mainly explained by a sudden re-activation of micro-organisms consuming the accumulated nutrients during the dry phase. For example, in tropical ecosystems soils accumulate inorganic nitrogen through N-fixing micro-organisms during the dry season. Water-stressed microbes trapped in the soil then become activated by the first rain event of the wet season and release NO as a by-product of nitrogen consumption (Davidson, 1992a). Furthermore, it is assumed that optimal soil water contents that provoke microbial activity are reached during both the wetting and subsequent drying-out of the soil. In addition to the quick response in microbial activity also other (abiotic) causes may contribute to the release of NO such as the efflux of intracellular solutes, extracellular enzymes from dead microbes or chemidesorption from the soil surface (Kleft et al., 1987; Warneke et al., 1999; Blagodatskava and Kuzyakov, 2013; Veres et al., 2014).

On a global basis, the fraction of sNO_x attributed to pulsing is in the range of 10 to 22 % (Davidson, 1992a; Steinkamp and Lawrence, 2011). Several studies utilizing satellite observation (e.g. Jaeglé et al., 2004; Bertram et al., 2005; Ghude et al., 2010; Hudman et al., 2012) point out that enhanced emissions of sNO_x occurring during the transition phase between the dry and wet season may significantly influence the annual total NO_x emissions.

NO release rates from soils. The release rates of NO from soils is typically quantified in terms of a mass flux of nitrogen (N). An extensive list summarizing studies on these soil emission rates was compiled by Stehfest and Bouwman (2006) and with focus on rewetting by Kim et al. (2012). In general, the release rates of NO from soils exhibit an extreme spatial and temporal variability and strongly depend on the individual soil type and prevailing environmental conditions. According to literature (e.g. Stehfest and Bouwman, 2006; Kim et al., 2012, and references therein), average soil NO release rates are in the order of 0.1 to 20 $\mathrm{ng\,N\,m^{-2}\,s^{-1}}$ while fertilized soils tend to show higher average fluxes of about 1 to 50 $\mathrm{ng\,N\,m^{-2}\,s^{-1}}$.

Many studies investigate pulsed emissions of sNO_x either observed in-field or by laboratory measurements of soil samples (e.g., Anderson and Levine, 1987; Williams et al., 1987; Johansson and Sanhueza, 1988; Davidson et al., 1991; Williams et al., 1992; Valente and Thornton, 1993; Guenzi et al., 1994; Levine et al., 1996; Scholes et al., 1997; Kirkman et al., 2001). They find that relative enhancements in sNO_x after rewetting can exceed 100 % to 4000 % (whereby fertilized soils show largest enhancements). In absolute numbers, such pulses typically range between 2 to 60 $\mathrm{ng\,N\,m^{-2}\,s^{-1}}$, but can be as high as 160 $\mathrm{ng\,N\,m^{-2}\,s^{-1}}$ (Valente and Thornton, 1993) or even 900 $\mathrm{ng\,N\,m^{-2}\,s^{-1}}$ as was recently observed by (Oikawa et al., 2015) in a high-temperature agricultural region in California, USA.

2.2.3 Sinks of NO_x

During daytime, NO_x is mainly removed from the atmosphere by oxidation with OH producing nitric acid (HNO_3) (Jacob, 1999; Monks, 2005) which is an important component of acid deposition and contributes to nitrate aerosol formation (Bassett and Seinfeld, 1983).

$$NO_2 + OH \longrightarrow HNO_3 \tag{2.15}$$

At night, N_2O_5 hydrolysis on aerosol surfaces is the dominant sink of NO_x (Jacob, 1999). This process is initiated when NO_2 reacts with ambient O_3 to form NO_3 and O_2.

$$NO_2 + O_3 \longrightarrow NO_3 + O_2 \tag{2.16}$$

NO_3 further reacts with NO_2 producing N_2O_5:

$$NO_3 + NO_2 + M \rightleftharpoons N_2O_5 \tag{2.17}$$

N_2O_5 can react heterogeneously with aerosols in the air producing two HNO_3 molecules.

$$N_2O_5 + H_2O \longrightarrow 2HNO_3 \tag{2.18}$$

NO_2 is mainly removed by wet deposition through either precipitation scavenging or fog water deposition on surfaces. Furthermore, NO_x is also removed by NO_2 deposition on vegetated surfaces (Ganzeveld et al., 2002).

For near-surface NO_2, the lifetime (τ) thus depends on ambient meteorological condition and humidity but also on the concentration of O_3 and OH. The lifetime of NO_2 can thus vary between a day for a clean and remote atmosphere to only 2 hours in a highly polluted environment.

Nitrogen containing gases (such as HNO_3, NO_3, N_2O_5 and others) that were produced in processes involving NO_x are typically summed as NO_y and represent a NO_x reservoir as some of these gases can be transformed back to NO_x through photolysis or other reactions. The most prominent and important reservoir species for NO_x, however, is peroxyacetic nitric anhydride ($CH_3COO_2NO_2$). This species is more commonly known as peroxyacetyl nitrate (PAN) and is formed by oxidation of non-methane volatile organic compounds (NMVOCs) in the presence of NO_x (Singh and Hanst, 1981). Due to its long lifetime of several months at low temperatures, it has significant implications for long-range transport of NO_x and is responsible for background levels of NO_x in the Troposphere.

2.2.4 Impact on tropospheric ozone

Tropospheric O_3 negatively impacts life on Earth by degrading air quality as the exposure to O_3 causes a wide range of health issues for humans (WHO, 2003) and also leads to diminished plant growth and crop production (e.g. Heck et al., 1986; Krupa et al., 2001; Grantz et al., 2006). Although the reactions within the NO-NO_2 feedback loop (Eq. 2.1

and 2.3) involve O_3, they do not lead to a net production of O_3.

However, in the presence of peroxy radicals (HO_2) or organic peroxy radicals (RO_2, with an organic group as R), which are both generated from the oxidation of VOCs, alternative pathways for the NO to NO_2 conversion arises that leads to a net O_3 production:

$$NO + HO_2 \longrightarrow NO_2 + OH \tag{2.19}$$

$$NO + RO_2 \longrightarrow NO_2 + RO \tag{2.20}$$

Both reactions do not consume an O_3 molecule for the production of NO_2 and even lead to additional O_3 formation as NO_2 is photolyzed in the following (Eq. 2.2).

In consequence, O_3 production increases almost linearly with an increase in NO concentration for low NO_x conditions (Fig. 2.9). Conversely, at high NO_x levels, the oxidation of NO_2 by OH (Eq. 2.15) suppresses the oxidation of CO and VOCs. This leads to less HO_2 and RO_2 and, thus, limits O_3 production.

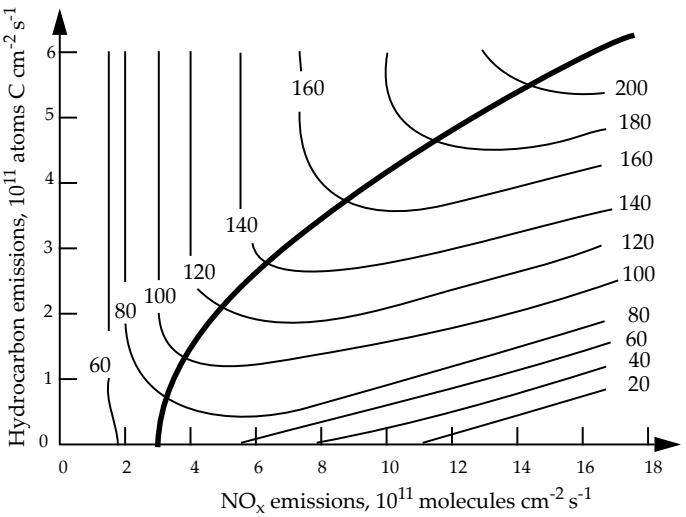

Figure 2.9: Illustration adapted from Sillman et al. (1990) and Jacob (1999) showing O_3 concentrations (ppbv) simulated by a regional photochemical model as a function of NO_x and hydrocarbon emissions. The bold black line distinguishes the NO_x-limited (top left) and hydrocarbon-limited (bottom right) regimes.

2.2.5 Impact on aerosol formation

During daytime, NO_x is mainly removed from the atmosphere by oxidation with OH producing HNO_3 (Eq. 2.15). When ammonia (NH_3) is present in the air, it reacts with HNO_3 to form ammonium nitrate (NH_4NO_3):

$$NH_3 + HNO_3 \rightleftharpoons NH_4NO_4 \tag{2.21}$$

NH_4NO_3 has direct implications on aerosol (and $PM_{2.5}$) levels as it can exist as solid particle or in solution (Finlayson-Pitts and Pitts, 2000). The solid particle starts to form a liquid solution at the deliquescence point of about 62 % relative humidity at 25 °C.

Due to enhanced emissions of NO_x and NH_3 from cultivated (and mostly strongly fertilized) soils, agricultural regions are prone to exhibit higher levels of ammonium nitrate aerosols.

Several studies (e.g. Hodan and Barnard, 2004; Blanchard and Hidy, 2005; Lelieveld et al., 2015; Pusede et al., 2016) point out that the reduction of emissions NO_x emissions can directly lead to drastic decreases in ammonium nitrate and $PM_{2.5}$ levels.

2.3 The role of HCHO in the Troposphere

Formaldehyde (HCHO), also known as *methanal*, is the simplest aldehyde and belongs to the group of volatile organic compounds (VOC). The latter are defined as gases that have a high vapour pressure at room temperature (owing to a low boiling point) and thus easily evaporate or sublimate at typical near-surface temperatures in the atmosphere. HCHO has a wide range of implications on tropospheric chemistry, for example being a precursor for HO_2 and, thus, indirectly impacting O_3 formation. Similar to other toxic air pollutants, HCHO can cause severe damage to human health both outdoor and indoor (from chemical treatment of furniture/wood/carpets).

2.3.1 Sources of HCHO

Primary sources of HCHO comprise (incomplete) combustion processes during fires / biomass burning, fossil fuel combustion as well as other industrial processes. In addition, HCHO is also formed as an intermediate in the oxidation of many hydrocarbons and VOCs which are abundant in the air (such as methane) or emitted from e.g. anthropogenic sources or vegetation. Thereby, one of the most important biogenic precursors of HCHO is isoprene (C_5H_8) which is emitted by plants and oxidized by ambient OH in the atmosphere (Carlier et al., 1986; Altshuller, 1993; Anderson et al., 1996; Kesselmeier, 2001).

HCHO in the background atmosphere is mainly a secondary product of the photochemical destruction of methane (CH_4) and other hydrocarbons. Due to the relatively long lifetime of methane in the Troposphere (about 5–10 years), methane oxidation provides an almost constant source for HCHO.

In addition, also the oxidation of non-methane hydrocarbons (NMHCs) such as ethane (C_2H_4), propene (C_3H_6) and isoprene (C_5H_4) lead to HCHO production. In consequence, volume mixing ratios of HCHO in the background atmosphere are between 0.1–2.0 ppbv. The following reaction path is exemplified for methane but is also applicable to other hydrocarbons. The main reaction of methane is with OH forming a methyl radical CH_3 and H_2O:

$$CH_4 + OH \longrightarrow CH_3 + H_2O \tag{2.22}$$

CH_3 then reacts rapidly with ambient O_2 to form a methyl peroxy radical CH_3O_2:

$$CH_3 + O_2 + M \longrightarrow CH_3O_2 + M \tag{2.23}$$

In regions where NO is present, CH_3O_2 reacts with NO to produce NO_2 and the methoxy radical CH_3O which is again a precursor for HCHO:

$$CH_3O_2 + NO \longrightarrow CH_3O + NO_2 \tag{2.24}$$

$$CH_3O + O_2 \longrightarrow HCHO + HO_2 \tag{2.25}$$

HO_2 produced in the latter reaction can further react with NO (Eq. 2.19) to form NO_2 and OH which, in turn, impacts O_3 production.

In result, HCHO is produced as a secondary product in the oxidation of a wide range of VOCs. This leads to enhanced HCHO mixing ratios in urban areas as well as in regions with extensive forests and vegetation cover due to enhanced emissions of biogenic VOCs. In consequence, volume mixing ratios of HCHO can exceed 1-20 ppb in polluted urban areas.

2.3.2 Sinks of HCHO

HCHO is mainly removed from the atmosphere either by the reaction with OH (Eq. 2.26) or by photolysis (Eq. 2.27 and 2.28).

$$HCHO + OH \longrightarrow HCO + H_2O \tag{2.26}$$

The photolysis of HCHO produces carbon monoxide (CO) or HCO and hydrogen radicals. Thereby two reaction paths are possible whereby Eq. 2.27 dominates for wavelengths greater than 325 nm and Eq. 2.28 at shorter wavelengths.

$$HCHO + hv \xrightarrow{\lambda<365\ nm} CO + H_2 \tag{2.27}$$

$$HCHO + hv \xrightarrow{\lambda<337\ nm} HCO + H \tag{2.28}$$

During night, HCHO can be also removed from the atmosphere through the reaction with NO_3, which happens, however, quite slowly.

$$HCHO + NO_3 \longrightarrow HNO_3 + HCO \tag{2.29}$$

H and HCO produced through the above reactions react rapidly with O_2 to produce HO_2 (and CO):

$$H + O_2 + M \longrightarrow HO_2 + M \tag{2.30}$$

$$HCO + O_2 \longrightarrow HO_2 + CO \tag{2.31}$$

Furthermore, HCHO can be also removed by wet and dry deposition (e.g. on vegetation surfaces).

Due to its numerous sinks, HCHO has a relatively short atmospheric lifetime of a few hours that depends on light conditions, OH and humidity. In consequence, elevated HCHO concentrations are mainly observed close to its emission sources such as urban

areas, traffic routes (including shipping lanes), biomass burning regions as well as forested areas such as the Tropics (Fig. 2.10).

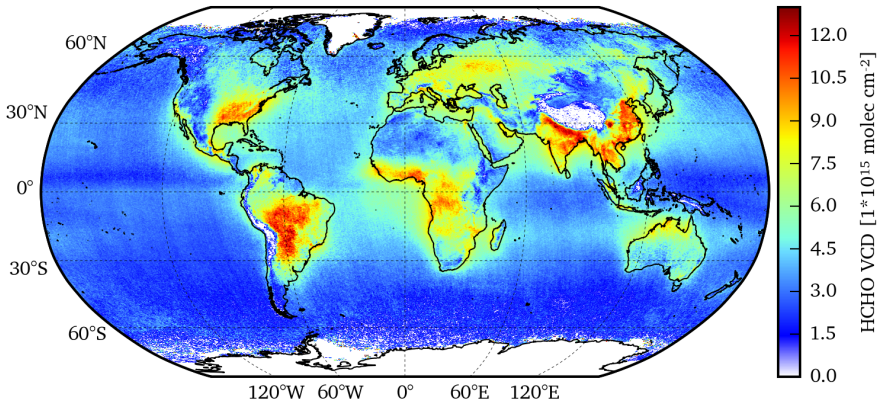

Figure 2.10: Tropospheric HCHO VCDs averaged over the years 2005 to 2009 as observed by the OMI satellite sensor. Level-2 data taken from http://www.temis.nl

2.3.3 Exchange with soils

Recent advances (Asensio et al., 2007; Peñuelas et al., 2014, and references therein) indicate that soils may act as relatively large reservoir and source for biogenic VOCs (including HCHO). VOC emissions from soils are mainly formed as an intermediate during (microbial) decomposing of litter and dead organic material (Isodorov and Jdanova, 2002; Gray et al., 2010; Leff and Fierer, 2008) but are also synthesized by micro-organisms in the soil or released during physiochemical ad- and desorption from organic matter. Leff and Fierer (2008) thereby found correlations between the release rates of VOCs and parameters like the microbial biomass, the total nitrogen and carbon content as well as the CO_2 production rates. However, it is assumed that biogenic VOC emissions from soils are about one to two orders of magnitude lower than those from the vegetation above (Peñuelas et al., 2014).

Soils may act both as a sink and as a source for HCHO depending on ambient conditions and concentrations of HCHO. Li et al. (2016), for example, showed that two-thirds of the adsorbed HCHO can be re-emitted to the atmosphere and stress that this kind of reversibility must be taken into account when studying the trace gas exchange between the soil and the atmosphere.

Veres et al. (2014) tested the effect of soil moisture and temperature on VOC emission rates in laboratory measurements and found that several VOCs including HCHO exhibit pulsed emissions when dry soils are first wetted. However, research studies on (pulsed) soil emissions of VOCs are scarce and thus the knowledge of their impact on the terrestrial system is still limited.

2.4 Remote sensing of trace gases in the UV/VIS

In this thesis, measurements from ground and space-based instruments are used to investigate the spatial and temporal distribution of NO_2 and HCHO. Both trace gases inhibit distinctive narrow absorption structures in the UV-VIS spectral range which enables their detection using absorption spectroscopy techniques. DOAS was put forward by Perner et al. (1976) and Platt et al. (1979) and has played a prominent role in understanding and describing the chemical composition of the atmosphere over the last decades. The following sections provide an overview over the DOAS measurement technique which is used for the analysis of NO_2 and HCHO in this thesis and is mainly based on knowledge from Platt and Stutz (2008).

2.4.1 The concept of absorption spectroscopy

Absorption spectroscopy is a measurement technique that, in principle, makes use of the wavelength-dependent absorption of (electromagnetic) radiation by matter. It is mainly founded on Lambert-Beer's law:

$$I(\lambda) = I_0(\lambda) \cdot e^{-\sigma(\lambda) \cdot c \cdot L} \tag{2.32}$$

Thereby, $I_0(\lambda)$ represents the initial intensity from a light source, $I(\lambda)$ stands for the intensity of the light after passing through a layer with a given thickness (L) and c is the concentration of a given absorber. The absorber is also characterized by its specific absorption cross-section (σ) at a given wavelength (λ).

Subsequently, average concentrations of the absorber in the medium can be calculated by:

$$c = \frac{\ln(\frac{I_0(\lambda)}{I(\lambda)})}{\sigma(\lambda) \cdot L} = \frac{D}{\sigma(\lambda) \cdot L} \tag{2.33}$$

Thereby, D is the optical density of the particular absorber. In the laboratory, Eq. 2.33 can be readily used as I and I_0 can be measured in laboratory conditions by taking a measurement with the absorber present in the medium and one measurement without the absorber. However, this simple method is not applicable to the open atmosphere motivating the advanced concept of DOAS.

2.4.2 Differential Optical Absorption Spectroscopy (DOAS)

The simple form of Lambert-Beer's law does not hold for applications in the atmosphere because the true I_0 cannot be accurately determined in presence of the manifold disturbances compared to a laboratory setting.

A typical measurement scenario in the open atmosphere is presented in Fig. 2.11 which shows the interplay of many processes such as absorption by trace gases, scattering by gas species, aerosols or water droplets (Rayleigh and Mie scattering) as well as turbulences which all lead to attenuation of the initial light (I_0). Thereby, the light extinction through

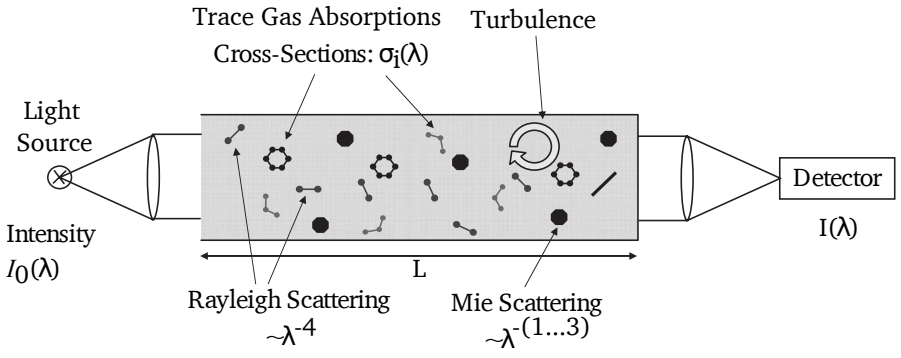

Figure 2.11: Schematic depiction of trace gas measurements in the open atmosphere involving a variety of scattering and absorption processes. Illustration from Platt and Stutz (2008).

scattering on small particles (Rayleigh scattering) is proportional to λ^{-4} (Strutt, 1899) and for scattering on larger particles (described by Mie theory) is proportional to λ^{-n}, where n depends on the particle's size and shape (Mie, 1908). In addition, trace gases and air particles are not homogeneously distributed in the open atmosphere and, in applications measuring scattered sun light, the light beams can follow complicated paths until they are registered at the detector.

To account for all these processes, Lambert-Beer's law (Eq. 2.32) needs to be reformulated for measurements in the open atmosphere as:

$$I(\lambda, L) = I_0(\lambda) \cdot \exp\left[-\int_0^L \cdot \sum_j \left(\sigma_j(\lambda) \cdot c_j(s)\right) + \varepsilon_R(\lambda, s) + \varepsilon_M(\lambda, s) \cdot ds\right] \cdot A(\lambda) \quad (2.34)$$

Thereby, $\varepsilon_R(\lambda)$ and $\varepsilon_M(\lambda)$ are the extinction coefficients for Rayleigh and Mie scattering respectively and $A(\lambda)$ accounts for potential instrumental effects and (the wavelength dependence of) the efficiency of scattering processes, which scatter sun light into the line of sight of the instrument.

In order to calculate the trace gas concentrations in the measured air mass, all factors attenuating the original light (I_0) need to be accurately quantified which is, however, not possible for the open atmosphere. Differential Optical Absorption Spectroscopy (DOAS) solves this problem by utilizing the characteristic spectral absorption features of the influencing factors described above. On the one hand, aerosol extinction, turbulence and many trace gases show smooth, broadband absorption structures while certain gas species show very narrow absorptions, on the other hand. DOAS separates these narrow- and broadband absorption features from one another (Fig. 2.12). The total absorption cross-section thus consists of both parts:

$$\sigma_j(\lambda) = \sigma_{j0}(\lambda) + \sigma'_{j0}(\lambda) \quad (2.35)$$

whereby $\sigma_{j0}(\lambda)$ shows weak variations with wavelength (λ) and $\sigma'_{j0}(\lambda)$ shows strong fluctuations with λ.

Updating Eq. 2.34 to also taking into account these narrow- and broadband absorptions

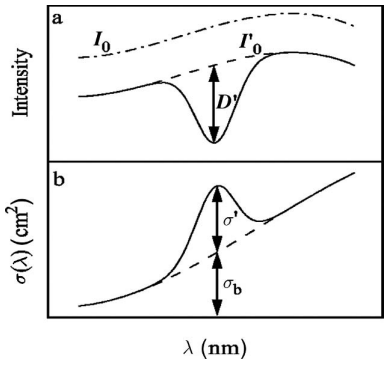

Figure 2.12: The DOAS principle, with I_0 and σ being separated by a filtering procedure into a narrow (D', and σ') and broad band part (I'_0 and σ_b). Illustration from Platt and Stutz (2008).

leads to:

$$I(\lambda, L) = I_0(\lambda) \cdot \exp\left[-\int_0^L \cdot \left(\sum_j (\sigma'_j(\lambda) \cdot c_j(s))\right) \cdot ds\right] \cdot \exp\left[-\int_0^L \cdot \left(\sum_j (\sigma_j 0(\lambda) \cdot c_j(s)) + \varepsilon_R(\lambda, s) + \varepsilon_M(\lambda, s)\right) \cdot ds\right] \cdot A(\lambda) \quad (2.36)$$

Thereby, the first exponential term represents the narrow fluctuations in the absorption spectrum of a gas species and the second term stands for the broader variations per wavelength caused by both gas absorption and scattering processes.

In consequence, the initial light intensity in absence of *differential absorption* can be defined as a new I'_0:

$$I'_0(\lambda) = I_0(\lambda) \cdot \exp\left[-\int_0^L \cdot \left(\sum_j (\sigma_j 0(\lambda) \cdot c_j(s)) + \varepsilon_R(\lambda, s) + \varepsilon_M(\lambda, s)\right) \cdot ds\right] \cdot A(\lambda) \quad (2.37)$$

In the DOAS process, the initial light intensity (I_0) and absorption cross-section (σ) are distinguished between the narrow part, i.e. the differential optical density (D') and differential absorption cross-section ($\sigma' j(\lambda)$), as well as the broad part, i.e. I'_0 and σ_b (Fig. 2.12). In practice, the broadband part of a measured spectrum is typically approximated by a polynomial function. The absorption cross-section of the gas species ($\sigma j(\lambda)$ and $\sigma' j(\lambda)$) are typically predetermined at very high spectral resolution in a controlled laboratory environment.

Based on these considerations, the differential optical density (D') can then be written as (following Eq.2.33):

$$D' = \ln \frac{I'_0(\lambda)}{I(\lambda)} = \int_0^L \left(\cdot \sum_j \sigma'_j(\lambda) \cdot c_j(s)\right) \cdot ds \quad (2.38)$$

Thus, it is now possible to calculate the gas concentrations based on the differential quantities D' and $\sigma'(\lambda)$. As different absorbing gas species in the probed medium each

have a distinct narrowband absorption structure they can be separately quantified in the analysis. A key quantity in DOAS measurements of trace gases is the *column density* (S) [molecules cm^{-2}] which is the integrated concentration of a certain trace gas along the light path in the atmosphere:

$$S = \int_0^L c_j(s) ds \tag{2.39}$$

In this section, the basic principle of the DOAS technique has been described. However, in practical applications a variety of additional factors have to be considered, such as the temperature and pressure dependence of the absorption cross-sections, the instrument function of the spectrometer as well as noise and error terms and, most importantly, the DOAS fitting algorithm. The latter is typically based on a combination of a linear least squares fit and the Levenberg–Marquardt algorithm (LMA) (Levenberg, 1944; Marquardt, 1963) which is a non-linear least-squares fitting process to minimise the difference between the measured and a simulated spectrum. For a detailed description of these topics it is further referred to Platt and Stutz (2008).

DOAS measurements can be acquired in many different measurement environments and set-ups. First and foremost, a distinction can be made between active systems which use an artificial light source (active DOAS) and passive systems that depend on a natural light source like the Sun, Moon or stars (passive DOAS). In this thesis work, both systems were employed and their concepts will be described in the following.

2.4.3 Ground-based approaches

2.4.3.1 Long-Path DOAS

Long-Path DOAS instruments were one of the first DOAS applications (Perner et al., 1976) and follow a (relatively) simple measurement concept: an artificial light source (typically Xenon-arc lamps) is used that sends out the initial light to a retro-reflector, installed several km away, and is then again captured by a spectrometer which is positioned at the light source. Thus, LP-DOAS measures the absorption by trace gases in the atmosphere along a well-defined light path and, furthermore, allows for the direct measurement of the initial light intensity. LP-DOAS systems typically also measure "background" spectra to account for scattered solar light.

Due to the fixed length of the light path during the measurement, average trace gas concentrations ($\bar{c}_j$) can be directly computed by rearranging Eq. 2.39:

$$\bar{c}_j = \frac{S_j}{L} \tag{2.40}$$

Further advantages of this measurement technique compared to passive systems is, on the one hand, the ability to measure at day- and night-time and, on the other hand, to cover a relatively wide spectral range including regions with low solar light such as the deep UV. However, LP-DOAS systems require highly sophisticated optical systems, are very power-intensive and as the instruments are typically large and heavy, the set-up is

cumbersome compared to, for example, the lightweight passive MAX-DOAS instruments.

2.4.3.2 Multi-Axis DOAS (MAX-DOAS)

The Multi-Axis DOAS (MAX-DOAS) measurement principle was introduced by Hönninger and Platt (2002) and Hönninger et al. (2004) and provides a flexible method to derive trace gas column densities for both low and high elevation angles. Previously, scattered-light observations were only performed for zenith-sky measurements, whereby the instrument points to the zenith (90° relative to the surface) and thus the measurements are most sensitive to trace gases in the stratosphere. The MAX-DOAS method also utilizes scattered sunlight which is collected by a telescope pointing towards different elevation angles, i.e. typically between 1° to 90° (Fig.2.13). Thereby, each elevation angle has a different sensitivity to trace gases in the atmosphere depending on the vertical distribution of the trace gases. As the length of the light path usually increases when pointing towards low elevation angles, MAX-DOAS observations are very sensitive to trace gases located in the lowermost atmospheric layer. If a sufficient number of elevation angles are scanned, also vertical profiles of trace gases can be derived.

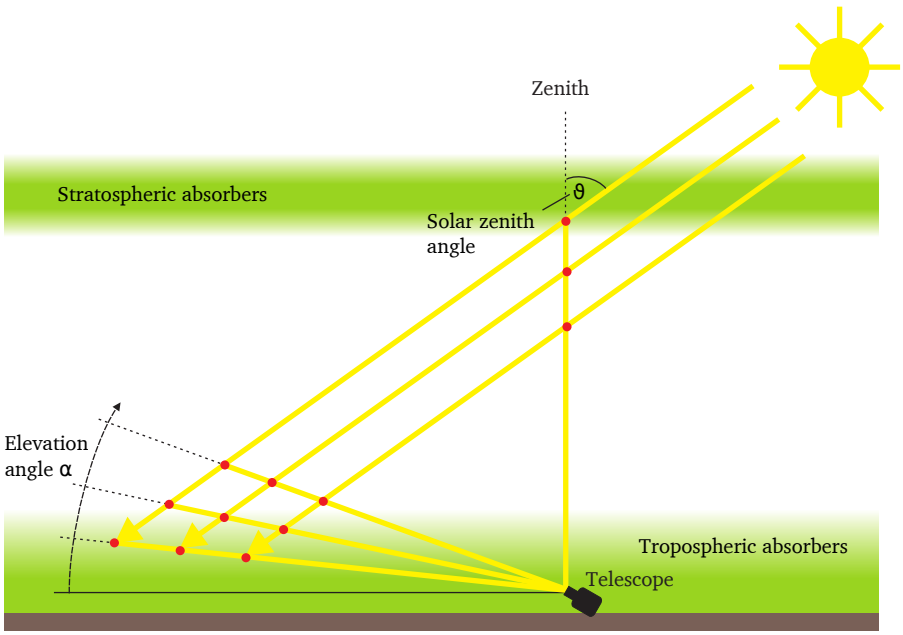

Figure 2.13: Simplified measurement geometry for MAX-DOAS observations adapted from Sinreich (2008). Sun light enters the atmosphere at a given solar zenith angle (SZA) and is scattered at the red points into the line of sight of the MAX-DOAS viewing angle. In reality, however, typically multiple scattering processes occur in the atmosphere affecting the light path. The green shaded areas represent layers with increased trace gas concentrations.

For (scattered) solar light observations, additional considerations need to be made for effects such as the *Fraunhofer Lines*. They originate from absorption and re-emission of radiation within the atmosphere of the Sun and cause strong absorption lines in the solar spectrum as measured from Earth. To account for this effect, a Fraunhofer reference

spectrum (FRS) is measured (by which the other measured spectra are divided). However, in spite of this correction, certain structures remain due to the so-called *Ring effect* (Grainger and Ring, 1962) which results in a filling-in of the Fraunhofer lines by light at neighbouring wavelengths due to inelastic rotational Raman scattering (e.g. Solomon et al., 1987; Wagner et al., 2009). The Ring effect is typically simulated and included as an additional absorber in the DOAS-fit.

The general procedure for MAX-DOAS measurements is straight-forward: typically, measurements of spectra are repetitively taken for a fixed list of elevation angles, e.g. 1°, 2°, 3°, 4°, 5°, 6°, 8°, 10°, 15°, 30° and 90°. So-called *slant column densities* (SCDs) can be then deduced using Eq. 2.39 for each measurement. Differential SCDs (DSCDs, ΔS) represent the difference between the SCD of a measurement (at a low elevation angle) and a reference measurement, typically a zenith measurement at 90° at the end of all low elevation scans. This reference measurement is not only necessary to minimize absorptions by Fraunhofer Lines but also to cancel out effects arising from instrumental instabilities and stratospheric absorptions (e.g. by NO_2 and O_3). Both measurements, the reference and the low elevation measurement, should be measured at approximately the same solar zenith angle (θ) and thus temporally close to each other.

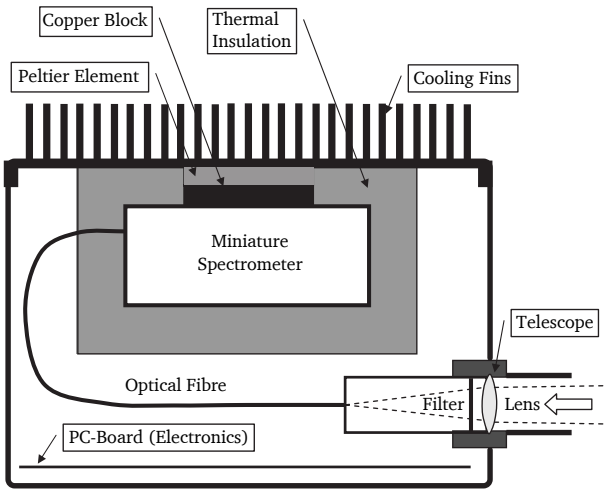

Figure 2.14: Composition a miniature MAX-DOAS system (adapted from Bobrowski (2005)) employed within this thesis project. For measurement scans at different elevation angles, the entire instruments is moved by an external motor.

However, at very large and rapidly changing solar zenith angles in the morning and evening, this becomes difficult as the time difference between the reference and low elevation scan can be about 15 minutes considering the long list of low elevation angles above, whereby each scan is for example integrated over one minute.

DSCDs can then be calculated by:

$$\Delta S(\theta, \alpha) = S(\theta, \alpha) - S(\theta, 90°) \tag{2.41}$$

SCDs can be separated into a tropospheric part (S_{trop}) and the stratospheric part (S_{strat})

which leads to:

$$\Delta S(\theta,\alpha) = (S_{trop}(\theta,\alpha) + S_{strat}(\theta,\alpha)) - (S_{trop}(\theta,90°) + S_{strat}(\theta,90°)) \tag{2.42}$$

Thereby, the SCD depends, on the one hand, on the SZA (mainly controlling the contribution from the stratospheric column), and, on the other hand, on the elevation angle (mainly controlling the contribution from the tropospheric column). As most molecular and particle scattering events occur in the lower part of the atmosphere and the light path through the stratosphere is approximately the same given a constant solar zenith angle (except for situations with, e.g., polar stratospheric clouds), it can be generally assumed that:

$$S_{strat}(\theta,\alpha) \approx S_{strat}(\theta,90°) \tag{2.43}$$

and thus:

$$\Delta S(\theta,\alpha) \approx S_{trop}(\theta,\alpha) - S_{trop}(\theta,90°) \tag{2.44}$$

Within this thesis work, miniature MAX-DOAS instruments (Mini-MAX-DOAS) were employed. Their schematic composition is presented in Fig. 2.14 and more detailed specifics are given in Section 5.3.1. The light is collected through a quartz lens and transported via a quartz fibre bundle to the spectrograph. The spectrograph is cooled by a (thermoelectric) Peltier element to a constant temperature to minimize changes in the optical properties of the spectrograph. A stepper motor outside of the metal box of the instrument rotates the entire instrument to different elevation angles.

2.4.4 Total columns and profiles from Multi-Axis DOAS

One of the most challenging tasks in passive DOAS applications is the retrieval of total columns and concentration profiles for different altitudes. In order to obtain total columns from the MAX-DOAS observations, either a geometric approximation or inverse modelling by radiative models can be conducted as outlined in the following. As shown in Eq. 2.39, SCDs strongly depend on the length of the light path and, thus, cannot be directly compared to one another. Thus, the concept of vertical column densities (VCDs, V) is introduced which is the vertically integrated concentration of trace gases from the ground to the top of the atmosphere (TOA):

$$V = \int_0^{TOA} c(z) \cdot dz \tag{2.45}$$

The use of the VCD is advantageous because it neither depends on the wavelength, nor on the light path or the measurement geometry and, thus, can be compared among different instrument types, i.e. ground-based and space-based systems. However, the VCD is not directly measured but must be inferred from the corresponding SCD which poses a large challenge especially for passive DOAS systems where the actual light path is not accurately known. The conversion from SCDs to VCDs is based on knowledge from radiative transfer calculations that simulate the state of the atmosphere at the time of the measurement. For

this purpose, the air mass factor (AMF) (Noxon et al., 1979; Solomon et al., 1987) accounts for various processes in the atmosphere and approximates the effective light path. It is defined as the ratio of the SCD and the VCD:

$$AMF = \frac{SCD}{VCD} \tag{2.46}$$

The AMF generally depends, on the one hand, one the measurement geometry and, on the other hand, on atmospheric conditions such as the aerosol and trace gas profiles or cloud coverage.

For simplistic considerations (neglecting refraction in the atmosphere), a direct, geometrical conversion of the SCDs to VCDs can be performed using the *geometrical approximation* (Hönninger and Platt, 2002) for tropospheric VCDs:

$$V_{trop} = \sin(\alpha) \cdot S_{trop}(\alpha) \tag{2.47}$$

and similarly for stratospheric VCDs:

$$V_{strat} = \cos(\theta) \cdot S_{strat}(\theta) \tag{2.48}$$

This approximation only holds for elevation angles (α) larger than 20° and solar zenith angles (θ) lower than 70° because of otherwise increased scattering within the trace gas layer. For such more complicated cases the use of radiative transfer models (RTMs) to estimate the AMF for a specific absorber is indispensable. RTMs require presumed atmospheric profiles of various parameters (e.g. pressure, temperature, humidity, aerosols, traces gases) as well as information on clouds, aerosols and the surface albedo which all may influence the radiative transfer in the atmosphere. The radiative transport model is then initialized by specifying the measurement geometry (position of the Sun and the detector). The modelling is typically performed in a two-way approach, i.e. one run including the absorber of interest and in a second run without the absorber. As a result, atmospheric profiles for the absorber as well as the SCD and VCD are simulated based on the atmospheric state and the corresponding AMF can be directly inferred from Eq. 2.46.

2.4.5 Space-based systems

Vertical column densities (VCDs) of trace gases such as NO_2 and HCHO can be retrieved from nadir-viewing satellite instruments in a similar fashion as for ground-based instruments, i.e. by analysing solar backscatter radiances in the UV-VIS spectral range using the DOAS approach (Richter and Wagner, 2011). Such satellite instruments traverse the Earth in a sun-synchronous polar orbit (Fig. 2.15) and cross the Equator always at the same local time (Burrows et al., 2011). They fly at a relatively low altitude (around 800 km) compared to geostationary satellites (at around 36 000 km) which permits the scan of the whole Earth with a high spatial resolution within one or few days (depending on the satellite sensor). The most important difference to MAX-DOAS arises from the different

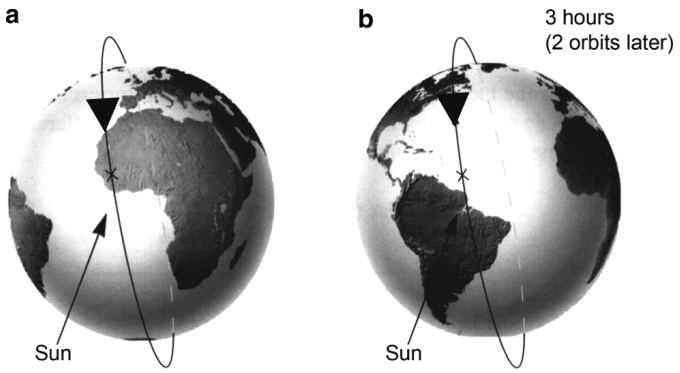

Figure 2.15: Schematic scheme, adapted from (Burrows et al., 2011), depicting a sun-synchronous polar orbit (Fig. 2.15) used for UV/VIS satellite instruments.

measurement geometry of the satellite instrument. Albeit the nadir view of the sensor is almost perpendicular to the Earth's surface, the viewing directions slightly changes in a periodic manner in order to expand the field of observation. Thus, the viewing geometry is given by the SZA, the line of sight (LOS) being the angle between the viewing direction and the nadir and the solar relative azimuth angle.

A simplified measurement geometry is depicted in Fig. 2.16 and also shows the impact of complex atmospheric scattering compared to pure surface reflection. Under clear-sky conditions and for SZAs lower than 70° the simplistic view from Fig. 2.16a can be used for the geometrical conversion of stratospheric SCDs to stratospheric VCDs:

$$AMF = \frac{1}{\cos(LOS)} + \frac{1}{\cos(SZA)} \tag{2.49}$$

For tropospheric absorbers, however, this is not possible because of increased scattering on air molecules (Rayleigh) towards the surface (Fig. 2.16b) and, hence, sophisticated RTM calculations have to be conducted to estimate the AMF. The latter is derived from RTMs taking into account information on ground albedo, aerosols and clouds, the vertical profile of the trace gas and the satellite viewing geometry (e.g. Palmer et al., 2001; Richter and Burrows, 2002; Martin, 2003).

In practice, tropospheric VCDs of NO_2 and HCHO are usually derived in a multi-step process (e.g. Leue et al., 2001; Boersma et al., 2004, 2007; De Smedt et al., 2008, 2012). First, total SCDs are retrieved by fitting the measured spectrum with a model taking into account all other absorbers in the atmosphere. Second, tropospheric SCDs are derived by subtracting the stratospheric column (NO_2) or a latitude-dependent bias estimated over the Pacific[1] (HCHO). Third, the tropospheric SCDs are then translated to tropospheric VCDs by dividing the SCDs by the simulated AMF. In practical applications a height-resolved AMF, i.e. a *Box-AMF*, is utilized which is, however, not discussed within this thesis. A more detailed description of the retrieval algorithms from satellite instruments is

[1]The standard deviation of HCHO columns over a clean equatorial Pacific region (no NMVOC oxidation and weak daily variation in CH_4 oxidation) are used as a measure of the random noise of the measurements (De Smedt et al., 2012).

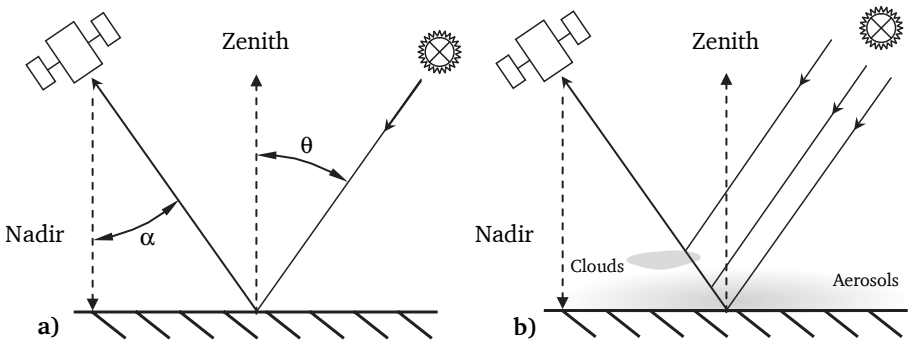

Figure 2.16: Simplified measurement geometry of a (near) nadir viewing satellite instrument adapted from Platt and Stutz (2008), with line of sight angle (LOS, ψ), solar zenith angle (SZA, θ) whereby **a)** shows a case without scattering in the atmosphere but only surface scattering and **b)** indicates the potential for many scattering events caused by clouds and aerosols.

given by Richter and Wagner (2011) and for the individual trace gas products by Boersma et al. (2004) and Boersma et al. (2007) for NO_2 and by De Smedt et al. (2008) and De Smedt et al. (2012) for HCHO.

Except for situations with very low tropospheric trace gas column densities, the tropospheric AMF dominates the uncertainty of tropospheric trace gas observations from space, e.g. caused by an insufficient description of the atmosphere in the RTM with respect to the trace gas profiles, aerosols, cloud properties and cloud cover (Boersma et al., 2004). For observations of trace gases in the boundary layer, which are the focus of this study, the main effect of clouds is that they shield the atmosphere below. Thus, in the presence of clouds the retrieved trace gas absorptions (SCDs) are usually decreased compared to clear-sky conditions. During the conversion to VCDs, the AMF compensates for this effect which, however, might lead to over- or underestimations of the trace gas column densities if the state of the atmosphere is not known precisely.

Throughout the manuscript, trace gas information retrieved from three different satellite instruments are used. Thereby, so-called 'level-2' data products, i.e. retrieved NO_2 and HCHO VCDs and SCDs, from the Tropospheric Emission Monitoring Internet Service (TEMIS) are used[2]. The satellite pixels, which are quadrilaterals by default, are screened for typical data quality flags and gridded on a global regular latitude-longitude grid using an area-weighted scheme (at a spatial resolution of 0.25° for the global study in Chapter 3 and at 0.1° for the regional study in Chapter 4). The individual satellite instruments which were used to measure the NO_2 and HCHO column densities are described in the following.

2.4.5.1 Ozone Monitoring Instrument (OMI)

The Ozone Monitoring Instrument (OMI) is a nadir-viewing near-UV/Visible 2-D CCD spectrometer aboard NASA's Earth Observing System's (EOS) Aura satellite (Levelt et al., 2000, 2006). Aura was launched in July 2004 and orbits the Earth in a polar Sun-

[2]TEMIS data is publicly available at: http://www.temis.nl

synchronous orbit at 705 km altitude and crosses the Equator at about 1:30 p.m. local time.

OMI measures back-scattered solar radiation in the UV and VIS spectral regions and can provide daily global coverage combining 14 orbits per day. The solar radiation that enters the telescope is split into two channels. The VIS channel covers the wavelength range between 365 to 500 nm with a resolution of 0.62 nm. The UV channel consists of two sub-channels (UV-1 and UV2) covering 270 to 310 nm and 310 to 365 nm with a resolution of 0.42 nm and 0.45 nm, respectively. OMI mainly operates in the 'Global measurement

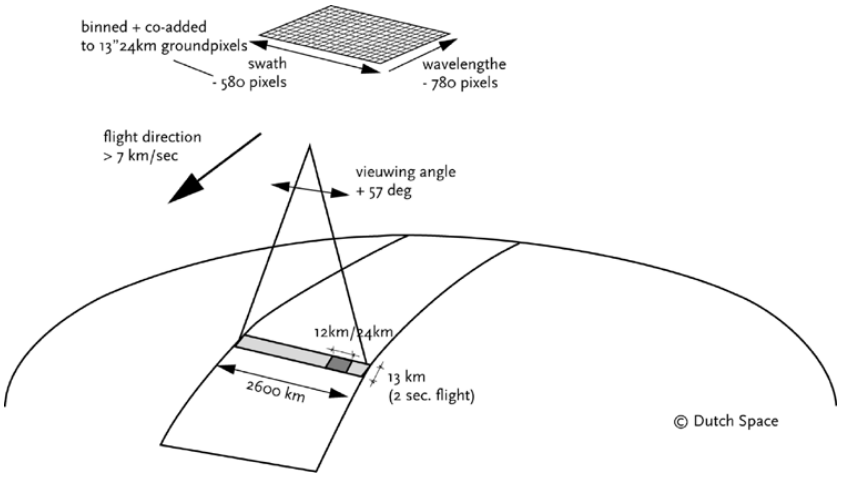

Figure 2.17: Illustration from Levelt et al. (2006) depicting the OMI Global measurement mode. Due to the wide field of view (114°), the pixel sizes steeply increase towards the edge of the swath.

mode' but also has two further modes, i.e. the Spatial zoom-in mode and the Spectral zoom-in mode, which are however infrequently used. In the Global measurement mode, OMI has a ground pixel size of 13x24 km^2 (for the UV-2 and VIS channels) at nadir and, due to its wide field of view of 114°, the pixel sizes steeply increase towards the far ends of the 2600 km^2 wide swath to about 150 km. The pixel size of the UV-1 channel is about 13x48 km^2 at nadir because of the optical design of the channel to reduce stray light. The 2-D CCD detector (780 x 576 pixels) of OMI permits the simultaneous measurement of spectral and spatial information and samples the Earth in a *push-broom* manner as the satellite orbits the Earth. The total integration time of a measurement is always 2 s, whereby typically five measurements à 0.4 s are co-added, which then results in a 13 km pixel size in the flight direction.

Since June 2007, an anomaly developed that affects the Earth radiance measurements at all wavelengths for particular viewing angles. This so-called *row anomaly*[3] (Boersma et al., 2011) can vary with time and location and affects OMI measurements by the (i) blockage effect, i.e. a decrease in the radiance level, (ii) direct solar radiation, i.e. an increase in the radiance level, (iii) a wavelength shift and (iv) additional light that is reflected from outside the nominal field of view entering the sensor.

[3]Official statement to the row anomaly available at: http://projects.knmi.nl/omi/research/product/rowanomaly-background.php

In this work, pixels affected by the row anomaly as well as the two outermost OMI pixels (pixels with the largest viewing angles and lowest spatial resolution) are screened out.

2.4.5.2 Global Ozone Monitoring Experiment 2 (GOME-2)

The Global ozone monitoring experiment 2 (GOME-2) (Callies et al., 2000; Munro et al., 2006; EUMETSAT, 2011) is a nadir scanning optical UV-VIS spectrometer aboard ESA's METOP-A satellite which was launched in October 2006. An identically constructed instrument was mounted on the METOP-B satellite launched in September 2012, which is, however, not used within the thesis work. The METOP-A satellite is on a polar Sun-synchronous orbit flying at about 817 km above Earth and crossing the Equator at about 9:30 a.m. local time.

The scanning mirror of GOME-2 enables across-track scanning in nadir and directs scattered sunlight from the Earth into the instrument which is then subdivided into four different wavelength regions (240–315 nm, 311–403 nm, 401–600 nm and 590–790 nm) with a spectral resolution (FWHM) between 0.25 nm and 0.5 nm. The spectrum is then captured by silicon photo-diode detector arrays containing 1024 pixels each. In addition, the mirror can also point sideways for polar coverage and measurements towards the Moon or to a Sun diffuser for direct sunlight measurements. GOME-2 also contains two Polarisation Measurement Devices (PMDs) that support the consideration of the polarisation state of the collected light.

Besides other scanning modes, the main measurement mode of GOME-2 scans the Earth across-track in nadir with a maximum off-nadir angle of 50° and thus a total swath-width of 1920 km allowing for a complete global coverage every $\sim$ 1.5 days. As the satellite instrument circles the Earth the mirror scans periodically from East to West within 4.5 s (forward scan) and back in 1.5 s (backward scan). This measurement scheme is also referred to as 'whisk-broom' scanning mode (Fig. 2.18). At a typical 187.5 ms integration time per spectrum, 24 measurements (or satellite pixels) are captured (with a ground footprint of 40x80 km^2) in forward direction and 8 measurements in backward direction (with a ground footprint of 40x240 km^2). These backward scan pixels are not used within this thesis because of their relatively large spatial resolution.

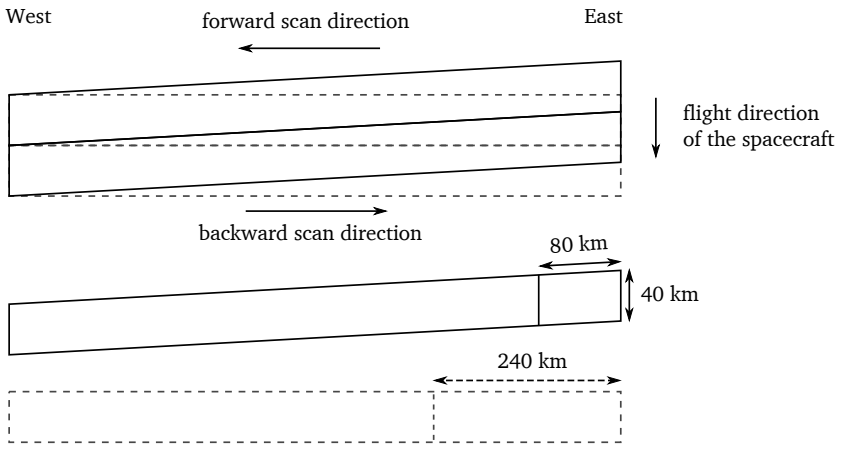

Figure 2.18: Illustration of the nadir 'whisk-broom' GOME-2 scan pattern adapted from EUMETSAT (2011). During a *forward scan*, the mirror scans from East to West and moves back about three times faster to the original position resulting in lower ground pixel resolution in the *backward scan*.

2.4.5.3 SCanning Imaging Absorption SpectroMeter for Atmospheric CHartographY (SCIAMACHY)

The SCanning Imaging Absorption SpectroMeter for Atmospheric CHartographY (SCIAMACHY) (Bovensmann et al., 1999; Gottwald et al., 2006) was a passive remote sensing spectrometer observing backscattered radiation from the Earth. It was mounted aboard the ENVIronmental SATellite (ENVISAT) which was launched in March 2002 and operated until 2012. ENVISAT was flying at 790 km in a polar, Sun-synchronous orbit with a local equator crossing time at 10:00 am.

SCIAMACHY was able to perform measurements in three different viewing geometries, i.e. in nadir, limb, and Sun or Moon occultations (Fig. 2.19). This peculiarity of the SCIAMACHY instrument facilitated not only the retrieval of nadir observations of trace gases and aerosols, but also the derivation of vertical distribution profiles (mainly for the stratosphere). Typically, alternating nadir and limb observations were performed, which resulted in consistent data gaps along track in either product and, thus, global coverage was reached only after six days.

The backscattered radiation was directed by the nadir mirror into a telescope focusing the beam onto the spectrometer. The wavelength range 240 nm to 1700 nm and further regions between 2000 nm to 2400 nm were recorded at a spectral resolution of 0.2 nm to 0.5 nm.

The SCIAMACHY instrument performed measurements in the 'whisk-broom' mode (similar to GOME-2) whereby, the achievable ground pixel size for the forward scans (in the VIS) were 15x30 km^2, but due to the restricted bandwidth for data transmission four observations were integrated which lead to a general ground footprint of about 60x30 km^2. For the UV wavelength range, the ground pixel size was about 120x30 km^2. The backward scans were divided into four pixels of 240 km each.

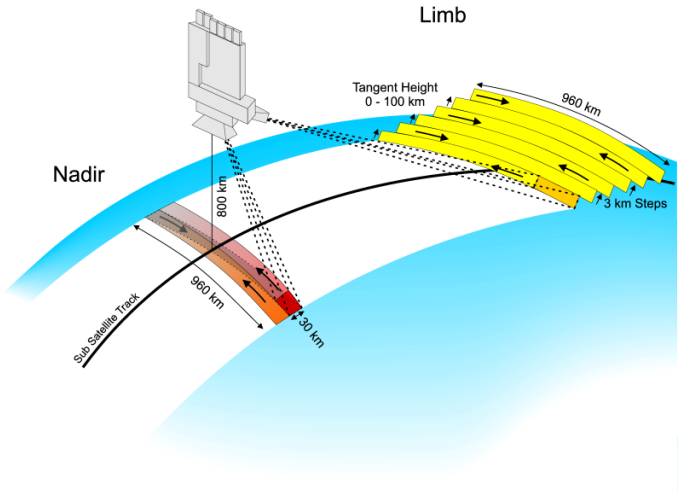

Figure 2.19: SCIAMACHY measurement geometry in Limb and Nadir scanning mode from Noël et al. (2000).

CHAPTER 3

Enhanced soil emissions of NO_x in semi-arid regions following precipitation

3.1 Research objectives and strategy

Hudman et al. (2012) showed that intense but short events of soil emissions, i.e. pulsed emissions, at the start of the wet season after a prolonged dry spell represent a large fraction of annual soil emissions in the Sahel region. As noted by Hudman et al. (2012) further research needs to be done to investigate to which degree the observed pulses by OMI (Ozone Monitoring Instrument) might be biased by the retrieval algorithm.

The main objective of this chapter is to quantify precipitation-induced short-term enhancements in soil emissions of NO_x, which show peak emissions on the scale of 1–3 days, from space-based instruments in semi-arid regions in the world. This is achieved by investigating the evolution of tropospheric NO_2 column densities from multiple satellite sensors before and after the first rainfall events on the onset of the wet season.

Here, an optimized algorithm is introduced that synchronizes and averages multiple time series of atmospheric variables either from one location only, or from a larger number of grid pixels, by aligning them on a relative timescale to each other. This algorithm enhances the basic approach described by Hudman et al. (2012) with several features: (i) performing the analysis globally with (ii) high spatial resolution, which is both achieved by expanding the time span of the study to several years (2007 to 2010) enabling an investigation of single grid pixels of 0.25° with reasonable statistics. (iii) The full track of the temporal evolution several weeks before and after a rain pulse is retained with daily resolution. (iv) By intercomparing measurements of NO_2 from multiple satellite instruments it is possible to quantify potential measurement artefacts and investigate the impact of different retrieval algorithms. Furthermore, sensitivity studies are conducted in order to evaluate the impact of the a priori assumptions on thresholds for daily rainfall, i.e. the definition of drought, and its requested duration.

The approach is a purely *top-down* method, in the sense that satellite data of trace gases are exclusively used to describe and quantify phenomena taking place on the Earth's surface and atmosphere. It is, therefore, extremely important to consider processes in the atmosphere that could trigger soil emissions or may affect the retrieved NO_2 column densities in other ways. In order to assess the prevailing meteorology, total columns of

water vapour, humidity, temperature as well as the wind direction are incorporated in the analysis. To verify that the observed responses in the trace gas column densities reflect the impact of emission fluxes from the soil, possible interferences from other parameters, e.g. fires, modified cloud fractions, coincidences with lightning events and horizontal transport from polluted regions, are also investigated.

This chapter also addresses the question whether HCHO emissions from semi-arid soils can be observed from satellite-borne sensors.

In contrast to previous satellite studies, this investigation makes a clear distinction between (i) pulsed emissions which show strong gradients on a day-to-day scale triggered by a singular precipitation event and (ii) background emissions which are not directly affected or could not be unambiguously related to a strong precipitation pulse. This facilitates the assessment of the contribution from single sNO_x pulses additionally to background levels.

The chapter is organized as follows: in Section 3.2, all data products used within this study are presented. In Section 3.3, the basic algorithm used for averaging the time series of environmental parameters along a relative time axis around the first day of precipitation is described. In Section 3.4, this approach is then applied to areas with different spatial extents. First, an analysis on a global scale is performed to delineate regions that show pronounced features in sNO_x in response to the first rain after a prolonged dry spell. In a second step, the focus is set on Africa and the Sahel region, in specific. For this region, a detailed description of the seasonalities that govern pulsed and seasonally enhanced sNO_x emissions is provided. Furthermore, fundamental relationships between soil emissions and some of their governing parameters, i.e. soil moisture content, temperature, air humidity or land cover type are investigated. Within this analysis, also possible interferences from other parameters are investigated and sensitivity studies of the algorithm are conducted. Finally, sNO_x emissions are inferred from the NO_2 VCDs based on a latitudinal background correction in Section 3.5.

3.2 Data

3.2.1 Satellite-derived trace gas products

For NO_2, the products GOME-2 TM4-NO2A version 2.3, SCIAMACHY TM4-NO2A version 2.3 and OMI DOMINO version 2.0.1 are used (Boersma et al., 2004, 2011). For HCHO the products GOME-2 version 12, SCIAMACHY version 12 and OMI version 14 are used (De Smedt et al., 2012). Data products are provided freely by the Tropospheric Emission Monitoring Internet Service (TEMIS) via http://www.temis.nl/.

Differences among the trace gas data products from the three satellite instruments are expected due to, among others, the calculation of the AMF, their different ground pixel size, local overpass time, cloud products used, the diurnal cycle of cloud conditions and the covered time period. Furthermore, the diurnal cycle of the instantaneous NO_x lifetime and emissions might also cause systematic differences between SCIAMACHY

and GOME-2 on the one hand, and OMI on the other.

Uncertainties of tropospheric NO_2 VCDs result mainly from uncertainties of the stratospheric correction (about 2×10^{14} molecules cm^{-2}) and tropospheric AMFs (about 35–60%) (Boersma et al., 2004).

Observations under low and high cloud fractions are analysed in this thesis using cloud information derived from FRESCO+ (Wang et al., 2008) for GOME-2 and SCIAMACHY and OMCLDO2 (Acarreta et al., 2004) for OMI.

3.2.2 Precipitation

The estimation of precipitation on a daily global scale is facilitated through the combination of radar, passive microwave, visible (VIS) and infrared (IR) sensors aboard low-Earth orbiting as well as geostationary satellites. In this study, three different products are used that employ such a blended precipitation scheme. All three data sets agree in their spatial resolution (0.25° x 0.25°) and provide data in 3-hourly time steps, i.e. 12UTC covering the period 22:30UTC to 1:30UTC and so on. They are briefly described below.

The Tropical Rainfall Measuring Mission (TRMM) Multisatellite Precipitation Analysis (TMPA) 3B42 Version 7 data set (Huffman et al., 2007) combines observations made by the TRMM satellite with other satellite systems, as well as land surface precipitation gauge analyses when possible. The passive microwave data, which has a strong physical relationship to the hydrometeors that result in surface precipitation, are collected from the Microwave Imager (TMI) on TRMM, Special Sensor Microwave Imager (SSM/I) on Defense Meteorological Satellite Program (DMSP) satellites, Advanced Microwave Scanning Radiometer-Earth Observing System (AMSR-E) on Aqua, and the Advanced Microwave Sounding Unit-B (AMSU-B) on the National Oceanic and Atmospheric Administration (NOAA) satellite series. The IR data, for the TMPA are collected by the international constellation of geosynchronous satellites. Additionally, data from TMI and the precipitation radar (PR) on TRMM are used as a source of calibration. The whole TMPA algorithm is constructed in four steps: (i) microwave precipitation estimates are calibrated and merged. (ii) IR precipitation data are produced using the calibrated microwave results. (iii) Then, the microwave and IR precipitation estimates are combined filling missing data. (iv) Lastly, rain gauge data are incorporated for the final product. For a detailed explanation of the TMPA algorithm see Huffman et al. (2007).

A similar approach is used for the CMORPH product (CPC MORPHing technique, Joyce et al., 2004) which uses passive microwave information from SSM/I, AMSU-B, AMSR-E and TMI. The main difference to TMPA is that data gaps are treated differently by transporting rainfall features via spatial propagation information which is obtained from geostationary satellite IR data (Joyce et al., 2004).

PERSIANN (Precipitation Estimation from Remotely Sensed Information using Artificial Neural Networks, Sorooshian et al. (2000)) assimilates IR precipitation estimates from geosynchronous satellites. These estimates are then calibrated using microwave precipitation from low Earth orbit satellites. It differs from the other above-described

precipitation algorithms as its calibration technique involves an adaptive training algorithm that updates the retrieval parameters when microwave observations of precipitation become available (Sorooshian et al., 2000).

Inter-comparison studies show good agreement with ground-based precipitation observations for these data products (e.g. Ebert et al., 2007; Novella and Thiaw, 2010; Romilly and Gebremichael, 2011; Liu et al., 2012; Pipunic et al., 2013; Pfeifroth et al., 2016, and references therein) which is, however, variable for different geographic regions, surface types and rain intensities.

In this study, each precipitation product is applied individually to differentiate between days with or without rain fall. The comparison of the corresponding results suggests that the uncertainties and differences among the precipitation data sets have only minor effects on the obtained results (see Fig. 3.26 and 3.30).

3.2.3 Soil moisture

The processes of nitrification and denitrification, which govern sNO_x fluxes, are closely related to the soil water content (Meixner and Yang, 2006). In situ measurements of soil moisture are sparse and difficult to extrapolate to broad geographic regions due to their highly heterogeneous nature. Combined satellite measurements of soil moisture overcome this issue by providing global coverage on a daily basis. Although the absolute value of soil moisture from merged satellite products has large uncertainties, relative variations triggered by precipitation events, should be evident in the time series.

Here, data from the Soil Moisture CCI (Climate Change Initiative) ECV project is used which merges level 2 soil moisture data derived from multiple satellite sensor products (Wagner et al., 2012) in order to construct a consistent long-time data set. Among the list of sensors that are included, are the C-band scatterometers on board of the ERS and METOP satellites and the multi-frequency radiometers SMMR, SSM/I, TMI, AMSR-E, and Windsat. The data sources include active (scatterometer) and passive (radiometer) microwave observations acquired preferentially in the low-frequency microwave range.

3.2.4 Other data sets

The data sets described above provide the basic information used in the study. To evaluate and understand other influences on the retrieved trace gas levels, however, further atmospheric and environmental parameters are considered.

Lightning NO_x. Lightning represents a natural source of NO_x in the upper troposphere, especially in the tropics (Bond et al., 2002) and, thus, has a potential impact on the measured NO_2 slant column densities. Estimates of lightning activity are captured by satellite instruments as well as ground-based stations like the World Wide Lightning Location Network (WWLLN, Lay et al., 2004; Rodger et al., 2006). WWLLN offers a continuous data set which is based on 20–30 ground-based sensors that detect impulsive signals from lightning discharges, *sferics*, in the very low frequency (VLF) band (3–30

kHz) (Dowden et al., 2002). This algorithm is, thus, more sensitive to cloud-to-ground flashes because of their stronger radiation in the VLF band compared to intra-cloud flashes. In order to be classified as a lightning event the lightning strike must be detected by at least five stations. The detection efficiency (DE) varies to a large extent due to the spatial distribution of contributing stations. For example, over Australia the DE is $\sim$ 80–90%, but only $\sim$ 10–20% over Africa (Rodger et al., 2006).

Fire activity. Biomass burning in specific regions is a major source of trace gases and aerosol particles (Crutzen and Andreae, 1990) and, therefore, must be considered in the analysis. The MODIS global monthly fire location product MCD14ML (Giglio et al., 2006) is used to filter out locations affected by fires.

Meteorology. In order to understand the prevailing meteorology and filter for special circumstances in the Sahel region, modelled data of soil and air temperature, pressure, humidity as well as wind fields are taken from the ECMWF ERA-Interim analysis (Dee et al., 2011). The model data are acquired at a spatial resolution of 0.25° and a temporal resolution of 6 hours over the period from 2007 to 2010. The data are publicly available via http://apps.ecmwf.int/datasets/.

Land cover. The analysis of trace gas time series is also split up for different land cover types as they are related to different soil compositions and, thus, different sNO_x potentials. Here, a land cover map for the year 2009 from the ESA initiated GlobCover project is used, which utilizes observations from the MERIS sensor on board the ENVISAT satellite mission with a spatial resolution of 300 m. The product is publicly available via http://due.esrin.esa.int/page_globcover.php and comprises 22 land cover classes defined with the United Nations (UN) Land Cover Classification System (LCCS) with an overall accuracy across all classes of 58% (Arino et al., 2007; Bontemps et al., 2011). The data are downscaled using a most-common-value approach to identify dominant land cover types and to match the resolution of the other data sets. Thus, misclassifications might occur particularly over heterogeneous terrain and transition zones, while classification over homogeneous terrain is expected to be robust.

Water vapour. Total column observations of H_2O VCDs from GOME-2 give insight into the absolute humidity of the atmosphere at the time of the NO_2 observation from GOME-2 and, thus, a temporally more reliable estimate compared to modelled ECMWF data. H_2O VCDs from GOME-2 are derived based on a DOAS retrieval using a H_2O absorption band around 650 nm. Remaining non-linearities due to saturation effects are accounted for by a simple correction function determined from a radiative transfer model (RTM). Empirical AMFs are derived from the simultaneously measured O_2 absorption. Retrieval details and validation of the H_2O VCDs can be found in Wagner et al. (2003, 2006) and Grossi et al. (2015).

3.3 Methodology

A daily global time series data set spanning from 2007 to 2010 for grid boxes of 0.25° x 0.25° is established comprising total precipitation and trace gas measurements. Level 2 products of the trace gases are screened for observations with effective cloud fraction above 20% and a solar zenith angle above 60°. Furthermore, observations coinciding with lightning or fire events on the same day and within the same grid box are filtered out.

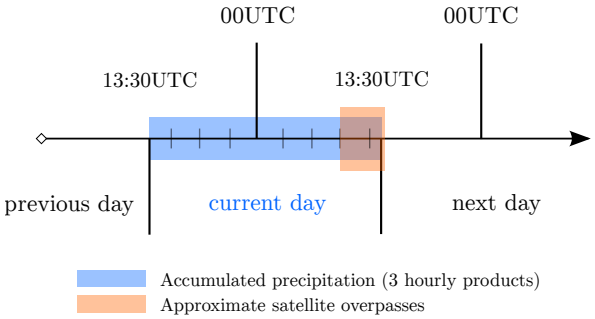

Figure 3.1: Schematic of the 24h time period selected for the integration of precipitation data. The eight 3-hourly precipitation rates prior to the overpass times of the SCIAMACHY, GOME-2 and OMI satellite sensors are summed.

The 3-hourly precipitation data are integrated over the 24 h period prior to the satellite overpasses of GOME-2, SCIAMACHY and OMI to collocate rainfall events and trace gas observations. For example, in the Sahel region, which is the main study region of this Chapter, the precipitation data are integrated from 13:30 UTC of the previous day to 13:30 UTC of the current day as this corresponds to the local overpass time of OMI. This 24h period is called *Day* in the following pages (see Fig. 3.1). For the global analysis, the temporal integration is shifted by 3 h in steps of 45° longitude.

As the highest soil emissions are expected at the start of a wet season after a long drought phase of several weeks to months, the transition between dry and rainy seasons is the primary focus of this work. However, the length of drought phases are quite different for semi-arid areas in the world, varying from very long (several months in winter) in the Sahel to shorter periods (several weeks in summer) in south-western Africa. The approach taken in this study considers grid boxes that experienced only little precipitation per day, e.g. < 2 mm, over a minimum number of days, e.g. 60 days, and a reasonable amount of precipitation on the first rain day (> 2 mm). Then, the trace gas column densities around this *first day of rainfall*, which is counted as *Day0* hereafter, are compared to the background levels during the preceding dry spell. The results vary slightly for different thresholds of the precipitation trigger, as shown in Fig. 3.28. These sensitivity tests also show that a threshold of 2 mm/day leads to good statistics as well as representative responses in NO_2 VCDs.

Fig. 3.2 depicts a typical time series of precipitation (left panel) and NO_2 VCDs (right

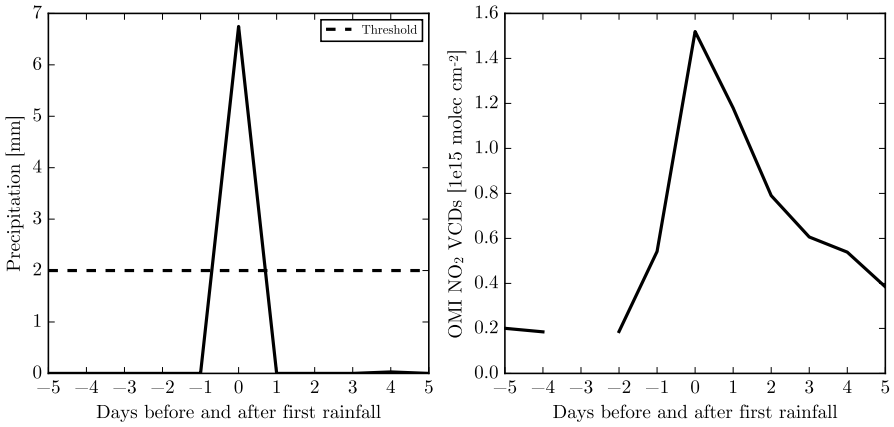

Figure 3.2: Time series of TMPA precipitation (a) and OMI NO_2 VCDs (b) for a 10 day period around the first rain event for a single grid pixel in the Sahel on 11/04/2008 at 15.25° N, 25.5° E. A threshold of 2 mm precipitation per day is chosen and at least 60 days of drought are required.

panel) for a 5 day period around the first rain event (on Day0) after a dry spell for a single grid pixel in the Sahel in April 2008. In the following, the days around the first day of rainfall are referred to as Day-3, Day-2, Day-1, Day0, Day+1, Day+2, Day+3 and so forth. It should be noted that there are almost no gaps in the precipitation time series, however, there are many in the trace gas time series. This is primarily due to the lower spatio-temporal coverage of trace gas products as well as the cloud, lightning and fire screening. In the example shown in Fig. 3.2 a 0.25° x 0.25° pixel is chosen which provides a complete NO_2 time series over 10 days. There is very little precipitation per day before the initial rain event. On Day0, precipitation exceeds a threshold of 2 mm, used to differentiate between 'rain' and 'no rain'. Investigating the time series of NO_2 around the first day of rainfall reveals a strong enhancement on Day0 and some smaller enhancement on Day-1 and Day1, whereas from Day-10 to Day-2 the NO_2 VCD is close to the pre-event level; i.e. the average NO_2 VCDs of Day-5 to Day-1. NO_2 VCDs after Day1 stay systematically higher than the background.

The time series for this single grid box represents the evolution of precipitation and trace gas VCDs around the first day of rainfall for a single grid pixel (experiencing first precipitation after an extended drought) demonstrating the basic principle of this study.

In order to achieve representative results with improved statistics, averaging the time series over many pixels is necessary. However, as the focus is set on pulsed soil emissions, averaging of time series from different pixels with rain events shifted in time has to be avoided. Furthermore, only a small subset of all possible pixels and their corresponding time series fulfils the conditions of the precipitation trigger. Thus, the individual time series are first synchronized in time relative to the first day of rainfall (Day0). The subsequent averaging method is applied, in the following section, either with focus on high spatial resolution or with focus on best statistics at the expense of losing spatial resolution by averaging over larger areas.

In the following sections a drought period of at least 60 days followed by a rain event (precipitation > 2 mm) is referred to as the reference case. The drought period of about 2 months is chosen, because the highest response in NO_2 is found with this setting. In Fig. 3.27, the impact of drought lengths on the derived soil emission pulses is investigated.

3.4 Results

3.4.1 Global Analysis

The algorithm described above, is applied to the full spatial extent covered by the TRMM/TMPA precipitation data set ($-180°$ to $180°$ longitude, $-50°$ to $50°$ latitude).

Fig. 3.3a displays the number of valid OMI observations on 1.25° x 1.25° grid pixels that fulfil the selection criteria, i.e. 60 days of drought and at least 2 mm of precipitation on Day0. For most regions in the world enough data points are found for the analysis; exceptions are regions with no pronounced seasonality in rainfall (e.g., tropical rainforests, North America, Europe) and regions where rain occasionally falls during the dry season (Southeast Asia). The chosen algorithm is not optimized for those regions.

The days prior to the first rain are assumed to represent a background level of NO_2. Fig. 3.3b depicts a corresponding background NO_2 map from OMI measurements obtained by averaging VCDs of the Day-10 to Day-2.

To examine variations in trace gas columns due to rain events, the enhancement of NO_2 VCDs on Day0 are considered with respect to the background. Fig. 3.3c shows the spatial distribution of these absolute differences for OMI. In Fig. 3.3d, data points within 2 times the standard deviation, σ, of the background variation in the respective grid cell are screened out.

Furthermore, the uncertainty from spatial representativeness (Boersma et al., 2016) needs to be taken into account. It arises when only few valid satellite pixels per grid cell are available. Therefore, at least 50% of possible data are requested per grid pixel in order to be considered in this analysis. The corresponding results for NO_2 VCDs observed by GOME-2 and SCIAMACHY are similar to Fig. 3.3d, but are more affected by noise due to poorer statistics (see Fig. 3.29).

The most eminent features are the high enhancements of OMI NO_2 column densities on Day0 in the distinct band of the Sahel region around 15° N. Single grid pixels in this distinct band exceed absolute enhancements of 1×10^{15} molecules cm^{-2} over background.

Similar enhancements in the Sahel were also observed by Hudman et al. (2012). In the south western part of Africa as well as over Australia spatially coherent enhancements are also present. Small-scale, local enhancements are found also e.g. over India (also investigated by Ghude et al. (2010)), regions nearby the Caspian Sea, the Middle East or China. An important finding is that there are no clustered reductions in NO_2 VCDs on Day0. Since no land-sea mask is applied, oceans serve as control regions for the algorithm: no significant differences in NO_2 are found over the vast majority of oceans area. However, over the Mediterranean sea and in proximity to coastal regions over oceans small-scale

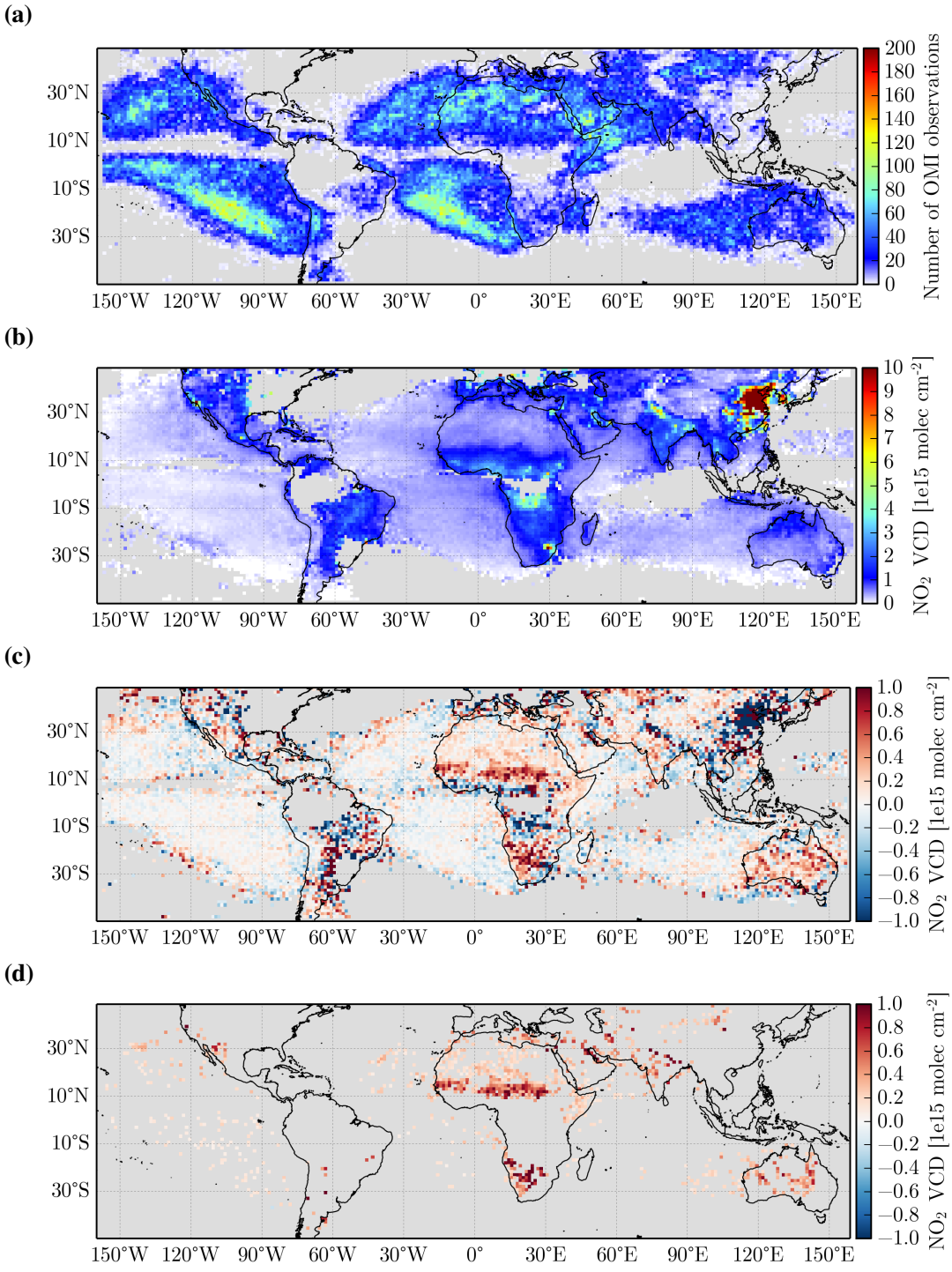

Figure 3.3: (a) Number of valid measurements per grid pixel on Day0. **(b)** OMI NO_2 background levels averaged for days -10 to -2 before the first rain event after 60 days of drought for each pixel (0.25° lat/long) and then averaged for boxes of 1.25° lat/long. **(c)** OMI NO_2 VCD absolute differences on Day0 (first day of rainfall) compared to Days -10 to -2. Reductions in NO_2 VCDs on Day0 depicted in blue colours, enhancements in red. **(d)** as (c) but screened for significant changes (see text). Extensive enhancements over the Sahel and South Africa are evident. Pixels containing less than 20 measurements on Day0 (or less then 50 measurements from Day-10 to Day-2) are screened out.

enhancements in NO_2 VCDs are detectable which might be related to advection.

The applied algorithm considers all data regardless of the season. Analysing the data based on different periods of the year reveals local enhancements in NO_2 VCDs in semi-arid areas matching dry-to-wet season transitions in these geographic regions (Fig. 3.4). In April/May/June, panel (a), the narrow band of the Sahel again is characterized by a mean enhancement of NO_2 of 1×10^{15} molecules cm^{-2}. This time period corresponds to the start of the rainy season in the Sahel after a long dry spell of 3–4 months. In September/October/November, panel (b), the strongest peaks in NO_2 VCDs are observed in south-western Africa representing the start of the local wet season.

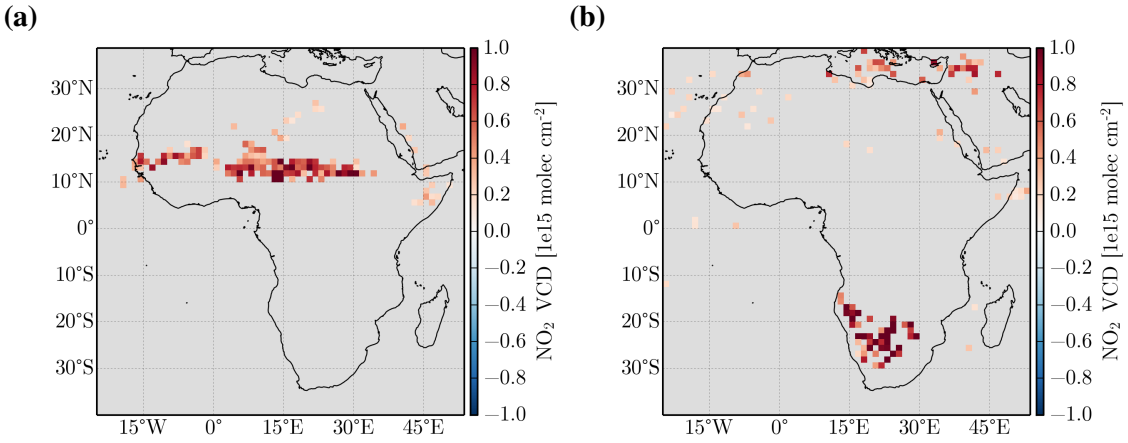

Figure 3.4: **(a)** Significant OMI NO_2 VCD enhancements (in 1×10^{15} molecules cm^{-2}) on Day0 compared to the background level for April-May-June (2007–2010) which represents the start of the wet season after the dry period in the northern part of Africa. Extensive enhancements in NO_2 over the narrow band of the Sahel can be seen. **(b)** The same for September/October/November (2007–2010), whereby strong enhancements are found in south-western Africa. This time period reflects the transition time between the dry and wet season in this region.

3.4.2 Detailed analyses over the Sahel region

3.4.2.1 Overview over the Sahel

The Sahel is a semi-arid region in north-central Africa spanning the complete width of the continent from the Atlantic Ocean in the West to the Red Sea in the East. The Sahel belt is loosely defined as a transition zone about 10° to 15° North between the Saharan desert in the North and the sub-humid savannah in the south. The expression *Sahel* originates from the Arabic *sāḥil* describing a coast or shore and in this respect the boundary between the northern sandy desert and the vegetated regions in the South which is distinguishable in Fig 3.5.

Semi-arid regions are characterized by seasonal water availability confined to very few months. In the Sahel, this seasonality in rainfall is primarily driven by the latitudinal displacement of the Inter-Tropical Convergence Zone (ITCZ) (Jäkel, 1984).

The northward movement of the ITCZ starts in March and the northernmost position is

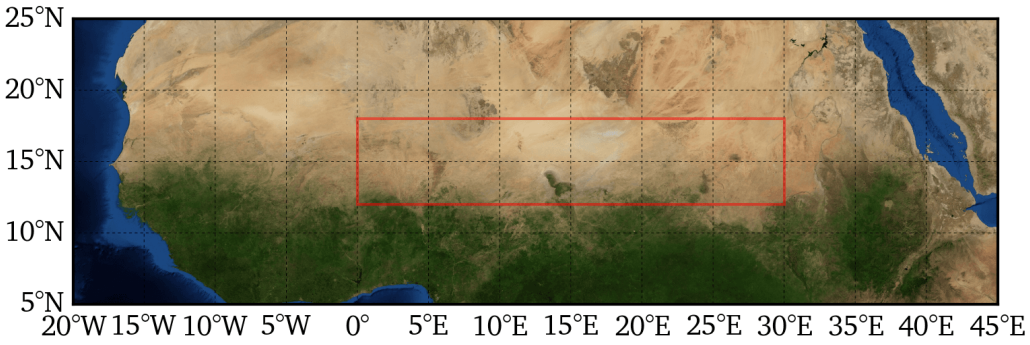

Figure 3.5: Map of Northern Africa with focus on the Sahel being the transition zone between the dry Saharan desert and the humid savannah and tropics of central Africa. The area highlighted in red is used for the analyses in Sections 3.4.2.3, 3.4.2.4 and 3.4.2.7. NASA's *Blue Marble* taken from Environmental Systems Research Institute (ESRI) MapServer: http://server.arcgisonline.com/ArcGIS/rest/services/ESRI_Imagery_World_2D/MapServer

reached, at 15° N, in August. In the following four months the Sahel region receives about 90% of its mean annual precipitation (Bell et al., 2000). The subsequent dry season begins in October and ends gradually with the start of the next wet season in April/May/June (AMJ period).

Previous studies (e.g. Jaeglé et al., 2004; Hudman et al., 2012) argue that in this distinct geographic band pulsed soil emissions of NO_x, which can be detected from space, occur at the beginning of the wet season in spring. Fig. 3.3d supports this finding and delineates the narrow band of the Sahel from 10° to 18° N and from the west coast of Africa essentially spanning the whole width of the continent (Fig. 3.4a). The pronounced sNO_x features in the band of the Sahel during the AMJ period enable a more detailed investigation of pulsed soil emissions.

3.4.2.2 Seasonalities within the Sahel

As in other semi-arid areas over the globe, life in the Sahel is governed by the seasonal alternation of dry and rainy seasons (GIZ, 2015). Humans, animals, vegetation, but also tiny microbes in soils in these regions strongly depend on the annual inflow of water in the form of precipitation. It is suggested in, e.g., Jaeglé et al. (2004) and Hudman et al. (2012) that soil emissions in the Sahel have the largest share of the NO_x budget at the start of the rainy season in April to June. It is, however, not yet clear how these seasonal variations in sNO_x reflect spatially in monthly means over the Sahel and how they compare to the seasonality in precipitation and vegetation cover.

This section, thus, investigates environmental parameters which can be directly observed from space-based instruments and elaborates on their spatio-temporal interrelation. Fig. 3.6 depicts the monthly time series of precipitation, the Normalized Difference Vegetation Index (NDVI) and NO_2 VCDs. As the ITCZ stretches northward in April, the first rainfall in the Sahel occurs after which precipitation gradually increases during summer

with a peak in August. In autumn, the ITCZ moves back to the south which leads to the decline in precipitation in September, October and November.

The NDVI is a measure for the relative density and photosynthetic activity of vegetation or simply the *greenness* of vegetation (e.g. Running, 1990; Yengoh et al., 2015). The chlorophyll in plant leaves absorbs visible light in the wavelength range between 0.4 to 0.7 µm as the energy source of photosynthesis. The cell structure of leaves reflects near-infrared light between 0.7 to 1.1 µm. These reflectance and absorption characteristics can be used to derive a quantity which relates to the amount of green vegetation by determining the relationship between red (RED) and near-infrared (NIR) reflected energy as follows (e.g. Running, 1990; Yengoh et al., 2015):

$$NDVI = \frac{NIR - RED}{NIR + RED} \tag{3.1}$$

The NDVI results in a ratio ranging from -1 to 1. A value close to zero (-0.1 to 0.1) means no vegetation, i.e. barren areas of rock, sand, or snow. Values above 0.1 represent higher density of green leaves and values below -0.1 typically represent water areas.

Fig. 3.6 shows NDVI values from the MODIS instrument on the Aqua satellite platform. The MODIS NDVI product is derived from the red (band 1: 620–670 µm) and NIR (band 2: 841–876 µm) spectral regions. The NDVI values averaged over the Sahel range between 0.14 at the end of the dry season in April to 0.24 in September where the vegetation cover reaches its maximum. It can be seen that the seasonal cycle in the NDVI time series follows the one from precipitation with a temporal lag of about one month.

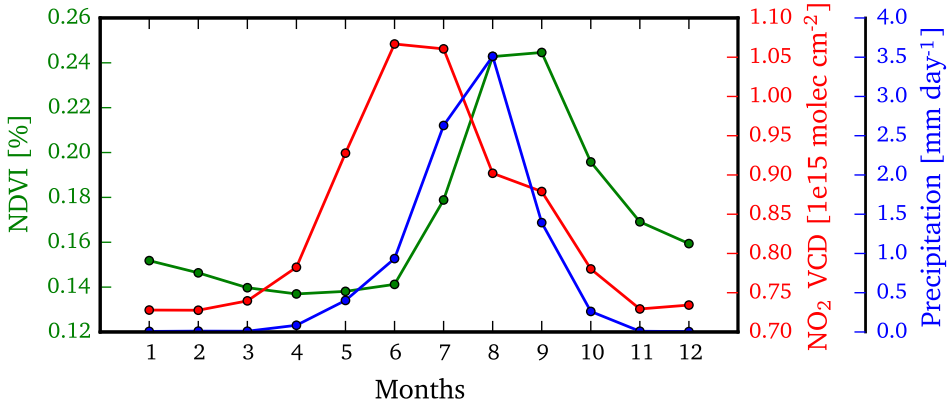

Figure 3.6: Time series of monthly averages of precipitation (TRMM/TMPA), NDVI (MODIS/MYD13C2) and NO_2 VCDs (OMI) for the Sahel (0-30° W, 12-18° N) for 2007–2011.

For the time series of NO_2 VCDs observed by OMI a similar strong seasonal cycle can be detected. The values range from about 0.73×10^{15} molecules cm^{-2} in the winter months to about 1.07×10^{15} molecules cm^{-2} in June. Interestingly, the seasonal cycle of NO_2 shows a strong enhancement about two months before the peak in the seasonal cycle of precipitation. The findings from Fig. 3.3d and 3.4a give rise to the assumption that pulsed sNO_x emissions may be responsible for the enhanced NO_2 VCDs in May/June/July

(Fig. 3.6).

Fig. 3.7 depicts elevation data for Northern Africa from NASA's Shuttle Radar Topography Mission (SRTM). The terrain height is a key parameter in understanding the spatial patterns of precipitation, NO_2 and other quantities discussed in this section. In principle, the Sahel is characterized by flat plains but is enclosed by mountainous areas to the north and to the east. The impact of the distinct orographic features within Northern Africa on the different quantities such as precipitation or NO_2 levels will be discussed below.

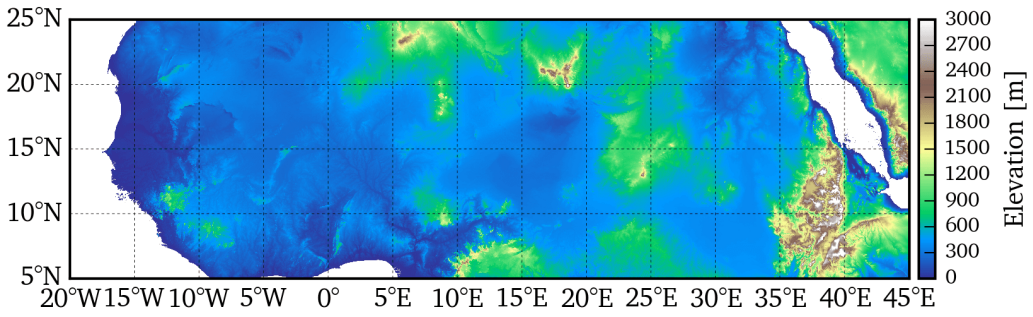

Figure 3.7: Elevation from SRTM for Northern Africa.

The following sections focus on the spatial patterns of the seasonal cycles of precipitation, NDVI, fires, lightning and NO_2 and present monthly averaged maps for the complete domain of Northern Africa (20° W – 45° E, 5-25° N). The large region is chosen to put the seasonal cycles observed over the part of the Sahel which is mainly discussed in this thesis (0-30° E, 12-18° N) into a broader context. It should be noted that only the months March to August are discussed in this chapter as spring and summer represent the seasons which are most relevant for soil emissions and potential influences on the NO_2 VCDs.

Monthly precipitation in the Sahel. Fig. 3.8 presents average precipitation for the months March to August and depicts how the ITCZ shifts northward during this period. In March, the precipitation systems reach no further than 10° North. Most heavy precipitation is observed over the Ivory Coast with about 6 mm day^{-1} precipitation. From April to July the ITCZ moves northward and brings more and more precipitation to the Sahel. In the western parts heavy precipitation (above 10 mm) is primarily found over the Atlantic ocean and blocked by the coast region. The northern most extent of the ITCZ (about 15° W) shows a clear East/West difference. From 15° West to 10° East precipitation reaches up to 25° North whereas in the eastern part almost no precipitation is registered. In August, precipitation generally intensifies over whole Northern Africa, but does not move further north. The centre of the ITCZ is located at about 10° North (as in July) and the stark contrast between the eastern and western parts of the Sahara also becomes stronger. An interesting feature evolves over these months in the eastern part of Northern Africa at about 35 to 40° E and 7 to 15° N. From March to August precipitation increases over this region and gets most intense in August. In these regions multiple volcanoes and high mountain ranges cause orographic precipitation at higher altitudes. In Fig. 3.7, the

prominent feature of this mountainous area as well as the depression zone clearly stick out. Also other smaller enhanced precipitation signals, e.g. over the Sahara, correlate well with the orography.

Vegetation response to seasonal wetting. As vegetation strongly depends on water supply, the seasonal cycle closely follows precipitation patterns and shows similar spatial behaviour. However, as vegetation needs some time to grow and fully develop, a time lag of about one month compared to precipitation exists (as noted above). In general, a strong latitudinal gradient in vegetation can be observed in all months as shown in Fig. 3.9. The Northern parts are characterized by very low NDVI indices of about 0.1 which corresponds to barren areas with very low or no vegetation. The green and wet southern parts show the highest values in the tropics of about 0.9. During spring and summer, vegetation develops in the Sahel, as the northward shift in the ITCZ brings more and more precipitation to the area. One particularly interesting feature is the area around Lake Chad (12.5 to 14.4 ° N and 13 to 15.3 ° E) which shows enhanced NDVI values compared to its surroundings in all months. A detailed description of this region is provided in Chapter 4. In general, the transition zone dividing the bare desert in the north and vegetated regions during the summer months reaches about 17° N in the western part of the Sahel and about 15° N in the eastern part.

OMI NO_2 VCDs. Tropospheric NO_2 VCDs in Northern Africa are dominated by NO_x emissions from (natural and anthropogenic) biomass burning, soil emissions and lightning (see, e.g. Jaeglé et al., 2004; van der A et al., 2008; Delon et al., 2010). The spatial patterns of average NO_2 VCDs for each month over Northern Africa depicted in Fig. 3.10 are, thus, governed by these three categories. The relative contribution of each category to the local NO_x budget strongly depends on the season. Anthropogenic emissions from bio-fuel as well as industries are expected to be generally low in Northern Africa and are mostly relevant for highly populated regions such as coastal regions like the Gulf of Guinea.

In general, biomass burning activity is highest in the dry season, i.e. in winter time, and decreases with the beginning of the wet season in summer (see Appendix A.3). The location of hot-spots in fire counts generally compares well with the enhanced levels of NO_2 in west Africa and in northern tropics. With the shift of the ITCZ northward and the accompanying rainfall, the number of fires decreases and, in consequence, the NO_2 VCDs in the biomass burning regions decrease as well.

With the arrival of large-scale precipitation systems in spring, lightning becomes more important with regard to NO_x emissions. The number of lightning strikes is highest over the tropics and centred over the ITCZ (see Appendix A.4). In general, precipitation and lightning show the same spatial patterns. In spite of the increase of the number of lightning strikes, NO_2 tends to decrease over the tropics in summer. This is probably because of the strict selection criteria of NO_2 VCDs which discards all observations with more than 20% cloud cover. A study by van der A et al. (2008) indicates that lightning-induced NO_x emissions can be better captured under cloudy circumstances as lightning typically occurs

in cloud-to-ground or intra-cloud situations.

From April to August NO_2 VCDs form an enhanced narrow band almost over the complete longitudinal extent of northern Africa. This enhanced band moves northward from April to June in conjunction with the northern edge of the ITCZ. The seasonal cycle observed in the time series of NO_2 VCDs (see Fig. 3.6) corresponds to the arrival of this enhanced band in May/June in the northern part of the Sahel. In August the NO_2 VCDs decrease over the entire Sahel region, indicating that (i) either the emission source is diminished, (ii) emissions are offset by wet deposition due to constant precipitation in the wet season or a combination of both. The spatial pattern of enhanced NO_2 VCDs coinciding with the first precipitation over dry savannah and sparsely vegetated regions in May/June further supports the hypthesis that (pulsed) soil emissions of NO_x are the dominant source of NO_x to the atmosphere in this period in the Sahel. Other potential emission sources, such as fires or lightning show different spatial and temporal patterns.

The NO_2 observations from OMI agree well with GOME-2 and SCIAMACHY with respect to the band of soil emissions in the Sahel as well as the northward movement. However, subtle difference among the products exists. First, the impact of biomass burning events, e.g. fires in western Africa, are captured by OMI but not by GOME-2 and SCIAMACHY. This may be due to the diurnal cycle of fires (lower fire counts in the morning). Second, the area of Lake Chad clearly sticks out in the OMI observations, but neither in GOME-2 nor in SCIAMACHY observations. One possible reason for this discrepancy is the diurnal cycle in sNO_x emissions which largely depends on temperature. As GOME-2 and SCIAMACHY scan the Earth in the morning and OMI in the early afternoon, the sNO_x signal may differ between the different overpass times. Lastly, smaller differences, such as the enhancement in OMI observations over the Bodélé Sand Dunes (at 18° E, 17° N), emerge probably due to different retrieval settings and different albedo maps (see Appendix A.5) used for the products.

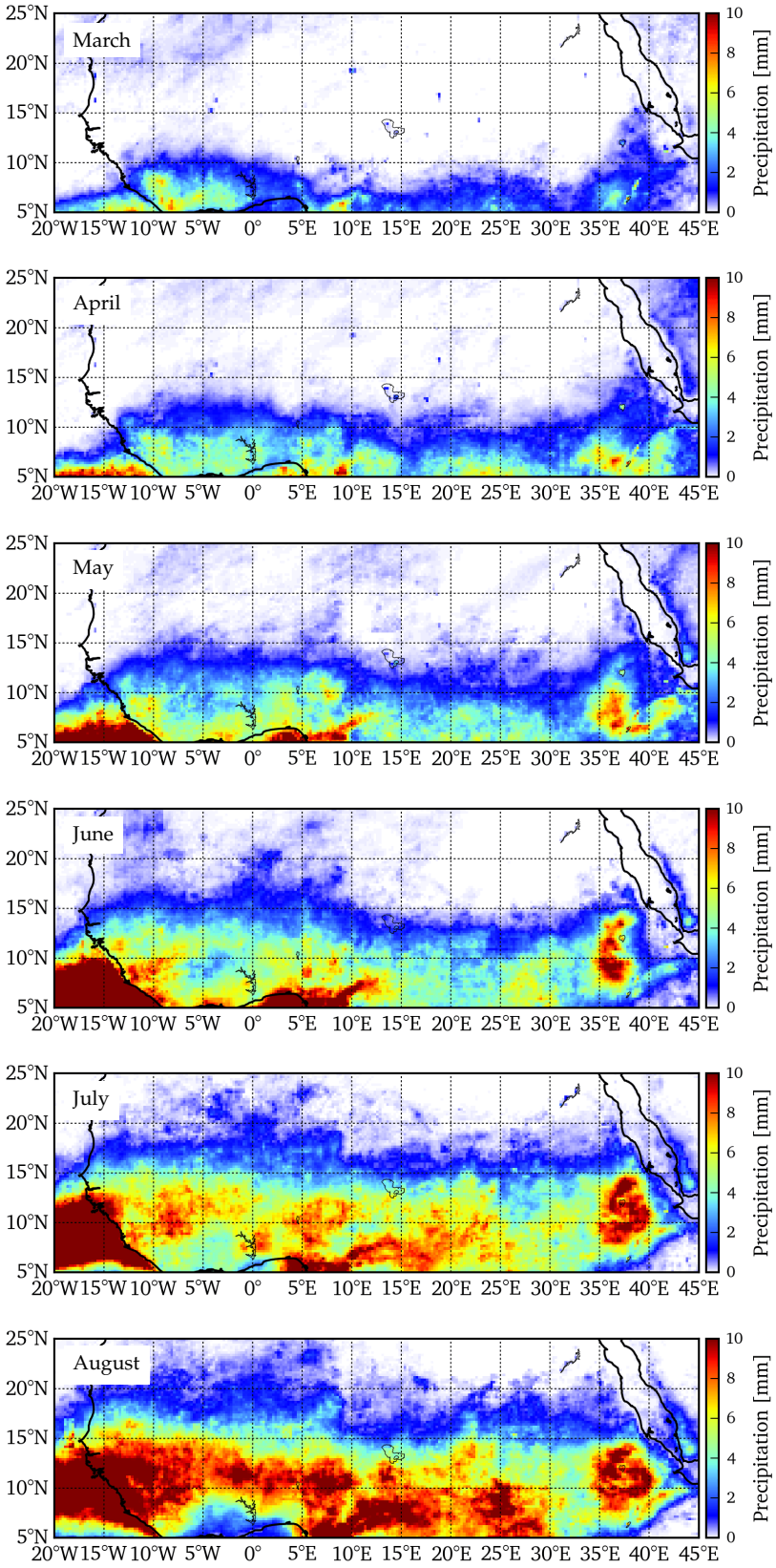

Figure 3.8: Average precipitation for the months March to August averaged over four year (2007–2011) from TRMM/TMPA 3B42v7.

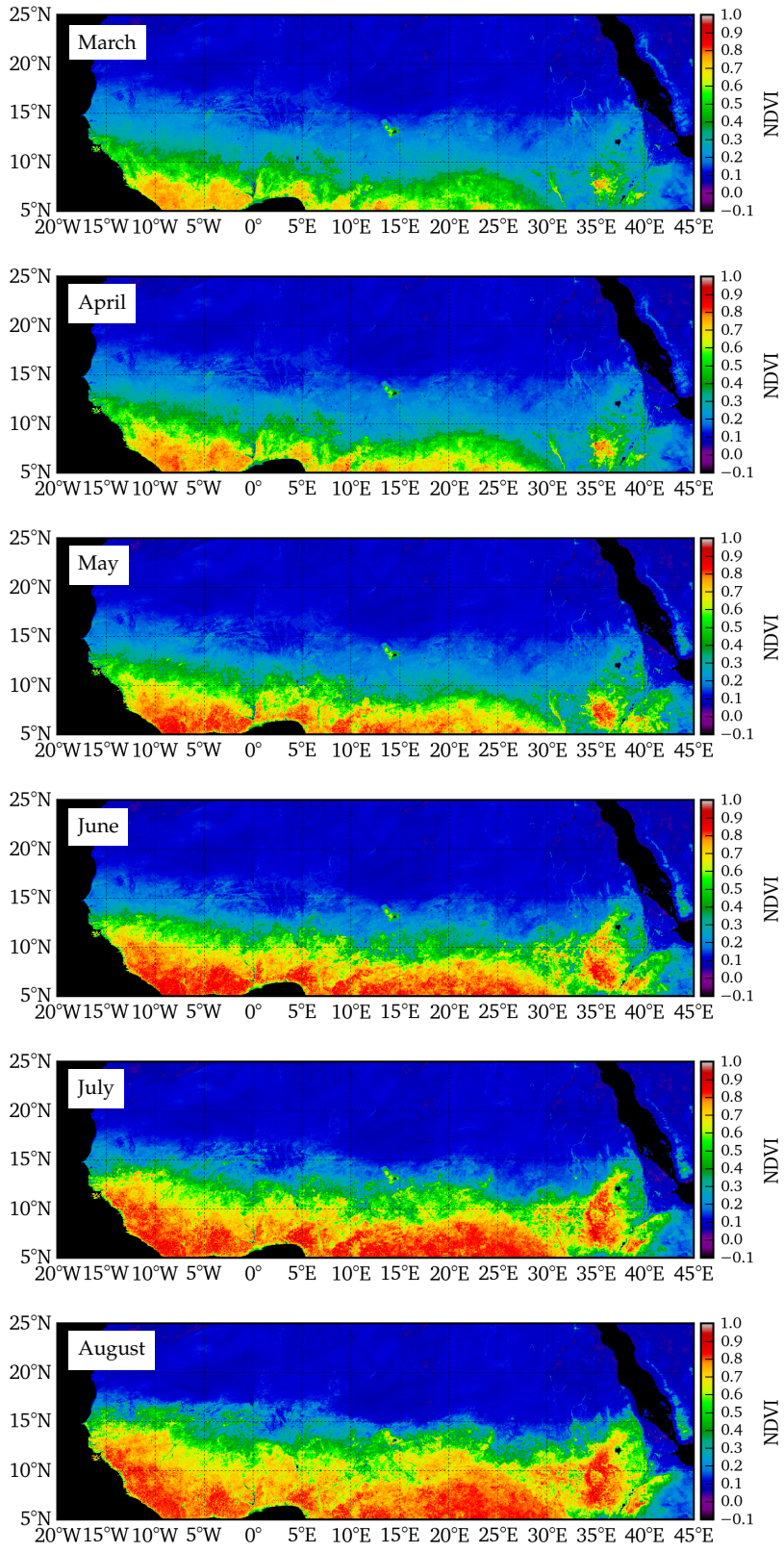

Figure 3.9: Average NDVI indices for the months March to August averaged over four years (2007–2011) from MODIS/MYD09CMG.

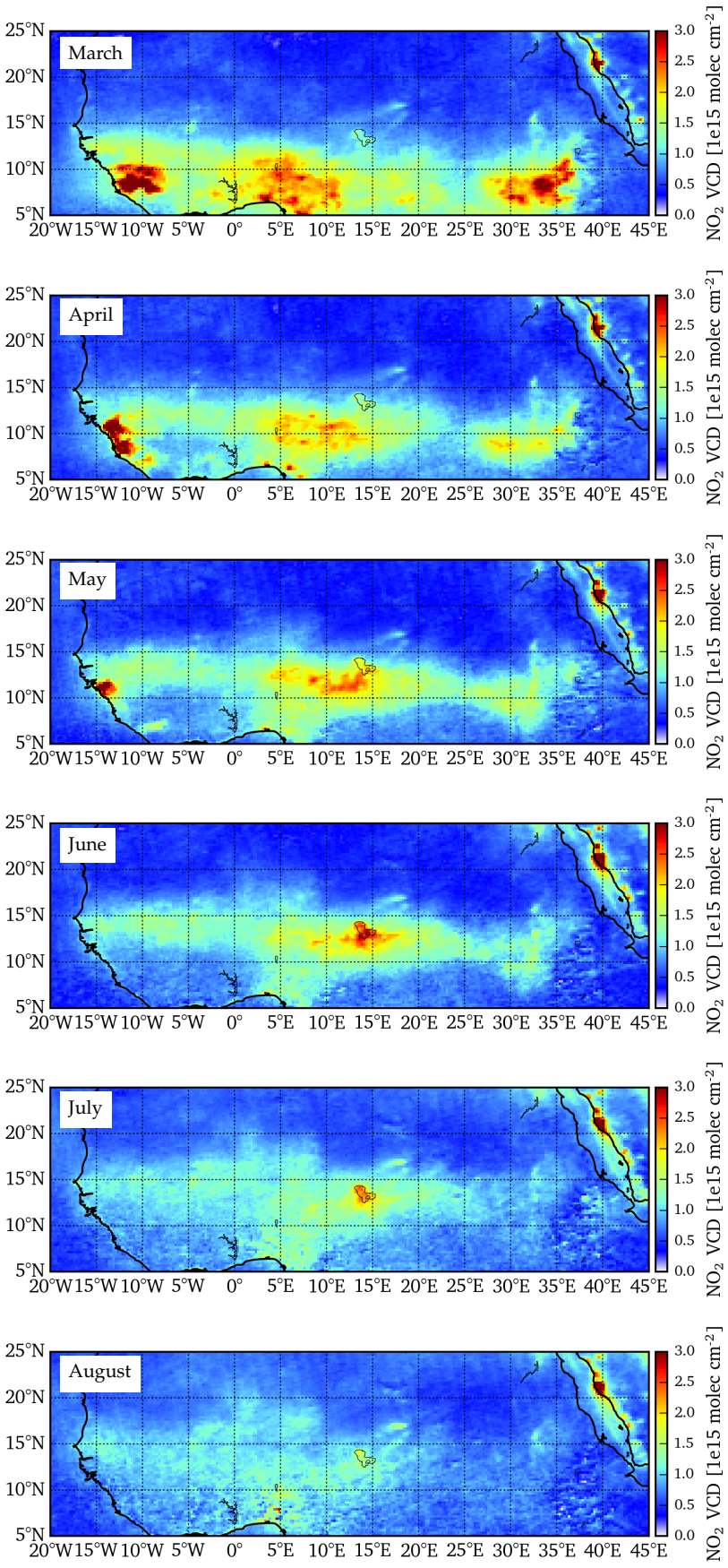

Figure 3.10: Average NO_2 VCDs from OMI for the months March to August averaged over four years (2007–2012).

Latitudinal averages of NO_2 VCDs. In the previous section, monthly average maps of NO_2 VCDs from OMI, GOME-2 and SCIAMACHY revealed a distinct summertime enhancement of VCDs almost over the entire width of Northern Africa. This section investigates differences among observations of OMI, GOME-2 and SCIAMACHY in terms of the latitudinal variation of NO_2 VCDs over Northern Africa. Fig. 3.11 shows latitudinal averages of VCDs for each month over a selected part of Northern Africa (20° W to 35° E and 5 to 20° N) for the three instruments.

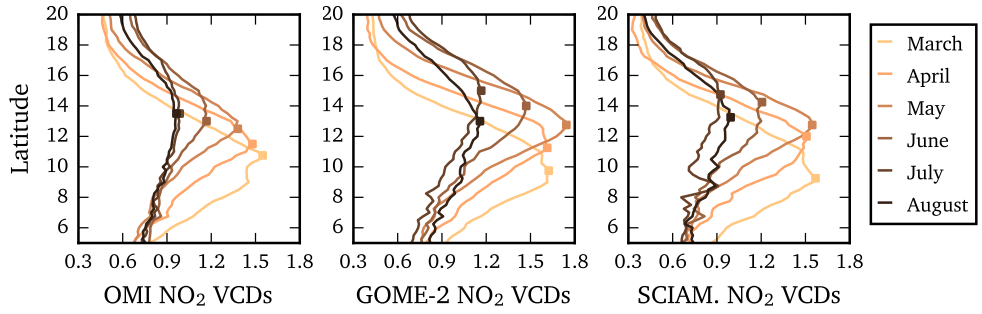

Figure 3.11: Latitudinal averages of VCDs in 1×10^{15} molecules cm^{-2} over a selected part of Northern Africa (20° W to 35° E and 5 to 20° N) for the three instruments: OMI **(left)** GOME-2 **(middle)** and SCIAMACHY **(right)**. Each coloured line represents the latitudinal average over the region per month. Filled squares indicate the highest NO_2 VCDs per month.

In all plots, a clear latitudinal dependence of NO_2 is detectable whereby the amplitude is highest in spring and lowest in the summer months. The northward movement of the peak can be observed best for the OMI data as it shows lowest fluctuations of the signal, but it can also be seen for GOME-2 and SCIAMACHY. Interestingly, the peak in NO_2 stays constant at about 13° N for OMI whereas GOME-2 observes a further shift to the north in July (SCIAMACHY as well, but less pronounced). GOME-2 shows generally higher values compared to OMI and SCIAMACHY whereby OMI observes the lowest VCDs. Bearing in mind the local overpass time of the satellite instruments (GOME-2: 9:30LT, SCIAMACHY: 10:00LT and OMI 13:30LT), this discrepancy may be due to the diurnal cycle of NO_2, which is reduced more quickly during midday than in the morning.

In summary, OMI, GOME-2 and SCIAMACHY generally agree in observing enhanced NO_2 VCDs over the Sahelian belt. This latitudinal enhancement moves northward from March to June/July whereby the amplitude of the signal is reduced in summer. Comparing these findings to the latitudinal displacement of the ITCZ in the same period leads to the conclusion that the precipitation may drive the enhanced emissions of NO_x, which is observed as enhanced NO_2 VCDs.

The corresponding northward-shifts in precipitation and vegetation mass over Northern Africa for the period from March to August are displayed in Fig. 3.12. As the ITCZ moves to the north, precipitation increases at higher latitudes accordingly. In July, the ITCZ reaches its northern-most position and reverses its path back south. The NDVI, however, shows no decline in August and indicates that the full vegetation mass is already reached in July. The NDVI indices increase throughout spring and summer at all latitudes

and show largest differences in the seasonal variation approximately between 8 and 15° N, i.e. the Sahelian belt.

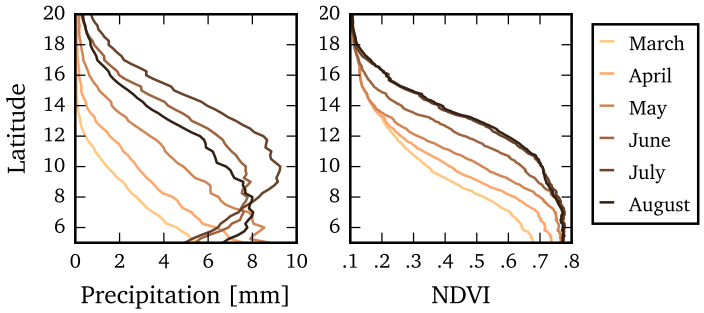

Figure 3.12: Latitudinal averages of precipitation (TRMM/TMPA) and NDVI (MODIS) over a selected part of Northern Africa (20° W to 35° E and 5 to 20° N). Each coloured line represents the latitudinal average over the region per month. For the NDVI averages, all values less than -0.1 are screened as they mostly represent water areas.

3.4.2.3 Daily variation in NO_2 VCDs after rewetting

In this section, the average enhancement in NO_2 VCDs following the first precipitation of the wet season is investigated on a daily scale (using the algorithm from Section 3.3). Thereby, the central and eastern part of the Sahel region (0° to 30° E, 12° to 18° N) is selected as main study region similar to previous studies (i.e. Jaeglé et al., 2004; Hudman et al., 2012). The western part of the Sahel is not included as it shows a slightly weaker NO_2 response to rain pulses. This might be related to different inter-annual variability patterns and seasonal cycles of precipitation regimes (Lebel and Ali, 2009).

In order to depict the general behaviour of trace gas responses and to improve the statistics, four years (2007–2010) of the AMJ period are averaged for the eastern part of the Sahel. Fig. 3.13 depicts the evolution of multiple environmental variables around Day0 averaged over the study region. The precipitation amounts from the three different products, indicated in grey shades in each panel of Fig. 3.13 generally agree in their relative variation, showing little rain before Day0, a heavy rain event on Day0 and slightly higher precipitation after the first rainfall event compared to Day-10 to Day-1. The discrepancies among TMPA, CMORPH and PERSIANN products indicate that some rain events might be missed or assessed differently by the individual data products. Nevertheless, considering CMORPH or PERSIANN data as trigger leads to comparable responses in trace gases around the first day of rainfall (Fig. 3.26).

The immediate wetting of the dry surface on Day0 is captured well by satellite observations of the volumetric soil moisture content as seen in Fig. 3.13a. After the initial wetting of the soil, the moisture content drops quickly during the following ^{3} days due to infiltration and evaporation. Similar behaviour is observed for total column densities of water vapour from GOME-2 in Fig. 3.13b. Water vapour content in the atmosphere gives

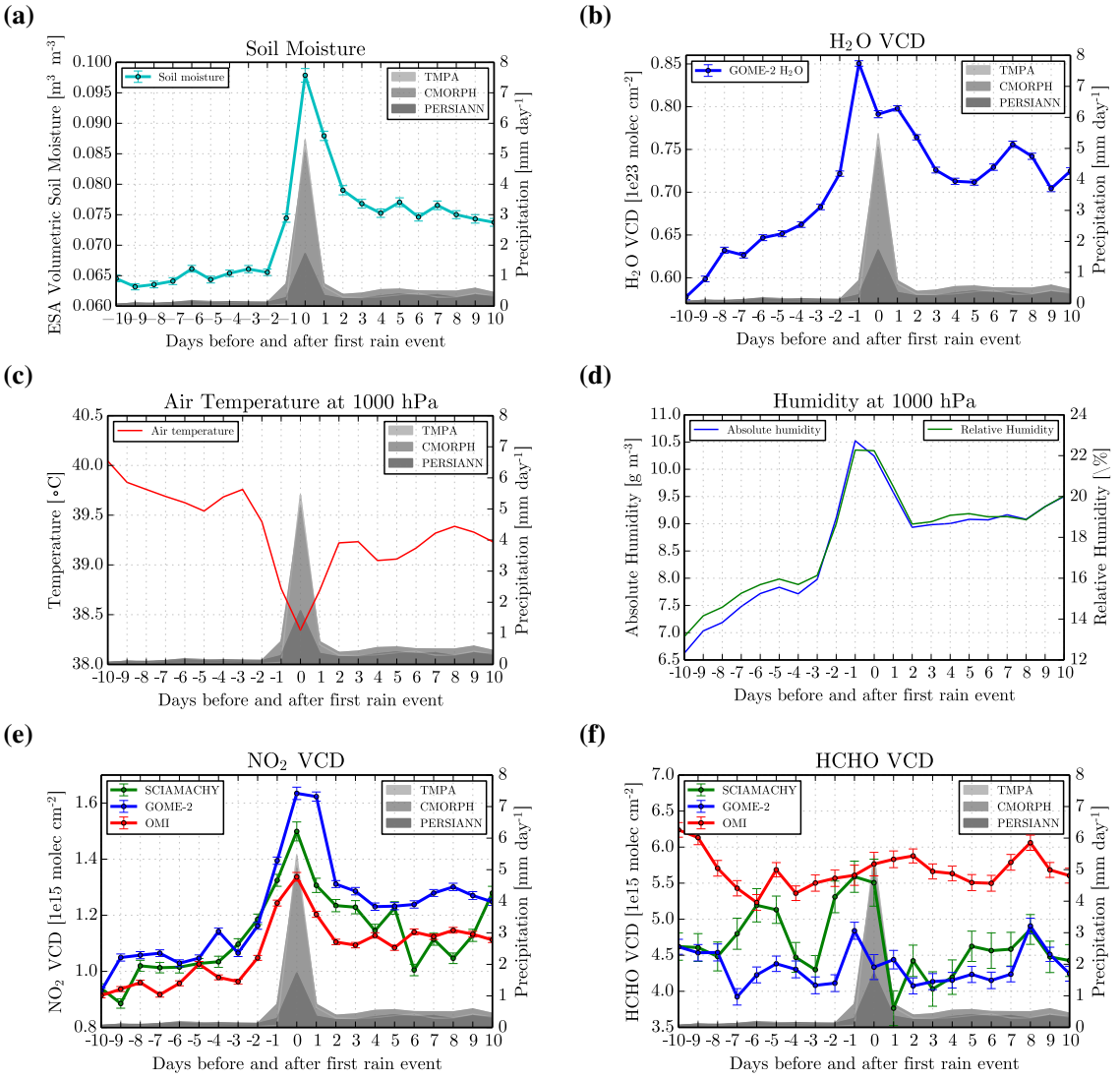

Figure 3.13: Temporal evolution of several quantities around the day with the first rain event for the Sahel region after at least 60 days of drought for April/May/June (2007–2010). Grey shaded areas represent precipitation estimates from TMPA, CMORPH and PERSIANN. **(a)** Blended ESA-CCV soil moisture. **(b)** Water vapour total column densities from GOME-2. **(c)** Temperature at 1000 hPa from ECMWF Interim Analysis. **(d)** Relative and absolute humidity at 1000 hPa from ECMWF Interim Analysis. **(e)** NO_2 VCDs from SCIAMACHY, GOME-2 and OMI with standard mean error (SME). **(f)** HCHO VCDs from SCIAMACHY, GOME-2 and OMI with SME.

insight into the ambient humidity and may indicate impending rain events, as humidity in the atmosphere typically rises prior to precipitation. On Days-10 to -2 water vapour steadily builds up in the atmosphere and peaks 1 day before the initial rain event. On Day0 and the following 3 days, the water vapour column densities drop, which is probably caused by, on the one hand, the removal of atmospheric water by precipitation and, on the other hand, by transport of dry air masses over the study area. The results for NO_2 VCDs using the three satellite instruments (OMI, GOME-2 and SCIAMACHY) show a consistent enhancement around the first day of rainfall (Fig. 3.13e). This points to a strong source

linked to the dry-wet transition, i.e. the precipitation trigger. However, the magnitude of the enhancement varies for the three instruments. The standard error of the mean (SME) value is indicated for each instrument and is generally smaller for OMI which has the best statistics.

The average absolute enhancement in the Sahel for GOME-2 NO_2 on Day0 compared to the background levels is about 5×10^{14} molecules cm^{-2}, whereas OMI and SCIAMACHY only observe an absolute enhancement of ~ 3 and 4×10^{14} molecules cm^{-2}, respectively.

The different magnitudes of the enhancements cannot be solely explained by differences in overpass time or pixel size as GOME-2 and SCIAMACHY are similar in both aspects. Furthermore, higher emissions are expected in the afternoon, i.e. at OMI overpass time, when the temperature is higher. The corresponding SCDs (Fig. 3.19e), however, indicate that the differences seen in the NO_2 VCDs are mainly caused by the different AMFs used for the conversion from SCDs to VCDs for the three data products.

Note that the enhancement is about 5×10^{14} molecules cm^{-2} on average, while it was shown in the previous section that for single 1.25° boxes the absolute enhancements can be as high as $\sim 1 \times 10^{15}$ molecules cm^{-2}. Smaller grid pixels show enhancements of up to $\sim 4 \times 10^{15}$ molecules cm^{-2}, and for single events even larger enhancements are found).

Another striking feature, similar to the results for soil moisture, water vapour and precipitation, is the generally higher NO_2 VCDs during the 10 days following the first rainfall event compared to the background levels before Day0. In sections 3.4.2.7 and 3.4.2.8, this important finding is studied more in detail by analyzing the NO_2 levels after Day0 depending on wind conditions and the precipitation on Day1 and beyond.

As indicated in Chapter 2, HCHO emissions from soils were found in several laboratory and field experiments (e.g. Veres et al., 2014). However, the time series of HCHO for OMI, GOME-2 and SCIAMACHY (Fig. 3.13f) show no significant enhancement around the day of the first rain event. Possible reasons are the low signal-to-noise ratio for HCHO observations or very low emission rates.

3.4.2.4 Land cover analysis

Soils from different regions and land types are differently affected by precipitation and vary strongly in their microbial composition, nitrogen availability and pH values which presumably leads to strong differences in emission fluxes from soils. In the following study, the ESA GLOBCOVER land cover classification is used to characterize different land cover types. The data set is scaled down from the initial 300 m resolution to the 0.25° x 0.25° grid using a most-common-value method. The resulting land cover map is shown in Fig. 3.14a.

For different land cover types, both the NO_2 response on Day0 and the background level of NO_2 vary systematically, see Fig. 3.14c. The observed NO_2 background VCDs per land cover type in the Sahel are mainly governed by biogenic emissions from soils and biomass burning. Anthropogenic activity and related emissions such as domestic fires or fertilized fields are at a very low level, and originate mostly from the southern, more

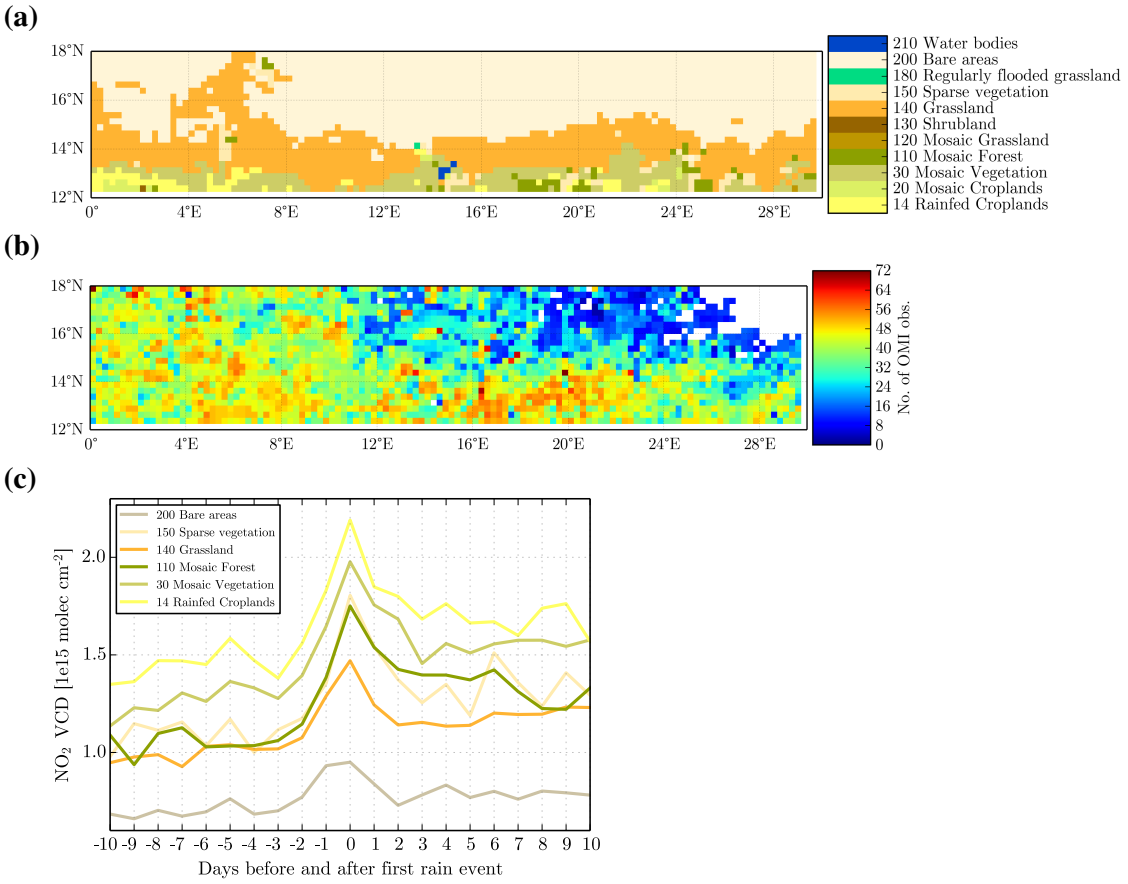

Figure 3.14: (a) ESA GLOBCOVER land cover classification for the Sahel downscaled to 0.25° x 0.25° resolution with the corresponding (official) identification number, short name and colour information for each class. **(b)** Spatial location and number of OMI observations for the reference case analysis (AMJ, 2007–2010). **(c)** Rain-triggered NO_2 enhancements from OMI for the Sahel region separated by the dominant land cover types.

populated part of the Sahel (Delon et al., 2010).

Systematic variations among the different land cover types are captured well: barren land, for example, shows the lowest levels of NO_2 compared to all other land cover types. Barren land relates to deserts with very low nitrogen input resulting in low sNO_x, even after wetting. This land type is also associated with fewer rainfall events, see Fig. 3.14b. Mosaic land covers (a mixture between various vegetation types, grassland, cropland or forest), refer in this area to the loose term *savannah* delineating the transition zone between tropical forests and deserts. Savannahs can comprise various land cover sub-types and are characterized by distinct dry and wet periods with strong vegetation density and productivity during the wet season in summer. It is expected that savannah and cultivated land used for agriculture show strongest responses to initial rain events due to their higher potential for soil emissions. Fig. 3.14c confirms these hypotheses: the largest NO_2 enhancements are found for cropland and savannah; grassland shows a significant, but smaller response; and the driest land cover type (bare area) shows only slightly enhanced NO_2 on Day0.

3.4.2.5 Analysis for different soil temperatures

In order to investigate the effect of different temperature regimes on the pulse on Day0, the (reference case) analysis is split up for different temperature ranges, i.e. 35–40 °C, 40–45 °C and 45–50 °C, based on ECMWF soil temperature data (Fig. 3.15). However, no clear dependence of the enhancement on Day0 on soil temperature is found.

By introducing such a temperature separation, the triggered incidences are attributed to different months of the year and locations within the study region, e.g. in April more southern pixels are selected and in June more northern pixels. The systematic relation between the seasonal cycles in the temperature and NO_2 VCDs as well as the spatial selection of the data complicates the interpretation of Fig. 3.15.

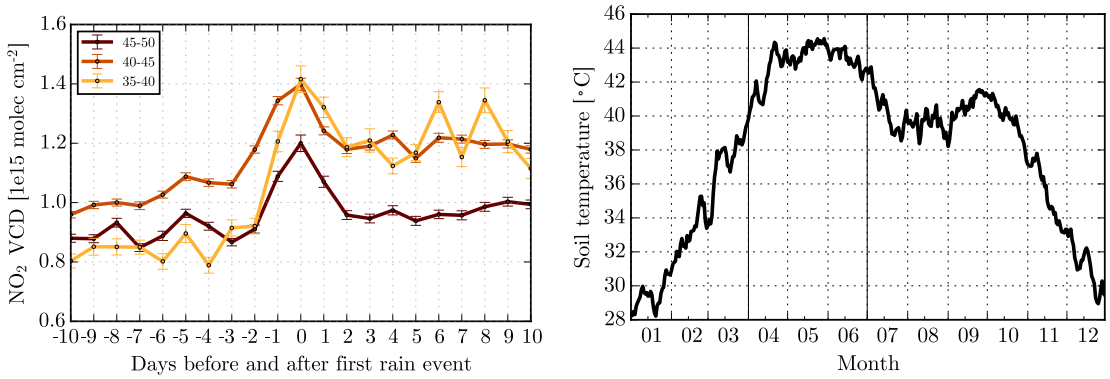

Figure 3.15: Left panel: NO_2 VCDs from OMI around the first day of rainfall for different soil temperatures on Day0 for the Sahel region (based on the reference case settings). **Right panel**: daily time series of soil temperature (from 12UTC ECMWF data) for the Sahel region (0–20° W, 12–18° N) averaged for the years 2007, 2008, 2009 and 2010.

3.4.2.6 Monthly maps of pulsed soil NO_x emissions in the Sahel

It was shown above that monthly averages of NO_2 VCDs over northern Africa show generally enhanced levels over the Sahel and that this enhanced band of NO_2 shifts northwards similarly to the northward movement of the ITCZ in the same period. This section compares these findings to pulsed emissions occuring on the first rainy day of the wet season. The focus is set on the reference case settings presented in Section 3.4.2, i.e. a drought of 60 days and a precipitation threshold of 2 mm.

The analysis with pulsed events confined to specific months (Fig. 3.16) agree with the previous findings by showing a clear spatio-temporal dependence of pulsed sNO_x emissions on the movement of the ITCZ.

3.4.2.7 Influence from other sources on the NO_2 signal

In this section, the effects of possible additional sources of NO_x such as fire or lightning and systematic errors in the satellite retrieval due to e.g. changes in cloud fraction are inves-

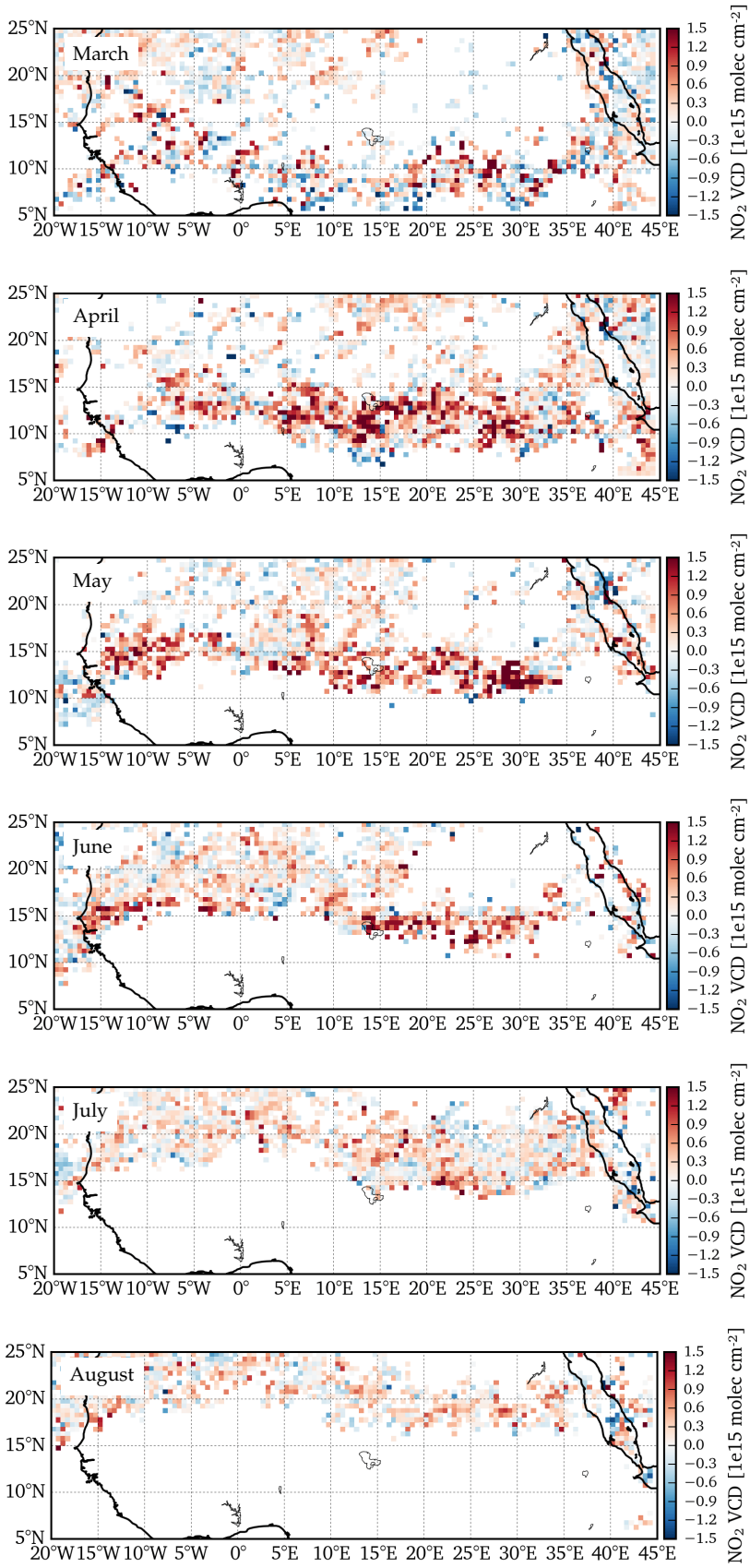

Figure 3.16: Absolute enhancements of NO_2 VCDs from OMI on Day0, i.e. the first day of precipitation after a prolonged drought akin to Fig. 3.3.d but for higher resolution (0.5°) and split up for cases where Day0 is in one of these months: March, April, May, June, July, August. Precipitation and NO_2 VCDs are for the years 2007–2011.

tigated. To minimize the influence of these effects, the algorithm excludes measurements where lightning, fires or an effective cloud fraction > 20% are detected.

Lightning NO_x. Lightning is a natural source of NO_x in the atmosphere and even represents the largest sources of NO_x in the upper troposphere (e.g. Schumann and Huntrieser, 2007, and references therein). Since lightning typically occurs in high convective clouds that may correlate with the first rain event, the analysis is potentially affected.

Fig. 3.17 depicts daily time series for NO_2 VCDs, precipitation and lightning counts averaged for the years 2007 to 2010. The seasonal evolution of the number of lightning strikes closely follows the precipitation patterns. Fig. 3.17 also illustrates that lightning is not a governing source of NO_x in the Sahel as no correlation between lightning strikes and NO_2 VCDs can be found, although a direct proportionality would be expected. Precipitation also does not correlate well with the observed seasonal cycle in NO_2. This is, however, expected as microbial emissions of NO_x from soils are not a linear function of soil moisture content or precipitation.

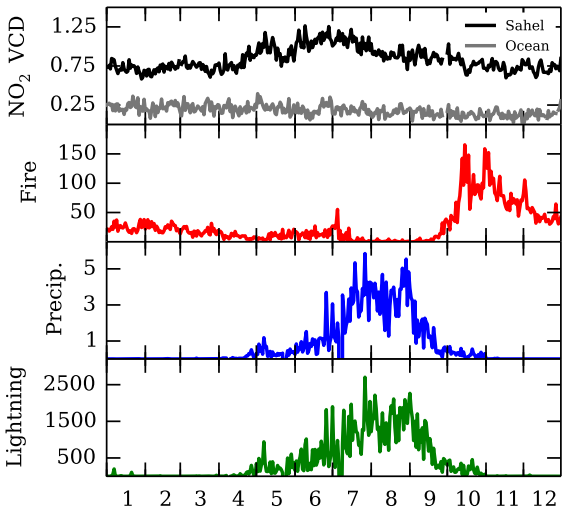

Figure 3.17: Daily time series for the Sahel region (0–30°W, 12–18°N) averaged for the years 2007, 2008, 2009 and 2010. The first row of each panel shows mean NO_2 VCDs from OMI in molecules cm^{-2} (black) and a clean ocean reference (grey, 130–150° W, 12–118° N). The second row shows the number of active fire counts in the Sahel from MODIS. The third row shows average precipitation from the TMPA/TRMM product in mm. The fourth row shows the number of lightning strikes detected by WWLLN.

Fig. 3.18 shows results for the reference case, similar to Fig. 3.13, but with (solid lines) and without (dashed lines) lightning screening, i.e. grid pixels coinciding with a lightning event are removed. Because of the low detection efficiency (DE) of the WWLLN in African regions ($\sim$ 20%) the lightning screening is also tested for central Australia (15°–30° W, 2°–10° S) where the DE of the WWLLN is very high (80–90%). Turning off the lightning screening leads to very similar results as for the reference case, but with a slightly stronger response in NO_2 VCDs on Day0 for all three instruments. While this enhancement might

be partly caused by the additional NO_x produced by lightning, also a larger number of true precipitation-triggered events that lead to soil emissions may be included in this analysis. This is conceivable as clouds and thunderstorms accompanied by lightning strikes lead to the most heavy precipitation events. As the screening only causes minor changes in peak NO_2 columns, lightning can be excluded as the main cause of the observed NO_2 enhancements.

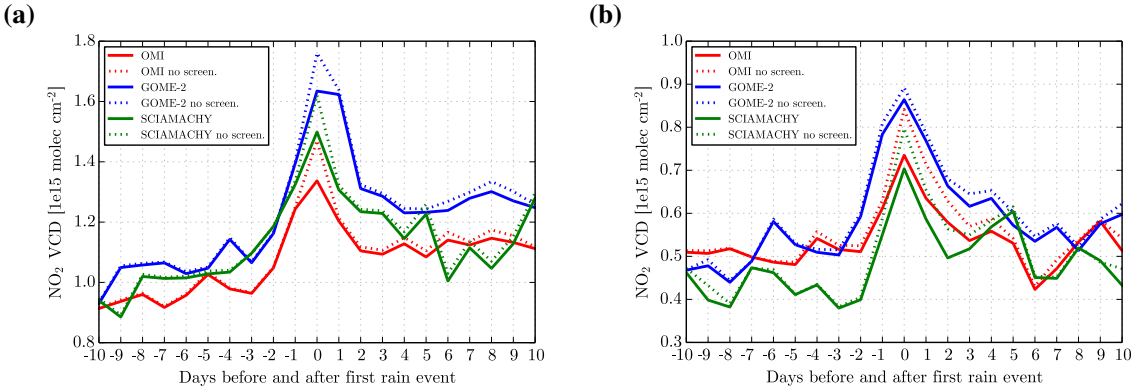

Figure 3.18: Effect of lightning screening on the response of NO_2 VCDs around the first day of rainfall after a prolonged dry spell. **(a)** NO_2 VCDs for the Sahel region from SCIAMACHY, GOME-2 and OMI without lightning screening (dashed lines) and with lightning screening (solid lines). **(b)** The corresponding results for central Australia (15–30° W, 2–10° S).

Fire. The seasonal cycle in fire counts, depicted in Fig. 3.17, shows the highest activity in the Sahel in October and November for the years 2007 to 2010, while average NO_2 VCDs are the highest in summer.

Switching off the routine data screening for pixels that coincide with fire events in the same 0.25° x 0.25° grid pixel results in no change of the NO_2 signal (not shown). This is due to the fact that only very few fires occur in the wet season, on average only in 0.002% of all individual time series on Day0 in the reference case, excluding fire as an important NO_2 source within the analysis.

Cloud effects. The influence of clouds on the results was analyzed through the temporal evolution of the mean cloud fractions (CF), NO_2 VCDs, and NO_2 SCDs around the precipitation event. SCDs were inspected because they provide the actual measured signal without involving a tropospheric AMF, which is generally very sensitive to clouds.

Fig. 3.19a depicts the mean effective CF for SCIAMACHY, GOME-2 and OMI for the Sahel region. The differences of the absolute value of the CF are probably related to the different cloud algorithms between GOME-2/SCIAMACHY (FRESCO+) and OMI (OMCLDO2). The different temporal variation might also be partly related to the different overpass times and pixel sizes among the three satellite instruments. These results suggest that the observed NO_2 peaks around Day0 are not caused by cloud effects for the following reasons: first, for all sensors only small cloud fractions (<11%) are found (for measurements

with CF < 0.2). Second, for SCIAMACHY and GOME-2 observations no systematic temporal variation of the CF is found. Third, the small but systematic enhancement of the CF around Day0 found in the OMI observations would rather lead to a decrease (due to the shielding effect) of the NO_2 SCDs around Day0 as soil emissions are expected to remain close to the surface. If only measurements with cloud fractions >20% are considered, no spike is observed in the SCDs (Fig. 3.19f); GOME-2 and OMI even show a dip on Day0, which is also seen in the respective VCDs (Fig. 3.19d). Interestingly, while there is a strong systematic enhancement of the FRESCO+ and OMCLDO2 cloud fractions, the NO_2 SCDs show no peak around Day0 for GOME-2 and OMI. This indicates that clouds effectively shield the pulsed soil emissions.

Influence of transport processes. Finally the possible influence of transport processes, which might be correlated with the occurrence of the first rain event, is investigated. As depicted in Fig. 3.20, a strong southerly wind is blowing at ground level (1000 hPa) the 2 days before the first rain event and on Day0 in the Sahel. In order to investigate whether polluted air from southern locations, especially the tropics, is transported northward into the Sahel, the analysis is repeated for days governed by either northerly or southerly winds (Fig. 3.21). For the distinction between both directions, the wind vectors from ECMWF at three different altitudes (600, 850 and 1000 hPa) are required to point to the same direction (either all to the north or all to the south). The left panel in Fig. 3.21 depicts results for northerly winds; the right panel for southerly winds. Although the background levels of NO_2 are reduced on days with northerly winds, enhancements in VCDs around the first day of rainfall remain apparent despite low statistics, especially for OMI and GOME-2 observations. For days with southerly winds the background is slightly higher and clear spikes for the OMI and GOME-2 observations can also be detected. Hence, these findings indicate that atmospheric transport has a systematic influence on the background NO_2 levels (see also Section 3.4.2.8), but not substantially on the enhancement around Day0.

3.4.2.8 Enhanced emissions after Day0

In the reference case analysis presented in the sections above (e.g. in Sec. 3.4.2.3), NO_2 VCDs show an enhancement with respect to the background, i.e. the average NO_2 VCDs before Day-1, not only on Day0, but also on Day-1, Day2 and Day3. It is assumed that the *background* NO_2 VCDs are not influenced by the precipitation-triggered sNO_x pulsing event and, thus, can be used as reference to derive an absolute enhancement in NO_2 VCDs predominantly induced by pulsed soil emissions. However, it is shown in Fig. 3.13e and Fig. 3.19c,e that the NO_2 VCDs after the pulsing event (Day3 to Day10) are consistently higher compared to the background before Day0. This could be related to inflow of soil NO_x from adjacent pixels ($i + n$) that receive the first rain shortly after the central pixel (i). However, initial tests (Fig. 3.22) show that the number of such incidents is quite small (less than 5%). The right panel of Fig. 3.22 shows the probability of neighbouring pixels

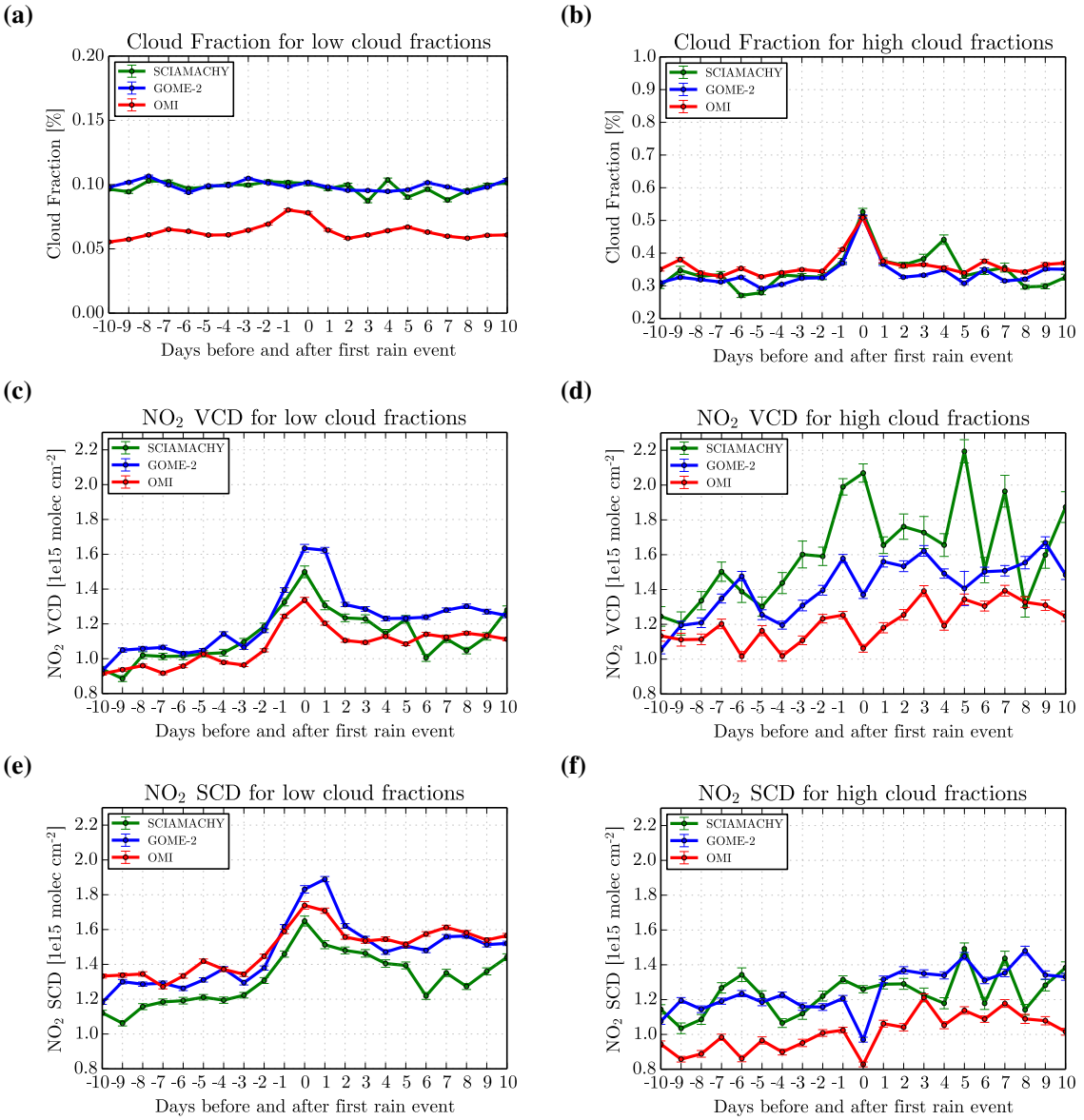

Figure 3.19: Investigation of cloud effects on the retrieved NO_2 SCDs and VCDs. **(a)** Mean cloud fraction of the three satellite instruments for the reference case (cloud fraction <20%). **(b)** Mean cloud fraction of the three satellite instruments but considering only observations with cloud fraction > 20%. **(c)** NO_2 VCDs for the reference case. **(d)** NO_2 VCDs only considering observations with high cloud cover (cloud fraction > 20%). **(e)** NO_2 SCDs for the reference case. **(f)** NO_2 SCDs only considering observations with high cloud cover (cloud fraction > 20%).

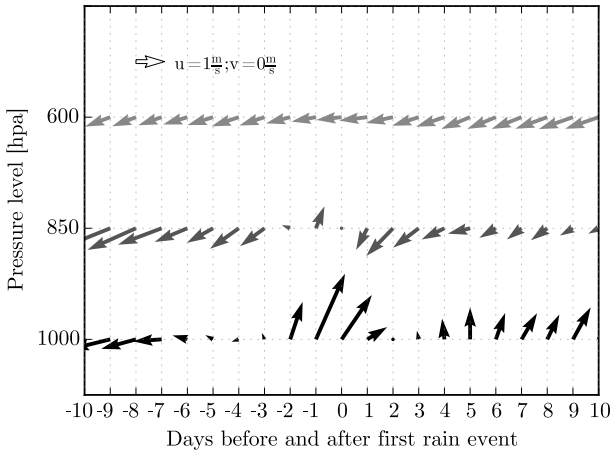

Figure 3.20: Mean ECMWF wind vectors at three different pressure levels. At the surface, a strong south-westerly wind is blowing the 2 days before the first rain event in the Sahel region followed by northerly winds. At 600 hPa winds are constantly from the north-west.

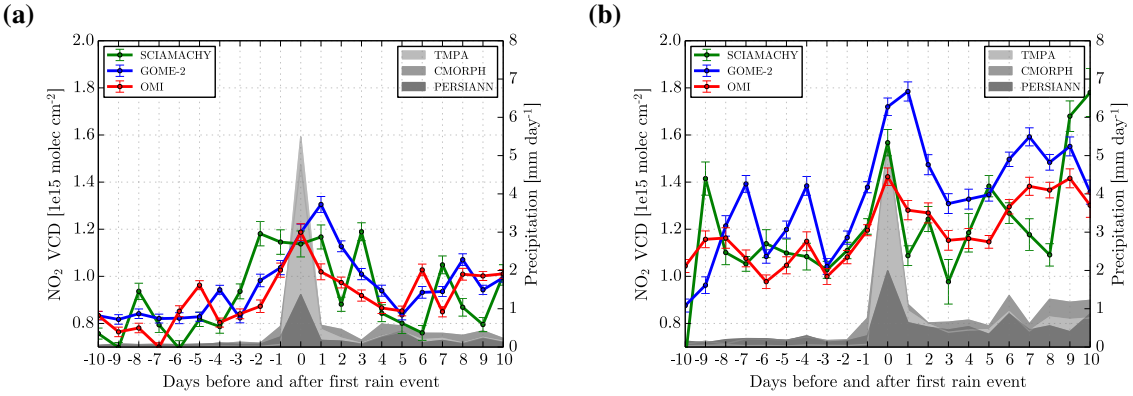

Figure 3.21: Same as Fig. 3.13d, but filtered for **(a)** northerly and **(b)** southerly winds. The filter criterion is fulfilled, if the wind direction at 600, 850 and 1000 hPa is north or south, respectively.

receiving the first rain after pixel *i* over a course of 60 days. This probability decreases with time and shows no particular drop at 14 days, in contrast to the time series of NO_2 VCDs in Fig. 3.24d,e. Furthermore, the average precipitation in a 10 pixel buffer around pixel i is almost constant over the course of the next weeks (left panel of Fig. 3.22).

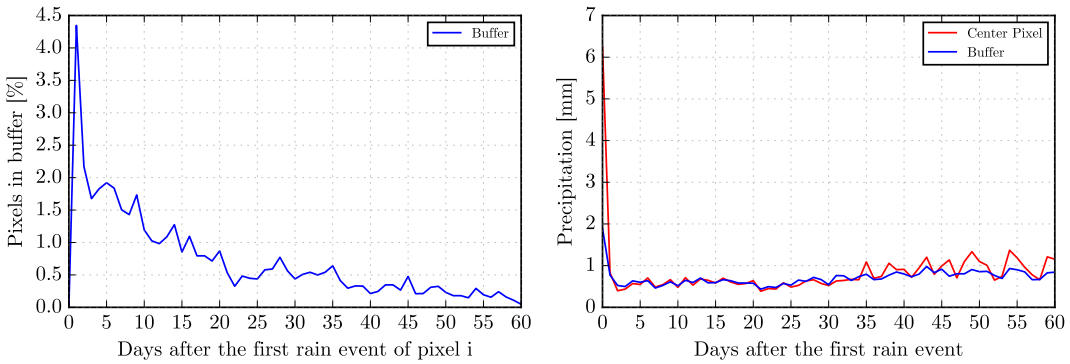

Figure 3.22: Left: Average precipitation over 60 days following Day0 in the central pixel (red) and for the neighbouring 10 pixel buffer (blue). **Right**: % of pixels in a 10 pixel buffer around pixel *i* experiencing the first rain event after pixel *i*.

For this reason, and because the effect is possibly offset by sNO_x advection out of the pixel of interest, it is assumed that the effect of inflow is not dominant. As events with strong emissions (compared to background) are studied, a "smearing effect" by advection leads to a consistent underestimation of the peak and subsequent emissions. Thus, it can be concluded that inflow cannot explain the enhancement for 14 days after the first rain event. Furthermore, it remains unclear to what extent the enhanced NO_2 VCDs are affected by a possible underlying change in the background.

This leads to four interesting questions. (i) Are the slightly enhanced NO_2 VCDs after Day0 related to the pulse on Day0? (ii) In case the enhanced NO_2 VCDs after Day0 are (partly) caused by other sources, what effect does a background correction have on the retrieved absolute enhancements in NO_2 VCDs around Day0? (iii) Is continuous precipitation the cause for the enhancement after Day0? (iv) In case the enhanced NO_2 VCDs after Day0 are only related to the pulsed rain event: is it possible to give quantitative estimates on these 'continuous' soil emissions?

Fig. 3.23a depicts the reference case analysis for the Sahel region with respect to 120 days around the first day of rainfall after the drought period. The NO_2 VCDs observed by the three satellite instruments show consistent patterns in the spike around Day0 and still slightly enhanced NO_2 VCDs 60 days after Day0.

To investigate whether the increased NO_2 VCDs after Day0 are related to the pulsed rain on Day0 or caused by a general change of the background NO_2 VCDs (e.g. related to a seasonal variation), the temporal evolution of the background (not affected by a pulsed rain event) is estimated in the following.

In a first attempt NO_2 VCDs are averaged over all grid pixels located at the same latitude as the identified rain events assuming latitudinal homogeneity in NO_2 background VCDs. This assumption is justified in the Sahel due to the latitudinal distribution of its land

cover types governing NO_2 VCDs (the corresponding results are depicted in Fig 3.23b). Compared to Fig 3.23a a much smoother temporal evolution is found (because more data are averaged), but apart from the much smaller spike on Day0, very similar values can be seen in both panels. This confirms the assumption that the main part of the increase of the background value is not caused by the precipitation on Day0. However, the spike in NO_2 VCDs around Day0 is still evident because this averaging method still considers the initial pixel with its adjacent neighbours, which are probably affected by either the overall precipitation pattern or spatial aliasing effects during the gridding of the NO_2 data products. Thus, in Fig 3.23c) a 10 pixel buffer is additionally applied to the algorithm. Screening out such pixels leads to a time series of NO_2 without the distinct spike around Day0.

The time series of NO_2 VCDs retrieved using the two latitudinal averaging methods is denoted as the prevailing background and is subsequently subtracted from the reference case analysis (Fig. 3.23). In the first case, without the application of an additional buffer (Fig. 3.23d), absolute enhancements of 0.43×10^{15} molecules cm^{-2} for GOME-2 and SCIAMACHY are found on Day0. Also a steady increase in NO_2 VCDs several days prior to Day0 is observed. Although the pronounced spike in NO_2 VCDs decreases rapidly in the days following Day0, it lasts several weeks until the VCDs reach a minimum (but stays still slightly higher than on Day-60 to Day-20). A similar behaviour is observed for the case study with buffer screening (Fig. 3.23e). Here, absolute enhancements of 0.4×10^{15} molecules cm^{-2} for OMI and 0.62×10^{15} molecules cm^{-2} for GOME-2 and SCIAMACHY are found on Day0.

It can be concluded that the slightly enhanced NO_2 VCDs after Day0 are related to the precipitation on Day0 at or close to the considered location. As the focus is on the quantification of the emission pulse triggered by the first rain of the wet season, it still needs to be clarified whether the enhanced NO_2 VCDs after Day0 are induced by the initial precipitation on Day0 or by continuous precipitation during the following days. To answer this question time series with the additional selection criterion of 3, 5, 10 and 20 days of no precipitation following Day0 are extracted. Fig. 3.24a depicts the OMI NO_2 VCDs for 0, 3, 5, 10 and 20 days without precipitation after Day0. The intercomparison of these time series is not straightforward as the background values vary for each case indicating that the time series are captured at different dates throughout the April-May-June period. Longer drought periods after Day0 are more likely at the very beginning of the wet season (April), whereas more constant rainfall dominates at a later stage, e.g. in June. In this time period background NO_2 VCDs generally increase in the Sahel. It is assumed for this analysis that the impact of the different dates only affects the background and not the enhancement on Day0 as the selection criteria (precipitation and drought length thresholds) presumably have the largest effect. In order to analyse the enhancement around Day0 only,the above described latitudinal background correction is applied to each time series individually which reduces the influence of the background drastically. Fig. 3.24b,c show the corresponding background NO_2 VCDs derived without and with the aforementioned buffer screening applied. Naturally, the absolute change between the

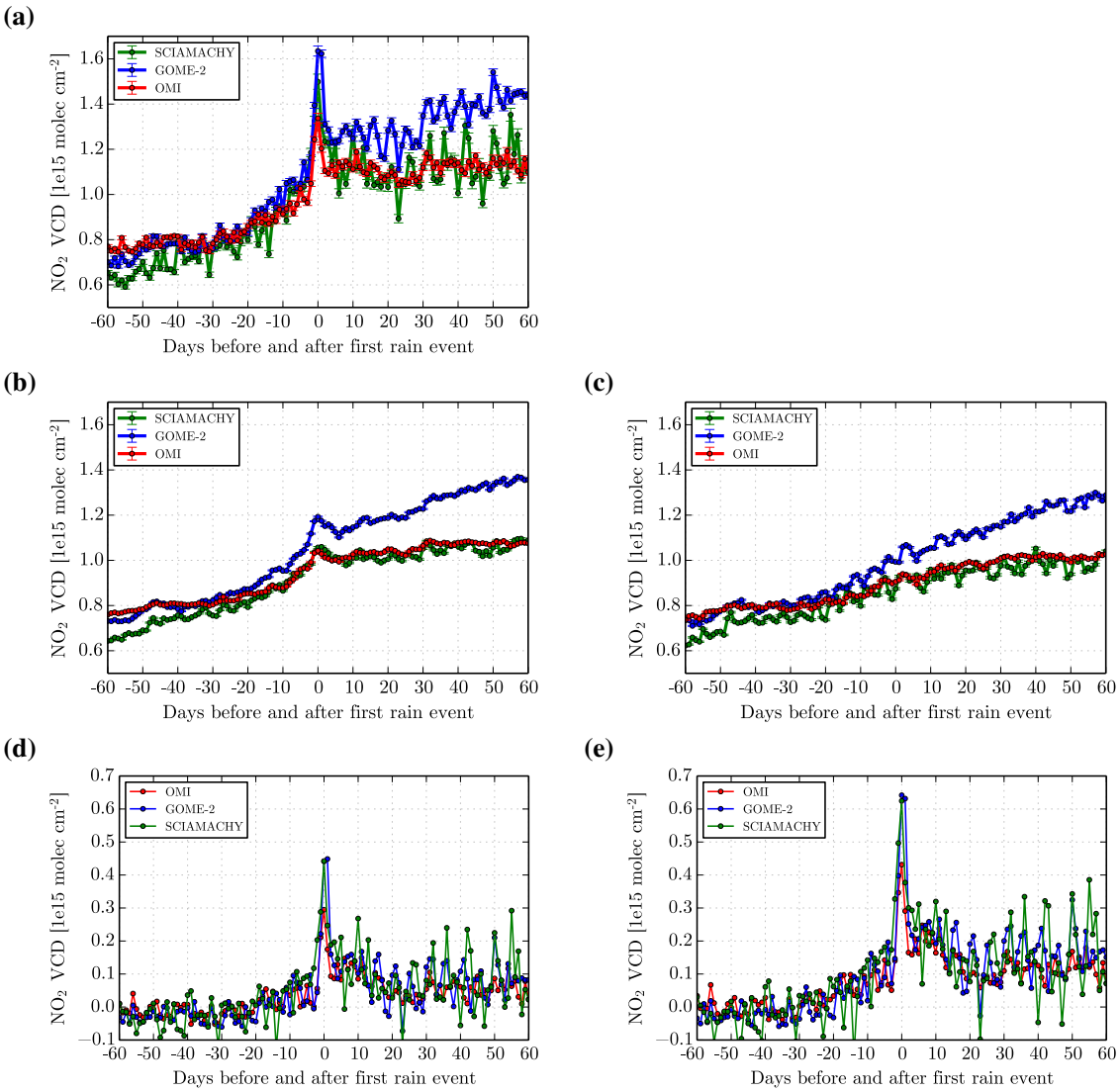

Figure 3.23: Analysis of NO_2 VCDs 60 days before and after the first day of rainfall in the April-May-June period for the Sahel region. **(a)** NO_2 VCDs from OMI, GOME-2 and SCIAMACHY. **(b)** Latitudinal-averaged NO_2 VCDs corresponding to the reference (for details see text). **(c)** Latitudinal-averaged NO_2 VCDs corresponding to the reference considering an additional buffer of 10 pixels around the actual-triggered pixel to avoid influence of enhanced NO_2 VCDs in the vicinity of the precipitation events. **(d)** Background corrected NO_2 VCDs: panel (a) - panel (b) **(e)** Background (with buffer) corrected NO_2 VCDs: panel (a) - panel (c)

different background time series is smaller compared to panel Fig. 3.24a as they represent averages over all pixels on the same latitude. The changes on panel Fig. 3.24c are even smaller because the pixels in proximity to the triggered rainy pixel are excluded from the averaging. Finally, Fig. 3.24d and e depict the differences between panel (a) and panels (b) and (c), respectively. As expected, the enhancements in NO_2 VCDs around Day0, are more pronounced for cases including a 10 pixel buffer during the background correction. Although the absolute enhancement on Day0 is almost identical for the different cases, the time series still differ in the observed background NO_2 VCDs. These systematic differences, seen in Fig. 3.24e and d, hint at more complex variations in the background which are not entirely resolved by the correction. They could also be related to the fact that for the cases with longer dry periods after Day0 the probability of precipitation in the vicinity of the considered location is lower. This implies, again, also differences in space and time of the observations which influences the observed NO_2 VCDs.

Generally it is found that the NO_2 VCDs stay enhanced after Day0 for a period of about 2 weeks, almost independent from the duration of the dry period after Day0. This gives rise to the assumption that the enhanced emissions are mostly caused by the initial rain event on Day0. Here, only results for OMI are presented because it has best statistics. Nevertheless, the analysis with data from the other instruments leads to the same conclusion.

3.4.3 Further study regions

As could be seen in the global analysis in Fig. 3.3, large-scale hot-spots in NO_2 VCD enhancements are not only detectable in the Sahel, but also in south-western Africa and in Australia. Subsequently, also the average NO_2 VCDs around the first day of rainfall for all three satellite instruments in these two regions are presented.

Fig. 3.25a depicts the results for south-western Africa (17–23° E, 22–28° S) for a drought period (precipitation < 2 mm) of at least 60 days in the months September/October/November 2007–2010 representing the transition phase between the dry summer and following wet season. Compared to the Sahel reference case, the evolution of NO_2 VCDs before and after the first day of rainfall increases and decreases more gradually without having a distinct spike on Day0. This might be due to different environmental conditions such as soil type or lower statistics because of the much smaller spatial extent. It is, thus, more difficult to estimate the absolute enhancement compared to a defined background level. The difference between highest and lowest NO_2 VCDs in the full time series is $\sim 0.5 \times 10^{15}$ molecules cm^{-2} for all three instruments.

Fig. 3.25b shows the analysis results for NO_2 VCDs for the central part of Australia (120–145° E, 22–31° S) for the time series from 2007 to 2010. Since the seasonality in rainfall in this region is less pronounced, the full time series is considered in the analysis. The well pronounced spikes shows an absolute enhancement of $\sim 0.3 \times 10^{15}$ molecules cm^{-2} for the three instruments, which is comparable to the findings from the Sahel and south-western Africa.

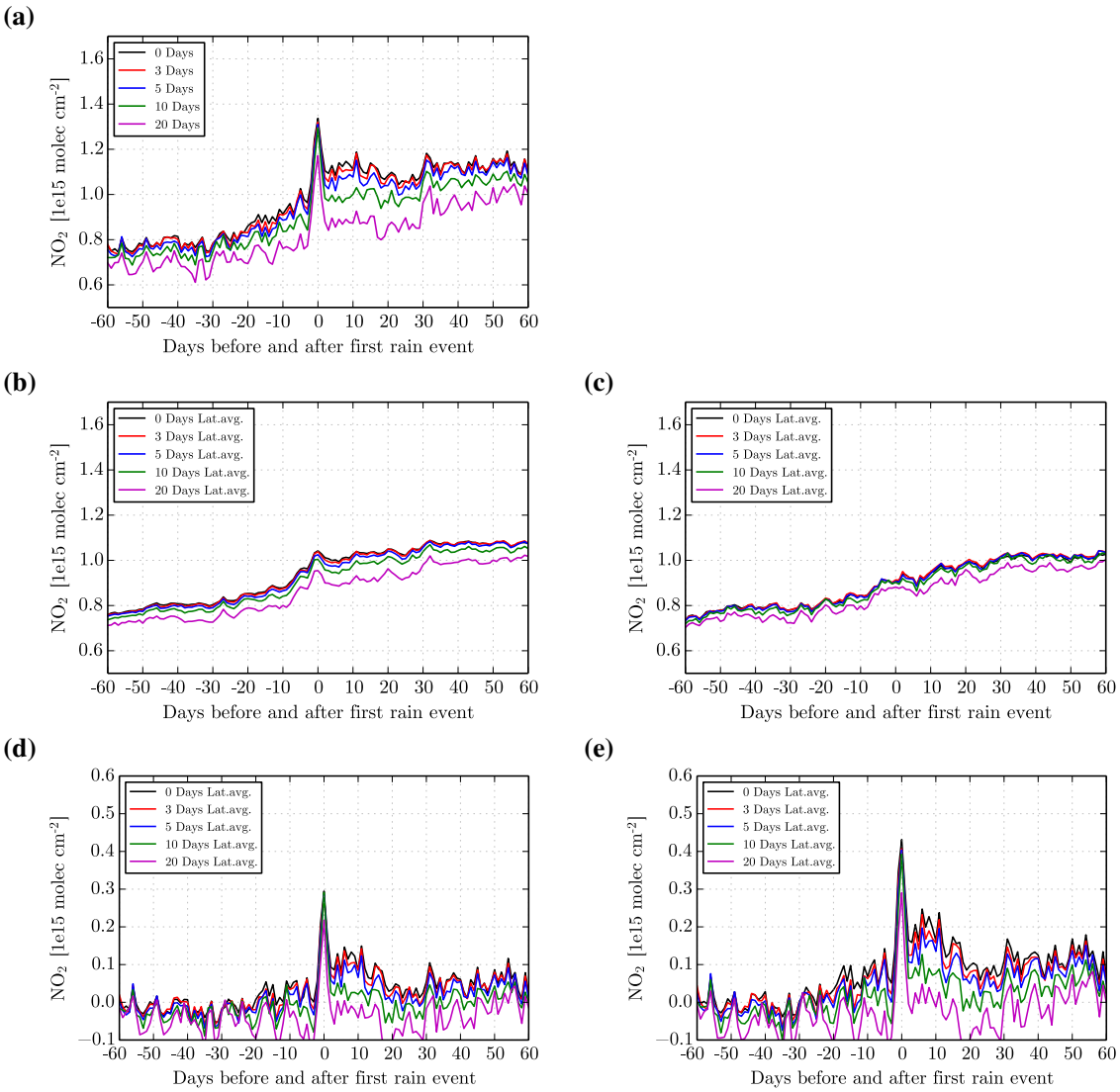

Figure 3.24: Investigation of the effect of different periods of dry days following Day0. **(a)** Reference case analysis for OMI NO_2 VCDs filtered for time series experiencing 0, 3, 5, 10 and 20 days of drought after Day0. **(b)** Background time series of NO_2 VCDs without buffer screening as presented in Fig. 3.23b for the corresponding time series experiencing 0, 3, 5, 10 and 20 days of drought after Day0. **(c)** The corresponding background time series of NO_2 VCDs with buffer screening as presented in Fig. 3.23c. **(d)** Differences between panels (a) and (b). **(e)** Differences between panels (a) and (c).

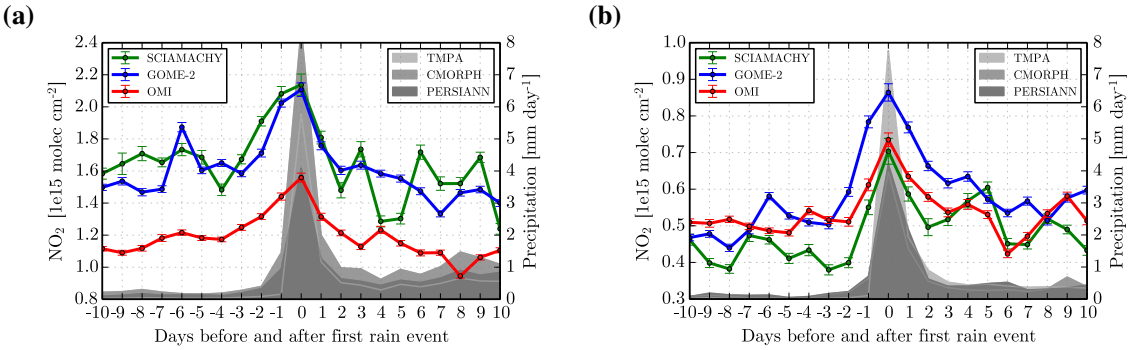

Figure 3.25: (a) NO_2 VCDs from SCIAMACHY, GOME-2 and OMI for south-western Africa in September-October-November around the first day of rainfall in this period. Precipitation is represented by the grey shaded areas. **(b)** Results for central Australia for the complete years 2007–2010.

3.4.4 Sensitivity studies

The following section presents sensitivity tests for the algorithm described in Section 3.3, i.e. analyses based on different thresholds and input data sets. Thereby, a precipitation threshold of 2 mm, a drought length of 60 days and the use of the TRMM/TMPA precipitation product are used as reference.

Different precipitation products as trigger. In Fig. 3.26, the analysis is run based on the (i) TRMM/TMPA, (ii) CMORPH and (iii) PERSIANN product used for the detection of precipitation. Although slight differences are found in the response of the NO_2 VCDs from OMI, GOME-2 and SCIAMACHY to the initial precipitation on Day0, the magnitude of the NO_2 pulse is detected similarly regardless of the underlying precipitation product used.

Different drought lengths before Day0. In Fig. 3.27, the analysis is run for different drought lengths prior to the initial precipitation event. It can be seen that longer drought periods ($\sim$ 20 days) generally lead to, on the one hand, lower background NO_2 VCDs before Day0 and, on the other hand, to stronger NO_2 enhancements on Day0. Thereby, a drought length of 60 days leads to, on average, the lowest background values prior to Day0 and the highest response on Day0.

Different precipitation thresholds on Day0. In Fig. 3.28, the analysis is run for different precipitation thresholds (based on TRMM/TMPA) on Day0. During the preceding drought period, no day experienced more than 0.1 mm precipitation. Due to strict filtering of the data, large uncertainties arise (especially for SCIAMACHY) but the analysis indicates that stronger rainfall on Day0 may lead to stronger responses in the NO_2 VCDs as observed by OMI and GOME-2.

Global Maps for other satellite instruments. Fig. 3.29 depicts the global analysis of strong enhancements in NO_2 VCDs on Day0 as observed by GOME-2 and SCIAMACHY. Thereby, similar spatial patterns in the enhancements over the Sahel region, South Africa and Australia are found compared to the findings for OMI (Fig. 3.3d). In addition, GOME-2 and SCIAMACHY measurements suggest strong and consistent enhancements over India on Day0.

Impact of a priori precipitation on the derived soil NO_x emissions. Lastly, Fig. 3.30 depicts the global analysis for OMI observations of NO_2 similar to Fig. 3.3d but for the CMORPH and PERSIANN products as criterion for precipitation. Although the observed enhancements in NO_2 over the Sahel vary for the three precipitation products, the derived mass flux rates (in terms of nitrogen) are similar as the choice of the precipitation data affects the background correction as well.

A1 TMPA

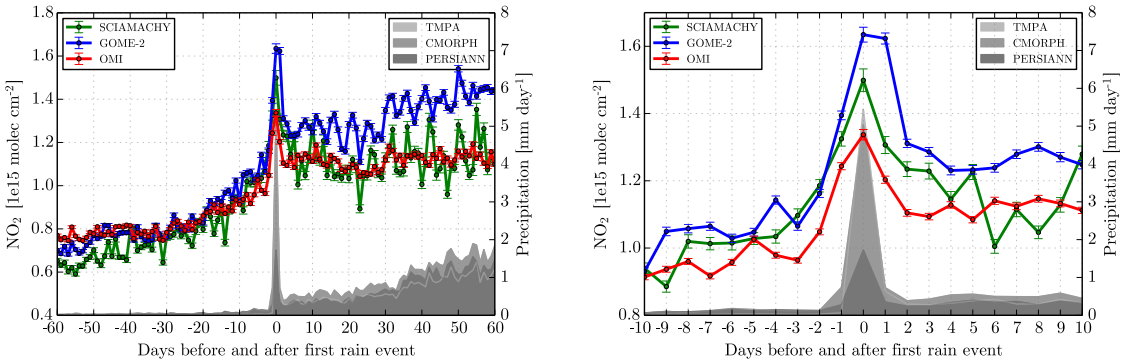

A2 CMORPH

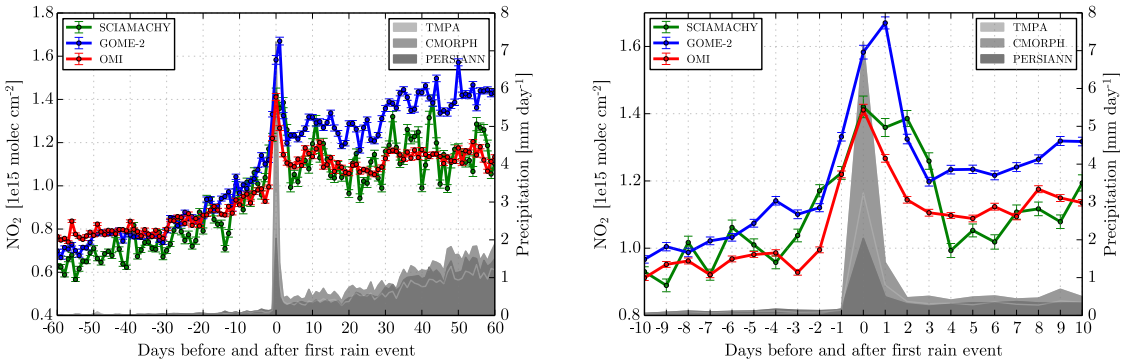

A3 PERSIANN

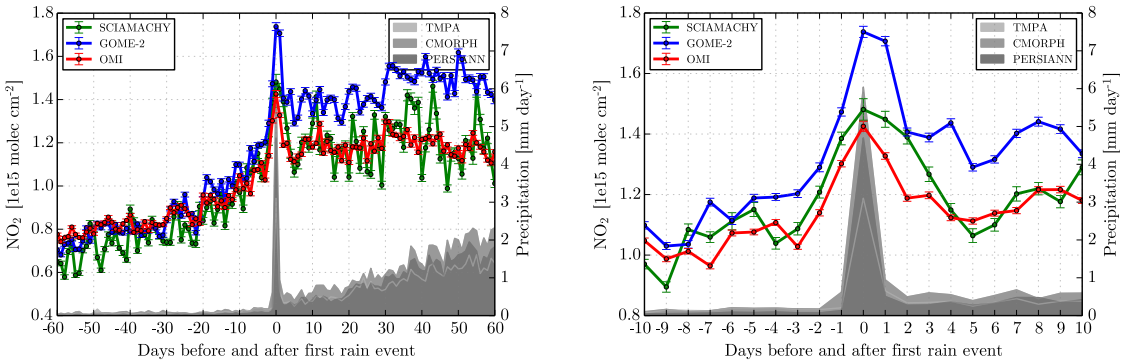

Figure 3.26: Reference case for different precipitation products as trigger. NO_2 VCDs are shown (akin to Fig. 3.13.e) from TRMM/TMPA (**A1**), CMORPH (**A2**) and PERSIANN (**A3**) around the first day of rainfall for different precipitation products as trigger for the precipitation threshold of 2 mm for the Sahel region. The left panels represent the full time series of 60 days before and after Day0, the right panels show a zoom-in for the 10 days before and after.

B1 OMI

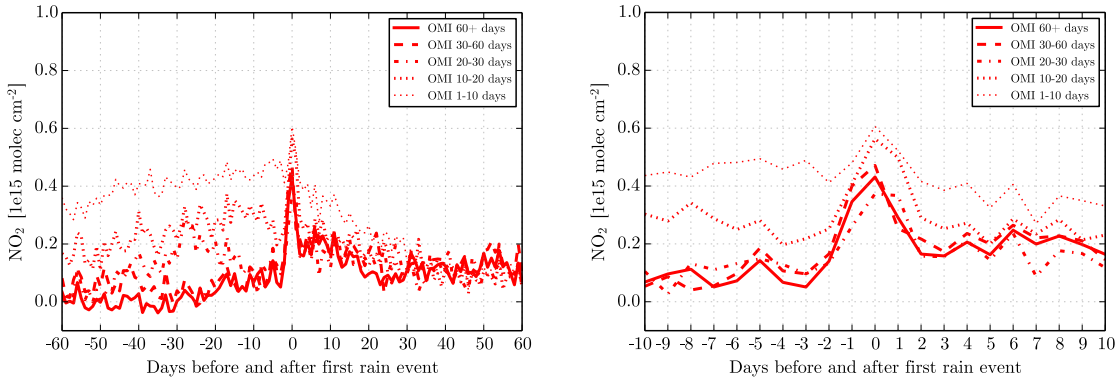

B2 GOME-2

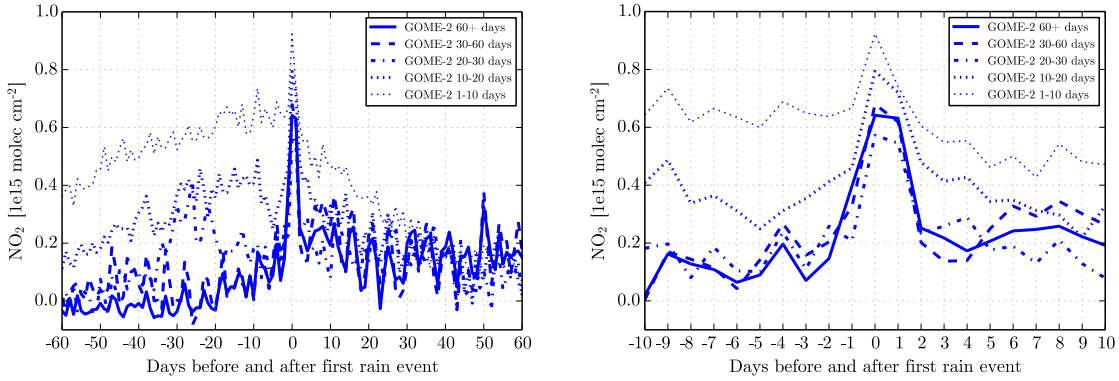

B3 SCIAMACHY

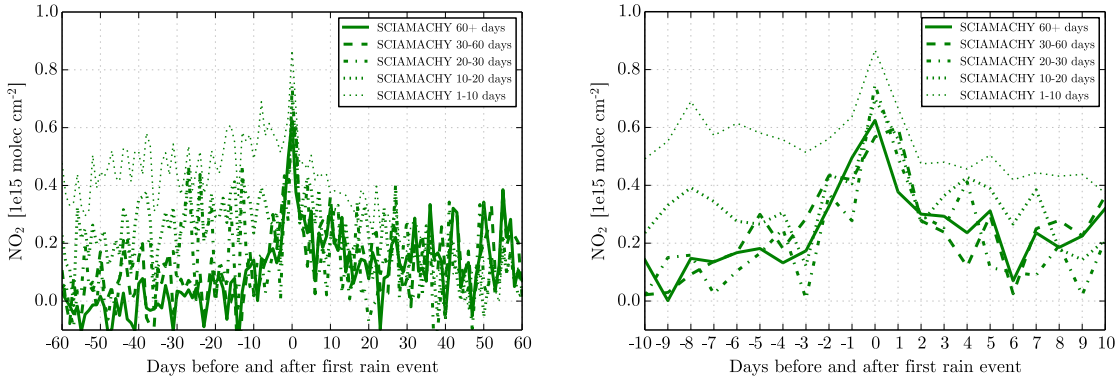

Figure 3.27: Different drought lengths for the reference case. NO_2 VCDs are shown from OMI (**B1**), GOME-2 (**B2**), SCIAMACHY (**B3**) around the first day of rainfall for different preceding drought periods for the Sahel region with a precipitation threshold of 2 mm. For better intercomparison, the latitudinal background correction with buffer as described in Section 3.4.2.8 is applied to each time series individually. The left panels represent the full time series of 60 days before and after Day0, the right panels show a zoom-in for the 10 days before and after.

C1 OMI

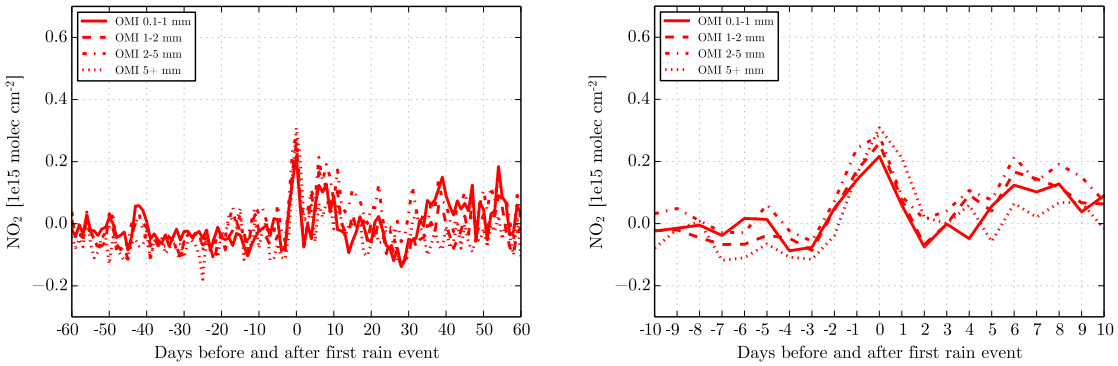

C2 GOME-2

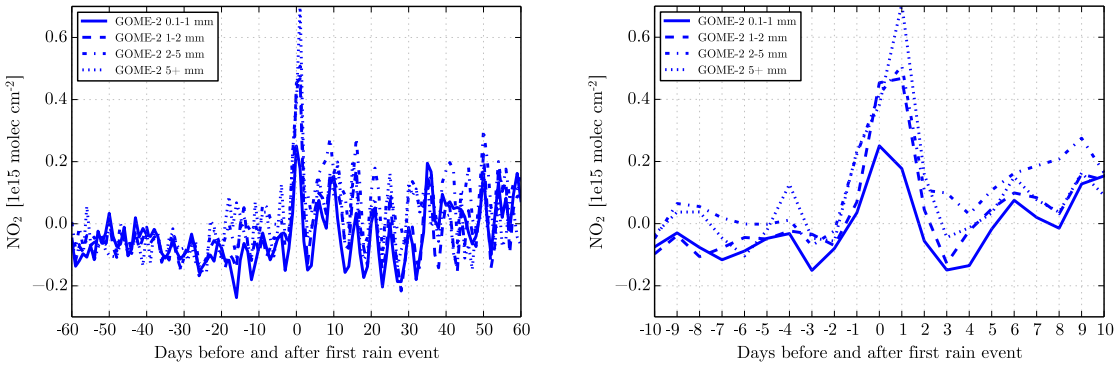

C3 SCIAMACHY

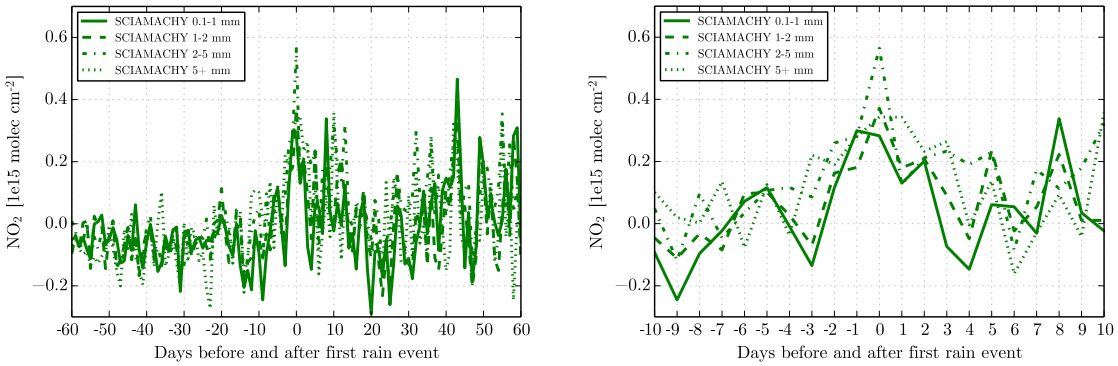

Figure 3.28: Different precipitation thresholds on Day0 for the reference case. NO_2 VCDs are shown from OMI (**C1**), GOME-2 (**C2**), SCIAMACHY (**C3**) around the first day of rainfall for the Sahel region for a drought period of at least 60 days. The results are separated for different intervals of the precipitation threshold on Day0. A drought day is defined by precipitation < 0.1 mm per day. For better intercomparison, the latitudinal background correction with buffer as described in Section 3.4.2.8 is applied to each time series individually. The left panels represent the full time series of 60 days before and after Day0, the right panels show a zoom-in for the 10 days before and after.

D1 GOME-2

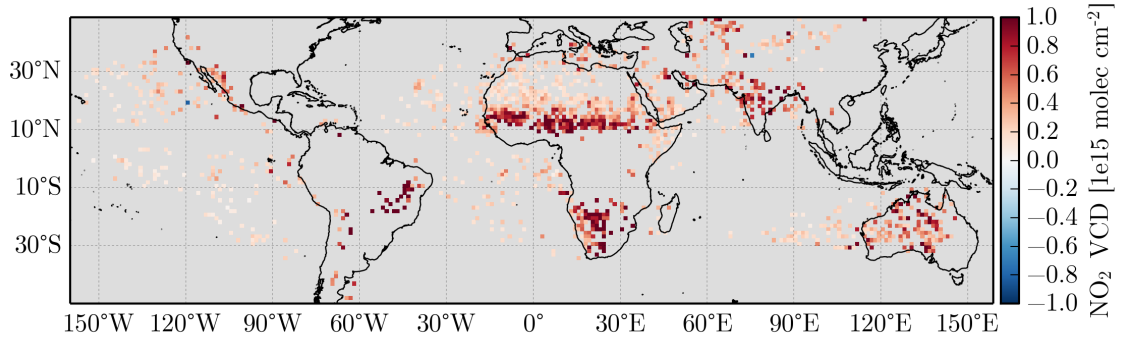

D2 SCIAMACHY

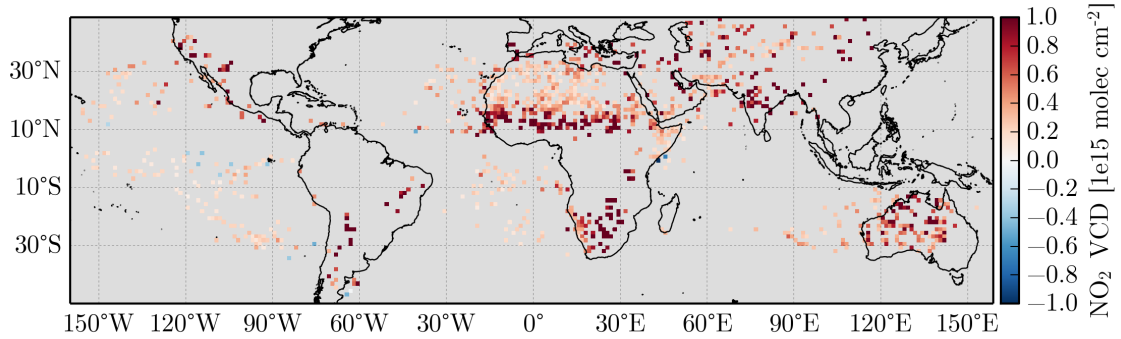

Figure 3.29: Global Maps for other satellite instruments (60 days of drought, 2 mm precipitation threshold). Absolute differences in NO_2 VCDs compared to Days -10 to -2 from GOME-2 (**D1**) and SCIAMACHY (**D2**) on Day0 (first day of rainfall) are depicted which were computed similarly as for OMI in Fig. 3.3.d for OMI. The data was screened for significant changes and pixels containing less than 20 measurements on Day0 (or less than 50 measurements from Day-10 to Day-2).

E1 CMORPH

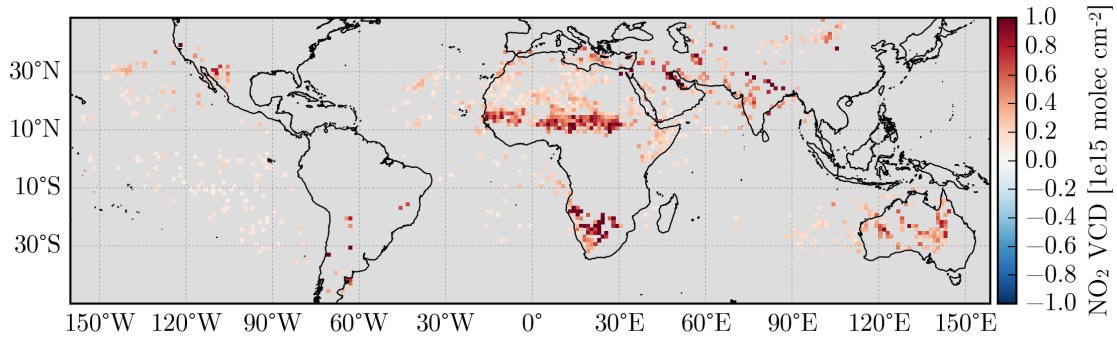

E2 PERSIANN

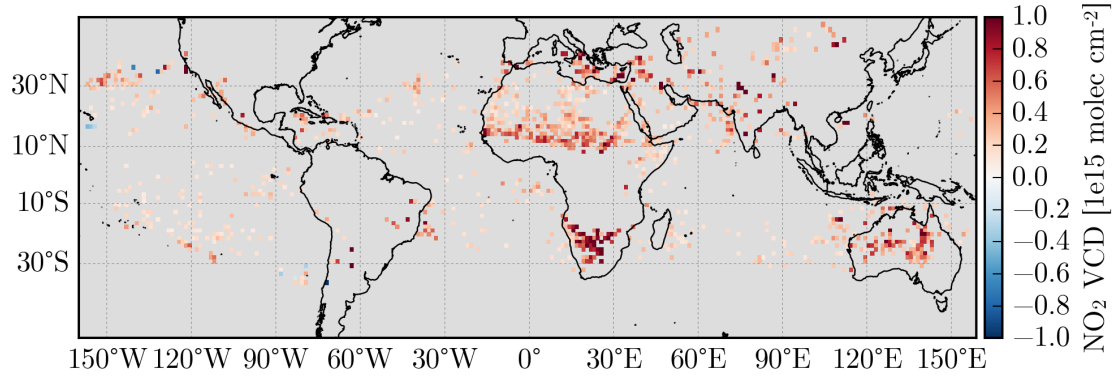

E3 Derived Fluxes

	TRMM	CMORPH	PERSIANN
∅ Day0 enhanc. [ngNm^{-2}s^{-1}]	**6.95**	7.75	6.62
max. Day0 enhanc. [ngNm^{-2}s^{-1}]	**64.61**	64.61	64.61
Day1-14 enhanc. [ngNm^{-2}s^{-1}]	**3.39**	3.07	2.42
Background (soil) [ngNm^{-2}s^{-1}]	**2.75**	3.39	4.36
Background (total) [ngNm^{-2}s^{-1}]	**14.54**	15.18	16.15

Figure 3.30: Figures **E1** and **E2** depict the NO_2 enhancement on Day0 as in Fig. 3.3d, but based on CMORPH and PERSIANN data, respectively. While the absolute values differ for the Sahel, the final emission estimates for pulsed emissions are quite similar (see Table **E3**), as the choice of the precipitation data affects the background correction as well.

3.5 Discussion

3.5.1 Estimated nitrogen emission fluxes from the emission pulse

Soil emissions of trace gases are not only limited to the specific days investigated in this study (based on the selection criteria for the temporal evolution of precipitation), but can play an important role in the atmosphere during specific seasons and throughout the whole year (Steinkamp et al., 2009). Global chemistry models considered the mean seasonal behaviour of soil emissions in the past, but they were insensitive to rapid changes on a daily basis, e.g. during the onset of the wet season. Pulsed emissions of sNO_x have been recognized to be a significant short-term local enhancement, which can be parametrized in GCMs as shown by Hudman et al. (2012) for the GEOS-CHEM model. The latter study investigates pulsed soil emissions of NO_x in the Sahel region and finds a comparable magnitude (49% relative increase of OMI NO_2 VCDs on Day0) and length of the pulsing event (1–2 days) with respect to the findings in this chapter. Here, further evidence is found supporting that and other reported studies, i.e. the observed enhancements in NO_2 VCDs are consistent for multiple instruments and are not introduced by retrieval errors or interfering sources.

For the Sahel region significant mean enhancements of about 4×10^{14} molecules cm^{-2} (observed by OMI) are found on the first day of rainfall in April-May-June after the prolonged dry spell. However, much stronger enhancements for single pixels can identified on the original fine resolution grid (0.25°) of up to $\sim 4 \times 10^{15}$ molecules cm^{-2}. Considering these values as upper and lower limits for the sNO_x enhancement on Day0, emission fluxes can be estimated. The top-down emission flux for NO_x can be inferred from the NO_2 VCD by mass balance:

$$E = \frac{\Omega_{NO_2}}{\tau_{NO_2}} \tag{3.2}$$

with Ω_{NO_2}, being the tropospheric NO_2 VCD and τ_{NO_2} the lifetime. The lifetime for τ_{NO_2} is mostly determined by the oxidation of NO_x to HNO_3 in the boundary layer and typically ranges between 4 and 10 hours in the tropics (Martin, 2003). Consequently, the emission flux of nitrogen (N) for pulsing events, considering an assumed NO_2 life time of 4 hours, in the Sahel is between 6 ng N m^{-2} s^{-1} for a conservative estimate and 65 ng N m^{-2} s^{-1} on the upper limit on Day0. This is in line with findings from Jaeglé et al. (2004) who gave an estimate of 20 ng N m^{-2} s^{-1} for rain-induced sNO_x pulses in June in the Sahel. Furthermore, field studies suggest emission fluxes of nitrogen of about 2–60 ng N m^{-2} s^{-1} (Johansson and Sanhueza, 1988; Davidson, 1992a; Levine et al., 1996; Scholes et al., 1997) which covers the estimated upper and lower limits.

After the first direct emission pulse, emissions remain at an enhanced level for a period of about 2 weeks as described in the previous chapter with approximately 3.3 ng N m^{-2} s^{-1} averaged over the Sahel. Analogous to the pulsed emission on Day0, this value probably represents a lower limit because of the rather low spatial resolution of the extracted time series. These emissions are almost independent from the period of dry days after Day0 which indicates that they are probably caused by the initial rain on Day0 and not by

subsequent precipitation the following days. Possible advection effects into or out of the considered pixels may thereby raise or lower the retrieved sNO_x fluxes. The analysis based on different dry phases after Day0 also changes the probability for first rain events in pixels in close proximity. Since no strong differences in the emissions for different dry phases after Day0 are found, it can be concluded that the inflow of NO_x from adjacent pixels is not the dominant source for the enhancement after Day0. In contrast, a systematic underestimation of the emissions is likely due to advection out of the central pixel. In sum, the integrated emissions after Day0 are potentially of the same order of magnitude as those from the first emission pulse on Day0.

It is found that peak emissions of sNO_x pulses occur on the scale of 1–3 days which is in accordance with present literature (Kim et al., 2012). Some studies, however, measure peak emissions several days after the first rewetting of the soil, e.g. 7 days as observed in field by Oikawa et al. (2015). The chosen algorithm does not specifically distinguish between such cases by taking average time series after the first precipitation event. Single pixels may exhibit peak emissions several days after the initial precipitation which would, however, not be resolved by the current analysis.

This chapter focuses on the quantification of pulsed soil emissions and determines the NO_2 enhancement on Day0 and the following days with respect to a determined background. However, the seasonal pattern of the determined background, i.e. the NO_2 enhancement at the onset of raining season (compare Jaeglé et al., 2004), clearly indicates that it is mainly driven by microbial emissions from soils as well: from pulsed emissions discarded by the strict selection criteria or continuous emissions during wet season. Note that the seasonal pattern of NO_2 over the Sahel, as shown in Fig. 3.17, can neither be explained by biomass burning nor lightning. Fig. 3.24c of the manuscript shows that the background NO_2 VCDs are about 0.9×10^{15} molecules cm^{-2}. This is about 0.17×10^{15} molecules cm^{-2} higher than background in winter. Thus, in addition to the pulsed emissions quantified above, a mean background of 0.17×10^{15} molecules cm^{-2} can be attributed to soil emissions as well. These estimates are based on TMPA precipitation data. For other precipitation products (CMORPH or PERSIANN), results change only slightly (see Fig. 3.30).

In summary, soil emissions in the Sahel can be distinguished based on the time period: (a) 1–3 days (initial peak), (b) 14 days, and (c) several months (background during the wet season). The separate quantification of soil emissions belonging to these three categories might also be adopted in model parametrizations of soil emissions. However, further research needs to be conducted on how these emission categories vary for different regions worldwide.

3.5.2 Seasonal soil nitrogen emissions in the Sahel

In this section total soil emissions, both due to pulsed emissions and background, are quantified for the Sahel region. For the pulsed emissions on Day0 (category a) and the following 2 weeks (b), the fluxes estimated above are multiplied by the area of the

investigated region (0–30° E, 12–18° N). The statistics of the analysis in the Sahel suggest that on average one large pulsing event (after 60 days of drought) occurs within a single pixel in the April-May-June period. Scaling up the Day0 emissions results in 1.2 Gg N and 12 Gg N, considering the lower and upper fluxes estimated above. Analogously, the emissions over the following 2 week period add up to 8.8 Gg N. Together this sums up to 10.1–20.8 Gg N emissions due to pulsing. As mentioned above, the observed increase of the background in the AMJ period of 0.17×10^{15} molecules cm^{-2} is mainly driven by microbial emissions from soils as well. When integrated over the complete April-May-June period, these seasonal soil emissions correspond to 46.4 Gg N (again based on a NO_x lifetime of 4 hours). Consequently, the emissions due to pulsing contribute about 21-44% additionally to seasonal soil emissions for the Sahel and dominate the local NO_x concentrations on the particular days.

Jaeglé et al. (2004) determined top-down total soil emissions from GOME-2 measurements of about 400 Gg N for North Equatorial Africa (0–18° N) in June alone. The estimated total soil emissions of nitrogen in this study (56.5–67.2 Gg N for AMJ) are smaller, but are determined for a smaller region as well which makes a direct comparison difficult.

3.5.3 Enhancements in NO_2 VCDs on Day-1

For all analysed study regions and individual grid pixels showing significant NO_2 spikes on Day0, enhancements in the NO_2 VCDs 1 to 2 days before the first day of rainfall are found. The phenomenon is especially pronounced for the study region in south-western Africa. The finding of enhanced NO_2 VCDs before Day0 stands in contrast to the general expectation that soil emissions, e.g. of NO_x, are only caused by the initial rain event and the subsequent wetting of the soil. However, absolute humidity shows a steady increase several days before the first rain event. Thus, reasons for the early increase of NO_2 VCD may be an increase in atmospheric moisture content and dewfall, a misclassification of rainfall intensity by the precipitation algorithms, transport of NO_2 from neighbouring regions or spatial aliasing effects during the gridding of the satellite observations, i.e. the overlap of the ground footprint onto multiple grid boxes of the precipitation products. The latter two can occur if the ground pixel observed by the satellite overlaps with two or more grid pixels of the precipitation products or vice versa. This error is difficult to estimate, but should be more pronounced for larger satellite ground pixels, i.e. from SCIAMACHY, and less for instruments with smaller footprints, i.e. OMI. The fact that all instruments observe similar enhancements already on Day-1 indicates that this possible error source is not the dominant cause for the early increase in NO_2 VCDs. The use of three instruments for detecting NO_2, each having different overpass times during the day, also makes it less likely that a temporal mismatch of the precipitation and trace gas products, as described in the "Methodology" section, leads to the enhancements on Day-1.

In Fig. 3.13b it is shown that water vapour (H_2O) VCDs in the atmosphere retrieved by GOME-2 increases continuously for 10 days before the first precipitation event and peaks on Day-1. It can be speculated that the moist air over the extremely dry top soil

layer induces initial sNO_x emissions (although the soil is not directly wetted by rain). Also an enhanced dew formation and water adsorption potential, which are both important sources of water in semi-arid areas, have a major effect on microbiological activity (Verheye, 2008). The probability for nightly condensation over drying soils increases with higher absolute humidity. Although observations of these quantities are sparse, measurements in Israel, Jordan and in South Africa hint at contributions of 12 to 40 mm water per year in semi-arid regions (Verheye, 2008; Nicholson, 2011, and references therein). Transport of polluted air from the tropics northward presumably also leads to enhanced NO_2 VCDs before Day0. However, this effect is expected to be quite low as the enhancements before Day0 are also seen for cases dominated by northerly winds coming from the Sahara which are generally associated with lower NO_2 VCDs (see Fig. 3.21).

3.6 Conclusions

This chapter presented a top-down approach to infer rain-induced emission pulses of NO_x based on space-based measurements of NO_2. This is achieved by synchronizing time series at single grid pixels according to the first day of rain after a dry spell of prescribed duration. The method is applied globally and provides constraints on pulsed soil emissions of NO_x in regions where the NO_x budget is seasonally dominated by soil emissions. This approach is similar to Hudman et al. (2012), but extended by (a) performing the analysis globally with (b) high spatial resolution, and (c) keeping full track of the temporal evolution several weeks before and after a rain pulse with daily resolution. The latter was used to (d) perform a sophisticated background correction, which turned out to be necessary in order to account for the seasonal variations in the time series and allows to (e) quantify rain-induced soil emissions also beyond the strong peak on the first day of rain.

Sensitivity studies were conducted in order to (i) evaluate the impact of the a priori assumptions on thresholds for daily rainfall, i.e. the amount of precipitation and the required duration, (ii) investigate to what extent other NO_x sources like biomass burning or lightning NO_x might interfere, and (iii) carefully check for possible retrieval artefacts (e.g. caused by clouds). None of these effects has shown to be critical for the conclusions.

Note, however, that the method was optimized for the quantification of pulsed soil emissions from space by demanding long droughts and good viewing conditions (low cloud fractions) on the day of precipitation onset. Thus, regions showing no clear response for these strict selections might still be capable of rain-induced soil emissions.

Strong peaks of enhanced NO_2 VCDs on the first day of rainfall after prolonged droughts are found in many semi-arid regions, in particular in the Sahel, south-western Africa, Australia and parts of India. A similar analysis for HCHO VCDs showed no indication for pulsed soil emissions. Closer inspection of the Sahel shows a strong dependence of precipitation-induced NO_x emissions on land type cover. This finding confirms similar results from laboratory measurements.

In addition, enhancements in NO_2 VCDs are registered one to two days before the

first rainfall of the wet season. These enhancements most likely originate from initial soil emissions induced by the increased humidity and dew-fall (raising the soil water content at the surface) shortly before the first rain.

For the Sahel region, absolute enhancements of the NO_2 VCDs on the first day of rain based on OMI measurements 2007–2010 are on average 4×10^{14} molecules cm^{-2} and exceed 1×10^{15} molecules cm^{-2} for individual grid cells. Results for SCIAMACHY and GOME-2 are comparable, and the slight differences can be primarily explained by different footprints, overpass times, cloud products, and retrieval schemes. Assuming a NO_x lifetime of 4 hours, this corresponds to soil NO_x emissions in the range of 6 ng N m^{-2} s^{-1} up to 65 ng N m^{-2} s^{-1} on Day0, in good agreement with literature values. Apart from the clear first-day peak, NO_2 VCDs are moderately enhanced (2×10^{14} molecules cm^{-2}) compared to background over the following 2 weeks suggesting potential further emissions during that period of about 3.3 ng N m^{-2} s^{-1}. With respect to the seasonal NO_x budget, a contribution between 21 to 44 % from these rain-induced intense pulsing events to total soil NO_x emissions can be assessed in the Sahel.

In conclusion, the findings facilitate a detailed characterization and estimation of emission budgets for intense sNO_x pulses, triggered by individual rain events, which can improve parametrizations in modelling studies by dividing soil emissions into several parts: (i) pulsed emissions on short timescales, (ii) enhanced emissions after the initial pulse, and (iii) seasonal background emissions.

CHAPTER 4

Case study of pulsed soil emissions around Lake Chad

Lake Chad plays a prominent role within the Sahel since it is one of the most important fresh water resources in Northern Africa. The surface area of the lake drastically decreased over the past century by about 90 % (GIZ, 2015) because of extreme droughts due to climate variability and unsustainable water utilisation by neighbouring countries. Still, the green patch of vegetation encircling Lake Chad is clearly visible on satellite imagery of Northern Africa (see Fig. 3.5 and Fig. 4.1). The region of Lake Chad also shows intriguing enhancements in mean NO_2 VCDs in June and July compared to its surroundings as observed by the OMI satellite instrument (see Fig. 3.10).

It was shown in the previous chapters that soil emissions of NO_x govern the local NO_x budget in the Sahel from April to June. It is, thus, hypothesized that the observed enhancement in NO_2 VCDs over Lake Chad is also related to enhanced microbial emissions of NO_x from soils at the beginning of the wet season. Consequently, the area around Lake Chad should exhibit strong sNO_x emission pulses at the start of the wet season.

The following sections investigate this hypothesis by considering a case study on the first intense precipitation event in the Lake Chad area in 2007.

4.1 The study region

Lake Chad is situated in the Sahel region at about 12.5 to 14.4 °N and 13 to 15.3 °E and is bordered by 4 countries, i.e. Niger, Nigeria, Chad and Cameroon. The entire drainage basin constitutes about 8 % surface area of the African continent (FAO, 2009) and is shared by a multitude of countries: Algeria, Cameroon, Central African Republic, Chad, Libya, Niger, Nigeria and Sudan. However, the actual lake area nowadays occupies only less than 1% of the area of the drainage basin. With mean depths between 0.5 m to 2 m and a maximum depth of about 11 m, the lake is relatively shallow (Coe and Foley, 2001; Lemoalle et al., 2012).

Lake Chad has experienced drastic changes in its size from 25 000 km^2 before 1963 to about 1.350 km^2 in 2007 (Coe and Foley, 2001). Major causes are attributed to climate variability and unsustainable water utilisation of the adjoining countries which have been pursuing massive irrigation projects draining the Lake Chad and its inlets (Coe and Foley, 2001; GIZ, 2015).

The water level of Lake Chad decisively depends on precipitation in the rainy season.

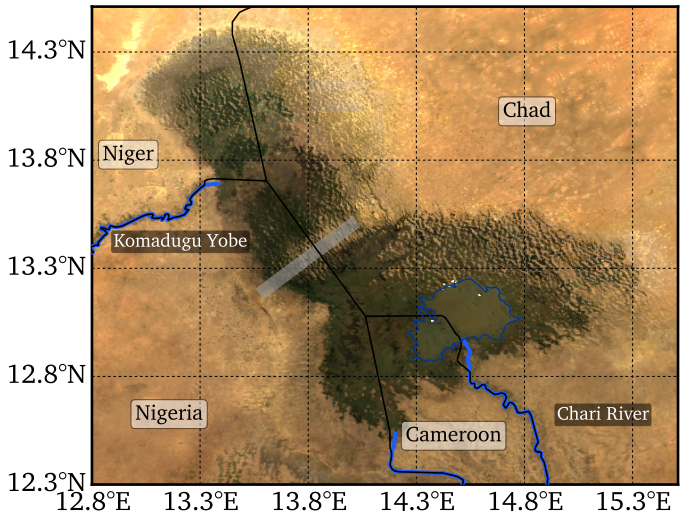

Figure 4.1: MODIS Aqua RGB image (Bands 1,4,3 from MYD09GA product) of Lake Chad on February 1st 2016. Country borders as well as main rivers feeding Lake Chad are highlighted. Lake Chad is divided into a northern and southern pool by the 'Great Barrier' which is highlighted with a grey bar. The approximate area of Lake Chad which is constantly filled with water throughout the year is encircled in blue.

This source of fresh water, however, has declined significantly since the early 1960s as can be seen in the historic Sahel precipitation index in Fig. 4.2. The latter describes anomalies in Sahelian precipitation compared to the long-term mean (1900–2013). Although Fig. 4.2 represents data for the western Part of the Sahel, the precipitation anomaly also agrees very well with data presented by Lemoalle et al. (2012) for the basin of the Chari river, which is the main inflow river for Lake Chad.

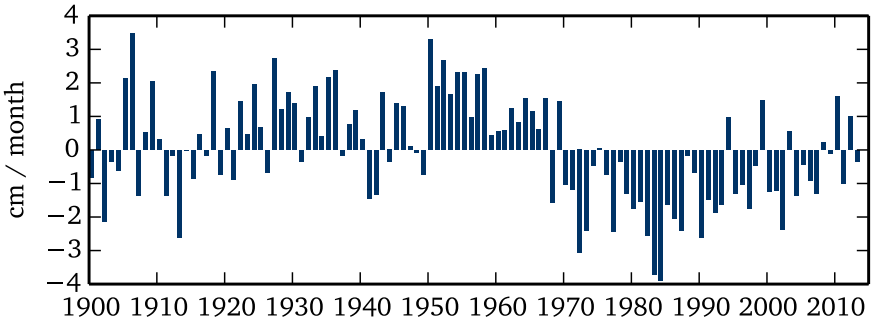

Figure 4.2: Adapted from the historic Sahel precipitation index (doi:10.6069/H5MW2F2Q). The anomalies are with respect to 1900–2013 and calculated from 20 °W to 10 °E and from 10 °N to 20 °N. Sahel precipitation was above the long-term mean from 1915 through the late 1930s and during the 1950s-1960s, after which it was persistently below the long-term mean, with the largest negative anomalies in the early 1980s.

Lake Chad is divided into the north and south basin separated by shoals called the "Great Barrier" (Lemoalle et al., 2012). The southern basin, which inhibits most open

waters of the lake, is mainly fed by water from the Chari river and to a lesser extent also by the El Beïd river (Lemoalle et al., 2012). In general, the northern basin is much drier and only receives little water supply from the Komadugu Yobe River and some seasonal precipitation, which is much lower compared to the southern part (Lemoalle et al., 2012).

The reduction in the lake area of about 90 %, consequently, goes along with extensive land cover changes over the last 50 years. Babamaaji and Lee (2014) investigate the transformation of the surrounding area of Lake Chad using classification of Landsat imagery and find that a considerable part of the previously inaccessible water area has been converted to farmland and cropland (see Fig. 4.3). Furthermore, shrub land showed a strong increase in the land area over the years 1975–1991.

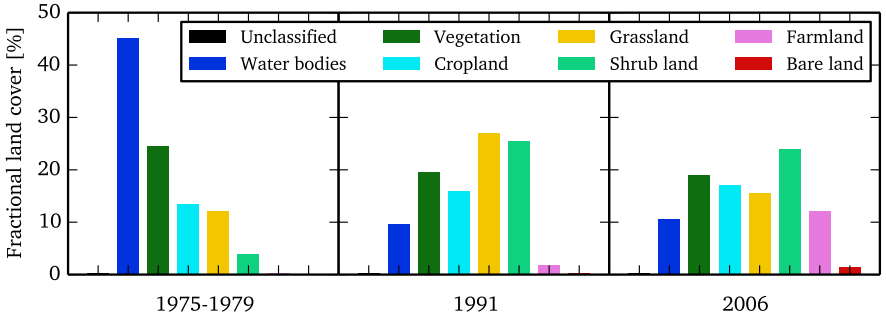

Figure 4.3: Area coverage in percent for each class of the land clover classification by Babamaaji and Lee (2014) for the Lake Chad region. 1975–1979: Mosaic Landsat-MSS land use/land cover map, 1991: Landsat-TM land use/land cover map, 2006: NigeriaSat-1 land use/land cover map.

Lake Chad and its ecosystems are indispensable to life in the entire region in providing fresh water, fishing grounds and arable lands to several million people in the basin region (GIZ, 2015). The majority of the population is engaged in agriculture, livestock farming and fishing. The encroachment of the desert and the drastic decline in area utilisable for labour, food and water supply, subsequently, threatens the social and economic well-being and creates tensions among communities in the surroundings of Lake Chad (FAO, 2009; GIZ, 2015).

4.2 Methodology

The goal of this chapter is to identify a particular day characterized by heavy precipitation in the vicinity of the Lake Chad on which the emission of rain-induced sNO_x can be investigated.

In a first step, a similar approach is undertaken as presented in section 3.3: time series of precipitation from TRMM/TMPA on the 0.25° latitude/longitude grid are used to find pixels experiencing the first strong rainfall of the wet season. Thereby, the same temporal adjustment as presented in Fig. 3.2 is chosen, i.e. the 3-hourly precipitation data is integrated over the 24 h period prior to the satellite overpasses of OMI to collocate rainfall events and trace gas observations. This means that the precipitation data are

integrated from 13:30UTC of the previous day to 13:30 UTC of the current day as this approximately corresponds to the OMI overpass. The OMI NO_2 data are screened for observations with an effective cloud fraction above 20 %. Additionally, the two outermost pixels of the swath are discarded.

The second step then differs from the methodology in section 3.3 by specifically (manually) selecting a day that shows a strong enhancement in NO_2 VCDs following an intense precipitation event. Furthermore, no data is averaged around *Day0*, i.e. the first day of rain fall.

Many enhancements in NO_2 VCDs for single pixels around Lake Chad have been detected matching the above criteria. The location of these enhancements (on coarser grids) as well as their average enhancement on *Day0* have been presented in Fig. 3.3.c,d.

Over the course of the analysis, one particular day (June 16th 2007) clearly stands out in the time series of precipitation as well as in NO_2 VCDs over Lake Chad in the year 2007 and, thus, will be discussed in detail in the following sections.

4.3 Time series of precipitation and NO_2 VCDs

In the previous chapters, average time series of precipitation and NO_2 VCDs over the years 2007–2011 have been presented for the Sahel region which show a systematic relationship at the onset of the wet season. In this section, similar time series are investigated but with a focus on Lake Chad by only considering pixels which lie within a 2 pixel radius, i.e. 0.5°, around the vegetated parts of the Lake Chad area (Fig. 4.4). In general, the same seasonal cycles and overall patterns in the time series can be observed as for the greater Sahel region. The time series of NO_2 shows no considerable variations from January to April and September to December of the year 2007. With the arrival of the first rain events in May and June, however, NO_2 levels start to increase and peak in the middle of June. Until late August average NO_2 VCDs decrease again to background levels. It should be noted, that the time series of NO_2 is largely influenced by the day-to-day variability in the number of pixels which are averaged over this relatively small region. As the NO_2 VCDs are screened for potentially erroneous observations, the observations may not fully cover the region every day: on some days only few pixels are averaged leading to high fluctuations in the time series.

On June 15th 2007, a large convective precipitation system passed over Lake Chad which led to the first intense rain fall of the year with more than 17 mm precipitation on average (Fig. 4.4, 4.5 and 4.6). Maps of the overpass of this particular precipitation system as observed by the TRMM/TMPA product are shown in Fig 4.5 in 3-hourly steps. The precipitation system started to develop in the afternoon of the 15th of July at about 15:00LT in the north-west of Lake Chad and moved in south-western direction over the following hours. At about 21:00LT heavy rains were detected over the Lake Chad area. Over the following hours, the precipitation system moved further south-west out of the study region.

Mean wind vectors from ECMWF ERA-INTERIM for 900 hPa as well as for 650 hPa

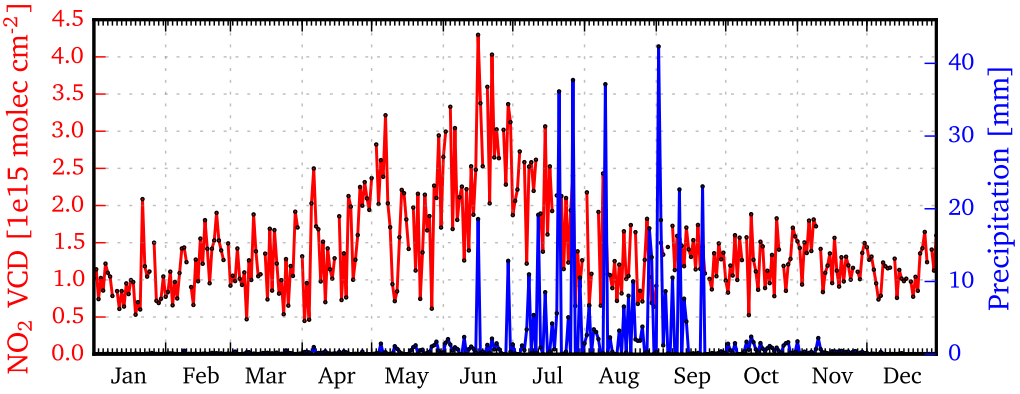

Figure 4.4: Daily time series for the year 2007 of precipitation (TRMM/TMPA) and OMI NO_2 VCDs averaged over Lake Chad.

levels are provided in Fig. 4.7 (averaged over 18 hours prior to the OMI overpass at 13:30LT on June 16th). On average, strong winds from the north-east are found consistently over the study region at 650 hPa. Wind vectors closer to the surface at 900 hPa indicate opposing winds in northerly direction over Lake Chad.

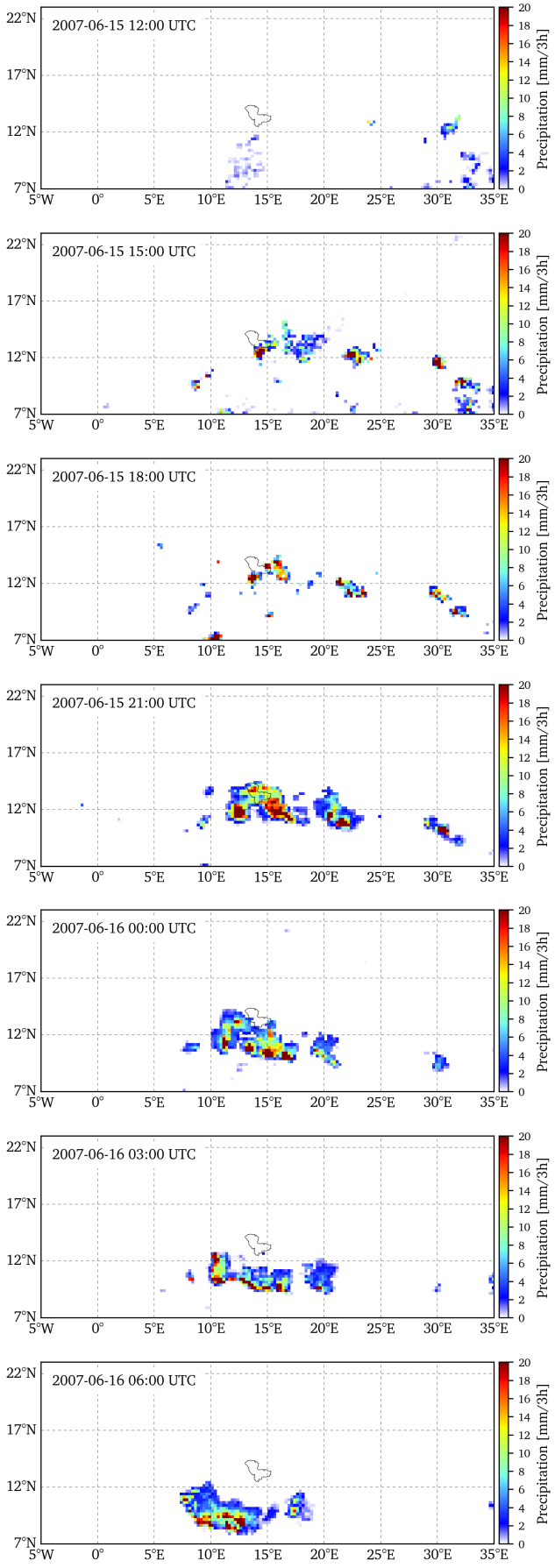

Figure 4.5: The evolution of the precipitation system on June 15th and 16th 2007 around Lake Chad.

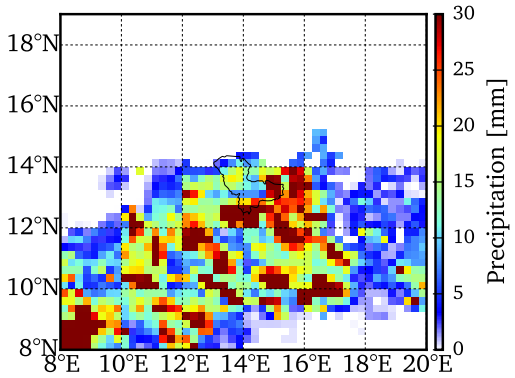

Figure 4.6: Precipitation summed over the period from June 15th 13:30LT 2007 until June 16th 13:30LT 2007

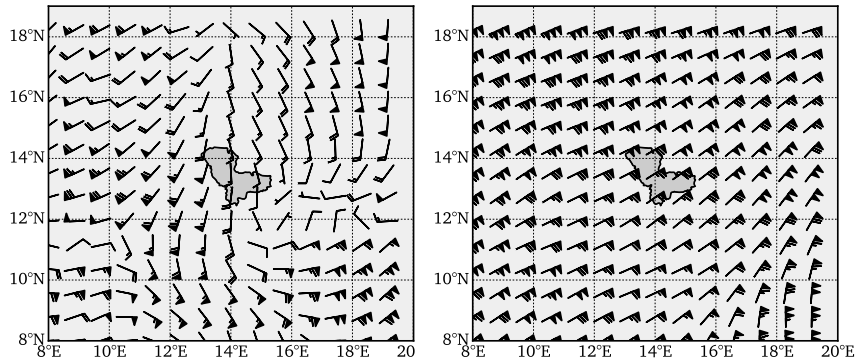

Figure 4.7: ECMWF mean wind speeds for the time period from June 15th 18:00LT to June 16th 12:00LT at 900 hPa (left) and 650 hPa (right).

4.4 Enhancement in OMI NO_2 VCDs

The intense precipitation event described in the above section coincides with the highest NO_2 VCDs from OMI in the time series in Fig. 4.4. Due to the quality screening of the OMI data (e.g. for erroneous measurements and cloud fractions > 20 %), OMI's row anomaly and the removal of the outermost two pixels of the swath, only a small number of pixels are averaged over the Lake Chad area on some days. On June 16th (and the days around), however, the coverage of the OMI instrument is sufficient for this study (Fig. 4.8).

Fig. 4.8 presents NO_2 VCDs from OMI in the vicinity of Lake for several days in June 2007. Fig. 4.8.a depicts mean NO_2 VCDs for the first fourteen days in June. The NO_2 VCDs range between 1×10^{15} molecules cm^{-2} in the southern and northern parts and about 2.5×10^{15} molecules cm^{-2} in the central region (at about ~12°N) and above Lake Chad. These are typical levels for semi-arid areas in this time period, but they are already slightly higher compared to the dry season in winter (see Fig. 4.4 and 3.10).

On June 16th at 13:30LT, about 14 hours after the intense precipitation over Lake Chad, OMI observes strongly enhanced NO_2 VCDs with maxima of about 6.5×10^{15} molecules cm^{-2} over the lake area. Averaged over the area around Lake Chad the mean NO_2 VCDs are about 2.5×10^{15} molecules cm^{-2} higher compared to the preceding 14-day period. In the southern and western parts of the study region, many pixels were discarded due to heavy cloud cover. The maps for June 15th and 17th (Fig. 4.8.c,d) also indicate an enhancement in VCDs over Lake Chad, albeit not as strong as on June 16th.

4.4.1 Potential sources of the NO_2 enhancement

The observed high NO_2 VCDs on June 16th over Lake Chad clearly stand out compared to the surrounding area and the 14-day period before. In the following, potential sources of these enhanced column densities are investigated.

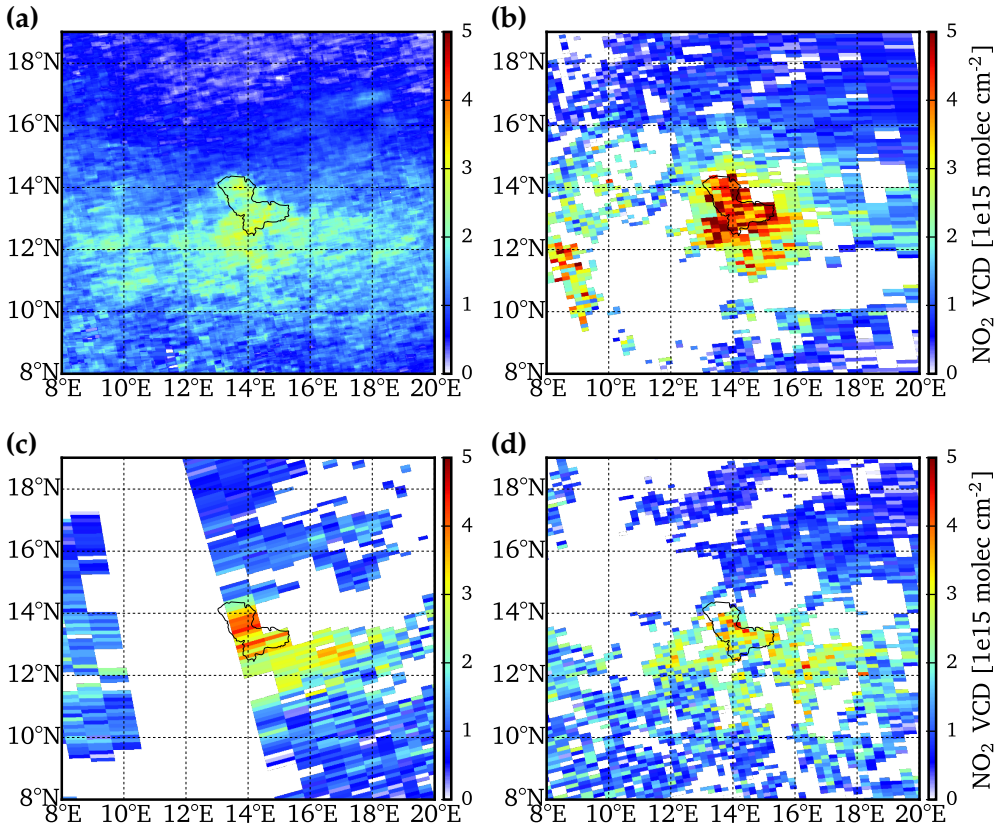

Figure 4.8: NO_2 VCDs as viewed by the OMI satellite instrument. Shown here are averages for the period from June 1st to 14[14] 2007 **(a)** and daily observations for June 16th **(b)** June 15th **(c)** and June 17th **(d)**. On June 15th the Lake Chad region is captured by the largest OMI pixels at the far end of the swath.

4.4.2 Cloud fraction and AMF

The largest error source of satellite retrievals of traces gases are inaccurate assumptions on the state of the atmosphere and the surface, e.g. on clouds and aerosols and the surface albedo, which directly affects the calculation of the AMF. In order to clarify whether the observed enhancements in the VCDs are due to incorrect AMFs, the cloud fraction and SCDs of each day are inspected.

Fig. 4.9 depicts cloud fractions from OMI averaged over a 14-day period (1^{st}–14^{th}) and for June 16^{th}. The average of the 14-day period shows generally slightly higher cloud fractions in the southern part and some distinct spatial structures which probably relate to artefacts in the albedo map affecting the cloud retrieval or persistent aerosol loads. For example, the rectangular artefacts at the border of the Lake Chad area emerge due to the coarse resolution of the albedo map (see Appendix A.5). Another striking feature is the enhancement at 17°N and 18°E which is probably linked to high aerosol load originating from frequent sand and dust storms from the Bodélé Depression (Washington and Todd, 2005; Koren et al., 2006). The spatial patterns in cloud fraction on June 16^{th} show no correlation to the enhanced features in NO_2 VCDs.

Fig. 4.10 depicts SCDs from OMI also averaged over a 14-day period (1^{st}–14^{th}) and the SCDs for the 16^{th} similarly as in Fig. 4.8a,b for the VCDs.

Comparison of Figs. 4.8 and 4.10 shows that the AMF is close to 1, i.e. SCD and VCD are almost equal.

For June 16^{th}, the NO_2 enhancement over Lake Chad is also very clearly seen in the SCDs, which indicates that erroneous AMFs are not the source of high NO_2 VCDs over Lake Chad. Closer inspection reveals that the shape of the enhanced features in the maps for SCDs and VCDs is different. Such an effect is to some extent expected as the AMF accounts for the state of the atmosphere in each pixel which may result in slightly different spatial features in the resulting map of the VCDs.

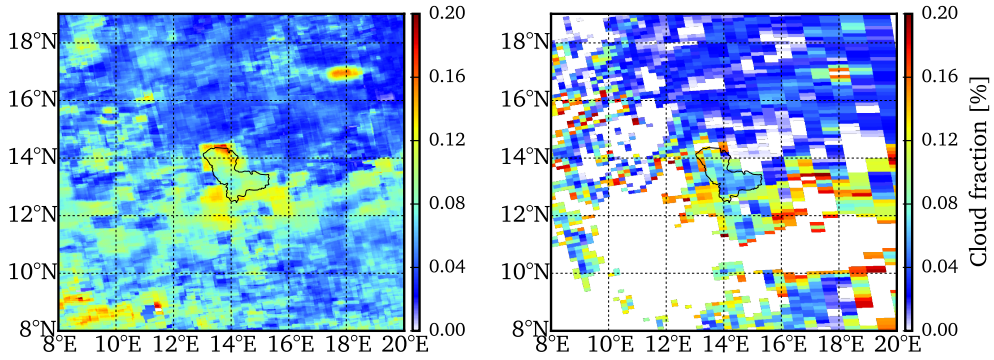

Figure 4.9: OMI cloud fraction averaged from 1^{st} to 14^{th} July 2007 (left) and OMI cloud fraction for June 16^{th} (right)

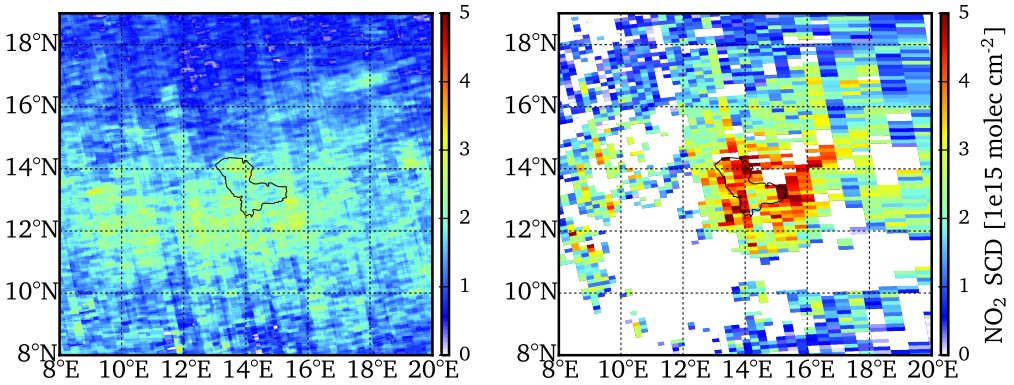

Figure 4.10: OMI NO_2 SCDs averaged from 1st to 14th July 2007 (left) and OMI NO_2 SCDs for June 16th (right)

4.4.3 Lightning emissions of NO_x

NO_x emissions from lightning represent a considerable source of NO_x globally especially in the Tropics and Sub-Tropics (Bond et al., 2002; Schumann and Huntrieser, 2007; Beirle et al., 2010; Miyazaki et al., 2014). As severe thunderstorms may produce large amounts of NO_x resulting from strong lightning activity, and the occurrence of thunderstorms coincides with heavy rains, this emission source has to be considered in this analysis as well. As stated above, a large precipitation system passed over Lake Chad at about 18:00LT on June 15th and moved in south-western direction over the course of the next hours.

There was a lot of lightning activity over Lake Chad on June 15th from about 14–24UTC (Fig. 4.11a-b). In the following hours, the precipitation system (and with it the lightning strikes) moved away from the lake in south-western direction (panels c-d and Fig. 4.7). The enhanced NO_x levels detected at 13:30UTC on the following day cannot be ascribed to lightning, as most of the NO_x produced up to 0:00UTC would have disappeared due to its short life time. Any residual NO_x would have moved south-west with the prevailing winds.

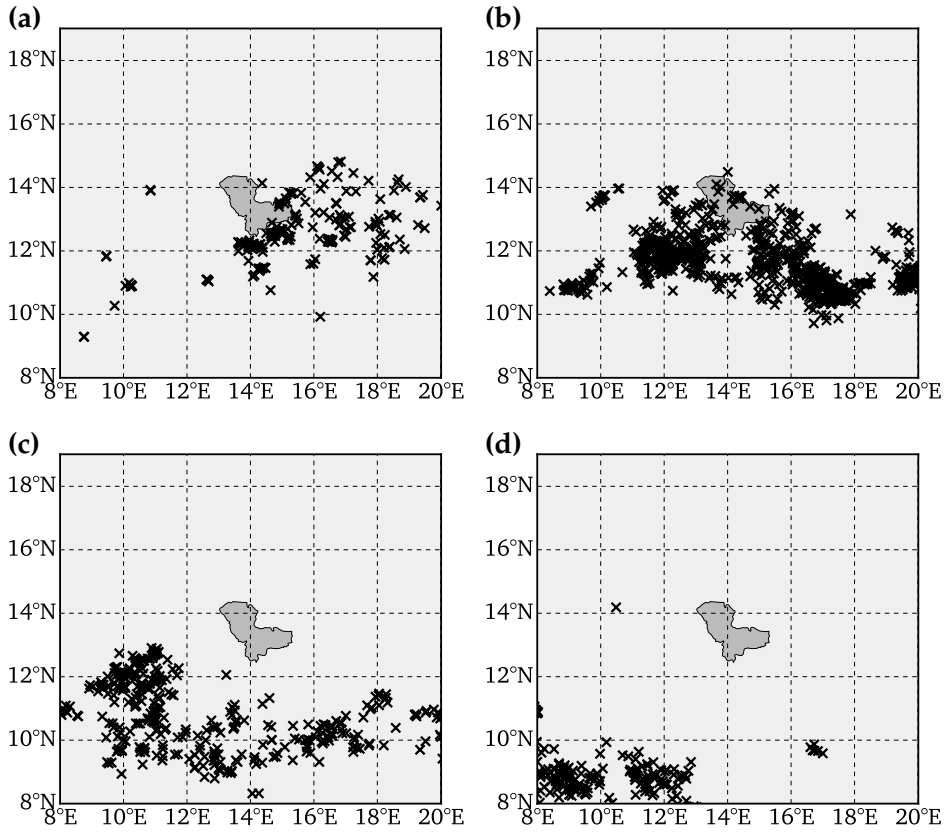

Figure 4.11: Spatial occurrence of lightning strikes as detected by WWLLN. The panels thereby show the location of lightning strikes in different time windows: June 15th 13:30LT to 18:00LT **(a)** June 15th 18:00LT to June 16th 0:00LT **(b)** June 16th 0:00LT to 6:00LT **(c)** June 16th 6:00LT to 13:30LT **(d)**

4.4.4 Fire emissions of NO_x

Emissions of NO_x from biomass burning typically increase in frequency and intensity at the end of the wet season when high vegetation density is present and droughts develop. In the Sahel, this predominantly happens in October and November. However, natural and anthropogenic fires occur over the whole year, especially in vegetated areas like in the surroundings of Lake Chad. To exclude strong emissions from fire as a source for the observed enhancement in NO_2 VCDs, this section investigates the occurrence and intensity of fires on this particular day. Fig. 4.12 illustrates that few fires are detected by the MODIS instruments on Terra and Aqua on June 16th in the vicinity of Lake Chad (compared to higher fire counts in October and November). The MOD/MYDA1 products provide gridded classifications for clouds, water and fire, whereby fires are classified with different uncertainties; the instrument on Aqua detected 15 fires with nominal uncertainty and 15 fires with high uncertainty; MODIS on Terra detected 1 fire with low uncertainty, 5 with nominal uncertainty and 4 with high uncertainty.

Within this study it was not feasible to estimate the NO_x emitted from these fires. Instead, a simplistic approach is undertaken by considering days with high biomass burning activity and investigating the impact on the corresponding satellite maps of NO_2 VCDs. For this comparison, 4 days with very high fire counts in close proximity to Lake Chad are selected (see Fig. 4.13). In general, the spatial location of fires agrees well with pixels showing enhanced NO_2 VCDs. However, it requires several hundreds of fires with high fire radiative power to impact on the NO_2 VCDs. Furthermore, spatially extensive enhancements in NO_2 VCDs are only detected for November 1st and 2nd 2007 where large regions are affected by fires. For smaller fires which are bound to single grid pixels no significant impact on large areas in the surroundings (e.g. of the size of Lake Chad) can be found. This, of course, depends on the prevailing winds and biomass which is burnt during fires, but from this simple comparison it is not expected that the few fires on June 16th may be responsible for such large scale enhancement in NO_2 VCDs around Lake Chad.

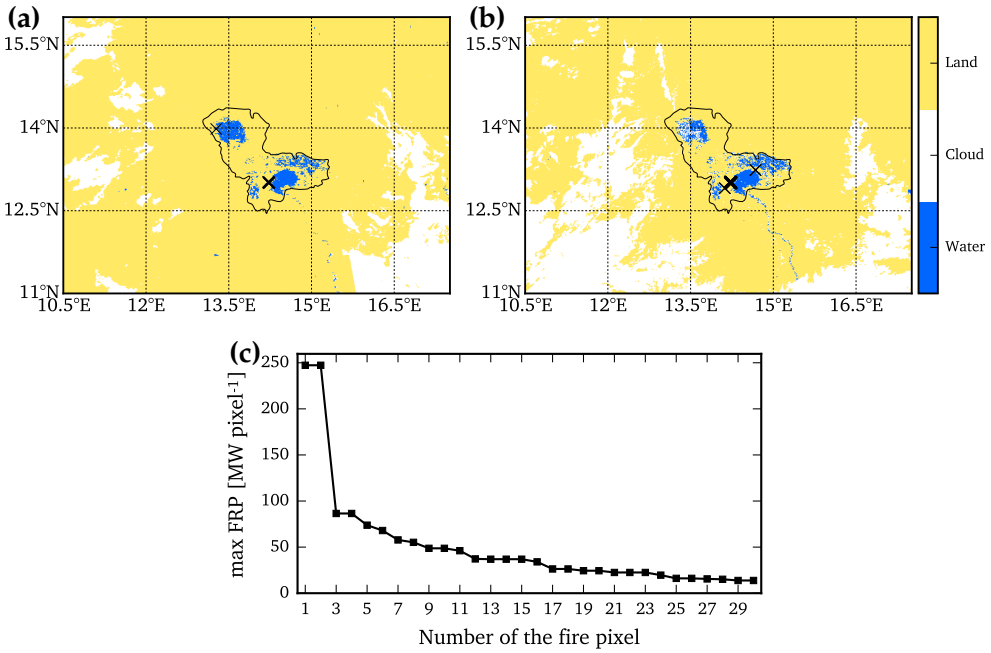

Figure 4.12: Fire locations (black crosses) and image classification from the MODIS instruments on Terra **(a)** and Aqua **(b)** derived from the MOD/MYDA1 products for June 16th on a 1 by 1 km resolution. Note, some fires lie close to each other and therefore appear as bigger crosses. The local overpass of MODIS Terra is at 9:30LT and for MODIS Aqua at 13:30LT. The maximum fire radiative power (max FRP) for each grid pixel is given in **(c)**.

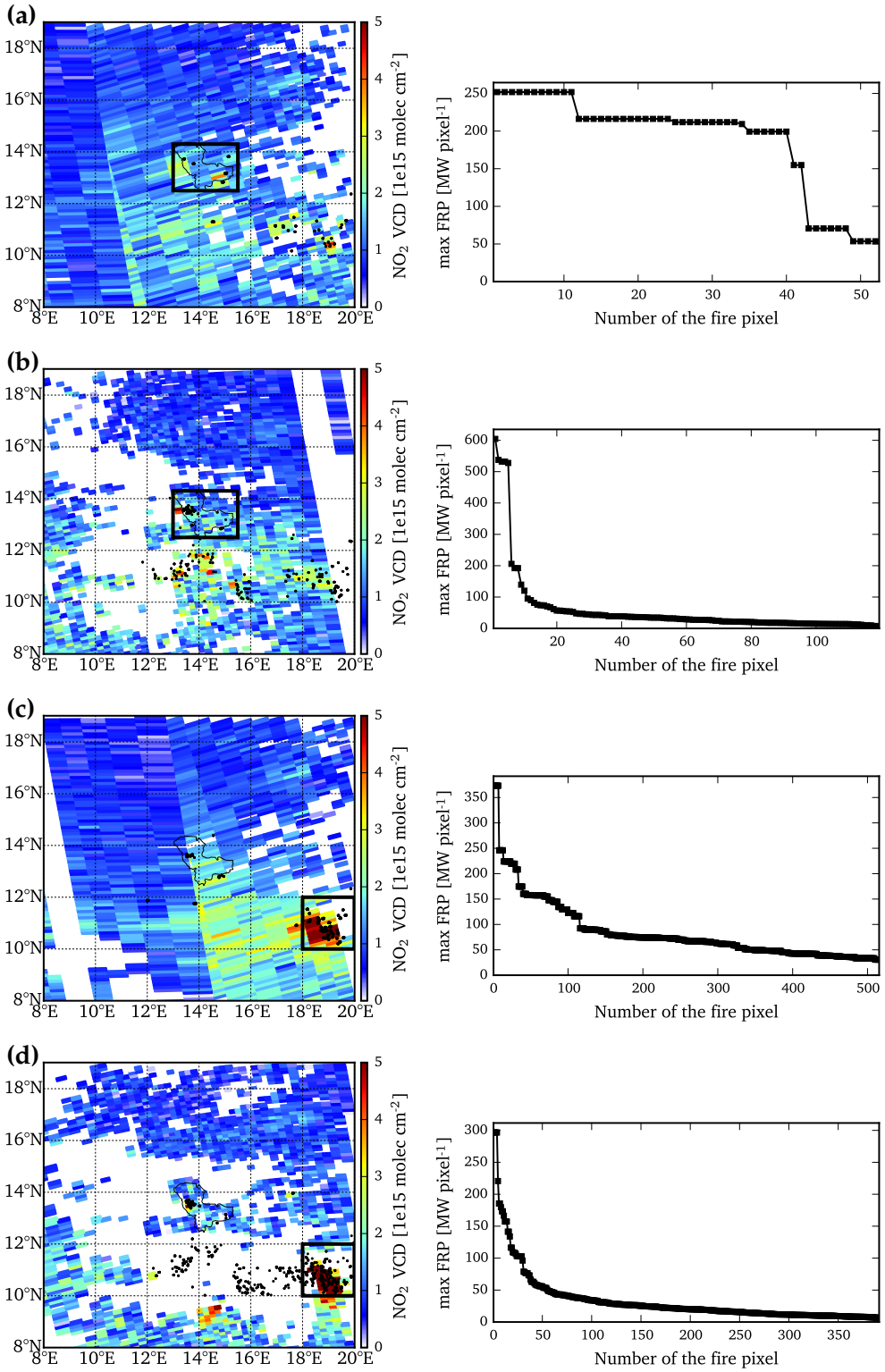

Figure 4.13: The left panels present days with high fire counts overlayed with the corresponding OMI NO_2 VCDs for this day: October 30th **(a)**, October 31st **(b)**, November 1st **(c)** and November 2nd **(d)**. Fire locations are from the MODIS instrument on Aqua (MYDA1 product). The maximum fire radiative power (max FRP) for each fire pixel of the particular day and for the area encircled in black in the map is provided in the right panels.

4.5 Discussion on pulsed soil NO_x emissions

It was shown in Fig. 4.4 that the precipitation event on June 16th 2007 led to more than 17 mm precipitation on average over Lake Chad and also represents the first heavy precipitation of the wet season. The enhanced NO_2 VCDs are observed approximately 14 hours later. Temperature in June is high and, consequently, evaporation as well leading to a quick drying out of soils in the morning and at midday prior to the OMI overpass. This gives rise to the assumption that the soil is not water-logged any more and an optimal soil moisture content could have been reached within this time period facilitating pulsed emissions of NO_x which are then detected by OMI as enhanced NO_2 VCDs.

Interestingly, the spatial extent as well as the pattern of the enhanced NO_2 VCDs resemble the vegetated and very fertile regions around Lake Chad quite well. As presented in Fig. 4.3 the land cover around Lake Chad is a mixture of farmland, cropland, shrubland, grassland and vegetation. It is expected that soil emissions over agricultural land are higher compared to uncultivated land due to the application of fertilizers, i.e. in this case of manure. This spatial correlation between land areas favouring soil emissions and the enhancement in NO_2 VCDs only hours after the first intense precipitation of the wet season further affirms the hypothesis that pulsed soil emissions are their main source.

To estimate the emission flux of nitrogen as well as total emissions over Lake Chad for the whole day on June 16th 2007, the same emission calculation is used as presented in section 3.5.1. Mean enhancement in NO_2 VCDs of about 2.5×10^{15} molecules cm^{-2} are found on June 16th compared to the preceding 14-day period. Assuming a NO_x lifetime of 4 hours, thus, leads to an emission flux of about 32.3 ng N m^{-2} s^{-1} on June 16th which is in medium range for fluxes calculated for the Sahel region in section 3.5.1. Multiplying this emission flux by the area that shows this enhancement in the vicinity of Lake Chad gives an estimated 65 t N for this particular day. Interestingly, enhanced NO_2 VCDs are found over Lake Chad the day before and after the peak emissions also in this case study which hints at additional soil emissions.

4.6 Conclusions

This chapter presented a detailed case study for a particularly strong sNO_x pulsing event over Lake Chad. It was shown that sNO_x pulsing events due to the sudden wetting of the desiccated soils can dominate the local NO_x budget on specific days. Mean emission fluxes of 32.3 ng N m^{-2} s^{-1} have been found for the fertile area surrounding Lake Chad on this particular day, which is in line with findings from Chapter 3 for pulsed emissions on *Day0*.

The biggest challenge in identifying days which show strong soil emissions around Lake Chad is that a very specific constellation of drought, first intense precipitation, low cloud cover and a coinciding OMI overpass need to be fulfilled. These prerequisites drastically limit the detection of more of such intense pulsing events. In the future, the presented approach can certainly be applied to other geographic regions which are more

easily accessible such as Australia or North America where the availability of ground measurements of soil moisture and other environmental parameters is high.

CHAPTER 5

Measurement campaign on soil emissions in an agricultural region

5.1 Research objectives and strategy

The algorithm presented in Chapter 3 is not sensitive to regions at high latitudes, e.g. Western Europe, as humid regions generally do not suffer from severe droughts lasting for several months which is, however, needed to substantially dry out the soil and for pulsed emissions to take place. Furthermore, the effective NO_x fluxes from soils to the atmosphere are potentially offset by "canopy reduction" where nitrogen oxides are quickly deposited on available vegetation surfaces (Ganzeveld et al., 2002). This effect becomes more important in regions with forests, grassland and meadows. Additionally, background concentrations of NO_2 are much higher for more populated regions due to increased traffic and industrial activity. Thus, short-term enhancements in soil emissions (of the same magnitude as in the Sahel) would be hardly detectable from space at the 0.25° resolution which was chosen for the previous analysis.

In order to investigate whether seasonal variations or short-term enhancements in soil emissions of NO_x from agricultural fields in a humid climate can be observed using ground-based DOAS measurements, an exploratory measurement campaign was organized within the framework of this PhD project. The measurement campaign was dedicated to the analysis of trace gases which were potentially emitted from soils in a region dominated by agriculture.

The primary objectives of the campaign were:

1. the characterization of NO_2 and HCHO levels in an agricultural environment on a seasonal, weekly and diurnal basis,
2. the study of the vertical distribution of NO_2 and HCHO through profile retrievals giving insight into their emission sources,
3. the estimation of upper limits of the contribution from soil emissions to ambient trace gas levels and
4. the investigation of the influence of sudden enhancements in soil moisture contents after dry conditions which favours pulsed trace gas emissions from soils

As soil emissions are assumed to be highest from lands predominantly used for agriculture, the Nördlinger Ries in Bavaria, Germany, a rural area which is dominated by

arable land, was chosen as study location. In order to capture a complete growing season, the time period of the measurement campaign was set from April to December 2014. The focus was on trace gases which can be measured using the DOAS approach in the UV/VIS spectral range, i.e. NO_2 and HCHO, using two mini-MAX-DOAS instruments and one Long-Path DOAS instrument. The retrieved NO_2 and HCHO column densities are first converted to vertical column densities (VCDs) and volume mixing ratios (VMRs) and then examined for long-term variations over the entire growing season and short-term events. In addition, the analysis of soil samples taken from fields may give further insights into soil activities.

This long-term measurement campaign was planned to be operated mainly from remote, meaning that all instruments are not supervised in person on a daily basis but maintained via internet connection. Thus, the number of instruments was kept small by focusing on the retrieval of slant column densities of the trace gases in focus (DOAS instruments) and environmental parameters such as air temperature, humidity, wind, soil temperature and moisture content (which are recorded by weather stations).

5.2 The study region

As the aim was to conduct a long-term measurement campaign measuring column densities of NO_2 and HCHO in an agricultural environment, several prerequisites were set on the choice of the study location. Most importantly, the study region needs to be dominated by arable land used for agriculture and no large cities or industry that could significantly impact local air pollution, e.g. on NO_2 levels, must be in close proximity. Secondly, since this campaign was planned to be operated over several months frequent field visits for the set-up of instruments, data collection and maintenance of the equipment are necessary. Thus, the study location should be reachable from the Max Planck Institute for Chemistry in Mainz within a few hours. Furthermore, local advisers and partners are needed who can support the organization of the campaign and host the DOAS-type instruments as well as weather stations in the field.

A suitable location was found in the *Nördlinger Ries* (henceforth Ries) which is a natural region in the Swabian Keuper-Lias Plains at 48.9°N, 10.6°E and is located in the centre of the city triangle of Munich-Stuttgart-Nuremburg in southern Germany (German: München-Stuttgart-Nürnberg). It is characterized by a circular-shaped flat plain with a diameter of about 25 km and is surrounded by forested ridges as high as 150 m enclosing the Ries (Fig. 5.1). This distinct landscape was formed by a meteorite impact about 14.5 million years ago in the Miocene (e.g. Shoemaker and Chao, 1961; Hüttner and Schmidt-Kaler, 2003). Nowadays, the Ries represents one of the most important regions for intensive agriculture in Bavaria. This is due to optimal soil conditions within the plain which mainly consist of loess and loess loam on which deep and fertile calcareous brown soil could develop (Höfling, 1991). In consequence, the land cover is dominated by cultivated fields (> 80 %) which are used to grow a variety of crops, including corn, cereals, sugar beets and potatoes.

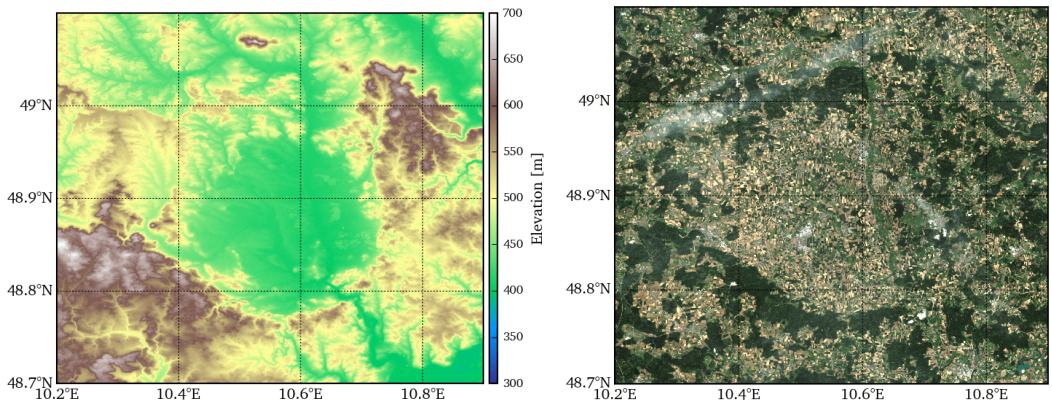

Figure 5.1: Left: Map depicting the elevation in the vicinity of the Nördlinger Ries based on data from NASA SRTM. Right: True colour (RGB) image from Landsat 8 on July 17th 2014 depicting the Nördlinger Ries. Dark green patches on the crater rim indicate forests and the yellow and brown patches within the Ries illustrate the large number of cultivated fields in the region.

Fig. 5.2 depicts an analysis of the agronomic yield potential for soils in Germany, conducted by the Federal Institute for Geosciences and Natural Resources[1] that shows highest yield potential in Bavaria of about 90 % in the vicinity of the Nördlinger Ries. This metric is calculated based on the *soil quality rating* (Müller et al., 2007) and assesses the suitability of soils for agricultural use by evaluating a certain location by means of several basic soil indicators such as the soil substrate or the effective rooting depth, and potential soil hazard indicators, such as the susceptibility to drought.

Owing to the good soil conditions, farming is of major importance in the Nördlinger Ries and a view from space reveals a patchwork of cultivated fields in this region (Fig. 5.1). The eastern part is separated from the western part of the Ries by the Wörnitz river and shows much more grasslands and forests (compared to the western part) due to the lowlands and meadows in proximity of the Wörnitz.

The background NO_2 VCDs in the Nördlinger Ries, as observed by the OMI satellite instrument, are relatively low at about 4×10^{15} molecules cm^{-2} compared to the more populated regions and surrounding cities such as Stuttgart, Munich and Nuremburg (Fig. 5.2). Nuremburg and Munich show slightly higher NO_2 VCDs at about 4.5 to 5×10^{15} molecules cm^{-2}. However, highest NO_2 VCDs are observed in Stuttgart, its surroundings and in the greater Rhine-Main-Area. The lower background level of NO_2 in the Ries facilitates the detection of small-scale variations in seasonal time series of NO_2 VCDs as very high background VCDs would otherwise superimpose weaker signals.

Nördlingen is the largest city within the Ries with a population[2] of about 19 000 (Fig. 5.3). Other cities in the Ries are Öttingen, with a population of about 5000 at the northern edge of the Ries, and Wemding with about 5700 inhabitants at the eastern edge. Just outside of the Nördlinger Ries are Bopfingen with a population of about 11 800 and

[1] Access to the data is provided at:
http://www.bgr.bund.de/DE/Themen/Boden/Ressourcenbewertung-management/Ertragspotential/Ertragspotential_node.html

[2] Population data from *Bayerisches Landesamt für Statistik*: https://www.statistik.bayern.de

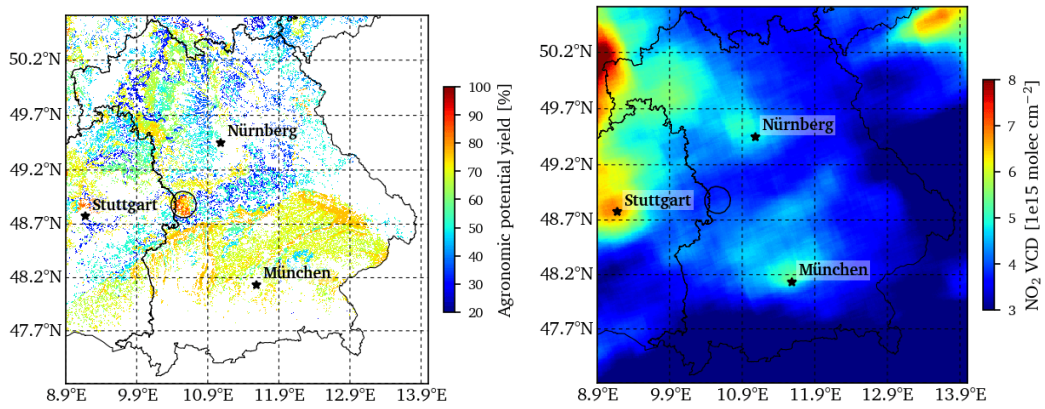

Figure 5.2: Left: Agronomic yield potential of soils in Bavaria calculated and provided by the Federal Institute for Geosciences and Natural Resources. The highest index is found in the Nördlinger Ries with about 90 %. Right: NO_2 VCDs from the OMI satellite instrument averaged over the time period from January 1st 2010 to December 31st 2013. The approximate location of the Nördlinger Ries is highlighted with a black circle. High values of NO_2 VCDs ($> 5 \times 10^{15}$ molecules cm^{-2}) are observed over the cities of Stuttgart, Nuremburg and Munich whereas NO_2 VCDs in the Ries are comparatively low ($< 4 \times 10^{15}$ molecules cm^{-2})

.

Harburg with about 5400. Several smaller villages are distributed across the Ries with less than 1500 inhabitants each. There are three major roads crossing the Ries plain: the B25 from north-west to south-east, the B29 coming from Bopfingen to Nördlingen and the B466 from Nördlingen to Öttingen. Traffic counts conducted by the regional authorities show that about 5100 cars cross the B25 at Fremdingen (north-eastern edge of the Ries) per day and about 13915 cars at the B25 in Harburg[3]. Thereby, heavy-duty vehicles make up a share of about 23 % and 16 %, respectively. The B29 between Bopfingen and Nördlingen is crossed about 9800 times per day[4] with a contribution of $\sim$ 8 % by motor trucks. Based on an average of 5 counting stations in the area, the reduction in traffic on Sundays and holidays amounts to about 25 % for passenger cars and about 90 % for motor trucks.

The climate diagram for Reimlingen in the Nördlinger Ries (at 48.8253°N, 10.5064°E), depicted in Fig. 5.4, gives an insight into average precipitation and temperature on a monthly basis for the period from 2006 to 2013. The average temperature over the year is 9 °C and the total precipitation per year is 750 mm. The warmest month is July with about 18 °C on average, whereas January is the coolest with 0 °C. Conversely, most precipitation falls in July ($\sim$ 120 mm) and the lowest precipitation is registered in February ($\sim$ 35 mm).

Thus, given the distance to major urban areas and the distinct agricultural landscape of the Ries it is suitable for the analysis of trace gas levels potentially emitted from cultivated fields using DOAS measurements. However, as several cities are located within the Ries plain and emissions from road traffic are expected to be of significance, such anthropogenic emissions of NO_2 (and also HCHO) need to be carefully investigated.

[3]Data from Bayerisches Straßeninformationssystem, Oberste Baubehörde im Bayerischen Staatsministerium des Innern, für Bau und Verkehr https://www.baysis.bayern.de

[4]Data from Straßenverkerszentrale Baden-Württemberg available at http://www.svz-bw.de

Figure 5.3: Street map of the Nördlinger Ries from ©OpenStreetMap data showing the main roads (orange lines) and cities in the vicinity. The largest city is Nördlingen in the centre of the Ries with a population of about 20.000. The border separating Baden-Württemberg (to the West) and Bavaria (to the East) is shown as a purple dashed line.

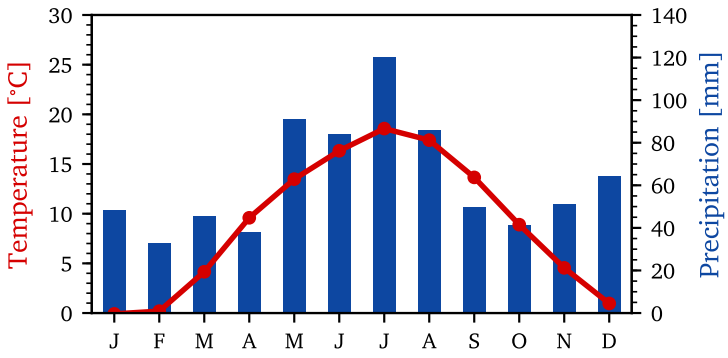

Figure 5.4: Climate diagram for the Nördlinger Ries in 2014 derived from temperature and precipitation data of the DWD weather station in Reimlingen/Ries. The average temperature is 9 °C and total precipitation per year is 750 mm; The altitude of the Reimlingen station is 435 m.

5.3 Instrumental set-up

Throughout the measurement campaign several measurement devices were installed in-field which can be divided into two groups: (i) DOAS-type instruments for the retrieval of trace gas column densities and (ii) weather stations for the measurement of ambient meteorological conditions and soil properties. The first category comprises two mini-MAX-DOAS instruments at two different locations in the Nördlinger Ries and one Long-Path-DOAS instrument taking measurements next to one of the mini-MAX-DOAS instruments. As the main focus of this work is on the retrieval and analysis of NO_2 and HCHO concentrations from the observations of the mini MAX-DOAS instruments, the corresponding data analysis will be covered in detail in the following sections.

In order to evaluate the retrieved trace gas concentrations and to gain more insight into the spatial and vertical distribution of the trace gases they are compared to measurements from a LP-DOAS (with very high sensitivity to near-surface concentrations)

and an air quality monitoring station (providing point measurements at ~ 2.5 m height). The LP-DOAS was operated by Philipp Eger and Dr. Denis Pöhler from the Institute for Environmental Physics (IUP) at the University of Heidelberg and the corresponding trace gas concentrations were also retrieved by the IUP-team. The in situ data from an air quality monitoring station is provided by the Bavarian Environment Agency (german: Landesamt für Umwelt, LfU) for a station in Öttingen. In addition to the own weather stations which were installed amidst crop fields during the campaign, also data from a fixed weather station which is operated by the German Weather Service (german: Deutscher Wetterdienst, DWD) is used in this work.

Table 5.1 summarizes the operational times of each instrument and the institute in charge of the instrument. The locations of the instruments within the Nördlinger Ries are provided in Fig. 5.5. In the following sections, the instrument as well as the measurement station will be described.

Table 5.1: Instruments and their operational time during the measurement campaign 2014. Abbreviations for the operating institutes: Max Planck Institute for Chemistry (MPIC), Institute of Environmental Physics, University of Heidelberg (IUP), Landesamt für Umwelt (LfU), Deutscher Wetterdienst (DWD).

Instrument	Start	End	Location	Operator
mini MAX-DOAS	April 10th	November 25th	Castle	MPIC
mini MAX-DOAS	July 30th	December 14th	Barn	MPIC
Long-Path-DOAS	April 10th	December 10th	Barn	IUP
Air quality station	continuous	continuous	Öttingen	LfU
DWD weather station	continuous	continuous	Reimlingen	DWD
In-field weather stations	June 16th	December 14st	Barn	MPIC

5.3.1 The mini-MAX-DOAS instruments

Throughout this campaign two mini MAX-DOAS instruments (produced by the Hoffmann GmbH) were used to acquire slant column densities of trace gases. The mini-MAX-DOAS instruments contain a crossed Czerny-Turner spectrometer (USB2000+, produced by Ocean Optics Inc.) which can measure spectra of scattered sunlight in the UV/VIS wavelength range between 320 nm to 460 nm with a spectral resolution of about 0.8 nm (for the instrument placed at the castle station) and about 0.6 nm (for the instrument placed at the barn station). The light is thereby collected through a quartz lens with a focal length of 40 mm and a field of view of $\sim 1°$ and, subsequently, transported via a quartz fibre bundle to the spectrograph. A one-dimensional CCD (Sony ILX511) with 2048 individual pixels is used as detector. The spectrograph is cooled by a (thermoelectric) Peltier element to a constant temperature to minimize changes in the optical properties of the spectrograph as well as to reduce the dark current. An electronic offset is added to the analogue signal before it is converted to a digital signal by a 12 bit converter. The digital signal is then transmitted through a USB connection to a laptop.

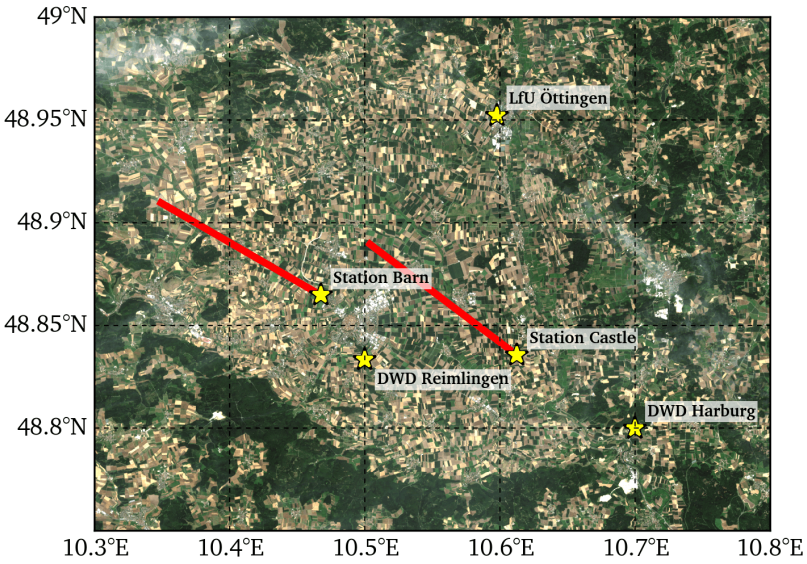

Figure 5.5: Measurement locations of the DOAS-type instruments at the castle and the barn station as well as the DWD weather stations and the LfU air quality monitoring station are indicated with a yellow star. Main viewing directions of the mini-MAX-DOAS instruments are indicated by the red lines (with a symbolic length of 10 km). The viewing direction of the LP-DOAS at the barn station is about the same as for the MAX-DOAS instrument (but has a fixed path length of 2.8 km).

A stepper motor outside of the metal box of the instrument rotates the instrument to different elevation angles. Both instruments were set-up to automatically record spectra at 12 angles, i.e. 0°, 1°, 2°, 3°, 4°, 5°, 6°, 8°, 10°, 15°, 30° and 90°, which was necessary to collect information on the vertical distribution of trace gases for the subsequent profile retrieval. For each elevation scan, the total integration time was set to 60 s which leads to approximately 4 complete elevation scan series over 1 h and about 36 series per day (depending on ambient light conditions and the time of the year).

The instruments and measurements were controlled by the DOASIS[5] program (Kraus, 2006) that regulates the integration time of the measurement, the temperature of the instrument, the sequence of elevation scans and regular offset and dark current measurements at night-time.

A power connection was available at each measurement site. However, a 12 V car battery was interconnected in order to ensure constant power supply. Remote access to the instruments for maintenance and data collection was facilitated through a mobile broadband modem attached to the operating laptop.

In the following, the measurement sites of the two instruments as well the configuration specifics of the mini MAX-DOAS instruments at the sites are described. For a more detailed description of the measurement principle as well as the technical structure of the mini MAX-DOAS instruments see Section 2.4.3.2.

[5]DOAS Intelligent System software package distributed by the Institute of Environmental Physics, University of Heidelberg

5.3.1.1 Castle Station

One mini MAX-DOAS instrument was installed on top of a ~ 30 m hill in the centre of the Nördlinger Ries. This hill is enclosed by a castle wall (Fig. 5.6.c) belonging to Castle Alerheim. This particular location provides a free view on the plain of the Nördlinger Ries and also facilitates MAX-DOAS observations at very low elevation angles, i.e. 0° and 1° due to its elevated position. The instrument was mounted on a metal construction which was carved into the ground and additionally tightly fixed on the wooden railings as can be seen in Fig. 5.6b. The main viewing direction (Fig. 5.5) of the mini-MAX-DOAS was set to 307° to continuously scan through the centre of the Ries. The laptop operating the MAX-DOAS instrument was put into a passively ventilated metal box next to the instrument. Additionally, a webcam for the observation of the sky condition (e.g. cloud coverage) was attached to the metal table below the mini MAX-DOAS instrument.

In addition to measuring spectra in the vertical, a turning table was mounted underneath the mini MAX-DOAS on August 14$^{\text{th}}$ 2007 which enabled measurements at different azimuth angles. This turning table was controlled by a V25-system (developed by the Electronics Department of the Max Planck Institute for Chemistry). For these horizontal observations 7 angles were chosen to cover the Ries plain, i.e. 247°, 267°, 287°, 307°, 327°, 347° and 7°. As the focus of this study was on trace gases originating from the surface, a low elevation angle (1°) was chosen for the measurements in the horizontal. This azimuth scanning mode was activated after every fourth normal measurement series consisting of the 12 elevation scans (0° to 90°). After the last elevation scan (i.e. 90°), the instrument rotated to a special vertical position (115°) which triggered a contact sensor attached to the turning table. Then, the turning table automatically moved the entire construction to the first horizontal position (247°). After each azimuth scan, the instrument turned to the 115° elevation angle triggering the turning table to go to the next azimuth position (e.g. from 247° to 267°). After all 7 azimuth scans were completed, the entire construction was positioned again to the main viewing direction (307°).

5.3.1.2 Barn Station

A mini MAX-DOAS instrument was installed next to a storage barn which is located amidst cultivated fields to the North-West of Nördlingen (Fig. 5.7) with free view to the fields in the West. The instrument was mounted on a metal table and fixed to the outer wall of the barn. The main viewing direction of the MAX-DOAS was set to 300°. The laptop operating the MAX-DOAS instrument was put inside the barn and all cables to and from the mini MAX-DOAS went through the wall of the barn. Unfortunately, frequent technical issues occured that lead to the interruption of the measurement script. Most of the time they could not be repaired from remote causing longer breaks in the time series.

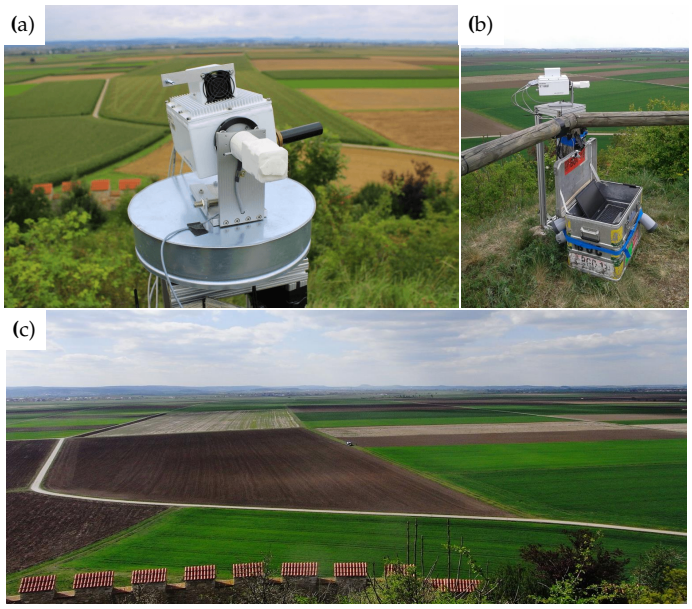

Figure 5.6: mini MAX-DOAS instrument at the "castle station". A turning table for movements in the azimuth (covered by a circular shaped metal plate) was mounted underneath the mini MAX-DOAS August 14th 2014.

Figure 5.7: Location of the "barn station" (marked with a yellow star) where a mini-MAX-DOAS and Long-Path DOAS were installed. In the right panel, the city of Nördlingen is visible in the lower right corner. Image data from Bing Maps ©2016 - Microsoft Corporation.

5.3.2 Long-Path DOAS

Within this measurement campaign, a LP-DOAS, operated by the Institute for Environmental Physics at the University of Heidelberg, was installed at the barn station from end of August to mid December measuring trace gases with high precision at day and night-time. The LP-DOAS was placed next to the mini-MAX-DOAS and pointed to a reflector (30 x 35 cm) in north-westerly direction (Fig. 2.4.3.1). The latter was mounted on an electrical tower about 2.8 km away from the telescope amidst crop fields. The light source, the spectrograph as well as controllers and measurement computers were placed in the barn. The telescope was located outside of the barn and connected to the spectrograph via 6 to 7 m long fibres. For a more detailed description of the measurement principle of the LP-DOAS see Section 5.8. Detailed information on the measurement set-up as well as the data analysis of the LP-DOAS measurements in the Nördlinger Ries can be found in

the master thesis by Philipp Eger (2014) submitted to the University of Heidelberg.

Volume mixing ratios (VMRs) for NO_2 were provided with a detection limit of 60 ppt and an average measurement error of 1 %. The detection limit for HCHO was 110 ppt and VMRs could be retrieved with an average measurement error of 10 %.

Figure 5.8: Measurement set-up of the LP-DOAS at the barn station. Left: the reflector amidst crop fields. Right: the telescope next to the barn.

5.3.3 Air quality monitoring station

Trace gas concentrations from an air quality monitoring station in Öttingen are acquired for the comparison to the measurements of the mini MAX-DOAS and LP-DOAS instruments. The station is part of the air pollution control system operated by the Bavarian Environment Agency (german: Bayerisches Landesamt für Umwelt, LfU) measuring in situ concentrations of trace gases such as NO, NO_2, O_3 and $PM_{2.5}$ at a site classified as 'background'. It is located at 48.952 18°N, 10.597 72°E in a suburban environment directly next to the open fields to the south-west (Fig. 5.9). However, it is also positioned next to a road and in close proximity to a school which potentially leads to a distinct enhancement in trace gas levels of NO, NO_2 and $PM_{2.5}$ in the morning due to a rush hour effect of car travels. The measurement station consists of a heat insulated concrete cabin which is air-conditioned at a constant temperature at about 22 °C. External air for the measurement inside the cabin is sucked in at a height of 1 m (for trace gases) and 1.5 m (for $PM_{2.5}$) above the cabin to ensure an undisturbed sampling. The air is then transported through inert pipes, made of materials like borosilicate glass or teflon, to the gaseous and particulate measurement devices.

At this station NO is measured by chemiluminescence (APNA-370 by HORIBA) with a detection limit of 0.7 µg m^{-3} and a measuring range from 0 to 1.25 mg m^{-3}. For NO_2 the same instrument type is used but with a detection limit of 1 µg m^{-3} and a measuring range from 0 to 1.91 mg m^{-3}. O_3 is measured by UV-absorption (APOA-370 by HORIBA) with a detection limit of 1 µg m^{-3} and a measuring range from 0 to 1 mg m^{-3}. The particle mass concentration is measured using attenuation of beta-radiation with a nephelometer (Sharp Modell 5030 by Thermo Scientific) with a detection limit of 0.5 µg m^{-3} and a measuring range from 0 to 1 mg m^{-3}.

Figure 5.9: Air quality monitoring station in Öttingen, Göthestraße. Image in the centre by LfU, ©Bayerische Vermessungsverwaltung 2014; Right image from Bing Maps ©2016 - Microsoft Corporation.

5.3.4 In-field weather stations

Within this study, several weather stations were installed in-field for the measurement of ambient meteorological as well as soil conditions which are later used for comparison to trace gas concentrations. The instruments were placed in close proximity to the barn station amidst crop fields in order to measure the soil moisture and soil temperature for different field types (Fig. 5.10). Here, the instruments where placed on a wheat, sugar beet and an onion field. The composition of instruments at each weather station was identical and the power supply for each station was provided by a solar panel (bp solar) facing south. Central was the data logger (CR200X, Campbell Scientific) for the storage of the data and power distribution to the individual devices. For measurements of ambient air temperature, humidity, pressure, wind speeds and directions as well as precipitation, the weather station sensor WTX520 by Vaisala was used. Other devices on the stations comprise: Global Radiation Sensor SR11-10, UMS Soil Moisture Probe (FTR), Oregon Scientific Remote Rain Gauge PCR800 and the Campbell Scientific Temperature Probe TP109.

5.3.5 Meteorological data from the DWD

Continuous observations of air temperature and precipitation was provided by the fixed weather station operated by the German Weather Service (german: Deutscher Wetterdienst, DWD). The station in Reimlingen is located at 48.8253°N, 10.5064°E in the south-west of Nördlingen. Furthermore, calculated daily estimates of soil moisture and temperature for the Reimlingen station is provided by the DWD[6] and computed by the AMBAV model[7]. The fixed DWD weather station in Harburg (48.7917 N, 10.7061 E, 502 m.a.sl.) provides data on ambient wind conditions (wind speed and direction) at the south-western edge of the Ries. Radar-derived hourly precipitation estimates on a 1 km grid were also provided by the Radolan system of the DWD[8].

[6]DWD Climate Data Center: Calculated daily values for different characteristic elements of soil and crops, version V0.x, 2016/04/08

[7]Agrarmeteorologisches Modell zur Berechnung der aktuellen Verdunstung

[8]Product and information available via: http://www.dwd.de/DE/leistungen/radolan/radolan.html

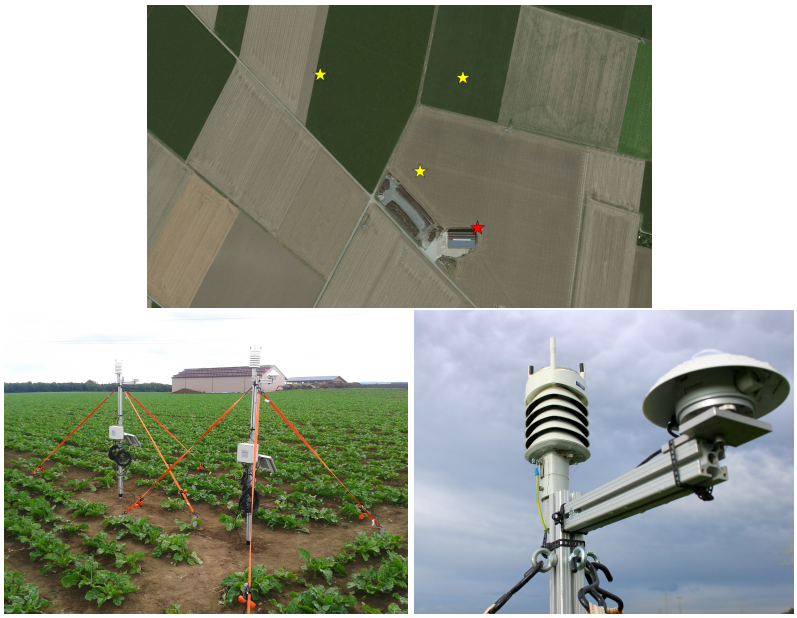

Figure 5.10: Top: Locations of the weather stations (yellow stars) in-field around the barn station (red star). Image data from Bing Maps ©2016 - Microsoft Corporation. Note, that the top image is just for reference and the crops on the depicted fields do not represent the actual crops at that time. Bottom images show the weather stations which were installed in the field. Two identical stations were installed next to each other at the beginning of the study for evaluation purposes. The lower left image shows the barn station in the background.

5.4 Trace gas and aerosol information from the MAX-DOAS instruments

Essential to the measurement campaign in the Ries was the retrieval of trace gas column densities as well as volume mixing ratios (VMRs) from the MAX-DOAS instruments. Therefore, a detailed description of the analysis of the measured spectra and further data analysis is provided in the following sections.

5.4.1 Correction of the raw spectra

The measured spectra of the mini MAX-DOAS instruments are affected by several interfering background signals which have to be corrected before conducting the DOAS analysis. For the correction of the dark current and electronic offset, night-time spectra of these quantities were subtracted from the measured day-time spectra (in the same procedure step as the stray light correction) as reasoned and described in the following.

Dark current. Dark current arises due to the self-dischargement of the CCD detector whereby thermally excited electrons hit the CCD detector and appear as an additional signal in the spectrum. As this effect increases with temperature, the temperature of the instruments is kept as low as possible and constant over the measurement period. The spectra are corrected for the dark current signal by subtracting a dark current spectrum

(from the measured spectrum at day-time) which was measured without incident light on the detector (e.g. at night-time) and weighted with the ratio of the integration times of a measured spectrum (day-time) and a dark current spectrum.

Electronic offset. The electronic offset is a fully artificial signal, and in the case of the OceanOptics USB2000+ spectrometer also temperature-dependent, introduced by the analogue-to-digital conversion to avoid negative signals caused by electronic noise at low intensity levels. This effect is corrected by taking a spectrum, typically with a very short integration time, when no incident light hits the detector (e.g. at night-time) and subtracting it from the measured spectra at day-time.

Stray light. Stray light within the spectrograph is caused by photons which have not traversed the destined path through the spectrograph. As a first-order approximation, this effect can be assumed to be distributed homogeneously over the lines of the CCD detector (Sinreich, 2008). Thus, during the spectral analysis a constant intensity offset was included in the DOAS fit to account for this effect.

5.4.2 Spectral Retrieval

For the retrieval of differential slant column densities (DSCDs), the measured spectra from April to December 2014 are analysed based on the DOAS approach. The Windoas software (Fayt and van Roozendael, 2001) was used for the wavelength calibration (using a high resolution solar spectrum from Kurucz et al. (1984)) of the spectra and the convolution of trace gas cross-sections to fit to the spectral resolution of the instrument. The trace gases and cross-sections considered in the DOAS retrieval are given in Table 5.2. In addition to the retrieval of NO_2 and HCHO, also O_4 was retrieved which is needed for the cloud classification and the profile retrieval in the following chapters. The DOAS retrieval was then performed using MDOAS (developed by Julia Remmers at the MPIC) which is a MATLAB[9]-based DOAS fitting routine. The main advantage of MDOAS over Windoas within this long-term measurement campaign is an easy and flexible application of a sequential Fraunhofer Reference Spectrum (FRS), meaning that either (i) the closest FRS or (ii) an average of the two closest FRS can be used for the retrieval of the tropospheric DSCDs opposing to just a single FRS for the whole time series. This is particularly important as the use of a FRS taken shortly before or after a lower elevation scan can, on the one hand, minimise fit errors arising from changes in instrumental properties over time and, on the other hand, reduce the impact of stratospheric absorptions in the DOAS fit which becomes important for measurements in the morning and evening when the solar zenith angle (SZA) is high. In this analysis, the FRS used for a DOAS fit was calculated as the mean of 2 sequential FRS measurements in log space. Each FRS was taken at a 90° elevation angle.

[9] © 1994–2016 The MathWorks, Inc.

In the following, several typical DOAS fits for the mini MAX-DOAS at the barn and castle stations are presented.

Table 5.2: Settings used for the DOAS retrieval of O_4, NO_2 and HCHO. *solar I_0 correction following Aliwell et al. (2002): 1×10^{17} molecules cm^{-2} for NO_2 and 1×10^{20} molecules cm^{-2} for O_3, **NO_2 at 220K was orthogonalized to NO_2 at 294K.

Parameter	**Data Source**	**Fitting interval**		
		O_4	**NO_2**	**HCHO**
Wavelength range		351–390 nm	400–455 nm	324–358 nm
NO_2	Vandaele et al. (1998), 220K, 294K	x, *, **	x, *, **	294 K, *
O_3	Bogumil et al. (2003), 223K, 243K	223 K, *	223 K, *	223 K, 243 K*
HCHO	Meller and Moortgat (2000), 293K	x		x
H_2O	(Rothman et al., 2005)		x	
BrO	Fleischmann et al. (2004), 223K			x
O_4	Thalman and Volkamer (2013), 293K	x	x	x
Ring	Two Ring spectra calculated with DOASIS (Kraus, 2006; Wagner et al., 2009)	x	x	x
Polynomial degree		3	3	5
Intensity offset		constant	constant	constant

5.4.2.1 DOAS fit examples for NO_2

NO_2 was fitted in the wavelength range between 400 to 450 nm including the cross sections of O_3 (at 223K and 243K), H_2O, O_4, a polynomial with a degree of 3 and a constant intensity offset. Rotational Raman scattering is accounted for by (i) the computation of a Ring spectrum by DOASIS and (ii) the inclusion of a second Ring spectrum which additionally accounts for the different wavelength dependencies of the Ring effect following Wagner et al. (2009). Fig. 5.11 shows typical DOAS fit results for NO_2 for the mini MAX-DOAS instruments at the barn and castle stations. The spectrum (at the barn station) was taken at an elevation angle of 1° on August 8th under clear-sky conditions at 12:07 local time. The corresponding NO_2 DSCD is 2.12×10^{16} molecules cm^{-2} with a root mean square error (RMS) of 6.43×10^{-4}. Assuming two times the fit error as a measure for the detection limit (DL), this leads to a DL of 1.76×10^{15} molecules cm^{-2}. The spectrum (at the castle station) was also measured at an elevation angle of 1° but on September 9th at 12:15 local time and lead to a NO_2 DSCD of 7.62×10^{16} molecules cm^{-2} with a RMS of 1.10×10^{-3}. The DL for NO_2 in this case was 3.03×10^{15} molecules cm^{-2}. Due to the lower spectral resolution of the mini MAX-DOAS instrument at the castle station compared to the one at the barn station, consistently higher residuals are found throughout the analyses. However, this hardly impacts on the resulting NO_2 DSCDs because of the relatively strong absorption features of NO_2.

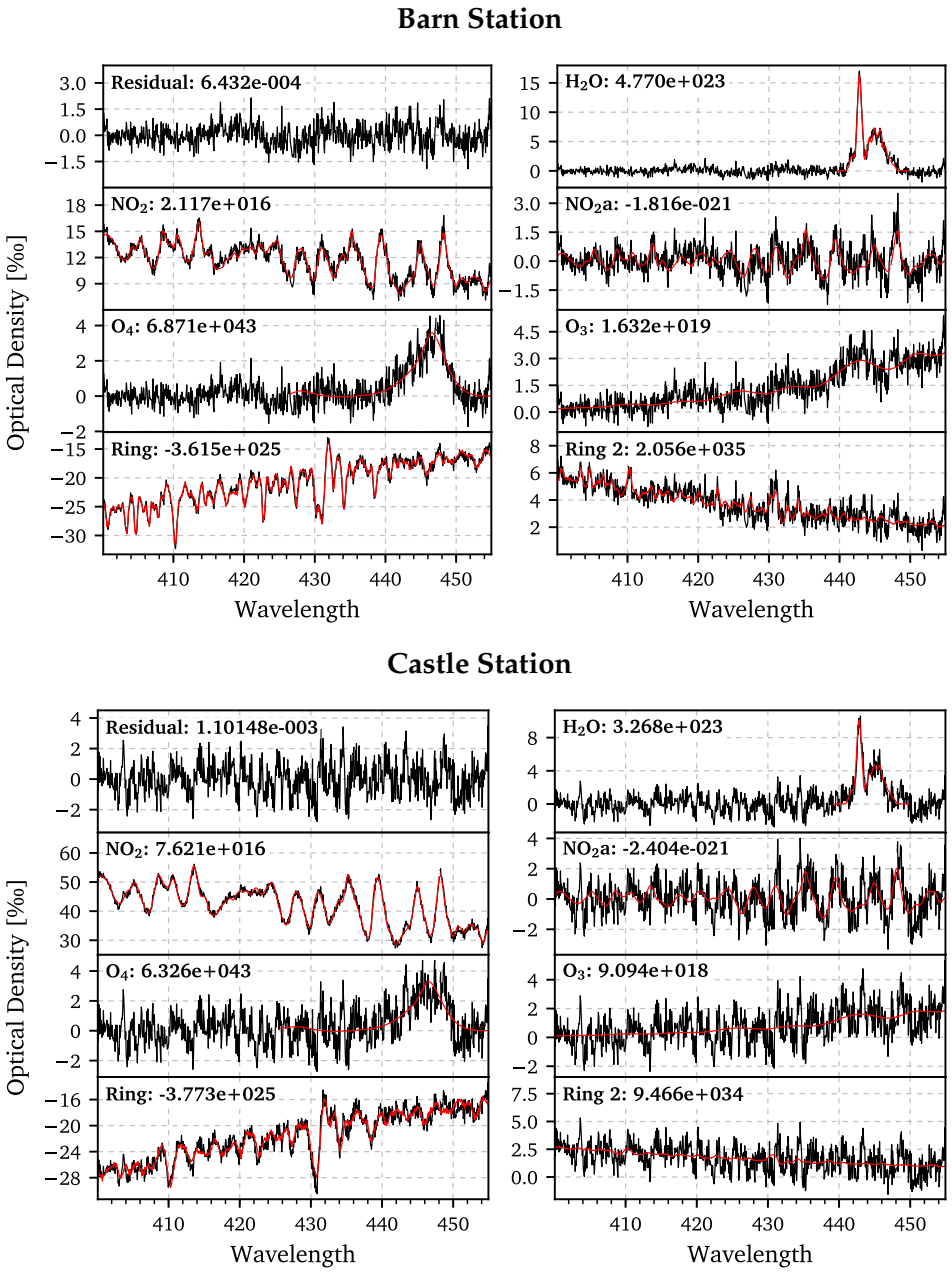

Figure 5.11: Top panels: example for a typical DOAS fit for NO_2 at the barn station at an elevation angle of 1° on August 8th under clear-sky conditions at 12:07 local time. The optical densities of the fitted species (red) and the residuals (black) are displayed as a function of wavelength. **Bottom panels:** example for a typical DOAS fit for NO_2 at the castle station at an elevation angle of 1° on September 9th under clear-sky conditions at 12:15 local time. The optical densities of the fitted species (red) and the residuals (black) are displayed as a function of wavelength.

5.4.2.2 DOAS fit examples for HCHO

HCHO exhibits structured absorption bands in the UV, between 240 nm and 360 nm. However, due to the enhanced ozone absorption below 320 nm, only the bands above 320 nm can be used for the retrieval of HCHO. Within this campaign HCHO was fitted in the wavelength range between 324 to 359 nm including the cross sections of O_3, H_2O, O_4,

two Ring spectra, a polynomial with a degree of 5 and a constant intensity offset. Fig. 5.12 shows DOAS fit results for HCHO for the mini MAX-DOAS instrument at the barn and castle stations. The measured spectrum at the barn station (the same as for the NO_2 fit example) was taken at an elevation angle of 1° on August 8th under clear-sky conditions at 12:07 local time. The HCHO DSCDs for this measurement are 3.70×10^{16} molecules cm^{-2} with a RMS of 6.34×10^{-4} and a subsequent DL of 4.99×10^{15} molecules cm^{-2}. In general, HCHO could be retrieved reasonably well by this instrument, as can be seen in the exemplary DOAS fit. However, the retrieval of HCHO using the mini MAX-DOAS at the castle station was more challenging due to the lower spectral resolution of the instrument. This becomes relevant as HCHO already exhibits weaker absorption features (e.g. compared to NO_2). Also, the residual structures are generally larger for the DOAS fits at the castle station as depicted in one typical DOAS fit in Fig. 5.12. The latter was taken at an elevation angle of 5° on July 24th under clear-sky conditions at 11:47 local time. The resulting HCHO DSCD is 3.87×10^{16} molecules cm^{-2} with a RMS of 9.28×10^{-4} and a calculated DL of about 7.46×10^{15} molecules cm^{-2}. Note that for this example a measurement taken at 5° was chosen, because the analysis of spectra taken at lower elevation angles generally resulted in very weak HCHO absorptions (and consequently high residuals).

5.4.2.3 DOAS fit examples for O_4

The DOAS retrieval for O_4 was performed in the wavelength range between 351 to 390 nm including the cross sections of O_3, H_2O, O_4, two Ring spectra, a polynomial with a degree of 3 and a constant intensity offset. Fig. 5.13 shows again typical DOAS fit results for O_4 for the two instruments. The O_4 DSCD for the measurement at the barn is about 3.00×10^{43} molecules cm^{-2} with a RMS of 5.71×10^{-4} and a DL of 8.47×10^{41} molecules cm^{-2}. The DOAS fit for the measurement at the castle results in O_4 DSCDs of about 2.93×10^{43} molecules cm^{-2} with an RMS of 1.05×10^{-3} and a DL for O_4 of 8.47×10^{41} molecules cm^{-2}.

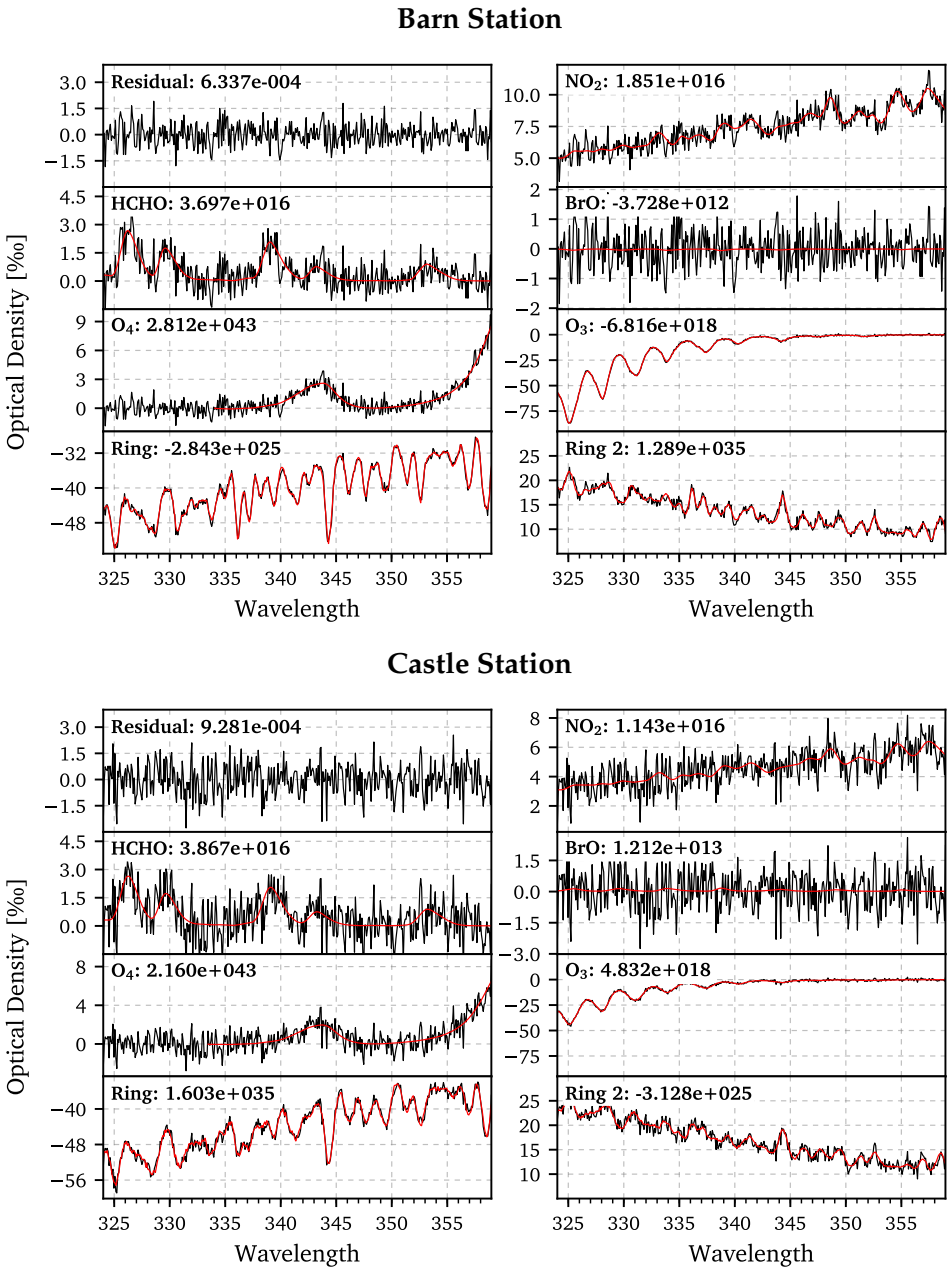

Figure 5.12: Top panels: example for a typical DOAS fit for HCHO at the barn station at an elevation angle of 1° on August 8th under clear-sky conditions at 12:07 local time. The optical densities of the fitted species (red) and the residuals (black) are displayed as a function of wavelength. **Bottom panels:** example for a typical DOAS fit for HCHO at the castle station at an elevation angle of 5° on July 24th under clear-sky conditions at 11:47 local time. The optical densities of the fitted species (red) and the residuals (black) are displayed as a function of wavelength.

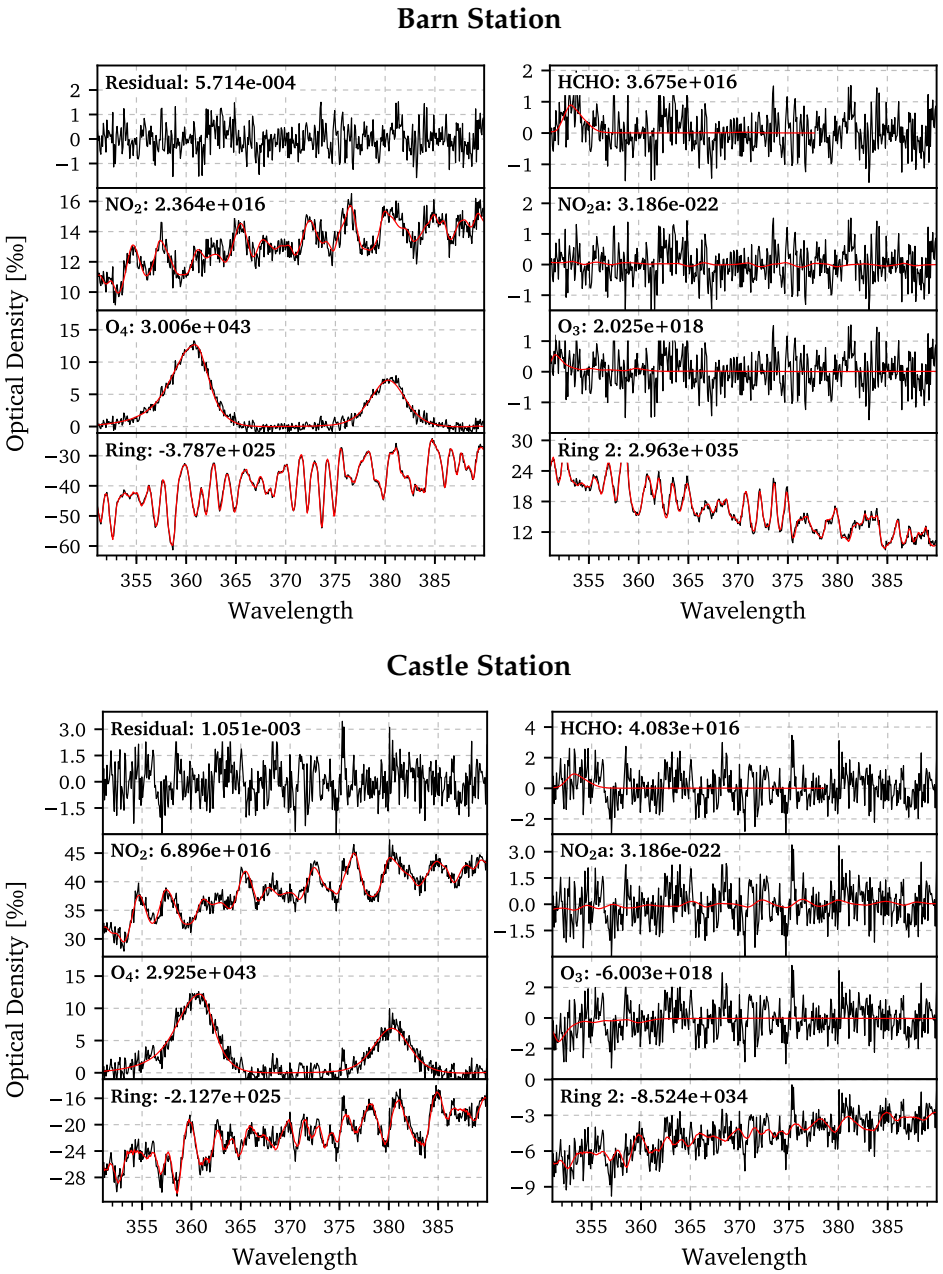

Figure 5.13: Top panels: example for a typical DOAS fit for O_4 at the barn station at an elevation angle of 1° on August 8th under clear-sky conditions at 12:07 local time. The optical densities of the fitted species (red) and the measured residuals (black) are displayed as a function of wavelength. **Bottom panels:** example for a typical DOAS fit for O_4 at the castle station at an elevation angle of 1° on September 9th under clear-sky conditions at 12:15 local time. The optical densities of the fitted species (red) and the measured residuals (black) are displayed as a function of wavelength.

5.4.3 Quality screening of the retrieved DSCDs

As the DOAS fitting routine is an automated process, the resulting DSCDs for the individual species still need to be inspected and screened for erroneous data. Here, a simplistic approach is chosen by investigating the NO_2 and HCHO DSCDs as function of the root mean square error (RMS), the relative intensity offset (RIO) and the solar zenith angle (SZA). Under the assumption that the bulk of the data is of good quality, outliers are screened out based on threshold values derived from the correlation plots.

In this analysis, DSCDs showing a large RMS of the residuals of the DOAS fit are screened out as this parameter is a measure for the overall quality of the DOAS fit. Furthermore, measurements with a large RIO are also screened out. Because of supposedly strong absorptions of stratospheric species, such as O_3 or also NO_2, and lower signal-to-noise ratios measurements at large SZAs (> 82°) are discarded from further analysis. The thresholds are chosen individually for each species and are based on their correlation to the above stated quality parameters as depicted in Fig. 5.14 and Fig. 5.15. The final thresholds chosen for each species as well as the percentage of data which was screened out is given in Table 5.3. In sum, the applied quality measures lead to about 9 % to 16 % data removal (of the total amount of measurements).

Table 5.3: Thresholds used for the data quality screening of the trace gas DSCDs. The columns '%' state the % of data which is screened by the corresponding threshold.

Station	Species	SZA	%	Offset	%	RMS	%	Total %
BARN	**NO_2**	82	5.01	-0.02 to 0.02	3.80	0.002	1.23	**8.81**
CASTLE	**NO_2**	82	4.33	-0.02 to 0.02	8.05	0.003	3.33	**12.37**
BARN	**O_4**	82	4.99	-0.02 to 0.02	9.18	0.002	3.67	**14.17**
CASTLE	**O_4**	82	4.32	-0.03 to 0.07	5.64	0.003	2.63	**9.96**
BARN	**HCHO**	82	4.97	-0.03 to 0.07	11.07	0.002	4.82	**16.04**
CASTLE	**HCHO**	82	4.32	-0.04 to 0.1	9.37	0.003	1.60	**13.69**

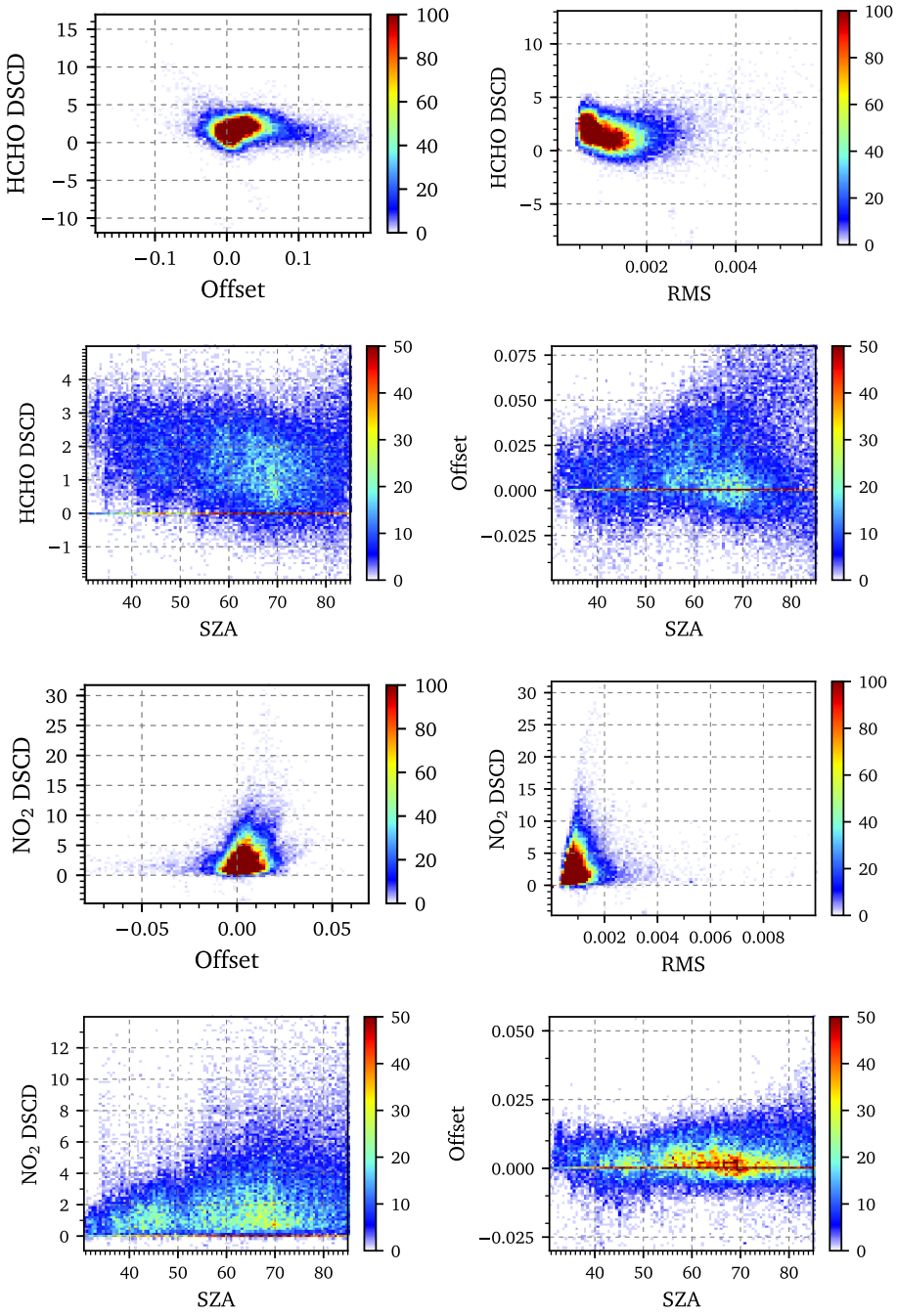

Figure 5.14: Quality analysis of the retrieved DSCDs of the trace gases for the mini MAX-DOAS instrument at the barn station. Plotted here are HCHO and NO_2 DSCDs [1×10^{15} molecules cm^{-2}] against the relative intensity offset [%], the RMS [optical density] and the SZA in degree. Additionally, the relative intensity offset is plotted against the SZA for the HCHO and NO_2 analyses.

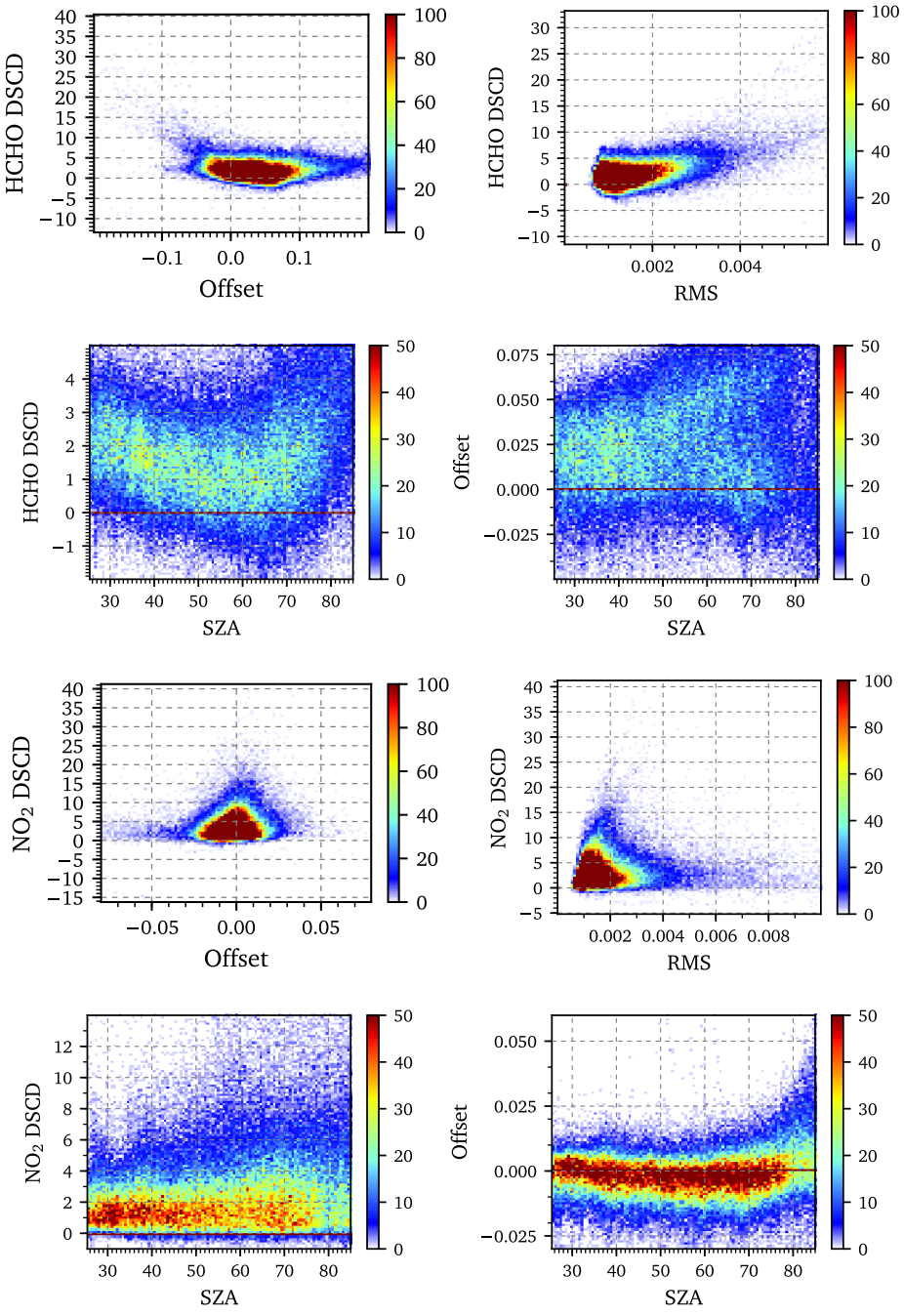

Figure 5.15: Quality analysis of the retrieved DSCDs of the trace gases for the mini MAX-DOAS instrument at the castle station. Plotted here are HCHO and NO_2 DSCDs [1×10^{15} molecules cm^{-2}] against the relative intensity offset [%], the RMS (optical density) and the SZA in degree. Additionally, the relative intensity offset is plotted against the SZA for the HCHO and NO_2 analyses.

5.4.4 Computation of trace gas profiles, mixing ratios and VCDs

In the previous section the procedure for the retrieval of slant column densities (SCDs) was described. These SCDs represent trace gas concentrations integrated along the light path of the photons traversing through the atmosphere. However, for long-term evaluations quantities are needed which can be compared to one another independently from the light path of the individual measurements and which can be also compared to data from different instrument types. Such more universal quantities are, on the one hand, volume mixing ratios (VMRs) which can be compared to LP-DOAS and air quality monitoring stations and, on the other hand, vertical column densities (VCDs) which can be compared to observations from satellite instruments. Within this campaign the optimal estimation based 'Profile inversion algorithm of aerosol extinction and trace gas concentration' (PriAM) (Wang et al., 2013b,a) was used which enables the calculation of VMRs for trace gases at different altitudes (in layers of 200 m from the ground to up to 4 km) as well as VCDs. Thereby, a similar retrieval process as described in Wang et al. (2016) was conducted.

In simple terms, it is a two-step algorithm by, firstly, retrieving tropospheric vertical profiles of aerosols based on the O_4 SCDs and, secondly, acquiring tropospheric profiles of trace gases from the SCDs of NO_2 and HCHO at different elevation angles. Based on the knowledge of trace gas DSCDs taken at different elevation angles one can draw conclusions on their concentrations at different altitudes, i.e. their atmospheric profiles. In PriAM this inverse retrieval problem is solved iteratively using the Levenberg-Marquardt modified Gauss-Newton algorithm following Rodgers (2000) and the SCIATRAN (v2.2) radiative transfer model (RTM) (Rozanov et al., 2005). For this procedure, initial profile shapes of aerosols and trace gases are needed which are then optimized in each retrieval step to fit to the measurements. However, as atmospheric profiles of aerosols, NO_2 and HCHO vary over time and their state is not known prior to the retrieval process, individual a priori profiles have to be assumed for each species.

Within this study, well-tested a priori profile shapes are used based on the work from Wang et al. (2016) who applied them on a long-term measurement series in China. For aerosols, a smoothed box-shaped a priori profile based on a Boltzmann distribution is used (Yilmaz, 2012). For NO_2, an exponential a priori profile similar to Yilmaz (2012) and Hendrick et al. (2014) is used. The a priori profile for HCHO is also based on a Boltzman distribution which was approximately found in MAX-DOAS and aircraft measurements over Milano in the summer 2003 (Wagner et al., 2011).

The RTM simulations were performed at 440 nm for NO_2 and 339 nm for HCHO for surface heights corresponding to the elevation at the measurement stations (420 m for the barn and 450 m for the castle station) and a surface albedo of 0.05. The retrieved aerosol extinction at 370 nm is converted to those at 339 nm for the HCHO retrieval and at 440 nm for the NO_2 retrieval using Ångström exponents of 1. The single scattering albedo was set to 0.9 and the asymmetry factor to 0.68.

5.4.5 Cloud classification

MAX-DOAS measurements of trace gases are substantially influenced by ambient cloud conditions and aerosol loads in the atmosphere. In consequence, the retrieval algorithm which was described in the previous section also relies on clear-sky conditions to accurately retrieve trace gas profiles. Thus, knowledge on sky conditions and cloud types is crucial in the analyses of the retrieved trace gas concentrations. Within this study, the cloud classification scheme described in Wagner et al. (2014) and Wang et al. (2015a) is used to separate the data based on different sky conditions. Thereby, information from the MAX-DOAS observations are directly used to infer the sky conditions, i.e. clear or cloudy sky, during the measurement. In specific, the classification system depends on three main parameters from the MAX-DOAS measurement (Wagner et al., 2014): firstly, the radiance being a measure for the brightness of the sky; secondly, the colour index which is generally defined as the ratio of two radiances at different wavelengths, i.e. within this study at 340 nm and 420 nm, and thus indicating the colour of the sky; and thirdly, the absorption of O_4 giving information about of the atmospheric light paths. Based on a complex set of threshold values for these quantities similar to (Wang et al., 2015b), each MAX-DOAS measurement is then assigned to one of the following categories: clear sky with low aerosol loads ('low aerosols'), clear sky with high aerosol loads ('high aerosol'), 'cloud holes', 'broken clouds', and 'continuous clouds'.

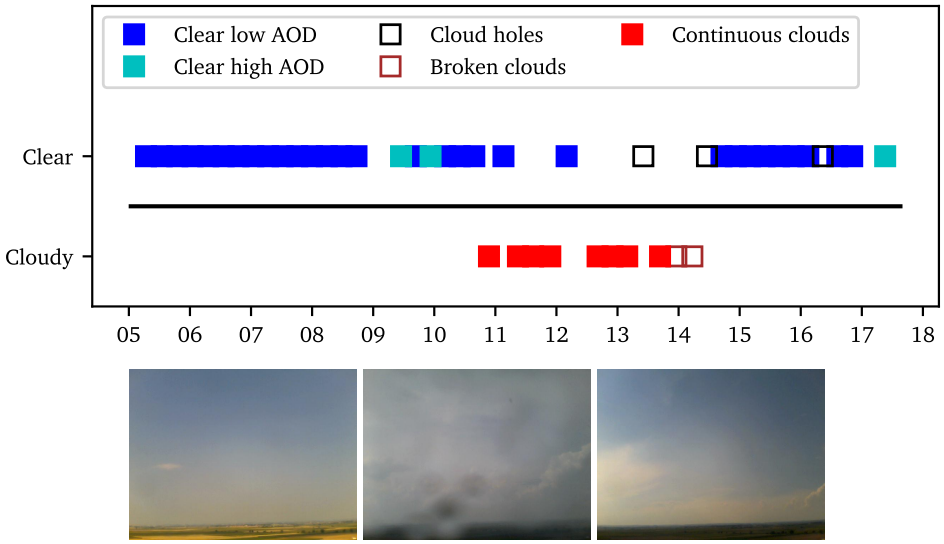

Figure 5.16: Top panel: Result of the cloud classification scheme for July 25th 2014 showing clear sky in the morning and evening and continuous cloud cover (and rain) in early afternoon. **Bottom panel:** Images from the webcam at the castle station at 9:00UTC, 12:00UTC and 17:00UTC

In addition to these 5 categories, measurements taken during very low visibility (such as during fog) are identified and discarded from further analyses as they do not contain reliable information on trace gas concentrations. In this study, such measurements are identified based on the principle that in foggy situations the atmospheric light paths are very short and become the same at every elevation angle. Hence, the O_4 differential air

mass factors (DAMF) are also homogeneous for all angles. In practice, all measurement within a single elevation scan series were tagged as 'foggy' when the division of at least one of the O_4 DSCDs by a standard VCD for the Ries (i.e. 1.253×10^{43} molecules cm^{-2}) is below a certain threshold value, i.e. 0.37 (Wagner et al., 2014).

5.5 Meteorology in the Ries during the campaign

The winter months in the year 2014 were relatively warm (+3 °C) compared to the mean from 2006–2013 in Fig. 5.4. Summer temperatures were about 18° (upper panel in Fig. 5.17). However, a larger discrepancy compared to the mean from 2006–2013 is found for precipitation which shows lower amounts during winter and higher in summer. During the months of May and June in 2014 relatively few precipitation occurred ($\sim$ 40.5 mm in May and $\sim$ 34 mm in June) compared to the long-term mean ($\sim$ 91 mm and $\sim$ 85 mm, respectively). In contrast, summer time precipitation was higher in July and August (132 mm and 100 mm) compared to the mean from 2006–2013 (120 mm and 85 mm).

The lower panels of Fig. 5.17 depict the dominant wind conditions within the Ries, on the one hand, from the own weather station close to the barn station and, on the other hand, for the DWD station in Harburg. As the in-field weather station operated from June to November 2014, the data presented here as well as the data for the DWD station is selected for the same period. In Germany, winds typically blow from the west which is also observed by the weather station at the barn station. Thereby, the largest share of the observed wind originated from western directions which also exhibits strongest winds ($> 4\,\mathrm{m\,s^{-1}}$). In contrast, the DWD weather station in Harburg detected quite different wind conditions during the same period, by showing (i) most and strongest winds from the north-west and (ii) a relatively low amount of wind speeds under $2\,\mathrm{m\,s^{-1}}$.

These findings point out that the ambient wind conditions during the year are very different for the two locations, i.e. one being in the centre of the Ries plain and one being at the south-eastern edge located at higher elevation.

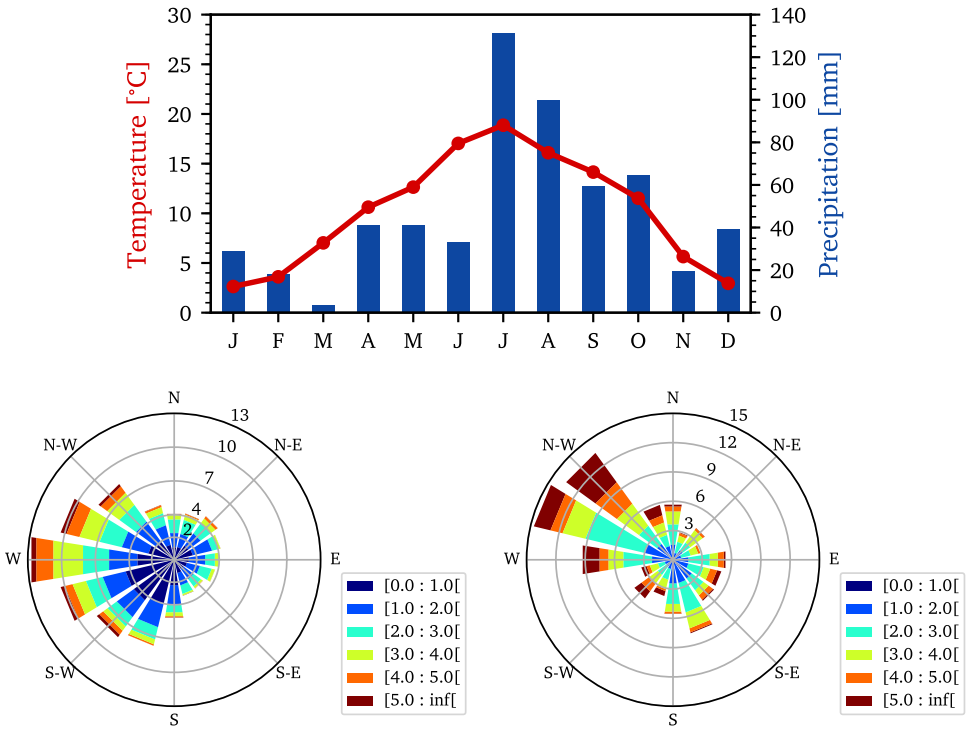

Figure 5.17: Top panel: climate diagram for the Nördlinger Ries in the year 2014. Bottom panel: average wind conditions (wind speed and direction) from June to November 2014 as observed by the in-field weather station with a 10-minute temporal resolution.

5.6 Results

5.6.1 Comparison of the measured to the simulated trace gas DSCDs

In the following sections, near-surface VMRs derived from the profile retrieval are used for most of the analyses and comparison to other instruments. These VMRs are inferred from the modelled DSCDs during the profile retrieval process of PriAM.

In order to get an impression of the overall quality of these modelled VMRs, a comparison between the measured NO_2 and HCHO DSCDs and the simulated DSCDs is presented in Fig. 5.18. The analysis is again split up for the data from the mini MAX-DOAS instruments at the castle and barn station.

Generally, the agreement between the measured and simulated NO_2 DSCDs is better compared to the same analysis for HCHO. For the NO_2 comparison, correlation coefficients (R^2) of 0.994 and 0.990 were found for the barn and castle station, respectively. The slope of the correlation between the measured and simulated NO_2 DSCDs is close to 1 (0.981 for the barn and 0.968 for the castle). For HCHO, lower R^2 are found for the two stations with a R^2 of 0.841 for the barn station and 0.789 for the castle station. In addition, the slopes for the HCHO analysis are 0.856 for the barn and 0.801 for the castle.

Furthermore, the right panels of Fig. 5.18 indicate that the correlation and bias of the modelled DSCDs to the measured DSCDs strongly depends on the elevation angle of the measurements. Interestingly, the shape of the bias (average difference between measured

and simulated DSCDs for each elevation angle) is similar for both stations and trace gases.

For NO_2, the simulation underestimates the measured DSCDs at very low elevation angles (< 3°) by about 0.5 to 1×10^{15} molecules cm^{-2} and generally overestimate the DSCDs at higher angles (> 4°). Thereby, the largest over-estimations ($\sim 0.8 \times 10^{15}$ molecules cm^{-2}) are registered for 6° to 15°. At 30°, the disagreement decreases again to about -0.2×10^{15} molecules cm^{-2}.

For HCHO, differences between the barn and castle location arise at very low elevation angles (1° and 2°) as the agreement between simulated and measured DSCDs is close to 0 for the barn station but shows an overestimation of HCHO DSCDs at the castle station of about 1×10^{15} molecules cm^{-2}. Furthermore, the overestimation of the simulated DSCDs at the castle station reaches a maximum of about 3.5×10^{15} molecules cm^{-2} (at 8°) whereas only about 2×10^{15} molecules cm^{-2} at the barn station (also at 8°).

In conclusion, the differences between the simulation and measurement of trace gas DSCDs are relatively small (especially for NO_2) indicating an overall good data quality.

5.6.2 Average trace gas and aerosol profiles

In order to get an overall picture of the vertical distributions of NO_2 and HCHO within the Ries, the VMRs for the trace gases at each altitude of the PriAM model layer are averaged for August to September 2014 for the barn and castle stations. Fig. 5.19 depicts these average trace gas profiles as well as the aerosol profile for the two stations together with the corresponding a priori profile of the species.

The bulk of NO_2 is located at the lowest model layer between 0 and 200 m and decreases rapidly with height. In these two months, the profile shapes for NO_2 VMRs of the barn and castle location are almost the same, but the absolute values are higher for the castle location. NO_2 VMRs in the lowest model layer in the vicinity of the castle station reaches about 2.05 ppb compared to $\sim$ 1.2 ppb near the barn station. The vertical distribution of NO_2 is similar to the a priori profile, however, the retrieved profiles show no considerable change after 1 km and above in the atmosphere (whereas the a priori does).

For HCHO, the profile shapes are also almost identical for the barn and castle station. However, higher VMRs are observed in proximity to the barn station at all altitudes up to 2 km. At both stations, an elevated layer of higher HCHO VMRs is found at about 1 km to 1.4 km altitude reaching about 1.8 ppb for the barn station and about 1.15 ppb for the castle station.

These enhanced HCHO VMRs at higher altitudes can potentially develop when (i) longer lived volatile organic compounds (VOCs) are uplifted and HCHO is formed through secondary formation from these VOCs at higher altitudes, or (ii) HCHO from the surface is quickly transported to these heights by strong vertical mixing.

The results show that HCHO VMRs then decrease towards the surface, but increase again in the lowest model layer. This is probably caused by either (i) direct emissions (ii) or rapid formation from VOCs near the surface. The near-surface HCHO VMRs for the

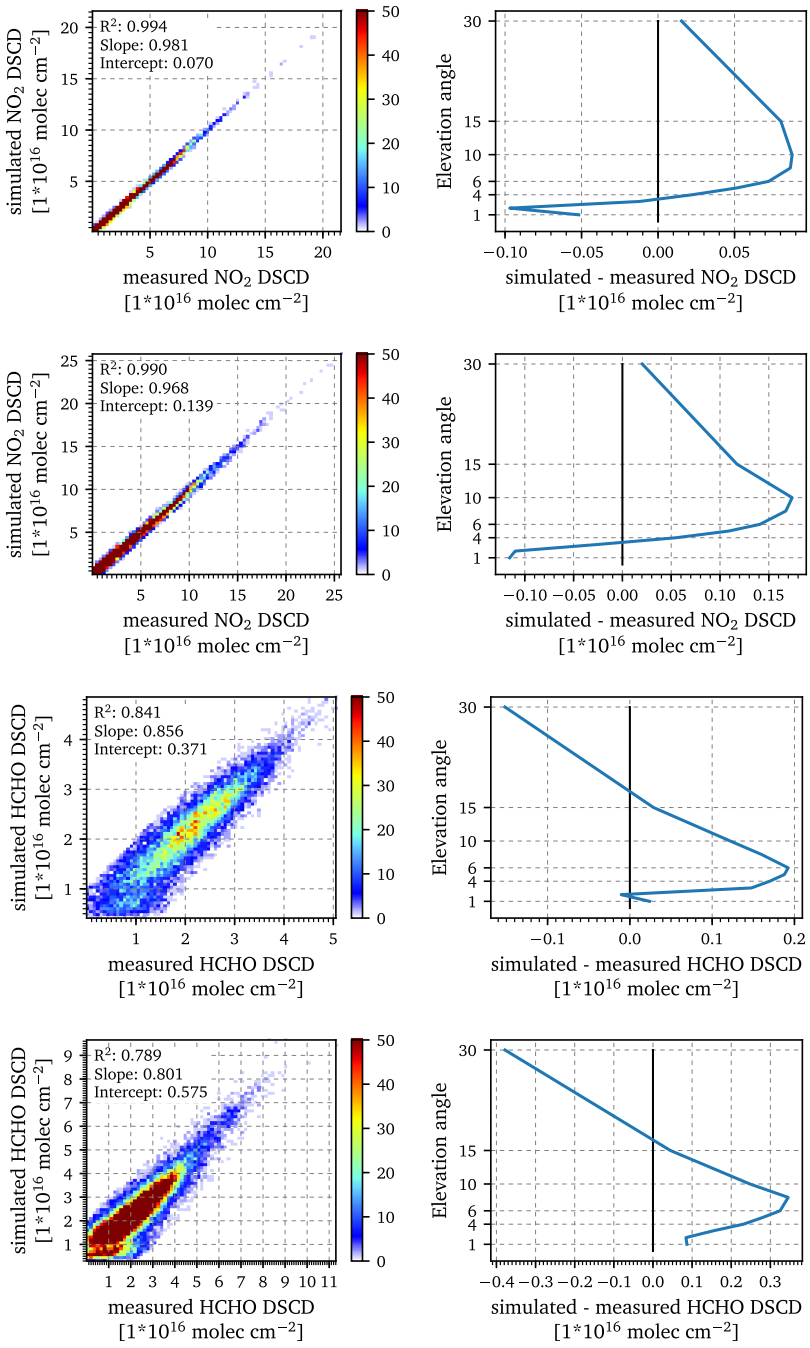

Figure 5.18: Evaluation of the simulated NO_2 and HCHO DSCDs from the profile retrieval. Left panels show the correlation between the simulated and measured DSCDs for the mini-MAX-DOAS instruments at the barn (first and third row) and castle station (second and forth row). The right panels show the absolute difference between the simulated and measured DSCDs for both trace gases and stations.

barn station are about 1.2 ppb and 0.98 ppb for the castle station. These average profiles for HCHO differ significantly from the a priori profile by showing this elevated enhancement, which is not implemented in the a priori profile.

For the aerosol extinction (AE), an a priori profile is assumed which shows no variation

between the ground and 1 km altitude. However, the profiles from the two stations show a steady increase in the AE towards the surface. The profiles for the two stations thereby differ in the AE detected in the altitude range between 0.2 to 1.5 km (higher AE in proximity to the barn). In the lowest layer, however, both stations observe similar AE of about 0.14–0.15.

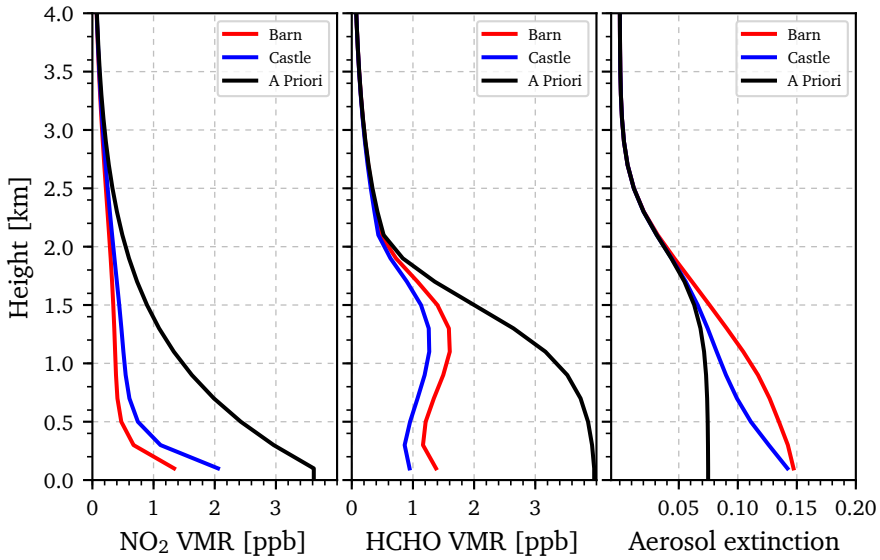

Figure 5.19: Average atmospheric profiles for HCHO, NO_2 and aerosol extinction (AE) deduced from the mini MAX-DOAS instruments at the barn (red lines) and castle station (blue lines) using the PriAM retrieval method. A priori profiles for each species are shown in black. The VMRs at each altitude were averaged over the period from August to September 2014.

5.6.3 Comparison of NO_2 VCDs to satellite observations

Vertical Column Densities (VCDs) of NO_2 calculated by the profile retrieval and based on data from the two MAX-DOAS instruments in the Ries are compared to space-based observations (from the OMI instrument) to further validate the retrieval approach (Fig. 5.20). In order to ensure that the same air masses are sampled by the instruments, strict coincidence criteria were chosen:

- a maximum cloud fraction of 20 % (taken from the OMI cloud product)
- a maximum distance of 20 km from the centre of the OMI ground pixel to the station
- a maximum of 30 min time difference between the measurements
- maximum 3 m s^{-1} wind speed to diminish the effect of transport

A total least squares fit (Cantrell, 2008) considering measurement errors of both instruments shows very good agreement between the MAX-DOAS instruments at the castle (R^2 0.93, slope 0.77) and the barn (R^2 0.97, slope 0.78) compared to OMI observations. The slopes being smaller than 1 indicates that the satellite underestimates the 'true' NO_2 VCDs

systematically. As the measurement period of the MAX-DOAS at the barn is much shorter, less coincidences were found for this comparison.

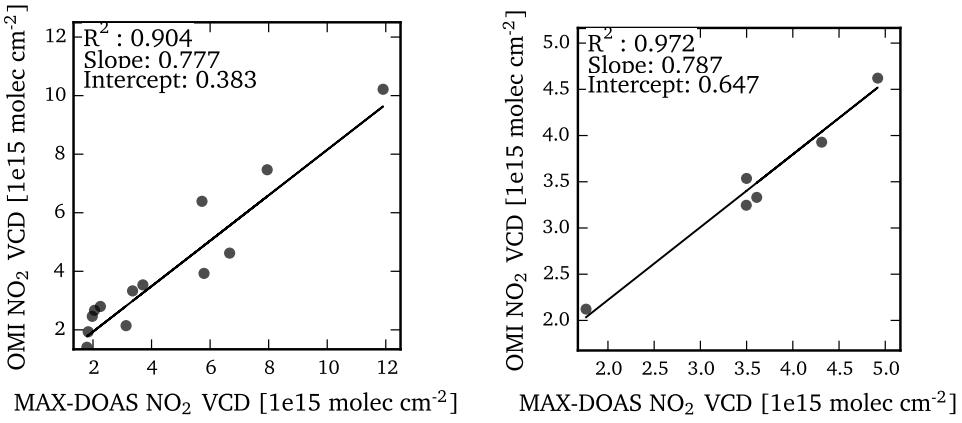

Figure 5.20: Correlation study between the NO_2 VCDs derived from the mini MAX-DOAS instruments and NO_2 VCDs from the OMI satellite instrument. Left panel: correlation study for the castle station showing good agreement (R^2 0.93) with OMI observations. Right panel: the correlation study for the barn station also shows good agreement with OMI observations (R^2 0.97), but only based on 6 data points.

5.6.4 Horizontal distribution of NO_2 and HCHO

In addition to the vertical distribution of the trace gases, also the horizontal distribution was studied to further characterize trace gas levels within the Ries plain. This is especially important to understand whether NO_2 is distributed homogeneously throughout the Ries or large emission sources are present which have to be considered in the further analyses. The horizontal scanning across the Ries plain was achieved by pointing the mini MAX-DOAS at the castle station to different azimuth positions using the turning table underneath the instrument. In practice, this was done automatically after each fourth regular elevation scan series. Then, 7 horizontal positions, i.e. 247°, 267°, 287°, 307°, 327°, 347° and 7°, were scanned by the mini MAX-DOAS with an elevation angle of 1°.

Fig. 5.21 shows the resulting NO_2 DSCDs grouped for different months and averaged over the period from August to November. Due to the different atmospheric lifetimes of NO_2, i.e. lower in summer-time and higher in winter-time, the observed NO_2 DSCDs are also lower in August and September compared to the colder months of October and November. However, in all months a similar horizontal pattern of the NO_2 DSCDs can be found, i.e. the slightly higher column densities at 287° matching the direction towards the city of Nördlingen. At 287° average NO_2 DSCDs of about 6.5×10^{16} molecules cm^{-2} are observed whereas about 5.5×10^{16} molecules cm^{-2} are observed at 247° to 267° and about 5.9×10^{16} molecules cm^{-2} from 307° to 7°. Because of typically westerly winds in southern Germany, it is thus assumed that the observed enhancement in the NO_2 DSCDs originates from NO_x emissions from Nördlingen.

No pronounced maximum in the spatial distribution is found for the HCHO DSCDs. However, a gradient from $\sim 1.2 \times 10^{16}$ molecules cm^{-2} at an azimuth angle of 247° to $\sim 1.4 \times 10^{16}$ molecules cm^{-2} at 7° can be delineated in the average data. This gradient is most pronounced in the data from November with a gradient of about 0.75×10^{16} molecules cm^{-2} from 247° to 7°.

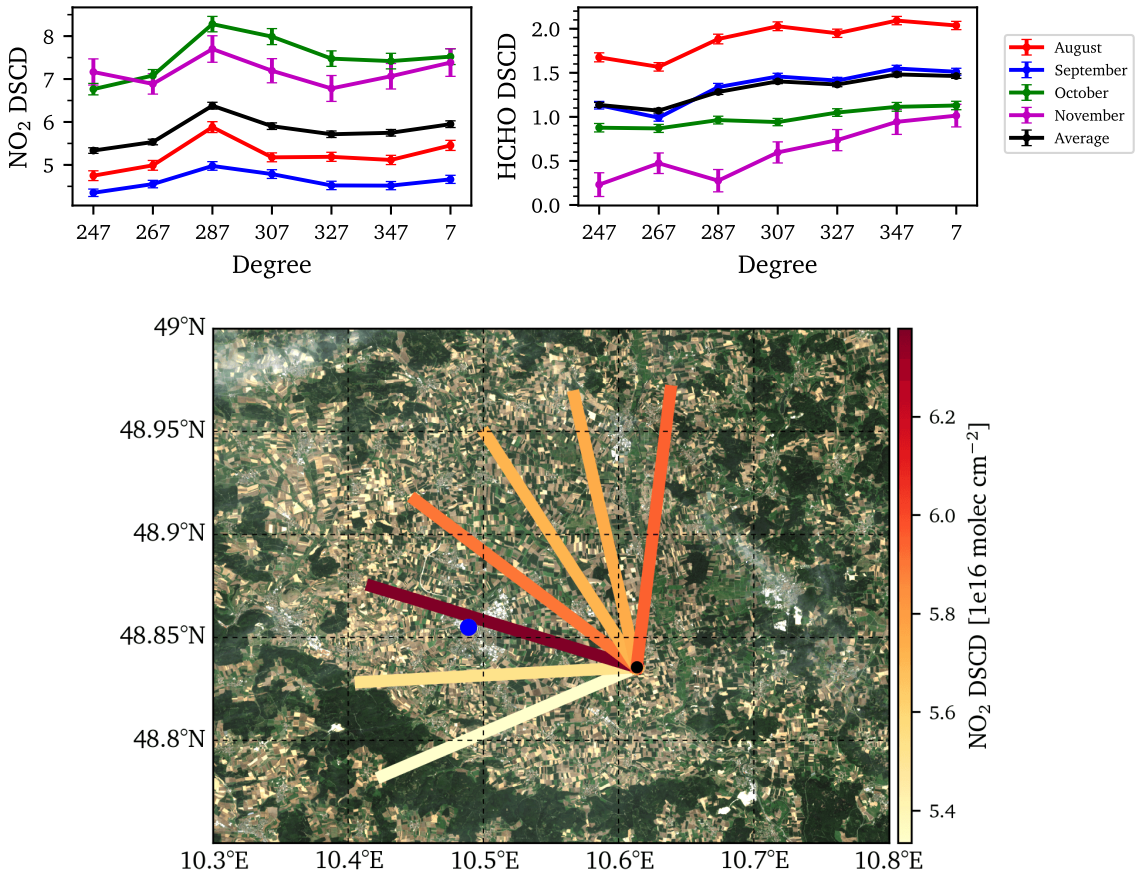

Figure 5.21: Top panels: NO_2 and HCHO DSCDs [1×10^{16} molecules cm^{-2}] of the azimuth scanning mode from the mini MAX-DOAS at the castle station grouped for different months. Shown are NO_2 DSCDs at 1° elevation at 8 defined azimuth directions: 247°, 267°, 287°, 307°, 327°, 347° and 7°. Error bars represent the standard error of the mean. Lower panel: Map of average NO_2 DSCDs (black line in the upper graph) for different azimuth positions. Different coloured lines represent the NO_2 DSCD whereby the length of the line is for illustrative purposes set to 15 km. The city of Nördlingen is marked in blue.

5.6.5 Temporal patterns of trace gas levels

In the following sections diurnal, weekly and monthly variations in NO_2 and HCHO near-surface VMRs are presented and compared among several instrument types: the mini MAX-DOAS instrument, the LP-DOAS and the LfU air quality monitoring station.

Such temporal variations in trace gas levels can provide information on the temporal variation in source emissions, secondary formation and removal processes. Anthropogenic

emissions of NO_2 and HCHO (mostly traffic-induced) can thereby significantly impact ambient trace gas levels. As anthropogenic activity and related emissions are usually strongest during the working week and can also show diurnal patterns, differences in trace gas VMRs between data for the working week and weekend can give information about the contribution of anthropogenic emissions to total emissions.

Additionally, near-surface concentrations of NO_2 and HCHO also depend on the height of the atmospheric boundary layer (BL) (in which trace gases are typically well mixed). Due to a decrease of the BL height at colder temperatures, i.e. at night and during winter, a compression of the air leads to a subsequent increase of trace gas VMRs close to the surface. The expansion of the BL at warmer temperatures thus leads to an expansion of air and a decrease of the VMRs.

5.6.5.1 Diurnal cycle

Fig. 5.22 presents NO_2 VMRs derived from the mini MAX-DOAS instruments at the castle and barn stations (from the lowest model layer of 0 to 200 m) as well as NO_2 VMRs from the LP-DOAS and LfU air quality monitoring station.

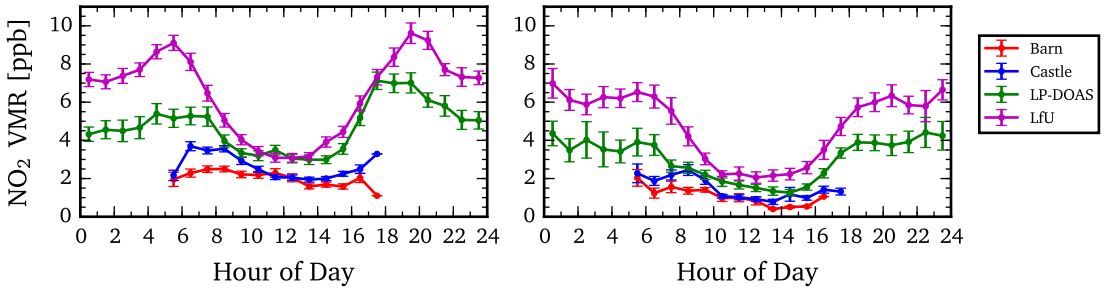

Figure 5.22: Diurnal cycle of NO_2 VMRs as observed by the two mini MAX-DOAS instruments (at the barn and castle station), the LP-DOAS and the air quality monitoring station from the LfU during the working week (left panel) and on weekends (right panel) in August and September 2014.

Because of the different measurement techniques as well as measurement locations, it could be expected that the instruments may observe different diurnal cycles of the VMRs. In general, the air quality station observed highest NO_2 VMRs with a very pronounced diurnal cycle showing highest values in the morning at 6 a.m. and evening at 8 p.m. and lowest values during midday. The LP-DOAS observed a similar diurnal cycle, however the magnitude is smaller and the peak in the evening is higher compared to the one in the morning. Another striking feature is that the night-time NO_2 VMRs are generally higher than the day-time VMRs. This is most likely due to, on the one hand, the variation in the BL height as explained above and, on the other hand, due to removal processes of NO_2 during the day, e.g. by OH or photolysis. The mini MAX-DOAS observations underestimate the near-surface NO_2 concentrations during the day by about 1–2 ppb. This is mainly because the MAX-DOAS VMRs are estimates for the first 200 m, in contrast to the close to the surface measurements of the LP-DOAS and LfU station. However, all

instruments are able to observe the diminished NO_2 mixing ratios on the weekend (right panel of Fig. 5.22) due to the lower anthropogenic contribution.

The diurnal cycles of HCHO (Fig. 5.23) show a peak in the afternoon, which is presumably originating mainly from biogenic emissions of VOCs and not from direct anthropogenic emission sources (e.g. as the diurnal cycle in traffic is expected to show highest activity in the morning and evening). The night-time observations from the LP-DOAS also indicate that HCHO levels are lower at night-time despite the lower BL height.

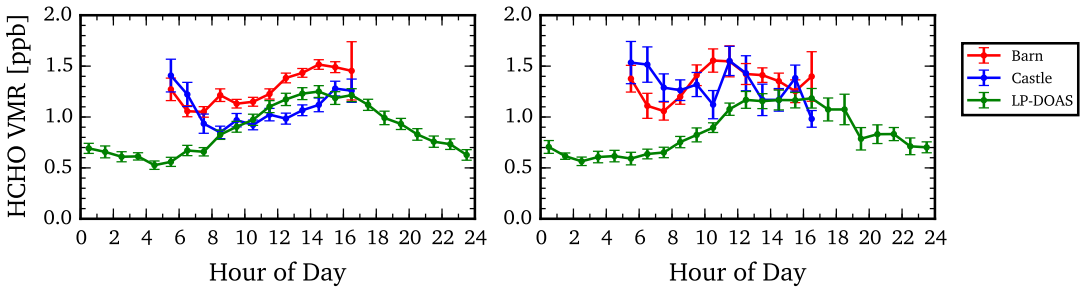

Figure 5.23: Diurnal cycle of HCHO VMRs from the four instruments during the working week (left panel) and on weekends (right panel) in August and September 2014.

The data for the average week day from the mini MAX-DOAS instruments compares well with the data from the LP-DOAS by showing the steady increase from 8 a.m. to about 4 p.m. However, HCHO VMRs from the mini MAX-DOAS instrument show enhanced values in the morning contrarily to the measurements of the LP-DOAS. The comparatively large standard errors of the mean values indicate that these enhanced values in the morning should be interpreted with care. A possible explanation could also be difficulties in the spectral retrieval at large SZAs due to the interfering stratospheric ozone absorption.

In general, higher HCHO VMRs are observed by the mini MAX-DOAS instruments which may give rise to the assumption that HCHO is not directly emitted from the surface but created via secondary formation processes from VOCs (which are emitted from the surface). This would also explain that the maximum in HCHO is located at higher altitude and not near the surface.

The diurnal cycles in HCHO VMRs on the weekend are similar to the working week indicating no dominant anthropogenic sources. The rather high scatter in HCHO VMRs from the mini MAX-DOAS observations originate from the lower signal-to-noise ratio of the measurements (compared to the LP-DOAS) and the relatively small amount of data which is averaged.

5.6.5.2 Weekly cycle

The weekly cycle (Fig. 5.24) reflects a characteristic reduction of NO_2 on the weekend, due to less anthropogenic emissions of NO_x (primarily from traffic), and is most pronounced on Sundays. Again, the NO_2 VMRs from the barn and castle stations are consistently lower compared to the other instruments, but generally agree well in the weekly cycle.

For the mini MAX-DOAS instruments, the difference between the NO_2 VMRs during the week and on the weekend is about 0.5–1 ppb. For the other instruments this difference is slightly higher and amounts to 1 to 1.5 ppb.

In contrast to the results for NO_2 no reduction on the weekend is found for the HCHO VMRs indicating the absence of a significant direct anthropogenic source.

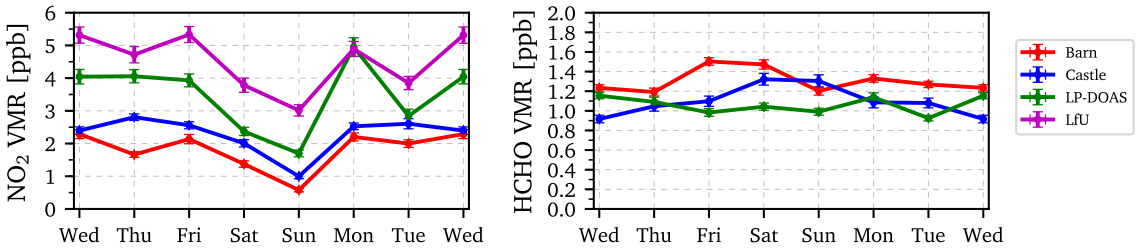

Figure 5.24: Weekly cycle of NO_2 and HCHO VMRs from the four instruments during the working week (left panel) and on weekends (right panel) in August and September 2014.

5.6.5.3 Seasonal variation

Monthly averages (Fig. 5.25) from the four instruments for the year 2014 show a typical seasonality in NO_2 and HCHO near-surface VMRs which is mainly governed by photochemistry (for NO_2 and HCHO) and biogenic emissions (for HCHO).

Subsequently, lowest NO_2 VMRs are found in summer-time and highest during winter. This seasonal pattern is observed by all three instrument types despite the different measurement techniques, location within the Ries plain and temporal-sampling of data (within a month).

Generally, only small differences are observed among the 4 stations ($\sim$ 1–2 ppb), however, in November larger differences arise between the mini MAX-DOAS instruments and the two other instruments ($\sim$ 3–4 ppb). One explanation for this discrepancy could be strong surface emissions of NO_x which stay close to the surface and are not well mixed up to higher altitudes (to which the mini MAX-DOAS instruments are more sensitive).

The long-term time series of HCHO VMRs for the year 2014 also shows a distinct seasonal variation, which is, however, not as pronounced as the one for NO_2. In July highest HCHO VMRs are observed by both mini MAX-MAX DOAS instruments. Lowest levels are detected in October and November (the extraordinarily high values for the castle station suffer from larger measurement errors and fewer observations which are averaged and should be interpreted with care).

In summary, all three instrument types agree well in capturing not only the seasonal cycles of NO_2 and HCHO but also the diurnal and weekly cycle of the species which further confirms the validity of the measurements.

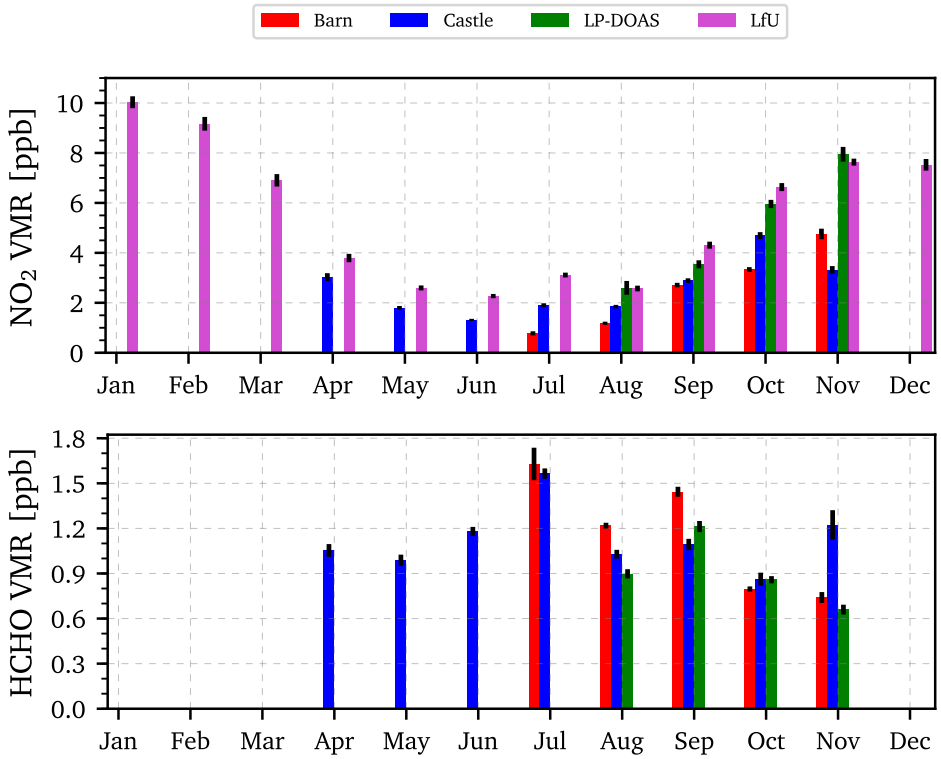

Figure 5.25: Monthly averages of NO_2 VMRs (top panel) and HCHO VMRs (bottom panel) from the four instruments for each month in the year 2014.

5.6.6 Trace gas VMRs under different sky conditions

As discussed above, MAX-DOAS measurements and the profile retrieval of trace gases can be substantially influenced by present cloud conditions and aerosol loads in the atmosphere. The applied cloud classification facilitates the examination of potential biases arising from such effects in the resulting trace gas VMRs.

In general, a change in cloud cover, or light conditions under high aerosol load, also goes along with associated variations in the observed global radiation and air temperature which both may affect the lifetimes of trace gases and partitioning for NO_2.

In order to investigate the impact on different cloud conditions on trace gas VMRs, Fig 5.26 presents the dependence of near-surface HCHO and NO_2 VMRs on the sky condition in the upper panels and the dependence of air temperature and global radiation as observed by the in-field station to the different sky conditions in the lower panels. Thereby, the cloud classification derived from the mini MAX-DOAS instrument at the barn station is also applied to collocated data from the LP-DOAS. Furthermore, the same classification is also applied to the data from the LfU air quality monitoring station under the assumption that the sky condition is fairly homogeneous within the Ries plain.

It is found that the mean HCHO VMRs, derived from the MAX-DOAS measurement, show no consistent dependence on the sky condition. Yet, at the times of clear sky with low aerosol optical depths (AODs) the mini MAX-DOAS instruments at the barn station

observes generally higher VMRs (about +0.5 ppb) compared to the station at the castle. This effect, however, should not be related to the sky condition but to the generally higher HCHO concentration in the vicinity of the barn station. In contrast, the measurements taken by the LP-DOAS show a mean reduction in HCHO VMRs in cases of broken and continuous clouds compared to the other categories. The maximum decrease of about -0.8 ppb is found for continuously cloudy scenes compared to clear sky with low AOD. This reduction could be explained by the lower global radiation and air temperature during cloudy skies and days (lower panels of Fig. 5.26) which potentially leads to fewer biogenic precursor emissions (VOCs) of HCHO.

For near-surface VMRs of NO_2, a consistent increase is found for observations from the two mini MAX-DOAS instruments at the times of continuous clouds compared to the other categories (about +1–1.8 ppb). The measurements from the LP-DOAS and also from the air quality monitoring station (LfU) compare well, indicating that the assumption on similar sky conditions between the two stations holds true. The measurements show a slight increase for completely cloudy situations. Thereby, a similar positive gradient in the NO_2 VMRs from the categories 'cloud holes' to 'broken clouds' and 'continuous clouds' is found for all 4 instruments. Discrepancies, however, arise in the observed NO_2 VMRs in case of clear sky. In these cases, the LP-DOAS and LfU station observe about 2–2.5 times as much NO_2 as the mini MAX-DOAS instruments.

Comparing these results to the ambient temperature and global radiation leads to three main conclusions; first, the reduction in visibility and temperature during clear sky with high AODs shows no impact on neither the mini MAX-DOAS estimates on NO_2 VMRs, nor the LP-DOAS and LfU station measurements. Second, the increase of NO_2 VMRs with increasing cloud coverage can either be associated with longer lifetimes of NO_2 (and a higher Leighton ratio) as consequence of the lower global radiation and air temperature or, in the case for the mini MAX-DOAS observations, originate from longer light paths below the clouds and subsequent NO_2 absorption. Third, based on these findings neither of these two potential sources can be definitely allocated to the enhancement during cloudy situations as it is probably a mixture of both. However, these results indicate that measurements taken under different sky conditions can significantly impact the retrieved NO_2 VMRs (and to a lesser extent also for HCHO).

5.6.7 Dependence of near-surface trace gas VMRs on wind

Knowledge on the horizontal movement of the sampled air masses is valuable to determine whether the measured concentrations of trace gases originate from local sources or were transported into the vicinity of the instruments. In this campaign, wind speed and direction were continuously recorded by the in-field weather station near the barn location (and also by the DWD station in Harburg which, however, showed systematically different wind directions). Under the assumption that the in-field weather station is representative for the Ries and the wind field is fairly homogeneous within the Ries plain, these measurements permit the separation of the near-surface trace gas VMRs from the 4

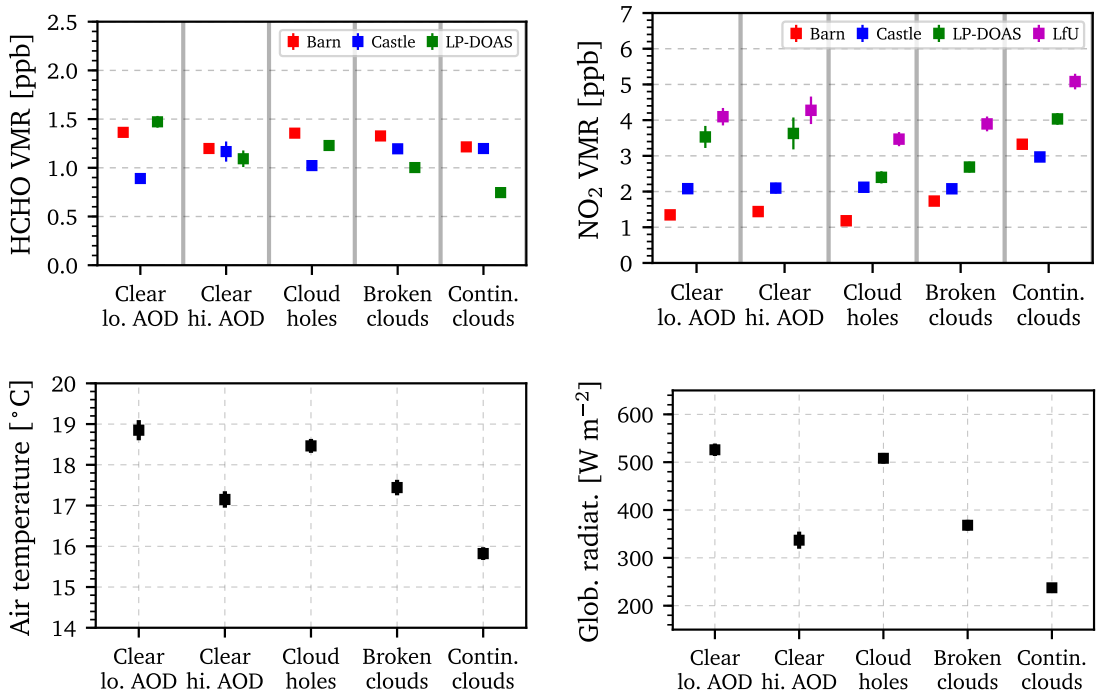

Figure 5.26: Upper panels: near-surface NO_2 and HCHO VMRs from the mini MAX-DOAS at the barn (red) and castle (blue) stations and from the LP-DOAS (green) separated for different sky conditions. Lower panels: Air temperature and global radiation (from the in-field weather station at the barn station) during different sky conditions.

instruments for low and high wind speeds as well as for different wind directions.

Fig. 5.27 depicts average NO_2 and HCHO VMRs during different wind conditions on a polar diagram whereby each angle represents the direction from which the wind was blowing, e.g. 270° represents wind from westerly direction.

It is found that HCHO VMRs are generally independent from the wind direction at low wind speeds ($< 3\,\mathrm{m\,s^{-1}}$) as observed by both, the mini MAX-DOAS instruments and the LP-DOAS. This indicates that no local, strong HCHO emission source is present but HCHO is rather homogeneously distributed. At higher wind speeds ($> 3\,\mathrm{m\,s^{-1}}$), the LP-DOAS detects relatively low VMRs (~ 0.6 ppb) when the wind comes from the west and higher VMRs (~ 1.2 ppb) when the wind comes from the east. The mini MAX-DOAS instrument at the barn station shows slightly enhanced HCHO VMRs when the wind is coming from the North (~ 0.3–0.6 ppb) compared to southerly winds. However, the mini MAX-DOAS instrument at the castle station observes higher HCHO VMRs when the wind is coming from the east and the west (~ 0.3 ppb) compared to northerly and southerly winds. Thus, no common dominant source direction for HCHO at higher wind speeds is found for the different instrument.

In contrast, the NO_2 VMRs show a very pronounced dependence on ambient wind conditions. At low wind speeds, highest NO_2 VMRs are observed by the LfU station for easterly winds (Öttingen) and lowest VMRs are found for winds coming from the open fields, i.e. south-west. Also at low wind speeds, the LP-DOAS observes highest NO_2

VMRs from the north-east which corresponds to the main street 'B25' and also higher NO_2 VMRs from the east (Nördlingen). The NO_2 VMRs derived from the mini MAX-DOAS instrument at the barn station thereby also show enhanced values for easterly winds.

At high wind speeds all instruments agree in their observation of very high NO_2 VMRs (about 9 ppb for the LfU station and LP-DOAS and 3.5–4.5 ppb for the mini MAX-DOAS instruments) when the wind is blowing from south-easterly direction (and very low VMRs from the other directions). This systematic pattern across all stations hints at a common source further away from the measurement stations. Assuming a NO_2 lifetime of about 4 hours (in summer) and a wind speed of $3\,\mathrm{m\,s^{-1}}$ suggests that this strong emission source is located within a distance of up to 43 km in south-westerly direction. Increased industrial activity is found around the city of Donauwörth (to the south-east of the Ries) where a large cogeneration plant ($\geq$ 50 MW) as well as two further power plants (0.1–50 MW and 20–50MW) are in the vicinity.[10] However, as the dominant wind direction in the Ries is from the west (Fig. 5.17) and south-easterly winds only a have share of about 9 %, the inflow of polluted air from Donauwörth has a minor impact on average NO_2 VMRs in the Ries throughout the year. Still, this potential bias has to be considered in the conclusions and measurements taken during strong winds from the south-east should be regarded with care.

The good agreement of the instruments, in this respect, affirms the validity and quality of the individual measurements. Moreover, the wind data captured by the in-field weather station could be applied to all measurement stations implying fairly homogeneous wind fields within the Ries.

[10] Bayerisches Staatsministerium für Wirtschaft und Medien, Energie und Technologie; data available at: http://geoportal.bayern.de/energieatlas-karten

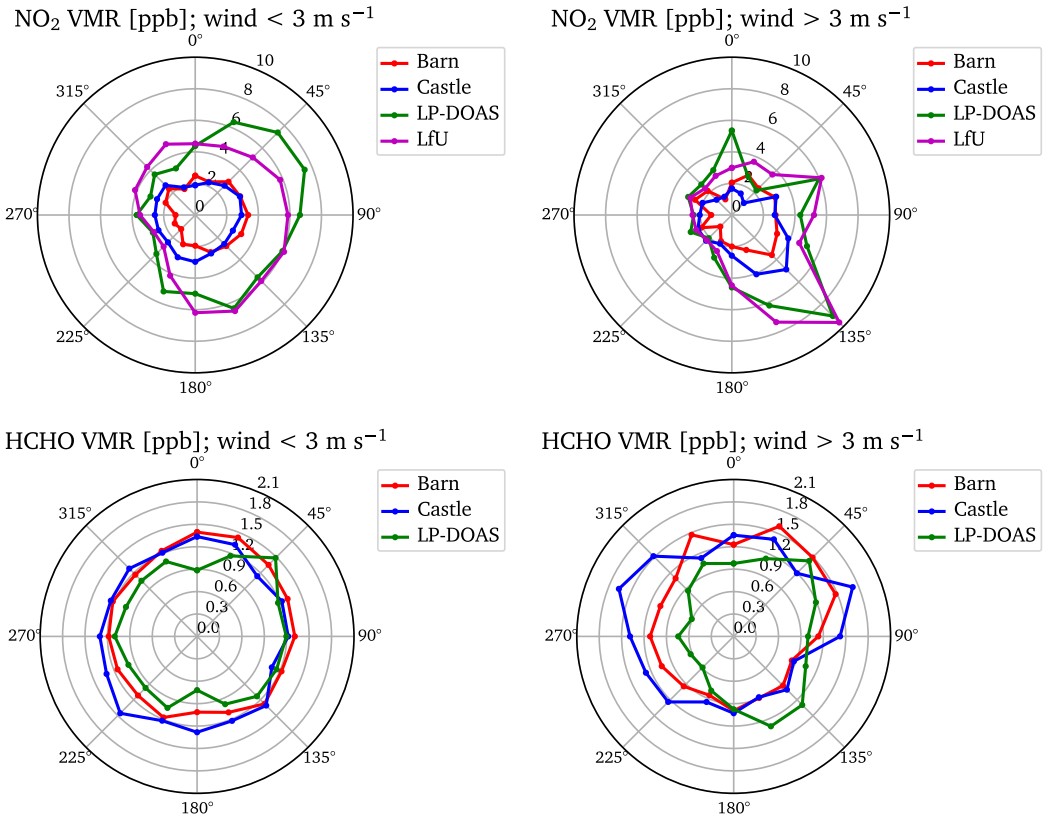

Figure 5.27: Near-surface NO_2 and HCHO VMRs from the 4 instruments (mini MAX-DOAS instruments at the barn and castle station, LP-DOAS and LfU air quality monitoring station) filtered for low wind conditions ($< 1\,m\,s^{-1}$) and windy conditions ($> 1\,m\,s^{-1}$).

5.6.8 Multiple regression analysis: trace gas VMRs and environmental parameters

In order to identify the environmental parameters that govern the near-surface NO_2 and HCHO VMRs, a basic multiple linear regression analysis is conducted. Thereby, the relatively long time-series allows for an analysis of daily-averaged parameters. This is particularly useful to diminish the effect of the diurnal cycle. These daily averages are calculated for the time period between 10:00UTC and 14:00 UTC. The explanatory variables are standardized so that the time series for each variable has a mean of 0 and a standard deviation of 1. This enables a direct comparison of the effect of each parameter in the final regression model. The following explanatory variables are used in the regression model:

weekvar A binary variable indicating whether the day is within the working week (0) or is a Sunday (1).

globrad Global radiation as measured by the in-field weather station at the barn station.

cloudy A variable indicating the dominating sky-condition for each day. It ranges from 0 (clear sky) to 1 (cloud covered). All observations from the cloud classification are

averaged whereby *clear sky with low AOD* and *clear sky with high AOD* correspond to 0 and all other categories correspond to 1.

airtemp, soiltemp, relhum and soilmoist Air temperature (airtemp), soil temperature (soiltemp), relative humidity (relhum) as well as the soil moisture content (soilmoist) are taken from the DWD station in Reimlingen.

windspeed and winddir_x The data on wind speed (windspeed) and wind direction are taken from the in-field weather station located at the barn station. The data on wind direction is split into quadrants of equal size, i.e. for the northeast (0°–90°, winddir_ne), southeast (90°–180°, winddir_se), southwest (180°–270°, winddir_sw) northwest (270°–360°winddir_nw). For each day, the fraction of the specific wind direction is calculated, i.e. a value between 0 and 1 is given to each quadrant.

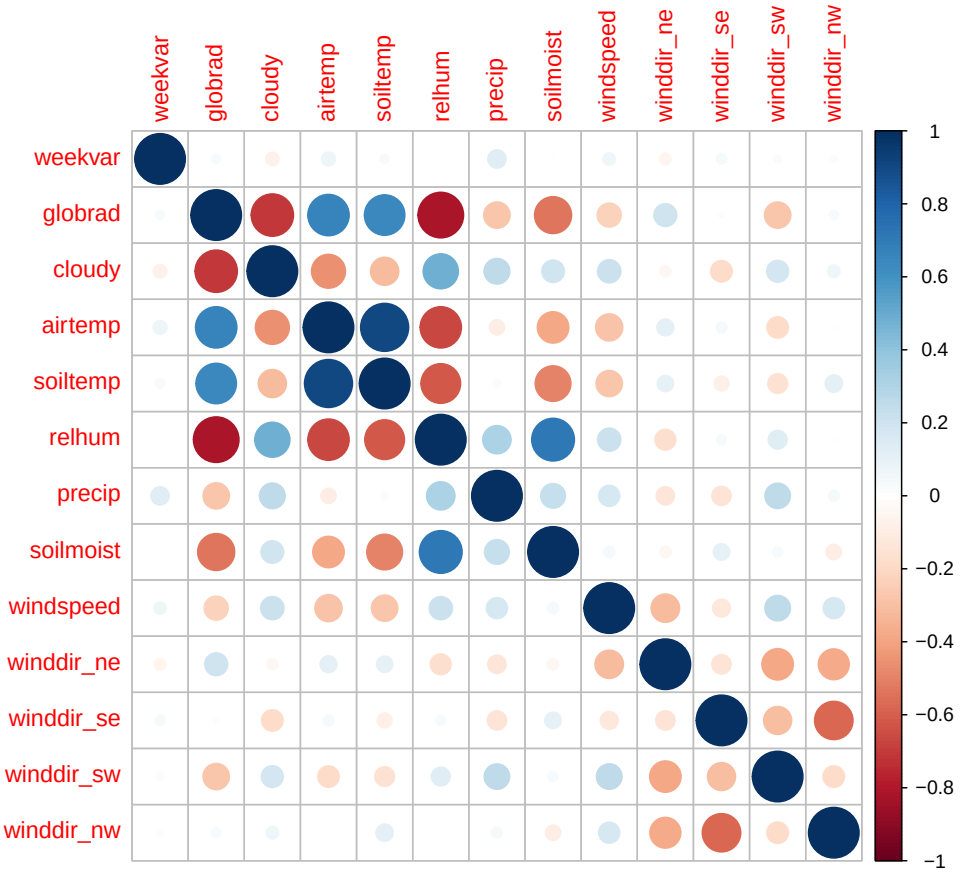

Figure 5.28: Correlation matrix of the environmental parameters chosen in Section 5.6.8 whereby the colour and size of each point represents the correlation coefficient.

The diagram in Fig. 5.28 presents an overview of the correlation between the predictor variables. A more detailed representation of the correlation matrix is provided in Fig. 5.29. It can be seen that most natural parameters are highly correlated, e.g. the global radiation

correlates well with the sky condition and the relative humidity. This is also known as *collinearity* (or: *multicollinearity* between two or more variables) and adversely affects the outcome of a multiple regression analysis. Collinearity does not reduce the overall validity of the regression analysis, but the individual importance of each predictor variable may be not captured accurately due to their redundancy. However, ignoring collinearity has a wide range of negative influences on the regression model, for example, it increases the standard errors of the coefficients, it may lead to models with high R^2 although no predictor variable is statistically significant, or it may lead to parameters with an incorrect magnitude or a reversed sign (e.g. Greene, 2003; Belsley et al., 2005; O'brien, 2007).

One possible measure for collinearity is the variance inflation factor (VIF). It quantifies how much the variance of a particular regression coefficient is increased due to the effect of collinearity. For instance, a VIF of 10 implies that the standard errors are ten times larger compared to a model without collinearity. VIF values between 5 to 10 are typically used as a threshold to discard redundant variables, but the exact criteria are debated (e.g. O'brien, 2007) and the removal of variables may not necessarily benefit the regression analysis.

In this work, however, it is known that some predictor variables are directly related to others. Therefore, an iterative approach is chosen to remove such variables whereby the one with the highest VIF is removed in each step until no VIF exceeds a threshold of 5 any more. Using this scheme, the variable for the air temperature (airtemp) was removed in the first step and the variable for global radiation (globrad) in the second step.

Furthermore, a multiple regression model is preferred which incorporates a concise set of predictor variables to explain the NO_2 and HCHO VMRs as unnecessary variables would add noise to the regression model otherwise.

Many different approaches for the identification of the optimal set of independent variables exist, such as, step-wise algorithms or determining the best model based on specific information criteria. Thereby, the R^2 may not be an optimal choice because, among others, each additional predictor variable leads to an increase of the R^2 and a high R^2 may be simply due to an "overfit" of the model, i.e. modelling random noise.

Here, all possible combinations of the above described variables are compared against each other in an automated routine (Calcagno and de Mazancourt, 2010). The ranking of the models is done using the Akaike information criterion (AIC) (Akaike, 1973, 1974), whereby the model with the minimum AIC value is chosen as optimum. This algorithm is based on information theory and aims at finding a balance between the goodness of fit and the complexity of the regression model.

Tables 5.4 and 5.5 present the results for the best multiple regression models found for the near-surface NO_2 and HCHO VMRs, respectively.

The R^2 of the models for NO_2 are 0.469 for the LfU station, 0.548 for the LP-DOAS, 0.566 for the castle station and 0.735 for the barn station. This indicates that much (and even more than half) of the variance in the near-surface VMRs can be explained by the chosen model parameters.

In specific, the reduction in near-surface VMRs on Sundays is observed at all stations and is significant for the MAX-DOAS at the castle station with a p-value < 0.01 and for the

others with a p-value < 0.05.

Contrariwise, cloudy conditions lead to higher NO_2 VMRs as observed by the MAX-DOAS instruments. The lower VMRs observed at the LfU station (with a p-value < 0.1) suggests that this effect might be caused by the change in light conditions (i.e. lower photolysis rate of NO_2). Interestingly, the enhancement caused by cloudy skies can outweigh the reduction in NO_2 VMRs on Sundays.

The regression analysis indicates that winds from south-easterly direction lead to an increase in the observed NO_2 VMRs at all measurement stations (also compare Fig. 5.27). Furthermore, high wind speeds reduce the observed NO_2 VMRs at the LP-DOAS and LfU station, i.e. advection of polluted air away from the measurement station. It assumed that this effect is not captured by the MAX-DOAS instrument due to their lower sensitivity to the near-surface air (wind speed is recorded at 2 m altitude).

The soil temperature acts as a significant predictor variable that is shared by all four models. Thereby higher temperatures generally lead to a decrease in NO_2 VMRs (warm conditions with higher insolation are associated with a shorter lifetime of NO_2). The models suggest that this is the dominant parameter in explaining the variation in NO_2 VMRs (without considering anthropogenic emissions). Conversely, higher relative humidity (which correlates with lower global radiation and temperatures) therefore favours an increase in the lifetime of NO_2 and, consequently, higher VMRs are observed by the MAX-DOAS at the barn station, the LP-DOAS and the LfU station. For the castle station, this effect is presumably expressed through the soil moisture (which increases at high humidity and low temperatures).

In sum, the observed NO_2 VMRs in the Ries are mainly governed by (i) the temperature, (ii) the sky condition, (iii) the wind speed and direction as well as by anthropogenic emissions. The uncertainty in the latter may be, to a large extent, responsible for the remaining unexplained variance in the regression models.

The regression analysis for HCHO indicates that the soil temperature (which is representative for the air temperature) is the most important factor governing the observed near-surface VMRs. Higher temperatures thereby lead to a significant enhancement in HCHO VMRs for all three stations. This is presumably due to increased biogenic emissions (mainly from vegetation) provoked by higher temperatures.

For the other parameters, however, the results of the regression analysis diverge and are more difficult to interpret. Therefore, only the parameters which show the largest impact on the regression model are stated. For the castle station, cloudy skies apparently lead to an increase in HCHO VMRs (which is not found for the barn station). Furthermore, cloudy conditions as well as precipitation lead to a significant decrease of near-surface HCHO VMRs as observed by the LP-DOAS. This suggests that the observed enhancement by the mini MAX-DOAS at the castle station may originate from measurement errors under cloudy conditions.

Interestingly, higher soil moisture contents favour higher HCHO VMRs as observed by the LP-DOAS. However, this effect is not observed by the MAX-DOAS instrument and it is, thus, difficult to interpret whether higher soil moisture leads to stronger biogenic

emissions. Both instruments, the mini MAX-DOAS at the barn station and the LP-DOAS show higher HCHO VMRs when the wind is coming from easterly directions (which corresponds to the B25 roadway and the city of Nördlingen).

In order to check whether there is a temporal lag between the environmental parameters and the observed near-surface NO_2 and HCHO VMRs, the data for NO_2 and HCHO is shifted by one day in either direction (Appendix B). The R^2 of the respective regression models decreased, but, based on this simple test, no further conclusions on the relationship between the parameters could be drawn.

Table 5.4: Multiple regression analysis of near-surface NO_2 VMRs from the four instruments against several environmental parameters. The independent variables as well as their selection process are explained in Section 5.6.8.

	Dependent variable:			
	NO_2			
	Castle	Barn	LP-DOAS	LfU
weekvar	-0.332^{***}	-0.297^{**}	-0.558^{**}	-0.337^{**}
	(0.110)	(0.139)	(0.259)	(0.152)
cloudy	0.524^{***}	0.695^{***}		0.304^{*}
	(0.119)	(0.159)		(0.179)
soiltemp	-0.811^{***}	-0.985^{***}	-1.054^{***}	-0.555^{***}
	(0.129)	(0.173)	(0.312)	(0.197)
soilmoist	0.352^{***}			
	(0.125)			
relhum		0.453^{**}	0.578^{*}	0.607^{***}
		(0.196)	(0.286)	(0.211)
windspeed			-0.750^{**}	-0.355^{**}
			(0.288)	(0.169)
winddir_ne				0.559^{***}
				(0.164)
winddir_se	0.489^{***}	0.630^{***}	1.200^{***}	1.042^{***}
	(0.113)	(0.140)	(0.266)	(0.160)
Constant	2.213^{***}	2.501^{***}	4.276^{***}	3.381^{***}
	(0.108)	(0.135)	(0.252)	(0.150)
Observations	140	74	48	146
R^2	0.566	0.735	0.596	0.469
Adjusted R^2	0.550	0.716	0.548	0.443
Residual Std. Error	1.281 (df = 134)	1.161 (df = 68)	1.743 (df = 42)	1.815 (df = 138)
F Statistic	35.016^{***} (df = 5; 134)	37.747^{***} (df = 5; 68)	12.379^{***} (df = 5; 42)	17.444^{***} (df = 7; 138)

Note: $^{**}p<0.05$; $^{***}p<0.01$
Standard deviation of the estimate in brackets.
All independent variables are standardized.

Table 5.5: Multiple regression analysis of near-surface HCHO VMRs from the four instruments against several environmental parameters. The independent variables as well as their selection process are explained in Section 5.6.8.

	Dependent variable:		
	HCHO		
	Castle	Barn	LP-DOAS
cloudy	0.198^{***}		-0.126^{***}
	(0.039)		(0.041)
soiltemp	0.284^{***}	0.242^{***}	0.344^{***}
	(0.039)	(0.036)	(0.044)
precip	0.069^{*}		-0.179^{***}
	(0.038)		(0.042)
winddir_sw	-0.090^{**}		
	(0.038)		
soilmoist			0.119^{**}
			(0.045)
winddir_ne		0.138^{***}	0.110^{***}
		(0.036)	(0.040)
winddir_se			0.116^{***}
			(0.040)
Constant	1.151^{***}	1.153^{***}	1.064^{***}
	(0.036)	(0.036)	(0.039)
Observations	136	71	49
R^2	0.373	0.469	0.746
Adjusted R^2	0.354	0.453	0.709
Residual Std. Error	0.416 (df = 131)	0.300 (df = 68)	0.270 (df = 42)
F Statistic	19.492^{***} (df = 4; 131)	30.000^{***} (df = 2; 68)	20.521^{***} (df = 6; 42)

Note: **p<0.05; ***p<0.01
Standard deviation of the estimate in brackets.
All independent variables are standardized.

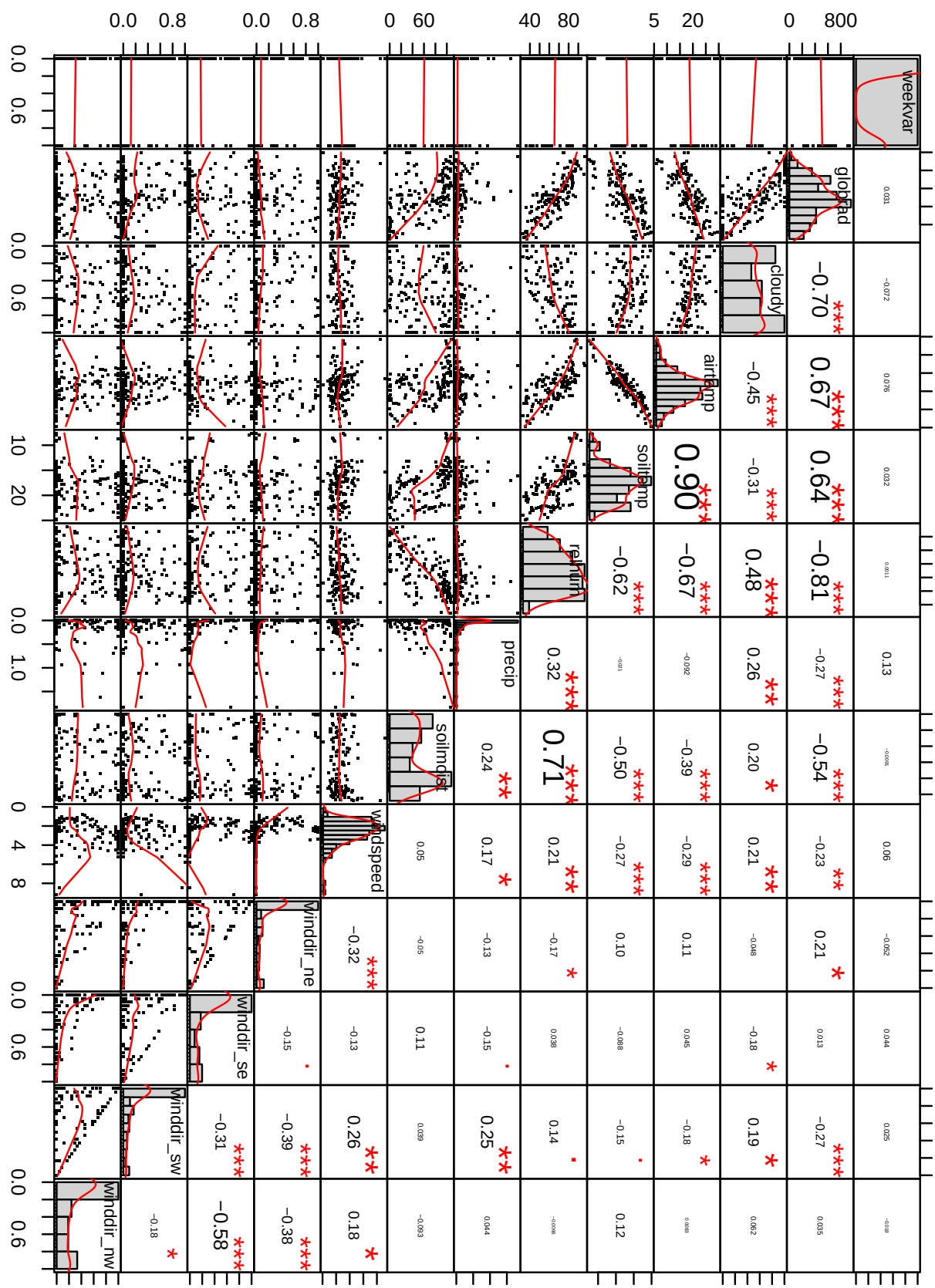

Figure 5.29: Detailed correlation matrix of the environmental parameters chosen in Section 5.6.8. The diagonal panels illustrate the distribution of each variable. The lower left panels (below the diagonal) show the bivariate scatter plots. The upper right panels (above the diagonal) show the correlation coefficient including the level of significance:: p-values(0, 0.001, 0.01, 0.05, 0.1, 1) correspond to the symbols("***", "**", "*", ".", " ").

5.6.9 Impact of sudden enhancements in soil moisture

The focus of this section is on the investigation whether temporal correlations between sudden enhancements in the soil moisture content and near-surface VMRs of trace gases can be detected. Rapid increases in soil moisture after dry conditions presumably lead to beneficial conditions provoking soil emissions of trace gases such as NO_x. Within the framework of this measurement campaign it is, however, not possible to allocate the observed trace gas VMRs to a single source. Yet, upper limits for soil emissions can be deduced when enhanced trace gas VMRs follow spikes in soil moisture.

In a first step, time series of several environmental parameters as well as trace gases for the entire measurement campaign are studied on a daily basis to identify days showing a rapid increase in soil moisture after dry conditions. In a second step, these days are then inspected in more detail to explore whether trace gas VMRs show elevated levels shortly after.

5.6.9.1 Daily environmental parameters and trace gases

Fig. 5.30 presents the time-series for several environmental data, trace gases as well as AE and $PM_{2.5}$ for the entire measurement campaign in 2014. In the following, each parameter is briefly described:

Soil Moisture. Information on the soil moisture content within the Ries was provided, on the one hand, by a sensor attached to the in-field weather stations next to the barn station and, on the other hand, by calculated daily estimates from the DWD for the station in Reimlingen. For the latter station, the average field capacity at 5 cm depth is provided by the DWD. Unfortunately, due to problems with the calibration of the soil moisture sensor at the in-field weather station only the raw data [in mV] (with a 10 min temporal resolution) is presented in Fig. 5.30. Although the absolute values of the different measured parameters differ, the relative variations correlate well and sudden enhancements in soil moisture (from very low to very high values) are captured well by both data sets. Two days can be identified during the measurement campaign that experienced several days of very low soil moisture content followed by a rapid enhancement, i.e. April 27th and June 29th. However, from July to the end of the campaign, no days with very low soil moisture contents (with an average field capacity of close to 0) are observed.

Precipitation. The precipitation data (1-hourly sums) presented in Fig. 5.30 was derived from the DWD Radolan product providing radar-based gridded estimates on precipitation for the entire Ries. As precipitation is the dominant source for the water content of soils, both data sets agree well. Subsequently, very strong precipitation events (> 2 mm per hour) lead to significant increases in the soil moisture content. The data also shows that during summer, the soil dries out more quickly (due to higher temperatures) compared to months with lower temperature.

NO_2 VMRs. In Fig. 5.30, the NO_2 VMRs are presented as midday averages (8–14UTC) which enables the study of day-to-day variations in NO_2. It is expected that precipitation events that induce significant increases in soil moisture also lead to further cloud coverage around the time of the precipitation. Thus, the NO_2 data is only screened for foggy observations but no distinction is made for different cloud types. Otherwise, almost no data would be available around the time of the wetting of the soils. The NO_2 VMRs show the same seasonal variation as already presented in Fig. 5.25. Although the data from the four instruments show good agreement on the seasonal scale, they differ in their measurements on individual days sometimes by several ppb. In general, higher variability in NO_2 VMRs is found in colder months whereas low variability is observed during summer. Thereby, several particular days (one at the end of April, one at the beginning of July and one in the middle of August) exhibit remarkably high NO_2 VMRs. The first two of these days match the times of a steep increase in soil moisture and are thus investigated in detail in the following sections.

HCHO VMRs. For HCHO, only data from the DOAS-type instruments is available which shows a high day-to-day variability (also based on midday averages). Highest near-surface HCHO VMRs were observed by the mini MAX-DOAS at the castle station in July and August with about 3.2–3.4 ppb. These days with highest HCHO correspond also to the two warmest days of the year as recorded by the weather stations.

Aerosol extinction and $PM_{2.5}$. Similar to NO_2 VMRs, the midday aerosol extinction (from the mini MAX-DOAS instruments) and $PM_{2.5}$ concentrations (from the LfU station) are highest in winter and lowest in summer. Thereby, the day-to-day variability is also lowest in the summer.

Air and soil temperatures. For the air and soil temperatures, midday averages are presented. The air and soil temperatures from the weather station agree well with the soil temperature from the DWD station. Both show that the warmest days of the year were in July (with 2 days having a midday temperature about 32 °C) and in August (2 days having a midday temperature about 29 °C).

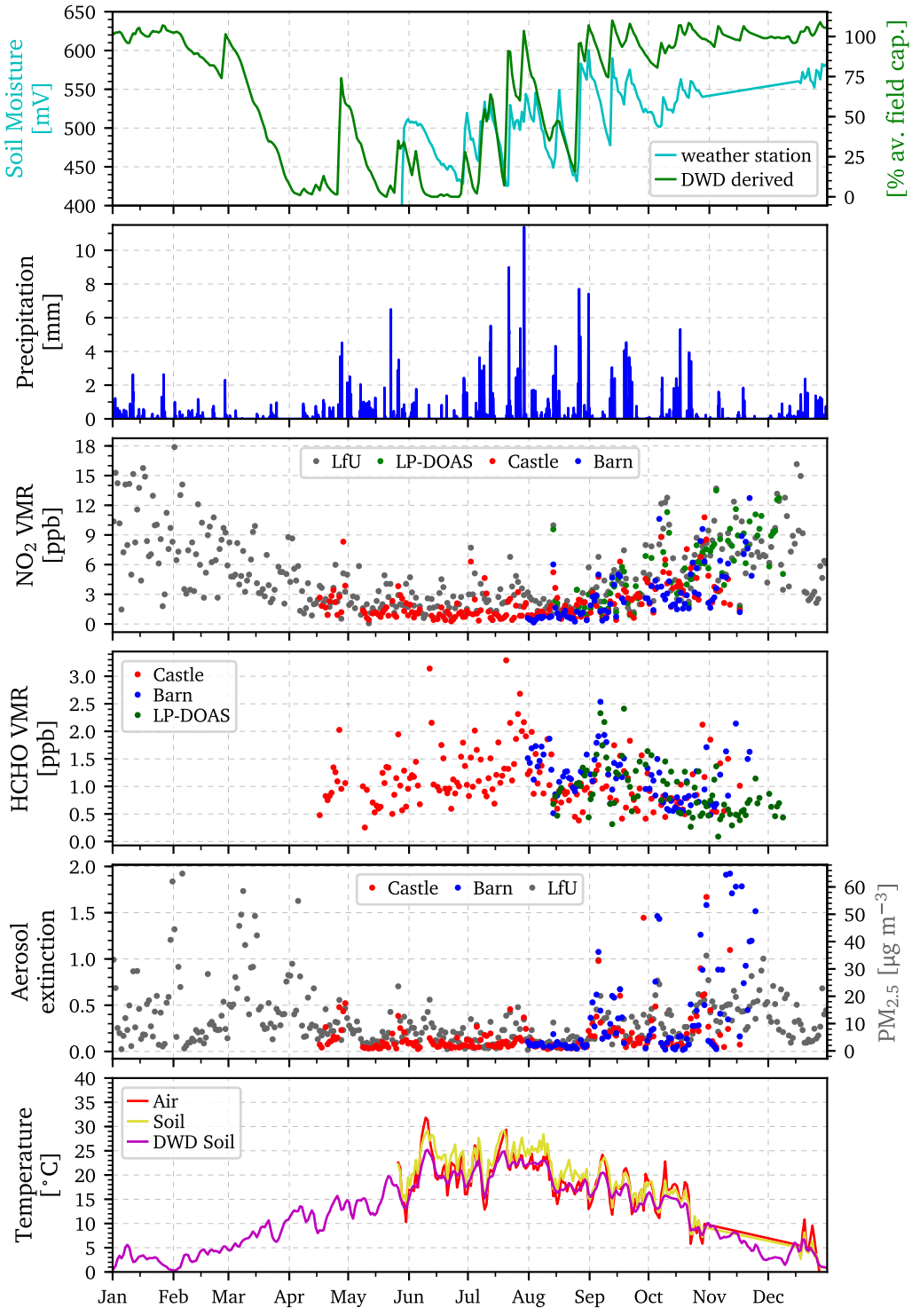

Figure 5.30: Time series of several environmental parameters, trace gases and aerosols during the measurement campaign in 2014. First row: soil moisture data from the in-field weather stations and the DWD calculated soil parameters. Second row: hourly precipitation sums derived from the DWD Radolan precipitation product. Third row: near-surface NO_2 VMRs derived from the mini MAX-DOAS instruments, the LP-DOAS and the LfU station (daily midday averages, 8–14UTC). Fourth row: near-surface HCHO VMRs derived from the mini MAX-DOAS instruments and the LP-DOAS (daily midday averages). Fifth row: near-surface AEs derived from the mini MAX-DOAS instruments and $PM_{2.5}$ from the LfU station (daily midday averages). Sixth row: soil and air temperature from the weather stations in-field as well as calculated soil temperature from the DWD station (both daily midday averages).

5.6.9.2 Days showing spikes in soil moisture and high trace gas VMRs

In the above section, two particular days, i.e. 04/27 and 06/29, were identified that show a sudden increase in soil moisture content after very dry conditions. A more detailed look at the time series of soil moisture and NO_2 VMRs on (Fig. 5.32 and 5.34) and around (Fig. 5.31 and 5.33) these days reveals that elevated NO_2 VMRs are found after 1 day and 3 days, respectively. However, no indication for enhanced HCHO VMRs is found. In the following, the evolution of NO_2 VMRs during these two days is explored in more detail.

Monday, April 28th, 1 day after intense precipitation. The cloud classification indicates an almost complete coverage of continuous clouds over the day which introduces uncertainty to the retrieved NO_2 VMRs from the mini MAX-DOAS at the castle station. However, enhancements in the VMRs due to cloud cover may not be responsible because, on the one hand, the days before are similarly cloudy and, on the other hand, the NO_2 observations at the LfU station agree in the elevated NO_2 VMRs on April 28th compared to the previous days.

The high near-surface NO_2 VMRs ($\sim$ 14 ppb) observed from the mini MAX-DOAS at 10.30UTC on April 28th are not observed by the LfU station. However, the diurnal variation is similar for both stations by showing a decrease in NO_2 VMRs followed by a rapid enhancement of about 9 ppb over a similar time frame but with a time-lag of about 2.5 h. This could be potentially explained by advection of NO_2-rich air through Ries from the south passing to the north (which would be first measured by the mini MAX-DOAS at the castle and later from the LfU station in Öttingen, Fig. 5.5). The weather station at the barn station was installed in June and, thus, only wind data from the DWD station in Harburg and the ECMWF model is available to clarify this hypothesis. However, as presented earlier (Fig. 5.17), data from the DWD station in Harburg may not be representative for wind fields within the Ries plain. The two available wind products show relatively calm winds (about 2 m s^{-1}) during the day coming from north-westerly direction. In the morning, however, the wind direction was changing from southerly to northerly winds between 6 to 10UTC.

The large variation in near-surface NO_2 VMRs of about 10 ppb on April 28th, i.e. the alternation of very high and low VMRs within two hours, either hints at a strong short-term enhancement in local emissions or, more likely, at an advection of polluted air masses through the Ries plain. However, the background level of NO_2 is relatively high on this day with about 5–6 ppb for the mini MAX-DOAS and about 5–7 ppb for the LfU station. The background is also higher than on a usual Monday by about 1–2 ppb for the LfU station and 2–2.5 ppb for the mini MAX-DOAS (Fig. 5.24). Thus, based on these results pulsed soil emissions of NO_x cannot be excluded as a possible contributor to the observed NO_2 VMRs.

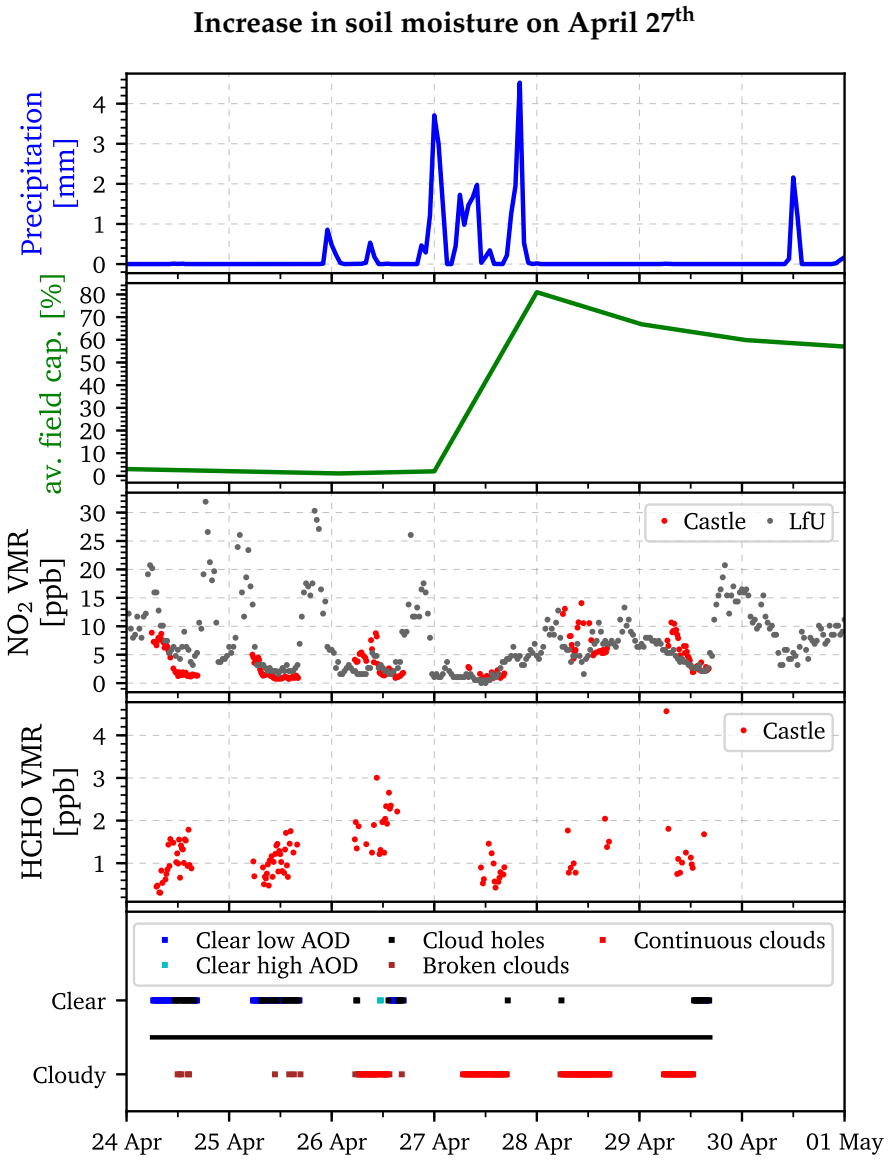

Figure 5.31: Zoom-in of the time series presented in Fig. 5.30 centered around April 27th for precipitation (from DWD Radolan), soil moisture (DWD and in-field weather station), near-surface NO_2 VMRs (mini MAX-DOAS at the castle station and LfU air quality monitoring station) as well as HCHO VMRs (mini MAX-DOAS at the castle). Both panels show a selected time period after the first intense precipitation (leading to a steep increase in soil moisture) after several days of no precipitation.

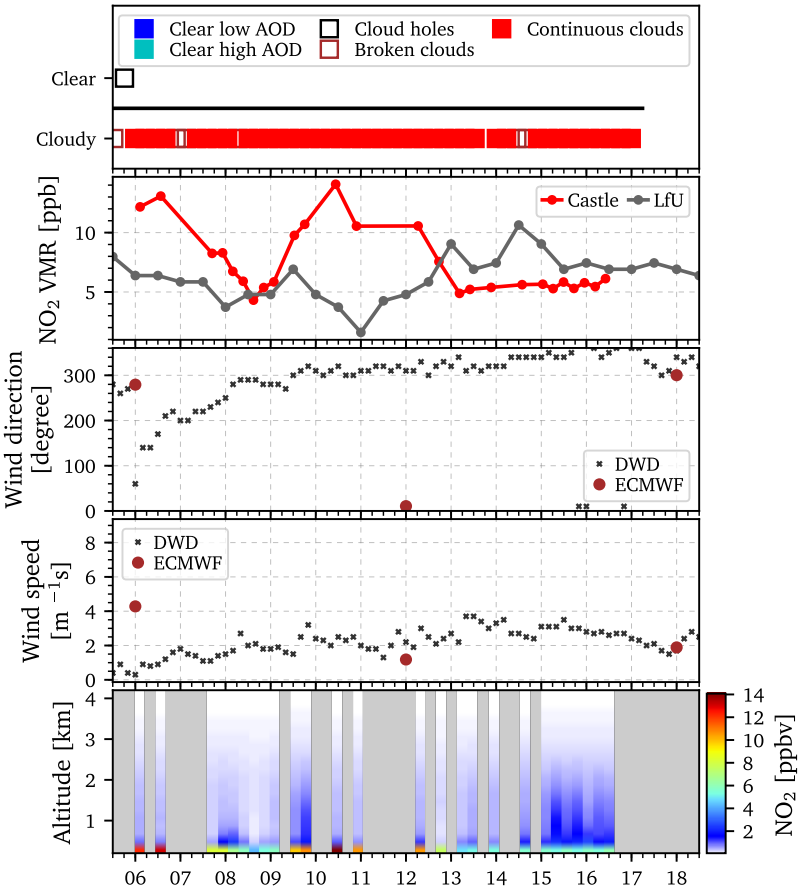

Figure 5.32: Analysis for April 28th 2014. First row: the cloud classification indicates an almost complete coverage of continuous clouds over the day. Second row: Near-surface NO_2 VMRs for the mini MAX-DOAS at the castle station and the LfU air quality monitoring station. Fourth and sixth row: near-surface wind speed and direction derived from the DWD weather station in Harburg and ECMWF. Sixth row: NO_2 profiles during the day show that most NO_2 is located close to the surface.

Wednesday, July 2nd - 3 days after intense precipitation. The days around the precipitation events are characterized by mostly cloudy skies and also on July 2nd an almost continuous cloud cover is detected by the cloud classification scheme. The mini MAX-DOAS instrument at the castle station and the LfU air quality monitoring station, agree well in their diurnal variation of NO_2 VMRs: high VMRs in the morning ($\sim$ 10 ppb), a small enhancement during midday, decreasing NO_2 VMRs in the afternoon and again a slight increase in the evening. Furthermore, the relatively low NO_2 VMRs during the precipitation as well as the relatively high VMRs two days after are captured similarly by both instruments. Therefore, it can be assumed that the effect of clouds is not responsible for the observed enhancements in NO_2 VMRs on July 2nd.

Wind information from the in-field weather station shows low wind speeds in the morning (from westerly direction) and increasing wind speeds in the afternoon (from southerly direction). This pattern correlates well with enhanced NO_2 VMRs in the morning and decreasing NO_2 VMRs in the afternoon.

The peak in NO_2 VMRs between 10–12UTC cannot be explained by advection processes as both stations observe this enhancement at the same time (and the wind blows from the south).

Based on the available measurements, the elevated NO_2 VMRs in the morning and the peak at noon (about 7 ppb for the LfU station and 3 ppb for the mini MAX-DOAS) cannot be directly attributed to a specific source.

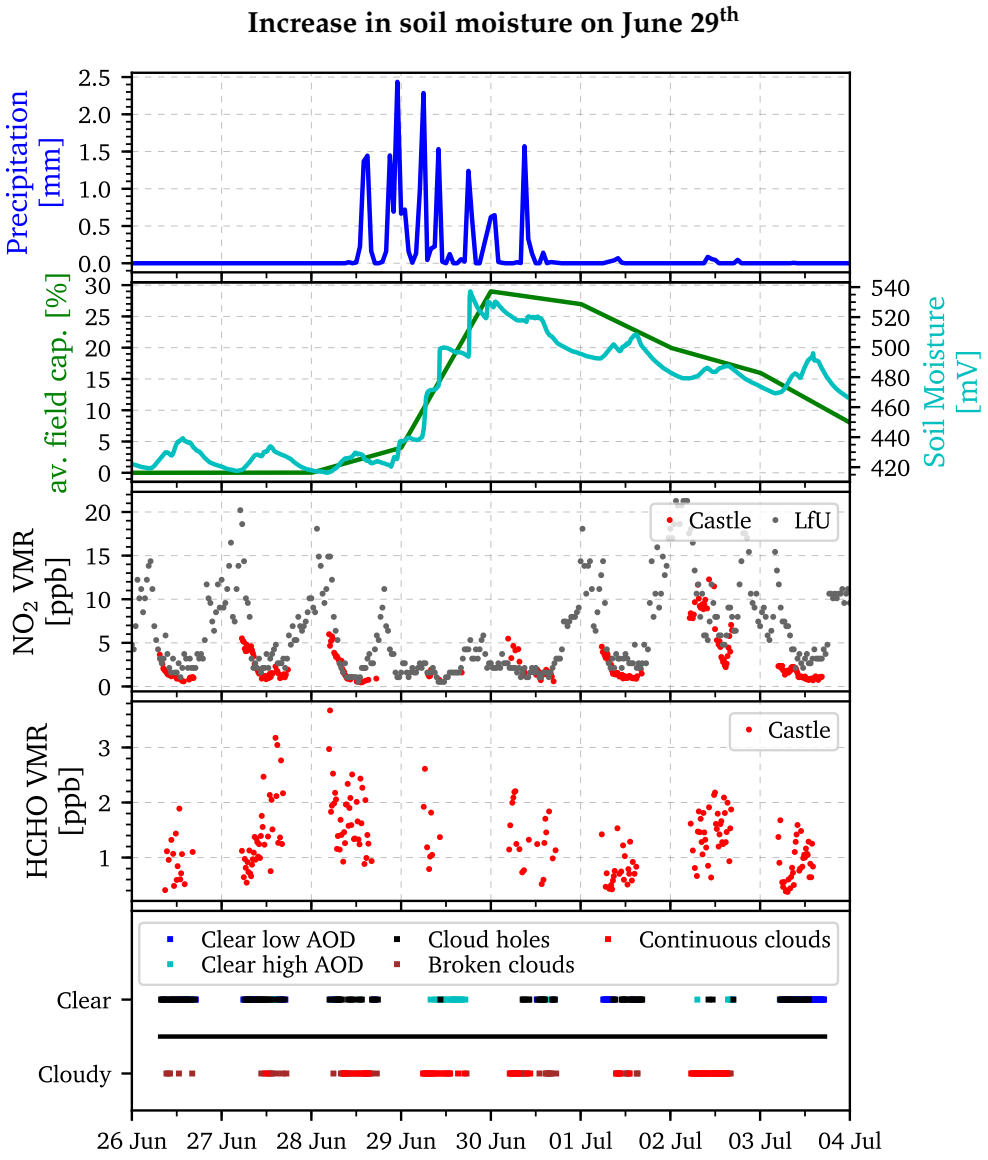

Figure 5.33: Same as Fig. 5.31 but centered around June 29th.

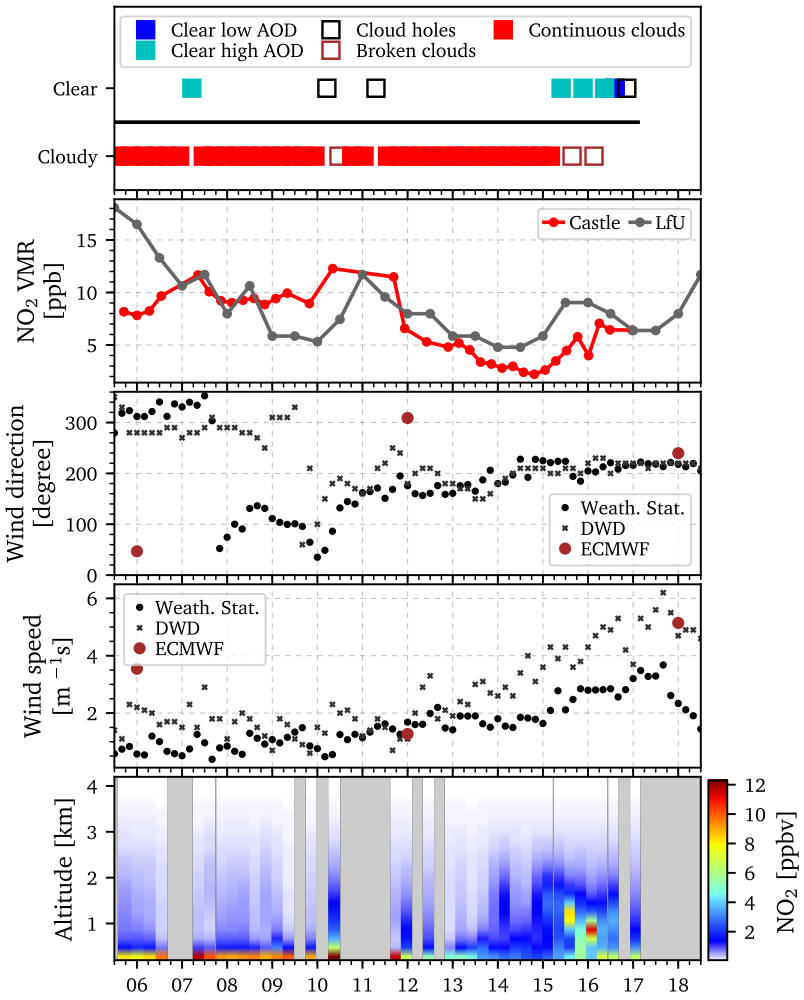

Figure 5.34: Analysis for July 2nd 2014. First row: the cloud classification indicates an almost complete coverage of continuous clouds over the day (except in the evening). Second row: Near-surface NO_2 VMRs for the mini MAX-DOAS at the castle station and the LfU air quality monitoring station. Third row: NO_2 profiles during the day show that most NO_2 is located close to the surface. Fourth and sixth row: near-surface wind speed and direction derived from the own in-field weather station, DWD weather station in Harburg and ECMWF.

5.7 Contribution of soil emissions to NO_2 VCDs

The results from the above sections indicate that anthropogenic emission sources of NO_x within the Ries (traffic-induced) and outside the Ries (industrial activity) largely drive the observed near-surface NO_2 VMRs. In order to estimate upper limits for the contribution of soil emissions to the observed NO_2 concentrations, the impact of these anthropogenic sources needs to be accounted for. This is accomplished by calculating NO_2 VCDs under relatively clean conditions by considering several prescribed conditions.

First, as traffic counts show a drastic decline by about 30 % in passenger cars and 90 % in trucks on Sundays (see Section 5.2), only these specific days are considered. This also implies that a non-negligible contribution of traffic-induced NO_x is still present on Sundays which, however, cannot be excluded from this basic analysis.

Second, it has to be ensured that no polluted air from the south-west (industrial region around Donauwörth) or from the city of Nördlingen is sampled (compare Fig. 5.21). Thus, only measurements when the wind was blowing from north-westerly directions are used, i.e. 307° to 347° (Fig. 5.35).

Third, in order to be sensitive to NO_2 originating from the Nördlinger Ries and not from remote regions, observations at low wind speeds ($< 1\,m\,s^{-1}$) are selected. The uncertainty of the wind direction for such low wind speeds is relatively high. Nevertheless, the selection criteria should decrease the influence from the urban and industrial emission sources on the NO_2 VCDs to a first approximation.

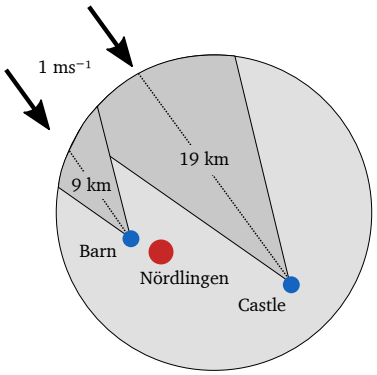

Figure 5.35: Schematic overview of the measurement stations at the castle and barn in the circular-shaped Nördlinger Ries. In Section 5.7, only observations at relatively low wind speeds ($< 1\,m\,s^{-1}$) from north-westerly direction (307° to 347°) are considered. The approximate distance an air mass travels through the Ries until it passes the measurements station (from this wind direction) is indicated in the Figure.

Fourth, measurements of the mini MAX-DOAS instruments taken under clear and cloudy sky are separated because of potential systematic biases that arise under cloudy skies (see previous sections). The distinction between clear/cloudy sky described in Section 5.6.8 is used.

Fifth, it has been found that NO_2 VMRs show enhanced levels during early morning and evening. Thus, only measurements taken during day-time (8–14UTC) are considered.

Following these conditions, average NO_2 VCDs are calculated (Table 5.6), whereby only the partial column from 0 to 600 m is considered as NO_2 concentrations typically show no variation at higher altitudes (as shown in Fig. 5.19). Due to the low number of observations on Sundays fulfilling all these criteria in the summer months, the data is averaged over four months (June to September).

It is found that the clear sky NO_2 VCDs show a distinct reduction on Sundays of about 69 % for the mini MAX-DOAS instrument at the castle station and of about 82 % for the instrument at the barn station. Thereby, the NO_2 VCDs on Sundays are about $0.57 \pm 0.06 \times 10^{15}$ molecules cm^{-2} at the castle station and about $0.24 \pm 0.01 \times 10^{15}$ molecules cm^{-2} at the barn station.

Interestingly, measurements under cloudy situations lead to very similar NO_2 VCDs. This means that clouds may have a larger impact on the retrieved near-surface VMRs (as shown in the earlier sections) than on the vertical columns of NO_2.

For comparison to other research studies, mass flux rates (in terms of nitrogen) are calculated from these VCDs based on Eq. 3.2 and the approach in Section 3.5.1. Considering the location of the castle station within the Ries plain (Fig. 5.35) and considering a constant NO_2-lifetime of 4 h, it is assumed that all NO_2 observed at the castle station was generated within the Ries (a wind speed of 1 m s^{-1} corresponds to a distance of 14.4 km traveled in 4 h). Subsequently, the observed NO_2 VCD at the castle on Sundays can be translated to about 9.21 ng N m^{-2} s^{-1}.

For the barn station, the same assumption does not hold because it is located close to the western edge of the Ries. In order to calculate the mass flux rate of nitrogen also for this measurement station, it has to be additionally assumed that there is no significant source of NO_2 outside of the Ries from this wind direction. Then, the mass flux can be estimated by considering the residence time of the air mass in the Ries plain, i.e. about 2.5 h at a wind speed of < 1 m s^{-1}. This results in about 6.20 ng N m^{-2} s^{-1}.

Both estimates, from the castle and barn stations, represent upper limits for potential soil emissions. However, they are probably overestimated due to the unknown contribution from anthropogenic emissions to the signal.

Table 5.6: Average NO_2 VCDs (partial column from 0–600 m) [molecules cm^{-2}] derived from the two MAX-DOAS instruments under low wind speeds (< 1 m s^{-1}) from north-westerly direction (307 to 347°) and partitioned for working week days and Sundays for the period from June to September. A distinction is made for observations taken during clear and cloudy sky.

	Station	Working Week	Sunday
clear	Castle	$1.84 \pm 0.95 \times 10^{15}$	$0.57 \pm 0.06 \times 10^{15}$
	Barn	$1.30 \pm 0.67 \times 10^{15}$	$0.24 \pm 0.01 \times 10^{15}$
cloudy	Castle	$1.79 \pm 1.02 \times 10^{15}$	$0.61 \pm 0.04 \times 10^{15}$
	Barn	$1.41 \pm 0.68 \times 10^{15}$	$0.25 \pm 0.04 \times 10^{15}$

Analysis of soil samples. Soil samples were taken during the measurement campaign from several cultivated fields (near the barn station) and were analysed in the laboratory

for soil emissions of NO (courtesy of Dr. Thomas Behrendt[11] and Rüdiger Bunk[12]) based on methods described in Behrendt et al. (2014) and Mamtimin et al. (2015, 2016). The potential mass fluxes in terms of nitrogen were then simulated based on the ambient soil moisture and soil temperature in the Nördlinger Ries between June and September 2014 (courtesy of Dr. Buhalqem Mamtimin[13]) similar to investigations in Mamtimin et al. (2015, 2016).

Initial findings from the laboratory analysis of soil samples suggest that cultivated soils in the Ries (soil samples from different fields were summarized) emitted about $2.98\,\mathrm{ng\,N\,m^{-2}\,s^{-1}}$ on average from June to September 2014. By assuming a lifetime of NO_x of 4 h, the mass flux rate corresponds to a NO_2 VCD of about $0.19 \times 10^{15}\,\mathrm{molecules\,cm^{-2}}$. The maximum release rate throughout the time period was at $20.84\,\mathrm{ng\,N\,m^{-2}\,s^{-1}}$ which corresponds to a NO_2 VCD of about $1.29 \times 10^{15}\,\mathrm{molecules\,cm^{-2}}$.

These results show that soil emissions of NO_x are well below the average NO_2 VCDs during the working week, but may be the dominating source of NO_x on Sundays. Furthermore, the estimated maximum release rates are of similar magnitude as the observed NO_2 VCDs even during the working week.

To arrive at the presented estimates, several assumptions and simplifications had to be made. These comprise, for instance, the limited selection of soil samples and the use of the soil temperature and moisture content from a single weather station, both are assumed to be representative for the entire Ries. Furthermore, the current estimates do not consider the contribution of HONO emissions from soils to the observed NO_2 VCDs (which would increase the soil emission estimates) and neglect the effect of NO consumption by soils (which would decrease the soil emission estimates).

Thus, the current results identify soils as a significant source of NO_x in the Nördlinger Ries, but a more detailed analysis has to be conducted in the future to improve the quantification of soil emitted NO_x.

5.8 Conclusions

The exploratory campaign in the Nördlinger Ries was initiated to investigate emissions of NO_x and HCHO from cultivated soils and potential pulsed emissions after rain events. For this task, two mini MAX-DOAS instruments have been installed to continuously measure trace gas column densities over the whole plain over the growing season in the year 2014. Supported by a LP-DOAS and an air quality monitoring station, a consistent time series of NO_2 and HCHO could be successfully recorded.

The measured trace gas SCDs from the mini MAX-DOAS instruments have been converted to near-surface VMRs using the PriAM profile retrieval algorithm.

In general, the results of the four instruments agree well in terms of the diurnal, weekly and seasonal cycles. However, systematic deviations arise due to their different locations

[11] Max Planck Institute for Biogeochemistry, Biogeochemical Processes Department, Jena
[12] Max Planck Institute for Chemistry, Biogeochemistry, Mainz
[13] Max Planck Institute for Chemistry, Satellite Remote Sensing Group, Mainz

and diverging sensitivities for trace gases at different altitudes. In particular, compared to the LP-DOAS and air quality station, the MAX-DOAS instruments observed consistently lower VMRs for trace gases located very close to the surface, i.e. NO_2, and slightly higher VMRs for trace gases with enhanced concentrations at higher altitudes, i.e. HCHO.

In spite of the rural and agricultural character of the Nördlinger Ries a relatively large anthropogenic contribution to NO_2 levels was found on a diurnal and weekly basis. This originates mostly from increased road traffic at peak hours in the morning and evening during the working week. Under specific wind conditions, systematic inflow of polluted air masses, i.e. NO_2-rich air from an industrial zone in south-easterly direction, can additionally increase the NO_2 levels in the Nördlinger Ries.

Yet, the relatively long time series enabled the analysis of trace gases at times with diminished anthropogenic contribution, e.g. on Sundays. Although an accurate source partitioning of the NO_2 VMRs was not feasible within the campaign, observations on such days represent an upper limit for the contribution from soil emissions. While average NO_2 VCDs between June and September are at about 1.30 to 1.84 $\times 10^{15}$ molecules cm^{-2} during the working week, they are drastically reduced on Sundays to about 0.24 to 0.57 $\times 10^{15}$ molecules cm^{-2}. This corresponds to maximum nitrogen emission rates from soils in the Ries of about 6.20 to 9.21 ng N m^{-2} s^{-1}. These estimates are likely to be overestimated due to the unknown remaining contribution from anthropogenic emissions to the signals.

Preliminary analyses from soil samples suggest that cultivated soils in the Ries emitted about 2.98 ng N m^{-2} s^{-1} on average from June to September 2014 which corresponds to a NO_2 VCD of about 0.19 $\times 10^{15}$ molecules cm^{-2}. These findings indicate that soil emissions of NO_x are well below the average NO_2 VCDs during the working week, but may be the dominating source of NO_x on Sundays. Furthermore, the estimated maximum release rates are of similar magnitude as the observed NO_2 VCDs even during the working week.

For HCHO no indications for a substantial primary ground-level source, such as soil emissions of HCHO, were found.

Enhancements in near-surface NO_2 VMRs (of about 1–8 ppb compared to the background) following rapid increases in soil moisture were found on two particular days. However, no consistent relationship between the soil moisture content or precipitation events to NO_2 or HCHO levels could be identified. This is partly due to the frequent cloud coverage and precipitation events that did not allow for sufficient drying-out of the soils (which is required for pulsed emissions). Furthermore, the contribution from anthropogenic emissions is uncertain and short-term enhancements in these emissions that might coincide with pulsed soil emissions could not be investigated.

In sum, the long-term measurement campaign in the Nördlinger Ries proved to be very successful (i) in determining high-quality trace gas VMRs in an agricultural environment with high quality, (ii) an in-depth characterization of the temporal evolution and spatial distribution across the Ries and (iii) in estimating upper limits of the contribution from soil emissions to the observed NO_2.

CHAPTER 6

General conclusions and outlook

Improving the air quality in both urban and rural areas for the benefit of human health and the environment is one of the most challenging tasks of our society. Much attention is thereby drawn to the reduction of anthropogenic emissions of NO_x which will help to lower the levels of particulate matter (PM) and tropospheric O_3 in proximity to urban agglomerations. A considerable source of NO_x, which is often neglected in such discussions, are soil emissions in the form of NO (and to a lesser extent also in the form of HONO) which are particularly strong from fertilized soils and in semi-arid regions following the first precipitation after severe droughts. Although the release rates of NO from soils have been subject to detailed studies in-field and in laboratory over the last decades, the knowledge of emission budgets over entire regions and continents remained limited. Therefore, simulations with global chemistry models are performed and compared to estimates from top-down approaches from satellites. However, significant differences remain on all scales and local emission budgets (on the scale of a few km) are difficult to establish using this technique.

The primary goal of this thesis was, hence, to gain a better understanding of the quantitative contribution of soil emissions to observed NO_2 concentrations in regions that feature favorable soil conditions. These are, on the one hand, semi-arid regions experiencing enhanced soil emissions at the onset of the wet season and, on the other hand, a rural region in Germany which is characterized by strongly fertilized soils used for agriculture. Within this thesis, space- and ground-based remote sensing instruments that capture scattered sun light were deployed and trace gas column densities were retrieved using the DOAS approach. Thereby, NO_2 column densities were used as a proxy for NO_x. This chapter provides general conclusions that can be drawn from the thesis work.

Soil NO_x emissions from semi-arid areas. Due to the very dry soil conditions during the dry season in semi-arid regions, soil emissions remain at a very low level over a large part of the year. The first precipitation of the wet season then suddenly raises the soil moisture content which induces strong short-term emissions of NO_x. These pulsed emissions are detected in this study as enhanced NO_2 VCDs and are found in many semi-arid regions over the world including the Sahel, south-western Africa, Australia and parts of India. This thesis provides a novel and in-depth characterization of this pulsing behaviour based on space-based observations and shows that the whole pulsing event needs to be subdivided into four parts:

1. pulsed emissions on short timescales (1–3 days after the initial precipitation),

2. enhanced emissions after the initial pulse (up to two weeks as shown for the Sahel),
3. slightly enhanced emissions 1–2 days prior to the first precipitation and
4. seasonal background emissions which gradually increase at the onset of the wet season

This newly introduced distinction can be directly implemented as a parametrization of pulsed soil emissions in modelling studies and thereby helps to improve the N mass balance in climate models. The first category, pulsed emissions after the initial precipitation, is by far the strongest and shows emission fluxes in terms of nitrogen of $6\,\mathrm{ng\,N\,m^{-2}\,s^{-1}}$ as averaged over the Sahel region and up to $65\,\mathrm{ng\,N\,m^{-2}\,s^{-1}}$ for individual locations within the Sahel.

Apart from the clear first-day peak, NO_2 VCDs are moderately enhanced compared to the background over the two weeks following the initial precipitation suggesting further emissions of about $3.3\,\mathrm{ng\,N\,m^{-2}\,s^{-1}}$.

It is also found that the pulsing event starts to develop already one to two days before the first rainfall of the wet season. This is most likely provoked by increased humidity and dew-fall shortly before the first rain which raise the moisture content at the soil surface.

In total, a contribution between 21 % to 44 % from these rain-induced intense pulsing events to total soil NO_x emissions (including the seasonal background) are assessed in the Sahel.

The majority of semi-arid regions are only sparsely populated and the impact of these intense soil emissions events on air quality would be limited to the above described few days of a year. However, the Sahel and the region around Lake Chad is home to tens of millions of people. It was shown that an intense and spatially extensive soil NO_x pulsing event dominates the local NO_x budget and leads to highest NO_2 concentrations of the whole year. This raises the question what impact such an event might have on aerosol and O_3 levels. However, this investigation was not within the scope of the thesis but should be certainly addressed in future work.

Soil NO_x emissions from agriculture. In order to investigate emissions of NO_x and HCHO from cultivated soils an exploratory campaign was conducted for the largest part of the year 2014 in the Nördlinger Ries, Germany. Thereby, two MAX-DOAS instruments were deployed in field and validated against observations from a LP-DOAS and an air quality monitoring station. The four instruments agreed well in terms of the diurnal, weekly and seasonal cycles of NO_2 despite their different measurement techniques.

In spite of the rural and agricultural character of the Nördlinger Ries a relatively large anthropogenic contribution to NO_2 levels was found on a diurnal and weekly basis which mainly stems from road traffic (at peak hours in the morning and evening) as well as the inflow of polluted air masses from an industrial zone outside the Ries. Yet, the relatively long time series enabled the analysis of trace gases at times with diminished anthropogenic contribution, e.g. on Sundays and under specific wind conditions.

Although an accurate source partitioning of the NO_2 VMRs was not feasible within the campaign, observations on such days represent an upper limit for the contribution from soil emissions. While average NO_2 VCDs between June and September are at about 1.30 to 1.84 $\times 10^{15}$ molecules cm^{-2} during the working week, they are drastically reduced on Sundays to about 0.24 to 0.57 $\times 10^{15}$ molecules cm^{-2}.

Preliminary results from a laboratory analysis of soil samples suggests that cultivated soils in the Ries emitted about 2.98 ng N m^{-2} s^{-1} (on average from June to September 2014) which corresponds to a NO_2 VCD of about 0.19 $\times 10^{15}$ molecules cm^{-2}. These initial findings indicate that soil emissions of NO_x are well below the average NO_2 VCDs during the working week, but may be the dominating source of NO_x on Sundays.

Two particular days show increased levels of NO_2 following rapid increases in soil moisture, yet no consistent relationship between the soil moisture content and NO_2 could be identified. A more detailed analysis of the extrapolated laboratory results is necessary to verify the enhancement in NO_2 VCDs on these two days.

HCHO emissions from soils. Although the studies conducted in this thesis focused mainly on NO_x emissions from soils, HCHO column densities were analyzed in parallel and inspected in a similar fashion. However, no indications for potential soil emissions were found within the analyses. With regard to pulsed emissions from soils in semi-arid regions this could mean that they either do not occur in the regions the algorithm was sensitive for or that they are too small to be detected from space — using the existing technologies.

The results from the measurement campaign in the Nördlinger Ries give rise to the assumption that no strong ground level emission source for HCHO is present and most of the HCHO at higher altitude is due to secondary formation from VOCs.

Previous studies indicate that both processes, the uptake and the release of HCHO from soils, can occur. If the rate of the uptake of HCHO outbalances the rate of emission, no signal could be measured by the DOAS-type instruments.

Suitability of the different instruments. The use of different measurement instruments and techniques was essential for the exploration of soil emissions of NO_2 on different spatial and temporal scales in this thesis. While the space-based instruments enabled the relatively consistent sampling of trace gases over remote and inaccessible regions from a 'top view', the ground-based instrument generally have a higher sensitivity to the lower-most atmospheric layer and offer a much higher temporal resolution for the (local) measurements.

The investigation of pulsed soil emissions in semi-arid regions could be applied to vast geographic regions and global maps could be created. However, in order to study diurnal variations in (soil) NO_x emissions in these remote areas and consequently explain differences among different satellite products, upcoming[1] sensors in a geostationary orbit

[1] such as: Sentinel-4, Tropospheric Emissions: Monitoring of Pollution (TEMPO) and Geostationary Environment Monitoring Spectrometer (GEMS)

are needed that capture the same area repetitively during the day. Unfortunately, no such instrument is planned at the moment that covers the semi-arid regions which showed strongest pulsing events in this thesis work. Thus, ground-based instruments could ideally support the investigation in these regions and additionally verify the observed enhancements following pulsing events.

The observations from three different measurement systems during the campaign in the Nördlinger Ries created an almost complete picture of the horizontal, vertical and temporal evolution of NO_2 and HCHO concentrations. The differences among the instruments could be explained by the different measurement techniques and their different sensitivity to trace gases at different altitudes. The information on the complete diurnal cycle, i.e. day- and nighttime, which was provided by the LP-DOAS and the air quality monitoring station, helped in interpreting the MAX-DOAS observations in early morning and evening (which show larger uncertainties due to low light conditions). Furthermore, the use of instruments measuring NO_2 that are not dependent on (scattered) sunlight also helped to verify the MAX-DOAS observations under cloudy situations. MAX-DOAS observations, however, were essential in understanding the vertical and horizontal distribution of NO_2 within the Ries and the quantity that is measured can be almost directly compared to satellite measurements and release rates of trace gases from soils.

Importance of soil emissions of NO_x. This study showed that soil emissions of NO_x do not only represent a considerable share of total NO_x emissions but, in fact, can dominate the observed NO_2 concentration during intense pulsing events in semi-arid regions and, as preliminary findings suggest, also in regions with strongly fertilized soils and low impact from anthropogenic emissions. Thereby, the estimates determined in this thesis might even be too low, as potential contributions of HONO emissions to the NO_x budget are not considered.

It was found that the enhanced soil emissions at the onset of the wet season in semi-arid regions govern the NO_x budget and, therefore, also significantly impact the local air quality. This natural process affects millions of people for instance in the Sahel region but is limited to few weeks of the year. However, soil emissions of NO_x from agriculture may influence the (summer-time) air quality to a much larger extent. This is, on the one hand, due to the direct emissions of NO_x and the enhanced secondary aerosol and O_3 formation downwind (as several previous studies point out) and, on the other hand, due to the omnipresence of cultivated and strongly fertilized fields in many developed countries.

The results therefore also raise awareness of the effect of excessive fertilization in agricultural regions and that subsequent soil emissions of NO_x degrade air quality in a number of ways.

Interestingly, as a consequence of the prevailing winds in the Ries, most of the soil NO_x that was produced within the Nördlinger Ries is typically transported away so that its secondary products mainly affect regions downwind (but only in some specific cases the population within the Ries).

Thus, it would be desirable to study these impacts in the context of agricultural regions

and pulsed soil emissions from semi-arid regions in more detail in future work.

Suggestions for future studies. The presented studies provide novel measurements of soil emissions in both semi-arid and agricultural regions and established a well-founded basis for future research.

In order to gain more insight into pulsed soil emissions of NO_x, the presented approach for semi-arid regions can be directly applied to more specific geographic regions at much finer spatio-temporal scale. These are, for instance, countries that possess semi-arid lands and at the same time provide high resolution data on precipitation, temperature and soil properties such as Australia or the United States of America. Together with the arrival of new space-based sensors with increased spatial resolution (e.g. TROPOMI) or temporal resolution (geostationary satellite sensors) an improved characterization of the soil NO_x pulsing behaviour over semi-arid lands could be achieved.

While the study in the Nördlinger Ries provided an exploratory assessment of agricultural soil emissions of NO_x, it also highlighted that some refinements can be made for future research campaigns.

If pulsed emissions from fertilized fields are studied in the future, then it is advised to choose a region with less summer-time precipitation and higher temperatures, e.g. a study region in southern Europe. Since it was found that anthropogenic emissions dominated the NO_2 signal in the Ries, which complicated the analysis, it is suggested to search for a study area which combines strongly fertilized areas and almost no urban agglomerations nearby. In addition, it is recommended to characterize the inflow and outflow of trace gases of the study region, e.g. by an improved spatial set-up of the instruments. This will simplify the calculation of the emission flux of NO_x from the region of interest and anthropogenic influences from outside the study region can be better accounted for.

Appendix A

Monthly averages of environmental parameters over Northern Africa

A.1 Monthly averages of GOME-2 NO_2 VCDs

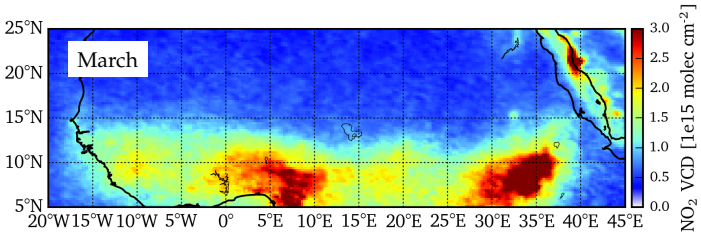

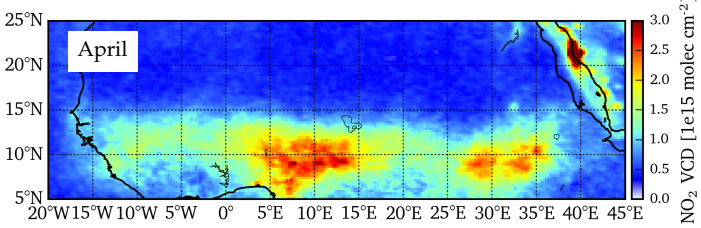

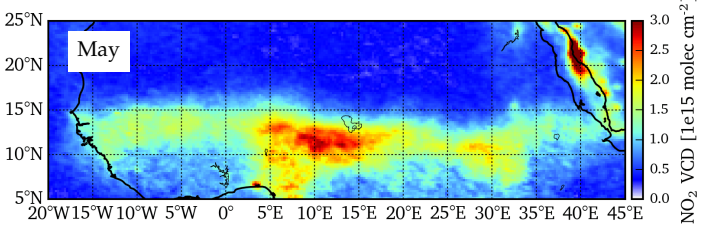

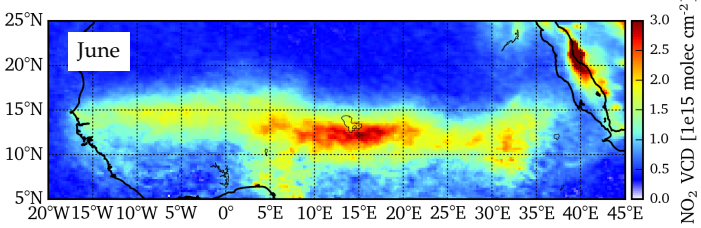

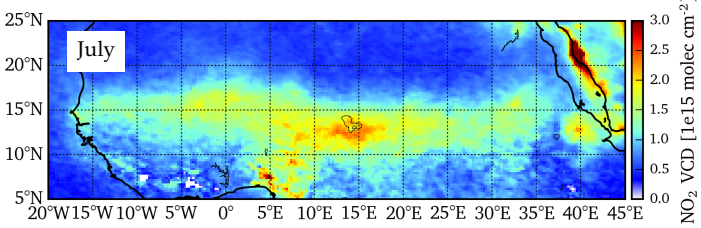

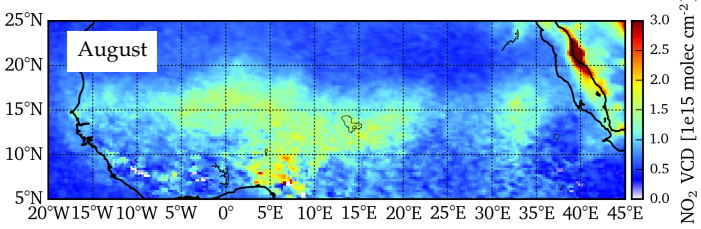

A.2 Monthly averages of SCIAMACHY NO_2 VCDs

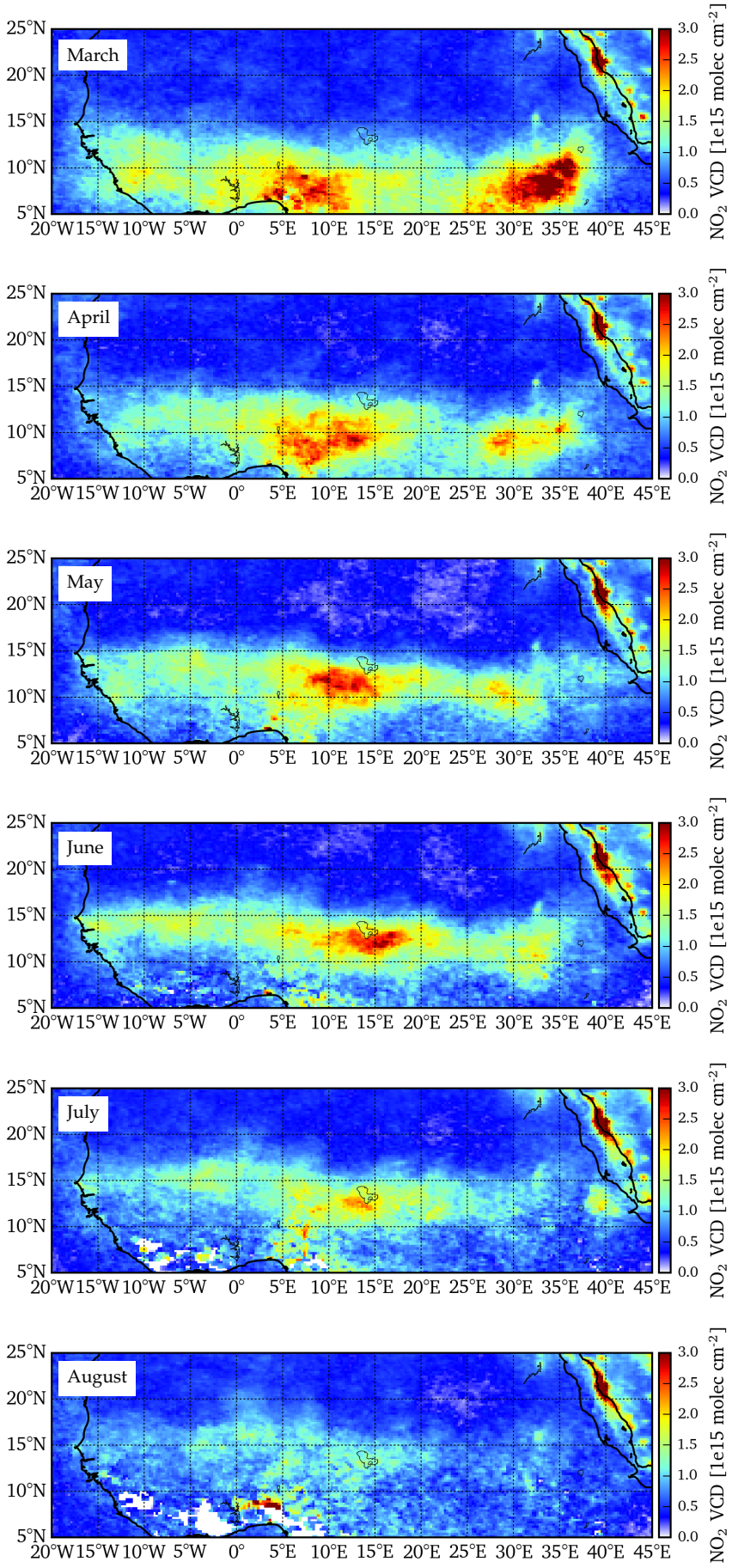

A.3 Monthly averages of daily fire counts

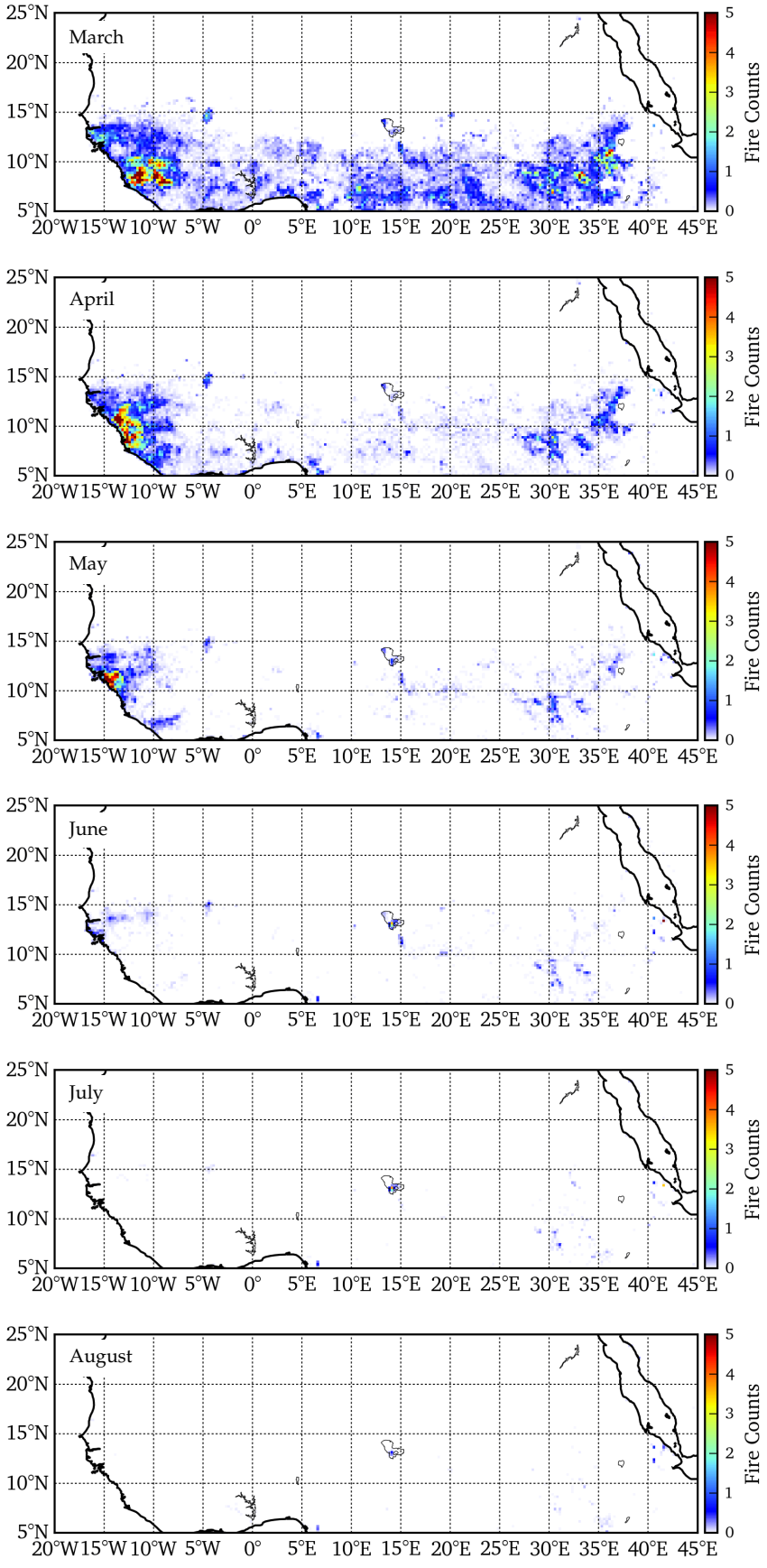

A.4 Monthly averages of daily lightning strikes

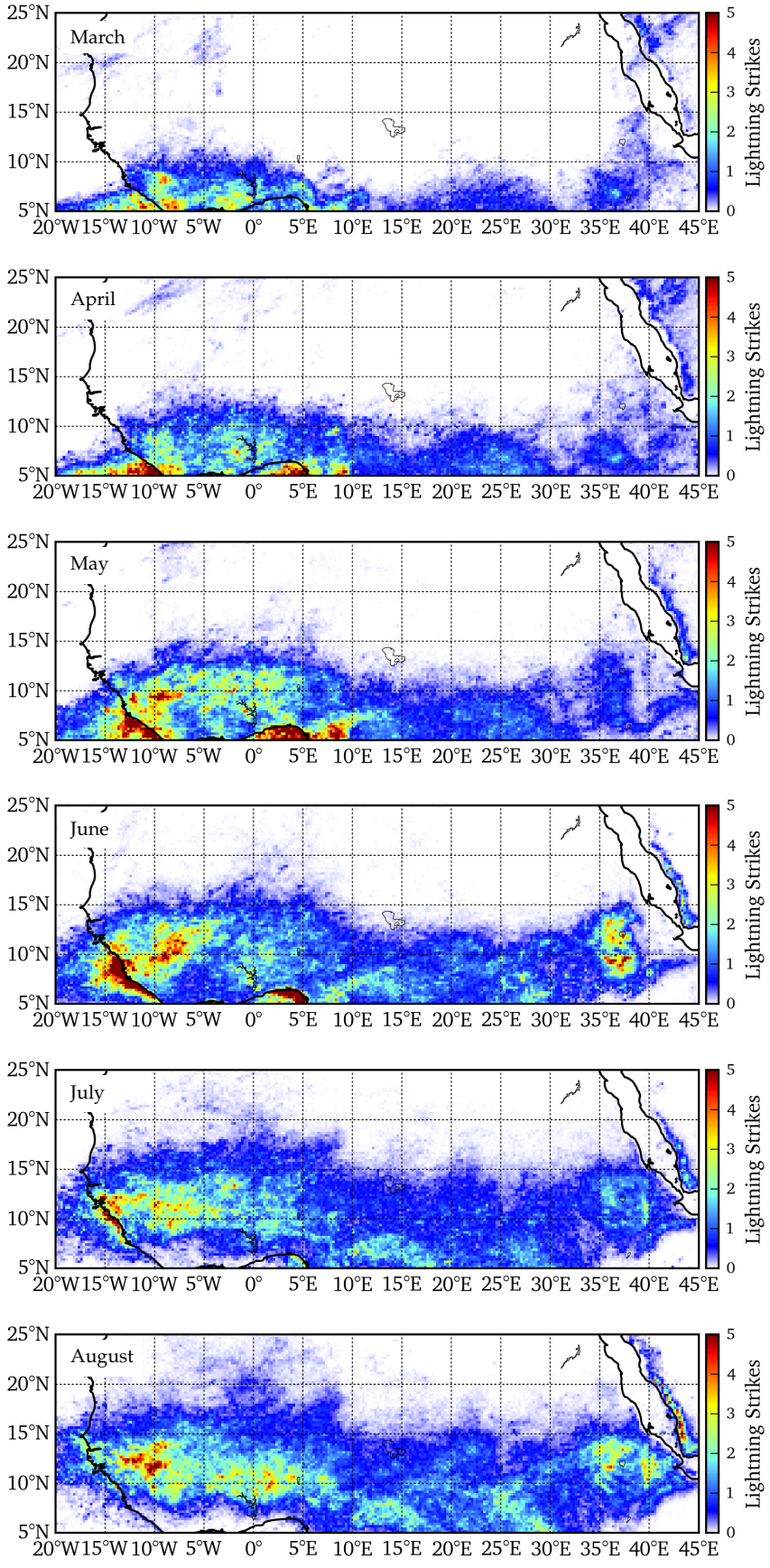

A.5 Albedo maps from the NO_2 products

A.5.1 OMI

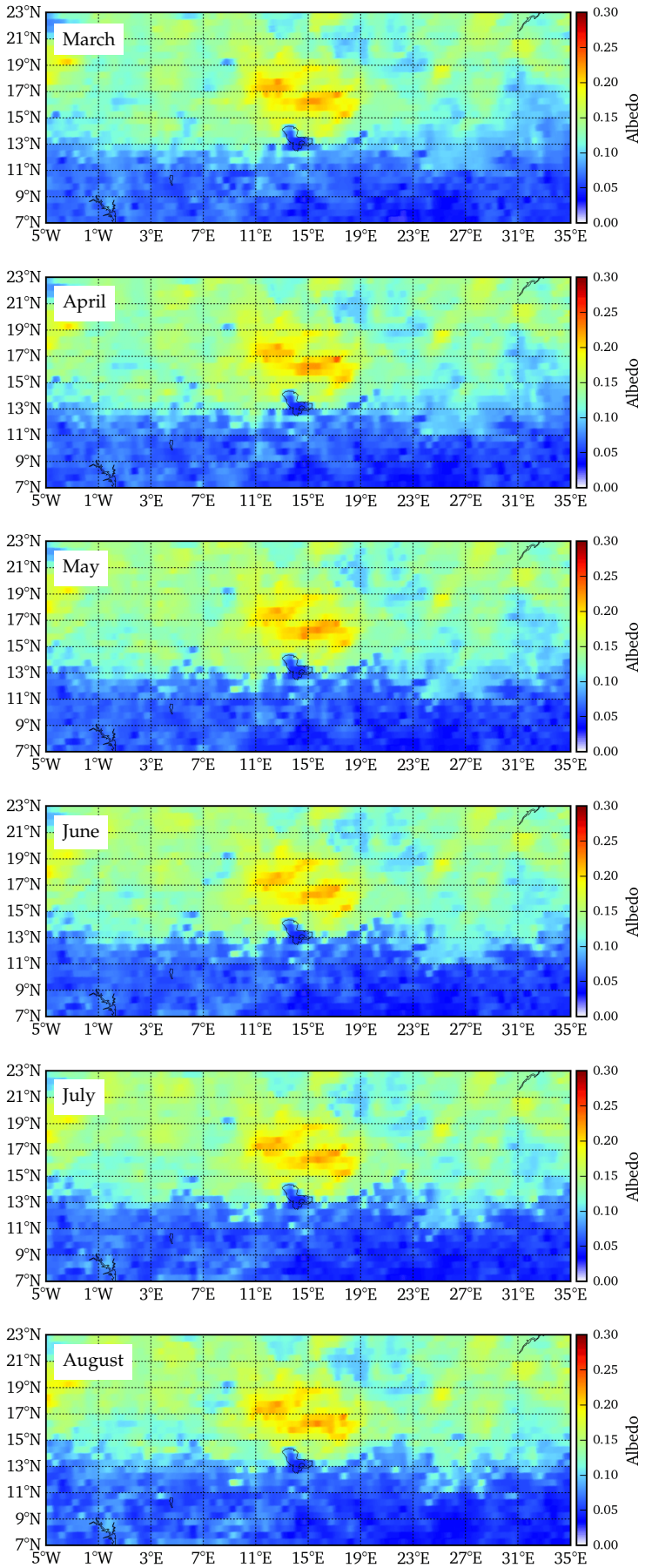

A.5.2 GOME-2

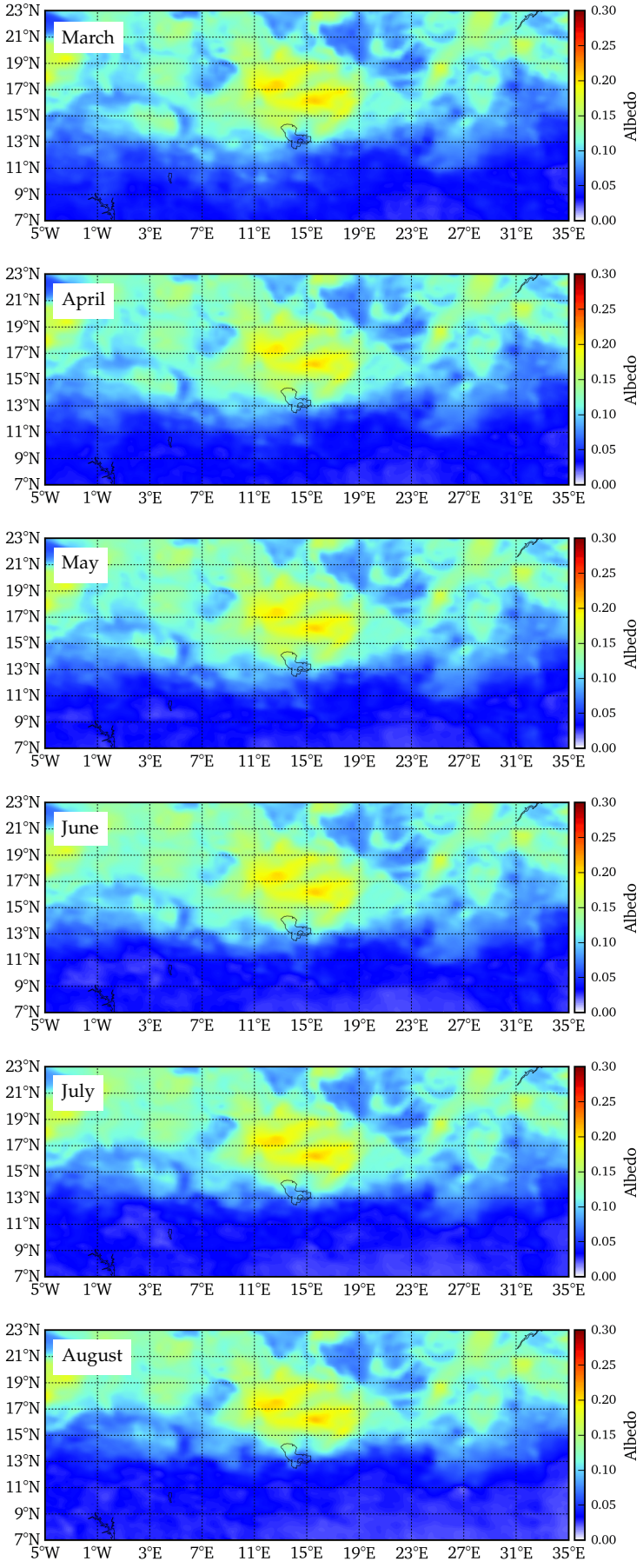
March
April
May
June
July
August
23°N
21°N
19°N
17°N
15°N
13°N
11°N
9°N
7°N
5°W
1°W
3°E
7°E
11°E
15°E
19°E
23°E
27°E
31°E
35°E
0.30
0.25
0.20
0.15
0.10
0.05
0.00
Albedo

A.5.3 SCIAMACHY

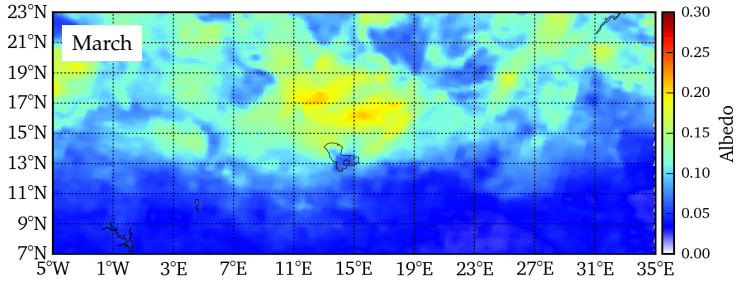

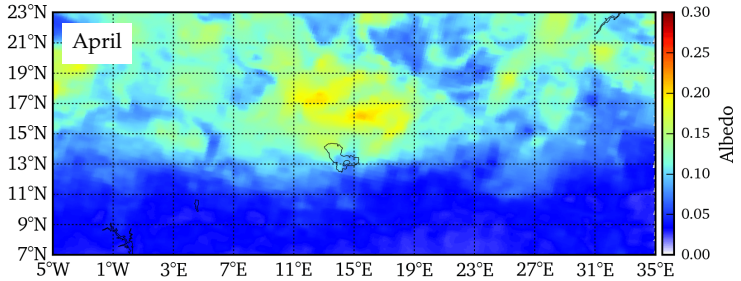

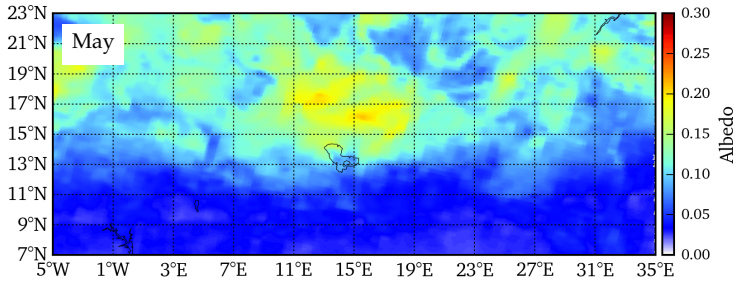

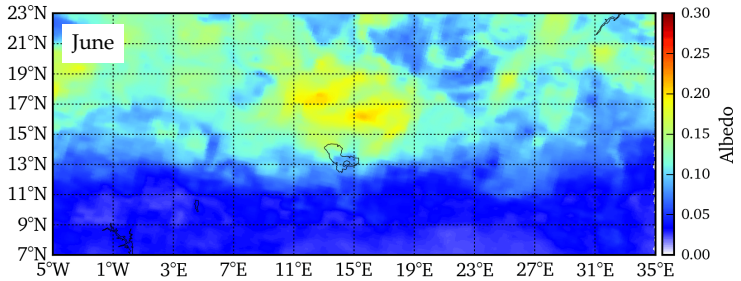

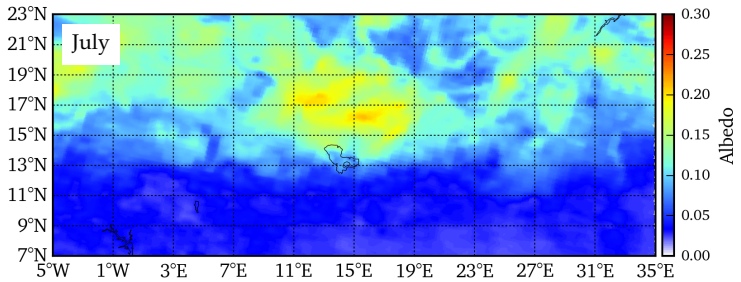

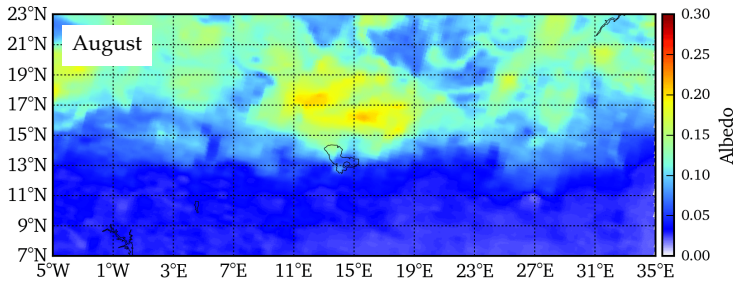

APPENDIX B

Dependence of trace gas levels in the Nördlinger Ries on environmental parameters

B.1 Summary statistics for the independent variables

B.1.1 NO_2

Table B.1: Summary statistics for the independent variables for the castle NO_2 analysis

Statistic	N	Mean	St. Dev.	Min	Max
weekvar	140	0.129	0.336	0	1
globrad	140	498.797	228.871	−0.214	959.784
cloudy	140	0.521	0.335	0.000	1.000
airtemp	140	18.640	4.464	5.794	29.631
soiltemp	140	17.827	3.816	7.599	24.900
relhum	140	64.906	15.891	32.771	92.583
precip	140	0.126	0.251	0.000	1.618
soilmoist	140	58.999	37.075	0.000	108.007
windspeed	140	2.635	1.319	0.087	9.157
winddir_ne	140	0.197	0.301	0.000	1.000
winddir_se	140	0.255	0.347	0.000	1.000
winddir_sw	140	0.215	0.295	0.000	1.000
winddir_nw	140	0.333	0.370	0.000	1.000

Table B.2: Summary statistics for the independent variables for the barn NO_2 analysis

Statistic	N	Mean	St. Dev.	Min	Max
weekvar	74	0.108	0.313	0	1
globrad	74	395.991	187.864	78.918	807.953
cloudy	74	0.517	0.344	0.000	1.000
airtemp	74	16.959	4.244	5.794	24.806
soiltemp	74	16.181	3.775	7.599	23.001
relhum	74	72.997	12.907	41.896	95.250
precip	74	0.098	0.204	0.000	1.169
soilmoist	74	80.931	25.117	15.510	110.000
windspeed	74	2.641	1.317	0.777	8.463
winddir_ne	74	0.153	0.237	0.000	1.000
winddir_se	74	0.342	0.388	0.000	1.000
winddir_sw	74	0.199	0.299	0.000	1.000
winddir_nw	74	0.306	0.364	0.000	1.000

Table B.3: Summary statistics for the independent variables for the LP-DOAS NO_2 analysis

Statistic	N	Mean	St. Dev.	Min	Max
weekvar	48	0.125	0.334	0	1
globrad	48	335.591	173.024	48.698	720.939
cloudy	48	0.578	0.349	0.000	1.000
airtemp	48	15.993	4.324	5.794	24.163
soiltemp	48	15.052	3.433	7.599	20.499
relhum	48	77.633	10.549	47.021	96.500
precip	48	0.175	0.344	0.000	1.830
soilmoist	48	91.046	17.438	43.490	110.000
windspeed	48	2.770	1.424	0.777	8.463
winddir_ne	48	0.171	0.245	0.000	1.000
winddir_se	48	0.308	0.369	0.000	1.000
winddir_sw	48	0.220	0.337	0.000	1.000
winddir_nw	48	0.301	0.378	0.000	1.000

Table B.4: Summary statistics for the independent variables for the LfU station NO_2 analysis

Statistic	N	Mean	St. Dev.	Min	Max
weekvar	146	0.137	0.345	0	1
globrad	146	493.184	231.878	−0.214	959.784
cloudy	146	0.526	0.342	0.000	1.000
airtemp	146	18.577	4.481	5.794	29.631
soiltemp	146	17.801	3.802	7.599	24.900
relhum	146	65.529	16.127	32.771	96.500
precip	146	0.138	0.285	0.000	1.830
soilmoist	146	59.567	37.193	0.000	108.007
windspeed	146	2.655	1.301	0.087	9.157
winddir_ne	146	0.198	0.304	0.000	1.000
winddir_se	146	0.259	0.350	0.000	1.000
winddir_sw	146	0.213	0.293	0.000	1.000
winddir_nw	146	0.329	0.370	0.000	1.000

B.1.2 HCHO

Table B.5: Summary statistics for the independent variables for the castle HCHO analysis

Statistic	N	Mean	St. Dev.	Min	Max
weekvar	136	0.125	0.332	0	1
globrad	136	509.989	227.427	−0.214	959.784
cloudy	136	0.521	0.335	0.000	1.000
airtemp	136	19.002	4.161	6.146	29.631
soiltemp	136	18.154	3.535	7.599	24.900
relhum	136	64.157	15.646	32.771	92.583
precip	136	0.126	0.250	0.000	1.618
soilmoist	136	57.197	37.174	0.000	108.007
windspeed	136	2.617	1.229	0.087	9.157
winddir_ne	136	0.198	0.308	0.000	1.000
winddir_se	136	0.240	0.341	0.000	1.000
winddir_sw	136	0.213	0.291	0.000	1.000
winddir_nw	136	0.349	0.375	0.000	1.000

Table B.6: Summary statistics for the independent variables for the barn HCHO analysis

Statistic	N	Mean	St. Dev.	Min	Max
weekvar	71	0.113	0.318	0	1
globrad	71	408.681	181.029	78.918	807.953
cloudy	71	0.501	0.341	0.000	1.000
airtemp	71	17.376	3.795	5.794	24.806
soiltemp	71	16.522	3.456	8.551	23.001
relhum	71	72.459	12.892	41.896	95.250
precip	71	0.101	0.207	0.000	1.169
soilmoist	71	80.090	25.296	15.510	110.000
windspeed	71	2.590	1.303	0.777	8.463
winddir_ne	71	0.159	0.240	0.000	1.000
winddir_se	71	0.329	0.379	0.000	1.000
winddir_sw	71	0.207	0.302	0.000	1.000
winddir_nw	71	0.305	0.359	0.000	1.000

Table B.7: Summary statistics for the independent variables for the LP-DOAS HCHO analysis

Statistic	N	Mean	St. Dev.	Min	Max
weekvar	49	0.122	0.331	0	1
globrad	49	342.088	177.150	48.698	720.939
cloudy	49	0.577	0.345	0.000	1.000
airtemp	49	16.073	4.315	5.794	24.163
soiltemp	49	15.110	3.421	7.599	20.499
relhum	49	77.342	10.635	47.021	96.500
precip	49	0.171	0.341	0.000	1.830
soilmoist	49	91.015	17.257	43.490	110.000
windspeed	49	2.755	1.414	0.777	8.463
winddir_ne	49	0.168	0.243	0.000	1.000
winddir_se	49	0.322	0.379	0.000	1.000
winddir_sw	49	0.215	0.335	0.000	1.000
winddir_nw	49	0.295	0.376	0.000	1.000

B.2 NO_2 VMRs shifted by one day

Table B.8: Multiple regression analysis of near-surface NO_2 VMRs from the four instruments against several environmental parameters. In this analysis, the NO_2 data is shifted backwards by one day. The independent variables as well as their selection process are explained in Section 5.6.8.

	Dependent variable:			
	NO_2			
	Castle	Barn	LP-DOAS	LfU
weekvar		0.459**		
		(0.191)		
soiltemp	−0.987***	−1.287***	−1.222***	−0.807***
	(0.132)	(0.236)	(0.312)	(0.189)
soilmoist	0.324**			0.538***
	(0.133)			(0.187)
winddir_se	0.568***		0.640**	0.426**
	(0.117)		(0.311)	(0.172)
relhum		0.432*		
		(0.250)		
precip		−0.409**	−0.510	
		(0.204)	(0.307)	
winddir_sw				−0.537***
				(0.173)
Constant	2.209***	2.597***	4.221***	3.348***
	(0.116)	(0.187)	(0.304)	(0.161)
Observations	134	69	50	146
R^2	0.518	0.536	0.355	0.346
Adjusted R^2	0.507	0.507	0.313	0.327
Residual Std. Error	1.338 (df = 130)	1.557 (df = 64)	2.150 (df = 46)	1.941 (df = 141)
F Statistic	46.558*** (df = 3; 130)	18.475*** (df = 4; 64)	8.442*** (df = 3; 46)	18.645*** (df = 4; 141)

Note: **p<0.05; ***p<0.01
Standard deviation of the estimate in brackets.
All independent variables are standardized.

Table B.9: Multiple regression analysis of near-surface NO_2 VMRs from the four instruments against several environmental parameters. In this analysis, the NO_2 data is shifted forwards by one day. The independent variables as well as their selection process are explained in Section 5.6.8.

	Dependent variable:			
	NO_2			
	Castle	Barn	LP-DOAS	LfU
weekvar	−0.185			
	(0.123)			
cloudy	−0.255*			
	(0.130)			
soiltemp	−0.801***	−1.402***	−1.269***	−0.404*
	(0.142)	(0.254)	(0.366)	(0.211)
precip				−0.366*
				(0.191)
soilmoist	0.448***	0.362		0.824***
	(0.138)	(0.231)		(0.219)
windspeed		−0.666***	−1.291***	
		(0.226)	(0.411)	
winddir_ne			−0.986**	
			(0.395)	
winddir_nw			−0.731**	
			(0.350)	
winddir_se				0.282
				(0.186)
Constant	2.128***	2.495***	4.165***	3.394***
	(0.122)	(0.199)	(0.329)	(0.181)
Observations	133	70	46	146
R^2	0.361	0.440	0.364	0.223
Adjusted R^2	0.341	0.415	0.302	0.201
Residual Std. Error	1.407 (df = 128)	1.664 (df = 66)	2.228 (df = 41)	2.189 (df = 141)
F Statistic	18.102*** (df = 4; 128)	17.313*** (df = 3; 66)	5.867*** (df = 4; 41)	10.131*** (df = 4; 141)

Note: **p<0.05; ***p<0.01
Standard deviation of the estimate in brackets.
All independent variables are standardized.

B.3 HCHO VMRs shifted by one day

Table B.10: Multiple regression analysis of near-surface HCHO VMRs from the three instruments against several environmental parameters. In this analysis, the HCHO data is shifted backwards by one day. The independent variables as well as their selection process are explained in Section 5.6.8.

	Dependent variable:		
	HCHO		
	Castle	Barn	LP-DOAS
soiltemp	0.229***	0.169***	0.253***
	(0.038)	(0.042)	(0.053)
precip			−0.091*
			(0.052)
winddir_ne		0.141***	0.204***
		(0.045)	(0.053)
winddir_sw		−0.075	
		(0.045)	
winddir_se			0.135**
			(0.053)
Constant	1.126***	1.154***	1.052***
	(0.038)	(0.041)	(0.051)
Observations	129	67	51
R^2	0.222	0.382	0.489
Adjusted R^2	0.216	0.352	0.445
Residual Std. Error	0.431 (df = 127)	0.338 (df = 63)	0.368 (df = 46)
F Statistic	36.188*** (df = 1; 127)	12.961*** (df = 3; 63)	11.008*** (df = 4; 46)

Note: **p<0.05; ***p<0.01
Standard deviation of the estimate in brackets.
All independent variables are standardized.

Table B.11: Multiple regression analysis of near-surface HCHO VMRs from the three instruments against several environmental parameters. In this analysis, the HCHO data is shifted forwards by one day. The independent variables as well as their selection process are explained in Section 5.6.8.

	Dependent variable:		
	HCHO		
	Castle	Barn	LP-DOAS
weekvar	0.061		
	(0.040)		
soiltemp	0.314***	0.242***	0.163**
	(0.049)	(0.039)	(0.069)
relhum	0.127**		−0.104
	(0.049)		(0.064)
windspeed	0.091**		−0.136**
	(0.043)		(0.060)
winddir_ne	0.104**	0.131***	
	(0.042)	(0.039)	
Constant	1.165***	1.158***	1.045***
	(0.040)	(0.038)	(0.054)
Observations	130	67	47
R^2	0.287	0.458	0.410
Adjusted R^2	0.258	0.441	0.369
Residual Std. Error	0.452 (df = 124)	0.315 (df = 64)	0.372 (df = 43)
F Statistic	9.978*** (df = 5; 124)	27.014*** (df = 2; 64)	9.974*** (df = 3; 43)

Note: **p<0.05; ***p<0.01
Standard deviation of the estimate in brackets.
All independent variables are standardized.

Bibliography

Acarreta, J. R., De Haan, J. F., and Stammes, P.: Cloud pressure retrieval using the O2-O2 absorption band at 477 nm, J. Geophys. Res.-Atmos., 109, DOI: 10.1029/2003JD003915, d05204, 2004.

Akaike, H.: Information theory as an extension of the maximum likelihood principle, in: Second International Symposium on Information Theory, edited by Petrov, B. and Csaki, F., pp. 267–281, 1973.

Akaike, H.: A new look at the statistical model identification, IEEE Transactions on Automatic Control, 19, 716–723, DOI: 10.1109/TAC.1974.1100705, 1974.

Aliwell, S. R., Van Roozendael, M., Johnston, P. V., Richter, A., Wagner, T., Arlander, D. W., Burrows, J. P., Fish, D. J., Jones, R. L., Tørnkvist, K. K., Lambert, J.-C., Pfeilsticker, K., and Pundt, I.: Analysis for BrO in zenith-sky spectra: An intercomparison exercise for analysis improvement, Journal of Geophysical Research: Atmospheres, 107, ACH 10–1–ACH 10–20, DOI: 10.1029/2001JD000329, 2002.

Altshuller, A. P.: Production of aldehydes as primary emissions and from secondary atmospheric reactions of alkenes and alkanes during the night and early morning hours, Atmos. Environ., 27A, 21–32, 1993.

Anderson, I. C. and Levine, J. S.: Simultaneous field measurements of biogenic emissions of nitric oxide and nitrous oxide, Journal of Geophysical Research: Atmospheres, 92, 965–976, DOI: 10.1029/JD092iD01p00965, URL http://dx.doi.org/10.1029/JD092iD01p00965, 1987.

Anderson, L. G., Lanning, J. A., Barrell, R., Miyagishima, J., Jones, R. H., and Wolfe, P.: Sources and sinks of formaldehyde and acetaldehyde: An analysis of Denver's ambient concentration data, Atmos. Environ., 30, 2113–2123, 1996.

Arino, O., Gross, D., Ranera, F., Leroy, M., Bicheron, P., Brockman, C., Defourny, P., Vancutsem, C., Achard, F., Durieux, L., Bourg, L., Latham, J., Gregorio, A. D., Witt, R., Herold, M., Sambale, J., Plummer, S., and Weber, J. L.: GlobCover: ESA service for global land cover from MERIS, in: 2007 IEEE International Geoscience and Remote Sensing Symposium, pp. 2412–2415, DOI: 10.1109/IGARSS.2007.4423328, 2007.

Asensio, D., Peñuelas, J., Filella, I., and Llusià, J.: On-line screening of soil VOCs exchange responses to moisture, temperature and root presence, Plant and Soil, 291, 249–261, DOI: 10.1007/s11104-006-9190-4, 2007.

Babamaaji, R. A. and Lee, J.: Land use/land cover classification of the vicinity of Lake Chad using NigeriaSat-1 and Landsat data, Environmental Earth Sciences, 71, 4309–4317, DOI: 10.1007/s12665-013-2825-x, 2014.

Barger, N., Belnap, J., Ojima, D., and Mosier, A.: NO Gas Loss from Biologically Crusted Soils in Canyonlands National Park, Utah, Biogeochemistry, 75, 373–391, DOI: 10.1007/s10533-005-1378-9, 2005.

Bassett, M. and Seinfeld, J. H.: Atmospheric equilibrium model of sulfate and nitrate aerosols, Atmos. Environ., 17, DOI: 10.1016/0004-6981(83)90221-4, 1983.

Behrendt, T., Veres, P. R., Ashuri, F., Song, G., Flanz, M., Mamtimin, B., Bruse, M., Williams, J., and Meixner, F. X.: Characterisation of NO production and consumption: new insights by an improved laboratory dynamic chamber technique, Biogeosciences, 11, 5463–5492, DOI: 10.5194/bg-11-5463-2014, 2014.

Beirle, S., Huntrieser, H., and Wagner, T.: Direct satellite observation of lightning-produced NO_x, Atmos. Chem. Phys., 10, 10 965–10 986, DOI: 10.5194/acp-10-10965-2010, 2010.

Bell, G. D., Halpert, M. S., Schnell, R. C., Higgins, R. W., Lawrimore, J., Kousky, V. E., Tinker, R., Thiaw, W., Chelliah, M., and Artusa, A.: Climate Assessment for 1999, Bulletin of the American Meteorological Society, 81, 1328–1328, DOI: 10.1175/1520-0477(2000)081<1328:CAF>2.3.CO;2, 2000.

Belnap, J. and Lange, O.: Biological Soil Crusts: Structure, Function, and Management, Ecological studies, Springer, Berlin, 2001.

Belsley, D. A., Kuh, E., and Welsch, R. E.: Regression Diagnostics: Identifying Influential Data and Sources of Collinearity, John Wiley & Sons, Inc., DOI: 10.1002/0471725153.fmatter, 2005.

Bertram, T., Heckel, A., Richter, A., Burrows, J. P., and Cohen, R. C.: Satellite measurements of daily variations in soil NOx emissions, Geophys. Res. Lett., 32, L24 812, DOI: 10.1029/2005GL024640, 2005.

Blagodatskava, E. and Kuzyakov, Y.: Active microorganisms is soil: critical review of estimation criteria and approaches, Soil Biol. Biochem., 67, 192–211, 2013.

Blanchard, C. L. and Hidy, G. M.: Effects of SO2 and NOx Emission Reductions on PM2.5 Mass Concentrations in the Southeastern United States, Journal of the Air & Waste Management Association, 55, 265–272, DOI: 10.1080/10473289.2005.10464624, 2005.

Bobrowski, N.: Volcanic gas studies by multi axis differential optical absorption spectroscopy, Ph.d. thesis, University of Heidelberg, Heidelberg, 2005.

Boersma, K., Eskes, H., Veefkind, J., Brinksma, E., van der A, R., Sneep, M., van den Oord, G., Levelt, P., Stammes, P., Gleason, J., and Bucsela, E.: Near-real time retrieval of tropospheric NO2 from OMI, Atm. Chem. Phys., pp. 2013–2128, 2007.

Boersma, K., Jacob, D., Bucsela, E., Perring, A., Dirksen, R., van der A, R., Yantosca, R., Park, R., Wenig, M., Bertram, T., and Cohen, R.: Validation of OMI tropospheric NO2 observations during INTEX-B and application to constrain emissions over the eastern

United States and Mexico, Atmos. Environ., 42, 4480 – 4497, DOI: doi:10.1016/j.atmosenv.2008.02.004, 2008.

Boersma, K. F., Eskes, H. J., and Brinksma, E. J.: Error analysis for tropospheric NO2 retrieval from space, J. Geophys. Res.-Atmos., 109, DOI: 10.1029/2003JD003962, 2004.

Boersma, K. F., Eskes, H. J., Dirksen, R. J., van der A, R. J., Veefkind, J. P., Stammes, P., Huijnen, V., Kleipool, Q. L., Sneep, M., Claas, J., Leitão, J., Richter, A., Zhou, Y., and Brunner, D.: An improved tropospheric NO_2 column retrieval algorithm for the Ozone Monitoring Instrument, Atmos. Meas. Tech., 4, 1905–1928, DOI: 10.5194/amt-4-1905-2011, 2011.

Boersma, K. F., Vinken, G. C. M., and Eskes, H. J.: Representativeness errors in comparing chemistry transport and chemistry climate models with satellite UV-Vis tropospheric column retrievals, Geosci. Model Dev., 9, 875–898, DOI: 10.5194/gmd-9-875-2016, 2016.

Bogumil, K., Orphal, J., Homann, T., Voigt, S., Spietz, P., Fleischmann, O., Vogel, A., Hartmann, M., Kromminga, H., Bovensmann, H., Frerick, J., and Burrows, J.: Measurements of molecular absorption spectra with the {SCIAMACHY} pre-flight model: instrument characterization and reference data for atmospheric remote-sensing in the 230–2380 nm region, Journal of Photochemistry and Photobiology A: Chemistry, 157, 167–184, DOI: 10.1016/S1010-6030(03)00062-5, atmospheric Photochemistry, 2003.

Bond, D., Steiger, S., Zhang, R., Tie, X., and Orville, R.: The importance of NOx production by lightning in the tropics, Atmos. Environ., 36, 1509–1519, DOI: 10.1016/S1352-2310(01)00553-2, 2002.

Bontemps, S., Defourny, P., Van Bogaert, E., Arino, O., Kalogirou, V., Perez, R., and Julio, J.: GLOBCOVER 2009 - Products description and validation report, p. 53 pp, vers. 2.2, 2011.

Bouwman, A., Boumans, L., and Batjes, N.: Emissions of N2O and NO from fertilized fields: Summary of available measurement data, Global Biogeochem. Cy., 16, 1058, DOI: 10.1029/2001GB001811, 2002.

Bovensmann, H., Burrows, J. P., Buchwitz, M., Frerick, J., L, S. N., Rozanov, V. V., Chance, K. V., and Goede, A. P. H.: SCIAMACHY - Mission objectives and measurement modes, J. Atmos. Sciences, 56, 125–150, DOI: 10.1175/1520-0469(1999)056<0127:SMOAMM>2.0.CO;2, 1999.

Burrows, J., Platt, U., and Borrell, P.: Tropospheric Remote Sensing from Space, Springer Verlag, Heidelberg, DOI: 10.1007/978-3-642-14791-3, 2011.

Calcagno, V. and de Mazancourt, C.: glmulti: An R Package for Easy Automated Model Selection with (Generalized) Linear Models, Journal of Statistical Software, 34, 1–29, DOI: 10.18637/jss.v034.i12, 2010.

Callies, J., Corpaccioli, E., Eisinger, M., Hahne, A., and Lefebvre, A.: GOME-2 - METOP's second-generation sensor for operational ozone monitoring, ESA Bull., 102, 28–36, 2000.

Cantrell, C. A.: Technical Note: Review of methods for linear least-squares fitting of data and application to atmospheric chemistry problems, Atmospheric Chemistry and Physics, 8, 5477–5487, DOI: 10.5194/acp-8-5477-2008, 2008.

Carlier, P., Hannachi, H., and Mouvier, G.: The chemistry of carbonyl compounds in the atmosphere - a review, Atmos. Environ., 20 (11), 2079–2099, 1986.

Coe, M. T. and Foley, J. A.: Human and natural impacts on the water resources of the Lake Chad basin, Journal of Geophysical Research: Atmospheres, 106, 3349–3356, DOI: 10.1029/2000JD900587, URL http://dx.doi.org/10.1029/2000JD900587, 2001.

Conrad, R.: Soil microorganisms as controllers of atmospheric trace gases (H2, CO, CH4, OCS, N2O, and NO), Microbiol Rev., 60, 609–640, 1996.

Cox, C. and Wathes, C.: Bioaerosols Handbook, CRC Press, 1995.

Crutzen, P. J. and Andreae, M. O.: Biomass burning in the tropics - impact on atmospheric chemistry and biogeochemical cycles, Science, 250(4988), 1669–1678, 1990.

Davidson, E. A.: Pulses of Nitric Oxide and Nitrous Oxide Flux following Wetting of Dry Soil: An Assessment of Probable Sources and Importance Relative to Annual Fluxes, Ecol. Bull., 42, 149–155, URL http://www.jstor.org/stable/20113115, 1992a.

Davidson, E. A.: Sources of Nitric Oxide and Nitrous Oxide following Wetting of Dry Soil, Soil Sci. Soc. Am. J., 56, DOI: 10.2136/sssaj1992.03615995005600010015x, 1992b.

Davidson, E. A., Vitousek, P. M., Matson, P. A., Riley, R., García-Méndez, G., and Maass, J. M.: Soil emissions of nitric oxide in a seasonally dry tropical forest of México, Journal of Geophysical Research: Atmospheres, 96, 15 439–15 445, DOI: 10.1029/91JD01476, 1991.

De Smedt, I., Müller, J.-F., Stavrakou, T., van der A, R., Eskes, H., and Van Roozendael, M.: Twelve years of global observations of formaldehyde in the troposphere using GOME and SCIAMACHY sensors, Atmos. Chem. Phys., 8, 4947–4963, DOI: 10.5194/acp-8-4947-2008, 2008.

De Smedt, I., Van Roozendael, M., Stavrakou, T., Müller, J.-F., Lerot, C., Theys, N., Valks, P., Hao, N., and van der A, R.: Improved retrieval of global tropospheric formaldehyde columns from GOME-2/MetOp-A addressing noise reduction and instrumental degradation issues, Atmos. Meas. Tech., 5, 2933–2949, DOI: 10.5194/amt-5-2933-2012, 2012.

Dee, D. P., Uppala, S. M., Simmons, A. J., Berrisford, P., Poli, P., Kobayashi, S., Andrae, U., Balmaseda, M. A., Balsamo, G., Bauer, P., Bechtold, P., Beljaars, A. C. M., van de Berg, L., Bidlot, J., Bormann, N., Delsol, C., Dragani, R., Fuentes, M., Geer, A. J., Haimberger, L.,

Healy, S. B., Hersbach, H., Hólm, E. V., Isaksen, L., Kållberg, P., Köhler, M., Matricardi, M., McNally, A. P., Monge-Sanz, B. M., Morcrette, J.-J., Park, B.-K., Peubey, C., de Rosnay, P., Tavolato, C., Thépaut, J.-N., and Vitart, F.: The ERA-Interim reanalysis: configuration and performance of the data assimilation system, Q. J. Roy. Meteor. Soc., 137, 553–597, DOI: 10.1002/qj.828, 2011.

Delon, C., Galy-Lacaux, C., Boone, A., Liousse, C., Serça, D., Adon, M., Diop, B., Akpo, A., Lavenu, F., Mougin, E., and Timouk, F.: Atmospheric nitrogen budget in Sahelian dry savannas, Atmos. Chem. Phys., 10, 2691–2708, DOI: 10.5194/acp-10-2691-2010, 2010.

Denman, K. L., Brasseur, G. P., Chidthaisong, A., Ciais, P., Cox, P. M., Dickinson, R. E., Hauglustaine, D. A., Heinze, C., Holland, E. A., Jacob, D. J., Lohmann, U., Ramachandran, S., da Silva Dias, P., Wofsy, S., and Zhang, X.: Couplings between changes in the climate system and biogeochemistry, in: Climate Change 2007: The Physical Science Basis. Contribution of Working Group I to the Fourth Assessment Report of the Intergovernmental Panel on Climate Change, Cambridge University Press, Cambridge, United Kingdom and New York, NY, USA, 2007.

Dowden, R., Brundell, J., and Rodger, C.: VLF lightning location by time of group arrival (TOGA) at multiple sites, J. Atmos. Sol.-Terr. Phy., 64, 817–830, DOI: 10.1016/S1364-6826(02)00085-8, 2002.

Ebert, E. E., Janowiak, J. E., and Kidd, C.: Comparison of Near-Real-Time Precipitation Estimates from Satellite Observations and Numerical Models, B. Am. Meteorol. Soc., 88, 47–64, DOI: 10.1175/BAMS-88-1-47, 2007.

EEA: Air quality in Europe — 2015 report, eEA Report No 5/2014, 2015a.

EEA: State of Environment Report - The European environment - state and outlook 2015, 2015b.

EUMETSAT: GOME-2 Product Guide, URL http://www.eumetsat.int/website/wcm/idc/idcplg?IdcService=GET_FILE&dDocName=PDF_V2C_GOME_2_PRODUCTS_GUIDE&RevisionSelectionMethod=LatestReleased&Rendition=Web, accessed: 10/01/2016, 2011.

Evans, R. and Ehleringer, J.: A break in the nitrogen cycles in aridlands? evidence from δp15N of soils, Oecologia, 94, 314–317, DOI: 10.1007/BF00317104, 1993.

FAO: Adaptive Water Management in the Lake Chad Basin, in: Addressing Current Challenges and Adapting Future Needs, FAO WATER, Stockholm, 2009.

Fayt, C. and van Roozendael, M.: Windoas 2.1. software user manual, ISAB/BIRA, Belgium, URL http://www.oma.be/BIRA-IASB, 2001.

Finlayson-Pitts, B. J. and Pitts, J. N., eds.: Chemistry of the Upper and Lower Atmosphere, Academic Press, San Diego, 1st edn., DOI: http://dx.doi.org/10.1016/B978-0-12-257060-5.50026-5, 2000.

Fleischmann, O., Hartmann, M., Burrows, J., and Orphal, J.: New ultraviolet absorption cross-sections of BrO at atmospheric temperatures measured by a time-windowing Fourier transform spectroscopy, J. Photochem. Photobiol. A.: Chem., 168, 117–132, 2004.

Ganzeveld, L., Lelieveld, J., Dentener, F., Krol, M., A.J., B., and G.-J., R.: Global soil-biogenic NO_x emissions and the role of canopy processes, J. Geophys. Res., 107, DOI: 10.1029/2001JD001289, 2002.

Ghude, S. D., Lal, D. M., Beig, G., van der A, R., and Sable, D.: Rain-Induced Soil NOx Emission From India During the Onset of the Summer Monsoon: A Satellite Perspective, J. Geophys. Res., 115, D16 304, DOI: 10.1029/2009JD013367, 2010.

Giglio, L., Csiszar, I., and Justice, C. O.: Global distribution and seasonality of active fires as observed with the Terra and Aqua Moderate Resolution Imaging Spectroradiometer (MODIS) sensors, J. Geophys. Res., 111, DOI: 10.1029/2005jg000142, 2006.

GIZ: Joint Environmental Audit on the Drying up of Lake Chad, Joint audit report, Deutsche Gesellschaft für Internationale Zusammenarbeit (GIZ) GmbH, 2015.

Gniffke, P.: National Trend Tables for the German Atmospheric Emission Reporting 1990–2014, Umweltbundesamt, Dessau, Germany, 2016.

Gottwald, M., Bovensmann, H., Lichtenberg, G., Noel, S., von Bargen, A., Slijkhuis, S., Piters, A., Hoogeveen, R., von Savigny, C., Buchwitz, M., Kokhanovsky, A., Richter, A., Rozanov, A. and, H.-P. T. a. B. K., Lambert, J.-C., Skupin, J., Wittrock, F., Schrijver, H., and Burrows, J.: SCIAMACHY, Monitoring the Changing Earth's Atmosphere, Published by DLR, 2006.

Grainger, J. F. and Ring, J.: Anomalous Fraunhofer Line Profiles, Nature, 193, 762–762, DOI: dx.doi.org/10.1038/193762a0, 1962.

Grantz, D. A., Gunn, S., and Vu, H.-B.: O3 impacts on plant development: a meta-analysis of root/shoot allocation and growth, Plant, Cell & Environment, 29, 1193–1209, DOI: 10.1111/j.1365-3040.2006.01521.x, 2006.

Gray, C. M., Monson, R. K., and Fierer, N.: Emissions of volatile organic compounds during the decomposition of plant litter, Journal of Geophysical Research: Biogeosciences, 115, DOI: 10.1029/2010JG001291, 2010.

Greene, W. H.: Econometric Analysis, Pearson Education, Inc., Upper Saddle River, New Jersey, 5th edn., 2003.

Grossi, M., Valks, P., Loyola, D., Aberle, B., Slijkhuis, S., Wagner, T., Beirle, S., and Lang, R.: Total column water vapour measurements from GOME-2 MetOp-A and MetOp-B, Atmos. Meas. Tech., 8, 1111–1133, DOI: 10.5194/amt-8-1111-2015, 2015.

Guenzi, W. D., Hutchinson, G. L., and Beard, W. E.: Nitric and Nitrous Oxide Emissions and Soil Nitrate Distribution in a Center-Pivot-Irrigated Cornfield, J. Environ. Qual., 23, 483–487, DOI: 10.2134/jeq1994.00472425002300030011x, 1994.

Heck, W., Heagle, A., and Shriner, D.: Effects on Vegetation: Native, Crops, Forests, in: Air Pollution 3rd Edition, edited by Stern, A., vol. Vol. VI, pp. 248–333, Academic Press, New York, NY, 1986.

Hendrick, F., Müller, J.-F., Clémer, K., Wang, P., De Mazière, M., Fayt, C., Gielen, C., Hermans, C., Ma, J. Z., Pinardi, G., Stavrakou, T., Vlemmix, T., and Van Roozendael, M.: Four years of ground-based MAX-DOAS observations of HONO and NO₂ in the Beijing area, Atmospheric Chemistry and Physics, 14, 765–781, DOI: 10.5194/acp-14-765-2014, 2014.

Höfling, R.: Böden und Bodenschätze, in: Landkreis Donau-Ries, Landkreis Donau-Ries, Donauwörth, 1991.

Hodan, W. and Barnard, W.: Evaluating the Contribution of PM2.5 Precursor Gases and Re-entrained Road Emissions to Mobile Source PM2.5 Particulate Matter Emissions, URL Availableatwww.epa.gov/ttnchie1/conference/ei13/mobile/hodan.pdf. AccessedAugust13,2016, prepared by MACTEC Under Contract to the Federal Highway Administration, 2004.

Hönninger, G. and Platt, U.: Observations of BrO and its vertical distribution during surface ozone depletion at Alert, Atmospheric Environment, 36, 2481–2489, DOI: 10.1016/S1352-2310(02)00104-8, air/Snow/Ice Interactions in the Arctic: Results from {ALERT} 2000 and {SUMMIT} 2000, 2002.

Hönninger, G., von Friedeburg, C., and Platt, U.: Multi axis differential optical absorption spectroscopy (MAX-DOAS), Atmospheric Chemistry and Physics, 4, 231–254, DOI: 10.5194/acp-4-231-2004, 2004.

Hüttner, R. and Schmidt-Kaler, H.: Meteoritenkrater Nördlinger Ries, vol. 10 of *Wanderungen in die Erdgeschichte*, Pfeil, Munich, 2003.

Hudman, R., Moore, N., Mebust, A., Martin, R., Russel, A., Valin, L., and Cohen, R.: Steps towards a mechanistic model of global soil nitric oxide emissions: implementation and space based constraints, Atmos. Chem. Phys., 12, 7779–7795, DOI: 10.5194/acp-12-7779-2012, 2012.

Huffman, G. J., Bolvin, D. T., Nelkin, E. J., Wolff, D. B., Adler, R. F., Gu, G., Hong, Y., Bowman, K. P., and Stocker, E. F.: The TRMM Multisatellite Precipitation Analysis (TMPA): Quasi-Global, Multiyear, Combined-Sensor Precipitation Estimates at Fine Scales, J. Hydrometeorol., 8, 38–55, DOI: 10.1175/JHM560.1, 2007.

Isodorov, R. S. and Jdanova, M.: Volatile organic compounds from leaves litter, Chemosphere, 48, 975–979, 2002.

Jacob, D. J.: Introduction to Atmospheric Chemistry, Princeton University Press, 1999.

Jaeglé, L., Martin, R. V., Chance, K., Steinberger, L., Kurosu, T. P., Jacob, D. J., Modi, A. I., Yoboué, V., Sigha-Nkamdjou, L., and Galy-Lacaux, C.: Satellite mapping of rain-induced nitric oxide emissions from soils, J. Geophys. Res.-Atmos., 109, DOI: 10.1029/2004JD004787, 2004.

Jaegle, L., Steinberger, L., Martin, R. V., and Chance, K.: Global partitioning of NOx sources using satellite observations: Relative roles of fossil fuel combustion, biomass burning and soil emissions, Faraday Discuss., 130, 407–423, DOI: 10.1039/B502128F, 2005.

Jain, A. K., Tao, Z., Yang, X., and Gillespie, C.: Estimates of global biomass burning emissions for reactive greenhouse gases (CO, NMHCs, and NOx) and CO2, Journal of Geophysical Research: Atmospheres, 111, DOI: 10.1029/2005JD006237, d06304, 2006.

Jäkel, D.: Rainfall Patterns and Lake Level Variations at Lake Chad, pp. 191–200, Springer Netherlands, Dordrecht, DOI: 10.1007/978-94-015-7692-5_19, 1984.

Johansson, C. and Sanhueza, E.: Emission of NO from savanna soils during rainy season, J. Geophys. Res., 93, 14 193–14 198, 1988.

Joyce, R., Janowiak, J., Arkin, P., and Xie, P.: CMORPH: A method that produces global precipitation estimates from passive microwave and infrared data at high spatial and temporal resolution, J. Hydromet., 5, 487–503, 2004.

Kesselmeier, J.: Exchange of Short-Chain Oxygenated Volatile Organic Compounds (VOCs) between Plants and the Atmosphere: A Compilation of Field and Laboratory Studies, Journal of Atmospheric Chemistry, 39, 219–233, DOI: 10.1023/A:1010632302076, 2001.

Kim, D.-G., Vargas, R., Bond-Lamberty, B., and Turetsky, M. R.: Effects of soil rewetting and thawing on soil gas fluxes: a review of current literature and suggestions for future research, Biogeosciences, 9, 2459–2483, DOI: 10.5194/bg-9-2459-2012, 2012.

Kirkman, G. A., Yang, W. X., and Meixner, F. X.: Biogenic nitric oxide emissions upscaling: An approach for Zimbabwe, Global Biogeochemical Cycles, 15, 1005–1020, DOI: 10.1029/2000GB001287, 2001.

Kleft, T. L., Soroker, E., and Firestone, M. K.: Microbial biomass response to a rapid increase in water potential when dry soil is wetted, Soil Biol. Biochem., 19, 119–126, 1987.

Koren, I., Kaufman, Y. J., Washington, R., Todd, M. C., Rudich, Y., Martins, J. V., and Rosenfeld, D.: The Bodélé depression: a single spot in the Sahara that provides most of the mineral dust to the Amazon forest, Environmental Research Letters, 1, 014 005, DOI: 10.1088/1748-9326/1/1/014005, 2006.

Kraus, S.: DOASIS a framework design for DOAS, Ph.D. thesis, 2006.

Krupa, S., Tuttle McGrath, M., Andersen, C. P., Booker, F. L., Burkey, K. O., Chappelka, A. H., Chevone, B. I., Pell, E. J., and Zilinskas, B. A.: Ambient Ozone and Plant Health, Plant Disease, 85:1, 4–12, 2001.

Kurucz, R. L., Furenlid, I., Brault, J., and Testerman, L.: Solar flux atlas from 296nm to 1300nm, in: National Solar Observatory Atlas, vol. No. 1, 1984.

Lay, E. H., Holzworth, R. H., Rodger, C. J., Thomas, J. N., Pinto, O., and Dowden, R. L.: WWLL global lightning detection system: Regional validation study in Brazil, Geophysical Research Letters, 31, DOI: 10.1029/2003GL018882, l03102, 2004.

Lebel, T. and Ali, A.: Recent trends in the Central and Western Sahel rainfall regime (1990-2007), J. Hydrol., 375, 52–64, DOI: 10.1016/j.jhydrol.2008.11.030, 2009.

Leff, J. W. and Fierer, N.: Volatile organic compound (VOC) emissions from soil and litter samples, Soil Biology and Biochemistry, 40, 1629 – 1636, DOI: http://dx.doi.org/10.1016/j.soilbio.2008.01.018, 2008.

Lelieveld, J., Evans, J. S., Fnais, M., Giannadaki, D., and Pozzer, A.: The contribution of outdoor air pollution sources to premature mortality on a global scale, Nature, 525, 367–371, DOI: 10.1038/nature15371, 2015.

Lemoalle, J., Bader, J.-C., Leblanc, M., and Sedick, A.: Recent changes in Lake Chad: Observations, simulations and management options (1973–2011), Global and Planetary Change, 80–81, 247 – 254, DOI: http://dx.doi.org/10.1016/j.gloplacha.2011.07.004, 2012.

Leue, C., Wenig, M., Wagner, T., Klimm, O., Platt, U., and Jähne, B.: Quantitative analysis of NO x emissions from Global Ozone Monitoring Experiment satellite image sequences, J. Geophys. Res.-Atmos., 106, 5493–5505, DOI: 10.1029/2000JD900572, 2001.

Levelt, P., van den Oord, B., Hilsenrath, E., Leppelmeier, G., Bhartia, P., Malkki, A., Kelder, H., van der A, R., Brinksma, E., van Oss, R., Veefkind, P., van Weele, M., and Noordhoek, R.: Science Objectives Of Eos-Aura's Ozone Monitoring Instrument (OMI), 2000.

Levelt, P., van den Oord, G., Dobber, M., Malkki, A., Visser, H., de Vries, J., Stammes, P., Lundell, J., and Saari, H.: The ozone monitoring instrument, IEEE T. Geosci. Remote., 44, 1093–1101, DOI: 10.1109/TGRS.2006.872333, 2006.

Levenberg, K.: A method for the solution of certain non-linear problems in least squares, Quart. Appl. Math., 2, 164–168, 1944.

Levine, J. S., Winstead, E. L., Parsons, D. A. B., Scholes, M. C., Scholes, R. J., Cofer III, W. R., Cahoon Jr., D. R., and Sebacher, D. I.: Biogenic soil emissions of nitric oxide (NO) and nitrous oxide (N2O) from savannas in South Africa: The impact of wetting and burning, J. Geophys. Res., 101, 23 689–23 697, DOI: 10.1029/96JD01661, 1996.

Li, G., Su, H., Li, X., Kuhn, U., Meusel, H., Hoffmann, T., Ammann, M., Pöschl, U., Shao, M., and Cheng, Y.: Uptake of gaseous formaldehyde by soil surfaces: a combination of

adsorption/desorption equilibrium and chemical reactions, Atmospheric Chemistry and Physics, 16, 10 299–10 311, DOI: 10.5194/acp-16-10299-2016, 2016.

Liu, J., Duan, Z., Jiang, J., , and Zhu, A.-X.: Evaluation of Three Satellite Precipitation Products TRMM 3B42, CMORPH, and PERSIANN over a Subtropical Watershed in China, Advances in Meteorology, DOI: 10.1155/2015/151239, 2012.

Ludwig, J., Meixner, F., Vogel, B., and Forstner, J.: Soil-air exchange of nitric oxide: an overview of processes, environmental factors, and modeling studies, Biogeochemistry, 52, 225–257, DOI: 10.1023/A:1006424330555, 2001.

Mamtimin, B., Behrendt, T., Badawy, M. M., Wagner, T., Qi, Y., Wu, Z., and Meixner, F. X.: Tropospheric vertical column densities of NO2 over managed dryland ecosystems (Xinjiang, China): MAX-DOAS measurements vs. 3-D dispersion model simulations based on laboratory-derived NO emission from soil samples, Atmospheric Chemistry and Physics, 15, 867–882, DOI: 10.5194/acp-15-867-2015, 2015.

Mamtimin, B., Meixner, F. X., Behrendt, T., Badawy, M., and Wagner, T.: The contribution of soil biogenic NO and HONO emissions from a managed hyperarid ecosystem to the regional NOx emissions during growing season, Atmospheric Chemistry and Physics, 16, 10 175–10 194, DOI: 10.5194/acp-16-10175-2016, 2016.

Marquardt, D. W.: An algorithm for least squares estimation of non-linear parameters, Soc. Indust. Appl. Math, 11, 431–441, 1963.

Martin, R.: Global inventory of nitrogen oxide emissions constrained by space-based observations of NO2 columns, J. Geophys. Res., 108, 4537, DOI: 10.1029/2003JD003453, 2003.

Meixner, F. and Yang, W.: Biogenic emissions of nitric oxide and nitrous oxide from arid and semi-arid land, in: Dryland Eco-hydrology, edited by D'Odorico, P. and Porporat, A., pp. 233–255, Springer, Dordrecht, 2006.

Meller, R. and Moortgat, G. K.: Temperature dependence of the absorption cross sections of formaldehyde between 223 and 323 K in the wavelength range 225–375 nm, Journal of Geophysical Research: Atmospheres, 105, 7089–7101, DOI: 10.1029/1999JD901074, 2000.

Merry, R.: Acidity and alkalinity of soils, in: Environmental and Ecological Chemistry, vol. 2, UNESCO-EOLSS Publishers, Paris, France, ed Sabljic A, 2009.

Mie, G.: Beiträge zur Optik trüber Medien, speziell kolloidaler Metallösungen, Ann. Phys., pp. 377–445, DOI: 10.1002/andp.19083300302, 1908.

Miyazaki, K., Eskes, H. J., Sudo, K., and Zhang, C.: Global lightning NO_x production estimated by an assimilation of multiple satellite data sets, Atmospheric Chemistry and Physics, 14, 3277–3305, DOI: 10.5194/acp-14-3277-2014, URL http://www.atmos-chem-phys.net/14/3277/2014/, 2014.

Müller, L., Schindler, U., Behrendt, A., Eulenstein, F., and Dannowski, R.: The Müncheberg Soil Quality Rating. Field Manual for Detecting and Assessing Properties and Limitations of Soils for Cropping and Grazing, vol. 1. Entwurf, Leibniz-Zentrum für Agrarlandschaftsforschung (ZALF), Müncheberg, 2007.

Monks, P. S.: Gas-phase radical chemistry in the troposphere, Chem. Soc. Rev., 34, 376–395, DOI: 10.1039/B307982C, 2005.

Munro, R., Eisinger, M., Anderson, C., Callies, J., Corpaccioli, E., Lang, R., Lefebvre, A., Livschitz, Y., and Albiñana, A. P.: GOME-2 on MetOp, in: Proc. of The 2006 EUMETSAT Meteorological Satellite Conference, Helsinki, Finland, 12–16 June 2006, EUMETSAT, p. 48, 2006.

Murray, L. T., Jacob, D. J., Logan, J. A., Hudman, R. C., and Koshak, W. J.: Optimized regional and interannual variability of lightning in a global chemical transport model constrained by LIS/OTD satellite data, J. Geophys. Res., 117, DOI: 10.1029/2012JD017934, 2012.

Nicholson, S. E.: Dryland Climatology, Cambridge University Press, DOI: 10.1017/CBO9780511973840, cambridge Books Online, 2011.

Noël, S., Bovensmann, H., Wuttke, M., Burrows, J., Gottwald, M., Krieg, E., and Mager, R.: SCIAMACHY nominal operations and special features, in: Proc. ERS-ENVISAT symposium Gothenburg, cDROM (SP-461), 2000.

Novella, N. and Thiaw, W.: Validation of Satellite-Derived Rainfall Products over the Sahel, Wyle Information Systems/CPC/NOAA, pp. 1–9, URL https://www.eumetsat.int/website/wcm/idc/idcplg?IdcService=GET_FILE&dDocName=PDF_CONF_P55_S6_32_NOVELLA_P&RevisionSelectionMethod=LatestReleased&Rendition=Web, accessed 2016 July 25, 2010.

Noxon, J. F., Whipple, E. C., and Hyde, R. S.: Stratospheric NO2. 1. Observational method and behaviour at midlatitudes., 84, 5047–5076, 1979.

O'brien, R. M.: A Caution Regarding Rules of Thumb for Variance Inflation Factors, Quality & Quantity, 41, 673–690, DOI: 10.1007/s11135-006-9018-6, 2007.

OECD: The Cost of Air Pollution, DOI: 10.1787/9789264210448-en, 2014.

Oikawa, P. Y., Ge, C., Wang, J., Eberwein, J. R., Liang, L. L., Allsman, L. A., Grantz, D. A., and Jenerette, G. D.: Unusually high soil nitrogen oxide emissions influence air quality in a high-temperature agricultural region, Nat. Commun., 6, DOI: 10.1038/ncomms9753, 2015.

Oswald, R., Behrendt, T., Ermel, M., Wu, D., Su, H., Cheng, Y., Breuninger, C., Moravek, A., Mougin, E., Delon, C., Loubet, B., Pommerening-Röser, A., Sörgel, M., Pöschl, U., Hoffmann, T., Andreae, M., Meixner, F., and Trebs, I.: HONO Emissions from Soil

Bacteria as a Major Source of Atmospheric Reactive Nitrogen, Science, 341, 1233–1235, DOI: 10.1126/science.1242266, 2013.

Palmer, P. I., Jacob, D. J., Chance, K., Martin, R. V., Spurr, R. J. D., Kurosu, T. P., Bey, I., Yantosca, R., Fiore, A., and Li, Q.: Air mass factor formulation for spectroscopic measurements from satellites: Application to formaldehyde retrievals from the Global Ozone Monitoring Experiment, J. Geophys. Res.-Atmos., 106, 14 539–14 550, DOI: 10.1029/2000JD900772, 2001.

Perner, D., Ehhalt, D. H., Pätz, H. W., Platt, U., Röth, E. P., and Volz, A.: OH-radicals in the lower troposphere, Geophys. Res. Lett., 3, 466–468, 1976.

Petetin, H., Sciare, J., Bressi, M., Gros, V., Rosso, A., Sanchez, O., Sarda-Estève, R., Petit, J.-E., and Beekmann, M.: Assessing the ammonium nitrate formation regime in the Paris megacity and its representation in the CHIMERE model, Atmospheric Chemistry and Physics, 16, 10 419–10 440, DOI: 10.5194/acp-16-10419-2016, 2016.

Peñuelas, J., Asensio, D., Tholl, D., Wenke, K., Rosenkranz, M., Piechulla, B., and Schnitzler, J.: Biogenic volatile emissions from the soil, Plant, Cell & Environment, 37, 1866–1891, DOI: 10.1111/pce.12340, 2014.

Pfeifroth, U., Trentmann, J., Fink, A. H., and Ahrens, B.: Evaluating Satellite-Based Diurnal Cycles of Precipitation in the African Tropics, J. Appl. Meteorol. Clim., 55, 23–39, DOI: 10.1175/JAMC-D-15-0065.1, 2016.

Pilegaard, K.: Processes regulating nitric oxide emissions from soils, Philos. T. Roy. Soc. B, 368, DOI: 10.1098/rstb.2013.0126, 2013.

Pipunic, R. C., Ryu, D. R., Costelloe, J., and Su, C.-H.: Evaluation of real-time satellite rainfall products in semi-arid/arid Australia, in: Piantadosi, J., Anderssen, R.S. and Boland J. (eds) MODSIM2013, pp. 3106–3112, Australia Modelling & Simulation Society of Australia & New Zealand, Canberra, Australia, 2013.

Platt, U. and Stutz, J.: Differential Optical Absorption Spectroscopy: Principles and Applications, Physics of Earth and Space Environments Series, Springer-Verlag Berlin Heidelberg, 2008.

Platt, U., Perner, D., and Pätz, H. W.: Simultaneous measurements of atmospheric CH2O, O3 and NO2 by differential optical absortion, J. Geophys. Res., 84, 6329–6335, 1979.

Pusede, S. E., Duffey, K. C., Shusterman, A. A., Saleh, A., Laughner, J. L., Wooldridge, P. J., Zhang, Q., Parworth, C. L., Kim, H., Capps, S. L., Valin, L. C., Cappa, C. D., Fried, A., Walega, J., Nowak, J. B., Weinheimer, A. J., Hoff, R. M., Berkoff, T. A., Beyersdorf, A. J., Olson, J., Crawford, J. H., and Cohen, R. C.: On the effectiveness of nitrogen oxide reductions as a control over ammonium nitrate aerosol, Atmospheric Chemistry and Physics, 16, 2575–2596, DOI: 10.5194/acp-16-2575-2016, 2016.

Richter, A. and Burrows, J.: Retrieval of Tropospheric NO2 from GOME Measurements, Adv. Space Res., 29, 1673–1683, 2002.

Richter, A. and Wagner, T.: Solar Backscattered Radiation: UV, Visible and Near IR - Trace Gases, Springer Verlag, Heidelberg, DOI: 10.1007/978-3-642-14791-3, 2011.

Rodger, C. J., Werner, S., Brundell, J. B., Lay, E. H., Thomson, N. R., Holzworth, R. H., and Dowden, R. L.: Detection efficiency of the VLF World-Wide Lightning Location Network (WWLLN): initial case study, Ann. Geophys., 24, 3197–3214, DOI: 10.5194/angeo-24-3197-2006, 2006.

Rodgers, C. D.: Inverse methods for atmospheric sounding, theory and practice, in: Series on Atmospheric, Oceanic and Planetary Physics, World Scientific, 2000.

Romilly, T. G. and Gebremichael, M.: Evaluation of satellite rainfall estimates over Ethiopian river basins, Hydrol. Earth. Syst. Sc., 15, 1505–1514, DOI: 10.5194/hess-15-1505-2011, 2011.

Rothman, L., Jacquemart, D., Barbe, A., Benner, D. C., Birk, M., Brown, L., Carleer, M., Jr., C. C., Chance, K., Coudert, L., Dana, V., Devi, V., Flaud, J.-M., Gamache, R., Goldman, A., Hartmann, J.-M., Jucks, K., Maki, A., Mandin, J.-Y., Massie, S., Orphal, J., Perrin, A., Rinsland, C., Smith, M., Tennyson, J., Tolchenov, R., Toth, R., Auwera, J. V., Varanasi, P., and Wagner, G.: The {HITRAN} 2004 molecular spectroscopic database, Journal of Quantitative Spectroscopy and Radiative Transfer, 96, 139 – 204, DOI: http://dx.doi.org/10.1016/j.jqsrt.2004.10.008, 2005.

Rozanov, A., Rozanov, V., Buchwitz, M., Kokhanovsky, A., and Burrows, J.: SCIATRAN 2.0 - A new radiative transfer model for geophysical applications in the 175-2400 nm spectral region, in: Atmospheric Remote Sensing: Earth's Surface, Troposphere, Stratosphere and Mesosphere - I, ADVANCES IN SPACE RESEARCH, edited by Burrows, J. and Eichmann, K., vol. 36, pp. 1015–1019, 2005.

Running, S. W.: Estimating Terrestrial Primary Productivity by Combining Remote Sensing and Ecosystem Simulation, pp. 65–86, Springer, New York, NY, DOI: $10.1007/978-1-4612-3302-2_4$, 1990.

Schindlbacher, A., Zechmeister-Boltenstern, S., and Butterbach-Bahl, K.: Effects of soil moisture and temperature on NO, NO2, and N2O emissions from European forest soils, Journal of Geophysical Research: Atmospheres, 109, DOI: 10.1029/2004JD004590, d17302, 2004.

Schneider, T., Bischoff, T., and Haug, G. H.: Migrations and dynamics of the intertropical convergence zone, Nature, 513, 45–53, DOI: 10.1038/nature13636, 2014.

Scholes, M., Martin, R., Scholes, R., Parsons, D., and Winstead, E.: NO and N2O emissions from savanna soils following the first simulated rains of the season., Nutr. Cycl. Agroecosys., 48, 115–122, DOI: 10.1023/a:1009781420199, 1997.

Schumann, U. and Huntrieser, H.: The global lightning-induced nitrogen oxides source, Atmos. Chem. Phys., 7, 3823–3907, DOI: 10.5194/acp-7-3823-2007, 2007.

Seinfeld, J. H. and Pandis, S. N.: Atmospheric Chemistry and Physics: From Air Pollution to Climate Change, Wiley-Interscience, Hoboken, New Jersey, 2 edn., 2006.

Shoemaker, E. M. and Chao, E. C. T.: New evidence for the impact origin of the Ries Basin, Bavaria, Germany, Journal of Geophysical Research, 66, 3371–3378, DOI: 10.1029/JZ066i010p03371, 1961.

Sillman, S., Logan, J. A., and Wofsy, S. C.: The sensitivity of ozone to nitrogen oxides and hydrocarbons in regional ozone episodes, Journal of Geophysical Research: Atmospheres, 95, 1837–1851, DOI: 10.1029/JD095iD02p01837, 1990.

Singh, H. B. and Hanst, P. L.: Peroxyacetyl nitrate (PAN) in the unpolluted atmosphere: An important reservoir for nitrogen oxides, Geophysical Research Letters, 8, 941–944, DOI: 10.1029/GL008i008p00941, 1981.

Sinreich, R.: Multi-Axis Differential Optical Absorption Spectroscopy Measurements in Polluted Environments, Ph.D. thesis, Ruperto-Carola University of Heidelberg, Germany, Heidelberg, Germany, 2008.

Solomon, S., Schmeltekopf, A. L., and Sanders, R. W.: On the interpretafion of zenith sky absorption measurements, J. Geophys. Res., 92, 8311–8319, 1987.

Sorooshian, S., Hsu, K.-L., Gao, X., Gupta, H. V., Imam, B., and Braithwaite, D.: Evaluation of PERSIANN System Satellite–Based Estimates of Tropical Rainfall, Bulletin of the American Meteorological Society, 81, 2035–2046, DOI: 10.1175/1520-0477(2000)081<2035:EOPSSE>2.3.CO;2, 2000.

Stavrakou, T., Müller, J.-F., Boersma, K. F., De Smedt, I., and van der A, R. J.: Assessing the distribution and growth rates of NOx emission sources by inverting a 10-year record of NO2 satellite columns, Geophysical Research Letters, 35, DOI: 10.1029/2008GL033521, l10801, 2008.

Stavrakou, T., Müller, J.-F., Boersma, K. F., van der A, R. J., Kurokawa, J., Ohara, T., and Zhang, Q.: Key chemical NOx sink uncertainties and how they influence top-down emissions of nitrogen oxides, Atmospheric Chemistry and Physics, 13, 9057–9082, DOI: 10.5194/acp-13-9057-2013, 2013.

Stehfest, E. and Bouwman, L.: N2O and NO emission from agricultural fields and soils under natural vegetation: summarizing available measurement data and modeling of global annual emissions, Nutrient Cycling in Agroecosystems, 74, 207–228, DOI: 10.1007/s10705-006-9000-7, 2006.

Steinkamp, J. and Lawrence, M. G.: Improvement and evaluation of simulated global biogenic soil NO emissions in an AC-GCM, Atmos. Chem. Phys., 11, 6063–6082, DOI: 10.5194/acp-11-6063-2011, 2011.

Steinkamp, J., Ganzeveld, L. N., Wilcke, W., and Lawrence, M. G.: Influence of modelled soil biogenic NO emissions on related trace gases and the atmospheric oxidizing efficiency, Atmos. Chem. Phys., 9, 2663–2677, DOI: 10.5194/acp-9-2663-2009, 2009.

Strutt, J. W.: On the Transmission of Light through an Atmosphere containing Small Particles in Suspension, and on the Origin of the Blue of the Sky, in: Scientific Papers, vol. 4, Cambridge Library Collection - Mathematics, Cambridge University Press, reprinted in 2009, 1899.

Stull, R.: An Introduction to Boundary Layer Meteorology (Atmospheric Sciences Library), Kluwer Academic Publishers, Dordrecht, 1988.

Su, H., Cheng, Y., Oswald, R., Behrendt, T., Trebs, I., Meixner, F. X., Andreae, M. O., Cheng, P., Zhang, Y., and Pöschl, U.: Soil Nitrite as a Source of Atmospheric HONO and OH Radicals, Science, 333, 1616–1618, DOI: 10.1126/science.1207687, 2011.

Thalman, R. and Volkamer, R.: Temperature dependent absorption cross-sections of O2-O2 collision pairs between 340 and 630 nm and at atmospherically relevant pressure, Phys. Chem. Chem. Phys., 15, 15 371–15 381, DOI: 10.1039/C3CP50968K, 2013.

Valente, R. J. and Thornton, F. C.: Emissions of NO from soil at a rural site in central Tennessee, Journal of Geophysical Research: Atmospheres, 98, 16 745–16 753, DOI: 10.1029/93JD01417, 1993.

van der A, R. J., Eskes, H. J., Boersma, K. F., van Noije, T. P. C., Van Roozendael, M., De Smedt, I., Peters, D. H. M. U., and Meijer, E. W.: Trends, seasonal variability and dominant NOx source derived from a ten year record of NO2 measured from space, Journal of Geophysical Research: Atmospheres, 113, DOI: 10.1029/2007JD009021, d04302, 2008.

van Groenigen, J. W., Huygens, D., Boeckx, P., Kuyper, T. W., Lubbers, I. M., Rütting, T., and Groffman, P. M.: The soil N cycle: new insights and key challenges, SOIL, 1, 235–256, DOI: 10.5194/soil-1-235-2015, 2015.

Vandaele, A., Hermans, C., Simon, P., Carleer, M., Colin, R., Fally, S., Mérienne, M., Jenouvrier, A., and Coquart, B.: Atmospheric Spectroscopy Applications 96 Measurements of the NO2 absorption cross-section from 42 000 cm-1 to 10 000 cm-1 (238–1000 nm) at 220 K and 294 K, Journal of Quantitative Spectroscopy and Radiative Transfer, 59, 171–184, DOI: http://dx.doi.org/10.1016/S0022-4073(97)00168-4, 1998.

Veres, K., Behrendt, T., Klapthor, A., Meixner, F., and Williams, J.: Volatile Organic Compound emissions from soil: using Proton-Transfer-Reaction Time-of-Flight Mass Spectrometry (PTR-TOF-MS) for the real time observation of microbial processes, Biogeosciences Discuss., 2014.

Verheye, W.: Soils of arid and semi arid regions, in: Land use, land cover and soil sciences, edited by Verheye, W. H., Encyclopedia of Life Support Systems (EOLSS), UNESCO-EOLSS Publishers, Paris, France, 2008.

Vinken, G. C. M., Boersma, K. F., Maasakkers, J. D., Adon, M., and Martin, R. V.: Worldwide biogenic soil NO_x emissions inferred from OMI NO_2 observations, Atmos. Chem. Phys., 14, 10 363–10 381, DOI: 10.5194/acp-14-10363-2014, 2014.

Virginia, R., Jarrell, W., and Franco-Vizcaino, E.: Direct measurement of denitrification in a Prosopis (Mesquite) dominated Sonoran Desert ecosystem, Oecologia, 53, 120–122, DOI: 10.1007/BF00377145, 1982.

Wagner, T., Heland, J., Zöger, M., and Platt, U.: A fast H_2O total column density product from GOME – Validation with in-situ aircraft measurements, Atmos. Chem. Phys., 3, 651–663, DOI: 10.5194/acp-3-651-2003, 2003.

Wagner, T., Beirle, S., Grzegorski, M., and Platt, U.: Global trends (1996–2003) of total column precipitable water observed by Global Ozone Monitoring Experiment (GOME) on ERS-2 and their relation to near-surface temperature, J. Geophys. Res.-Atmos., 111, DOI: 10.1029/2005JD006523, d12102, 2006.

Wagner, T., Beirle, S., and Deutschmann, T.: Three-dimensional simulation of the Ring effect in observations of scattered sun light using Monte Carlo radiative transfer models, Atmospheric Measurement Techniques, 2, 113–124, DOI: 10.5194/amt-2-113-2009, 2009.

Wagner, T., Beirle, S., Brauers, T., Deutschmann, T., Frieß, U., Hak, C., Halla, J. D., Heue, K. P., Junkermann, W., Li, X., Platt, U., and Pundt-Gruber, I.: Inversion of tropospheric profiles of aerosol extinction and HCHO and NO₂ mixing ratios from MAX-DOAS observations in Milano during the summer of 2003 and comparison with independent data sets, Atmospheric Measurement Techniques, 4, 2685–2715, DOI: 10.5194/amt-4-2685-2011, 2011.

Wagner, T., Apituley, A., Beirle, S., Dörner, S., Friess, U., Remmers, J., and Shaiganfar, R.: Cloud detection and classification based on MAX-DOAS observations, Atmospheric Measurement Techniques, 7, 1289–1320, DOI: 10.5194/amt-7-1289-2014, 2014.

Wagner, W., Dorigo, W., Jeu, R. D., Fernandez, D., Benveniste, J., Haas, E., Ertl, M., Sensing, R., Amsterdam, V. U., Sciences, G.-e., Agency, E. S., Galilei, V. G., Systems, G. I., and Cycle, W.: Fusion of active and passive microwave observations to create an Essential Climate Variable data record on soil moisture, ISPRS Annals of the Photogrammetry, Remote Sensing and Spatial Information Sciences, I-7, 315–321, 2012.

Wallace, J. M. and Hobbs, P. V.: Atmospheric Science: An Introductory Survey, Academic Press, San Diego, second edition edn., DOI: http://dx.doi.org/10.1016/B978-0-12-732951-2.50001-6, 2006.

Wang, L., Manzoni, S., Ravi, S., Riveros-Iregui, D., and Caylor, K.: Dynamic interactions of ecohydrological and biogeochemical processes in water-limited systems, Ecosphere, 6, 1–27, DOI: 10.1890/ES15-00122.1, art133, 2015a.

Wang, P., Stammes, P., van der A, R., Pinardi, G., and van Roozendael, M.: FRESCO+: an improved O_2 A-band cloud retrieval algorithm for tropospheric trace gas retrievals, Atmos. Chem. Phys., 8, 6565–6576, DOI: 10.5194/acp-8-6565-2008, 2008.

Wang, Y., McElroy, M. B., Martin, R. V., Streets, D. G., Zhang, Q., and Fu, T.-M.: Seasonal variability of NOx emissions over east China constrained by satellite observations: Implications for combustion and microbial sources, J. Geophys. Res.-Atmos., 112, DOI: 10.1029/2006JD007538, 2007.

Wang, Y., Li, A., Xie, P. H., Chen, H., Mou, F. S., Xu, J., Wu, F. C., Zeng, Y., Liu, J. G., and Liu, W. Q.: Measuring tropospheric vertical distribution and vertical column density of NO2 by multi-axis differential optical absorption spectroscopy, Acta Phys. Sin., 16, DOI: 10.7498/aps.62.200705, 2013a.

Wang, Y., Li, A., Xie, P. H., Chen, H., Xu, J., Wu, F.-C., Liu, J.-G., and Liu, W.-Q.: Retrieving vertical profile of aerosol extinction by multi-axis differential optical absorption spectroscopy, Acta Phys. Sin., 16, DOI: 10.7498/aps.62.180705, 2013b.

Wang, Y., Penning de Vries, M., Xie, P. H., Beirle, S., Dörner, S., Remmers, J., Li, A., and Wagner, T.: Cloud and aerosol classification for 2.5 years of MAX-DOAS observations in Wuxi (China) and comparison to independent data sets, Atmospheric Measurement Techniques, 8, 5133–5156, DOI: 10.5194/amt-8-5133-2015, 2015b.

Wang, Y., Lampel, J., Xie, P., Beirle, S., Li, A., Wu, D., and Wagner, T.: Ground-based MAX-DOAS observations of tropospheric aerosols, NO_2, SO_2 and HCHO in Wuxi, China, from 2011 to 2014, Atmospheric Chemistry and Physics Discussions, 2016, 1–61, DOI: 10.5194/acp-2016-282, 2016.

Warneck, P. and Williams, J.: The Atmospheric Chemist's Companion: Numerical Data for Use in the Atmospheric Sciences, Springer, Berlin, 2012.

Warneke, C., Karl, T., Judmaier, H., Hansel, A., Jordan, A., Lindinger, W., and Crutzen, P. J.: Acetone, methanol, and other partially oxidized volatile organic emissions from dead plant matter by abiological processes: significance for atmospheric HOx chemistry, Global Biogeochem. Cy., 13, 9–17, 1999.

Washington, R. and Todd, M. C.: Atmospheric controls on mineral dust emission from the Bodélé Depression, Chad: The role of the low level jet, Geophysical Research Letters, 32, DOI: 10.1029/2005GL023597, l17701, 2005.

Weber, B., Wu, D., Tamm, A., Ruckteschler, N., Rodríguez-Caballero, E., Steinkamp, J., Meusel, H., Elbert, W., Behrendt, T., Sörgel, M., Cheng, Y., Crutzen, P. J., Su, H., and Pöschl, U.: Biological soil crusts accelerate the nitrogen cycle through large NO

and HONO emissions in drylands, P. Natl. Acad. Sci. USA, 112, 15 384–15 389, DOI: 10.1073/pnas.1515818112, 2015.

WHO: Health Aspects of Air Pollution with Particulate Matter, Ozone and Nitrogen Dioxide, URL http://www.euro.who.int/__data/assets/pdf_file/0005/112199/E79097.pdf, accessed: 08/01/2016, 2003.

Williams, E. J., Parrish, D. D., and Fehsenfeld, F. C.: Determination of nitrogen oxide emissions from soils: Results from a grassland site in Colorado, United States, J. Geophys. Res.-Atmos., 92, 2173–2179, DOI: 10.1029/JD092iD02p02173, 1987.

Williams, E. J., Hutchinson, G. L., and Fehsenfeld, F. C.: NOx And N2O Emissions From Soil, Global Biogeochem. Cy., 6, 351–388, DOI: 10.1029/92GB02124, 1992.

Yengoh, G. T., Dent, D., Olsson, L., Tengberg, A. E., and Tucker, C. J.: Use of the Normalized Difference Vegetation Index (NDVI) to Assess Land Degradation at Multiple Scales: Current Status, Future Trends, and Practical Considerations, Springer International Publishing, Cham, DOI: 10.1007/978-3-319-24112-8_1, 2015.

Yienger, J. and Levy, H.: Empirical model of global soil-biogenic NOx emissions, J. Geophys. Res., 100, 1995.

Yilmaz, S.: Retrieval of Atmospheric Aerosol and Trace Gas Vertical Profiles using Multi-Axis Differential Optical Absorption Spectroscopy, Phd-thesis, Ruperto-Carola University of Heidelberg, 2012.

Yu, J., Meixner, F. X., Sun, W., Liang, Z., Chen, Y., Mamtimin, B., Wang, G., and Sun, Z.: Biogenic nitric oxide emission from saline sodic soils in a semiarid region, northeastern China: A laboratory study, Journal of Geophysical Research: Biogeosciences, 113, DOI: 10.1029/2007JG000576, g04005, 2008.

Zel'dovich, Y.: The Oxidation of Nitrogen in Combustion Explosions, Acta Physicochimica U.S.S.R., 21, 577–628, 1946.

Zhao, C. and Wang, Y.: Assimilated inversion of NOx emissions over east Asia using OMI NO2 column measurements, Geophys. Res. Lett., 36, DOI: 10.1029/2008GL037123, 2009.

Zörner, J., Penning de Vries, M., Beirle, S., Sihler, H., Veres, P. R., Williams, J., and Wagner, T.: Multi-satellite sensor study on precipitation-induced emission pulses of NO_x from soils in semi-arid ecosystems, Atmospheric Chemistry and Physics, 16, 9457–9487, DOI: 10.5194/acp-16-9457-2016, 2016.

List of abbreviations

AE . . . . . Aerosol extinction

AOD . . . . . Aerosol optical depth

CMORPH . . . CPC MORPHing technique

CTM . . . . . Chemistry Transport Model

DSCD . . . . . Differential Slant Column Density

DOAS . . . . . Differential Optical Absorption Spectroscopy

DOASIS . . . . DOAS Intelligent System

DWD . . . . . Deutscher Wetterdienst

DOMINO . . . Derivation of OMI tropospheric NO_2 project

ECMWF . . . . European Centre for Medium-Range Weather Forecasts

FRESCO . . . . Fast Retrieval Scheme for Clouds from the Oxygen A-band

GCM . . . . . Global Chemistry Model

GIS . . . . . Geographical Information System

GOME . . . . . Global Ozone Monitoring Experiment

GOME-2 . . . . Global Ozone Monitoring Experiment 2

ITCZ . . . . . Inter-Tropical Convergence Zone

IUP . . . . . Institute of Environmental Physics, University of Heidelberg

LfU . . . . . Bayerisches Landesamt für Umwelt

LP-DOAS . . . Long-Path DOAS instrument

MAX-DOAS . . Multi AXis Differential Optical Absorption Spectroscopy

MPIC . . . . . Max Planck Institute for Chemistry

MERIS . . . . . MEdium Resolution Imaging Spectrometer

MODIS . . . . . Moderate Resolution Imaging Spectroradiometer

NDVI . . . . . Normalized Difference Vegetation Index

NO_x . . . . . Nitrogen oxides

OMI . . . . . Ozone Monitoring Instrument

OMCLDO2 . . Cloud Pressure and Fraction using O_2-O_2 absorption

PERSIANN . . Precipitation Estimation from Remote Sensing Information using Artificial Neural Network

PM . . . . . Particulate matter

SCIAMACHY . SCanning Imaging Absorption SpectroMeter for Atmospheric CHartographY

SCD . . . . . Slant column density

sNO$_x$ . . . . . Soil-emitted NO$_x$

TROPOMI . . . TROPOspheric Monitoring Instrument

VCD . . . . . Vertical Column Density

UTC . . . . . Coordinated Universal Time

UV . . . . . Ultra-Violet

VIS . . . . . VISible

VMR . . . . . Volume mixing ratio

WWLLN . . . . World Wide Lightning Location Network

List of Figures

2.1 Spatial and temporal scales of variability for some atmospheric constituents from Wallace and Hobbs (2006). 6
2.2 A typical mid-latitude vertical temperature profile (adapted from Wallace and Hobbs (2006)). 7
2.3 Day- and night-time behaviour of the planetary boundary layer (adapted from Stull (1988)). 8
2.4 General global atmospheric circulation (adapted from Wallace and Hobbs (2006)). 9
2.5 Illustration from Schneider et al. (2014): Global annual-mean precipitation and surface winds. The ITCZ over oceans (precipitation maximum) is marked by red lines. The right panel shows the zonal-mean precipitation. Precipitation data is taken from TRMM/TMPA for 1998–2012. The wind data are from ECMWF for the same years. The longest wind vector over the central Pacific corresponds to a wind speed of $8.1\,\mathrm{m\,s^{-1}}$ 10
2.6 Tropospheric NO_2 VCDs averaged over the years 2005 to 2009 as observed by the OMI satellite sensor. Level-2 data taken from http://www.temis.nl 12
2.7 Left: global mean sNO_x emission rates [$\mathrm{ng\,N\,m^{-2}\,s^{-1}}$] for the period from 1990 to 2000 calculated by an improved sNO_x model by Steinkamp and Lawrence (2011) based on the YL95 scheme (Yienger and Levy, 1995). Right: Difference between the updated and original model as implemented in the EMAC model. 13
2.8 Overview of the schematic dependence of NO emission rates on several soil parameters: nitrogen availability, temperature, soil water content and pH value adapted from Pilegaard (2013). 15
2.9 Illustration adapted from Sillman et al. (1990) and Jacob (1999) showing O_3 concentrations (ppbv) simulated by a regional photochemical model as a function of NO_x and hydrocarbon emissions. The bold black line distinguishes the NO_x-limited (top left) and hydrocarbon-limited (bottom right) regimes. 18
2.10 Tropospheric HCHO VCDs averaged over the years 2005 to 2009 as observed by the OMI satellite sensor. Level-2 data taken from http://www.temis.nl 21
2.11 Schematic depiction of trace gas measurements in the open atmosphere involving a variety of scattering and absorption processes. Illustration from Platt and Stutz (2008). 23
2.12 The DOAS principle, with I_0 and σ being separated by a filtering procedure into a narrow (D', and σ') and broad band part (I_0' and σ_b). Illustration from Platt and Stutz (2008). 24

2.13 Simplified measurement geometry for MAX-DOAS observations adapted from Sinreich (2008). Sun light enters the atmosphere at a given solar zenith angle (SZA) and is scattered at the red points into the line of sight of the MAX-DOAS viewing angle. In reality, however, typically multiple scattering processes occur in the atmosphere affecting the light path. The green shaded areas represent layers with increased trace gas concentrations. 26
2.14 Composition a miniature MAX-DOAS system (adapted from Bobrowski (2005)) employed within this thesis project. For measurement scans at different elevation angles, the entire instruments is moved by an external motor. 27
2.15 Schematic scheme, adapted from (Burrows et al., 2011), depicting a sun-synchronous polar orbit (Fig. 2.15) used for UV/VIS satellite instruments. 30
2.16 Simplified measurement geometry of a (near) nadir viewing satellite instrument adapted from Platt and Stutz (2008), with line of sight angle (LOS, ψ), solar zenith angle (SZA, θ) whereby **a)** shows a case without scattering in the atmosphere but only surface scattering and **b)** indicates the potential for many scattering events caused by clouds and aerosols. 31
2.17 Illustration from Levelt et al. (2006) depicting the OMI Global measurement mode. Due to the wide field of view (114°), the pixel sizes steeply increase towards the edge of the swath. 32
2.18 Illustration of the nadir 'whisk-broom' GOME-2 scan pattern adapted from EUMETSAT (2011). During a *forward scan*, the mirror scans from East to West and moves back about three times faster to the original position resulting in lower ground pixel resolution in the *backward scan*. 34
2.19 SCIAMACHY measurement geometry in Limb and Nadir scanning mode from Noël et al. (2000). 35

3.1 Schematic of the 24h time period selected for the integration of precipitation data. The eight 3-hourly precipitation rates prior to the overpass times of the SCIAMACHY, GOME-2 and OMI satellite sensors are summed. 42
3.2 Time series of TMPA precipitation (a) and OMI NO_2 VCDs (b) for a 10 day period around the first rain event for a single grid pixel in the Sahel on 11/04/2008 at 15.25° N, 25.5° E. A threshold of 2 mm precipitation per day is chosen and at least 60 days of drought are required. 43

3.3 **(a)** Number of valid measurements per grid pixel on Day0. **(b)** OMI NO_2 background levels averaged for days -10 to -2 before the first rain event after 60 days of drought for each pixel (0.25° lat/long) and then averaged for boxes of 1.25° lat/long. **(c)** OMI NO_2 VCD absolute differences on Day0 (first day of rainfall) compared to Days -10 to -2. Reductions in NO_2 VCDs on Day0 depicted in blue colours, enhancements in red. **(d)** as (c) but screened for significant changes (see text). Extensive enhancements over the Sahel and South Africa are evident. Pixels containing less than 20 measurements on Day0 (or less then 50 measurements from Day-10 to Day-2) are screened out. 45

3.4 **(a)** Significant OMI NO_2 VCD enhancements (in 1×10^{15} molecules cm^{-2}) on Day0 compared to the background level for April-May-June (2007–2010) which represents the start of the wet season after the dry period in the northern part of Africa. Extensive enhancements in NO_2 over the narrow band of the Sahel can be seen. **(b)** The same for September/October/November (2007–2010), whereby strong enhancements are found in south-western Africa. This time period reflects the transition time between the dry and wet season in this region. 46

3.5 Map of Northern Africa with focus on the Sahel being the transition zone between the dry Saharan desert and the humid savannah and tropics of central Africa. The area highlighted in red is used for the analyses in Sections 3.4.2.3, 3.4.2.4 and 3.4.2.7. NASA's *Blue Marble* taken from Environmental Systems Research Institute (ESRI) MapServer: http://server.arcgisonline.com/ArcGIS/rest/services/ESRI_Imagery_World_2D/MapServer 47

3.6 Time series of monthly averages of precipitation (TRMM/TMPA), NDVI (MODIS/MYD13C2) and NO_2 VCDs (OMI) for the Sahel (0-30° W, 12-18° N) for 2007–2011. 48

3.7 Elevation from SRTM for Northern Africa. 49

3.8 Average precipitation for the months March to August averaged over four year (2007–2011) from TRMM/TMPA 3B42v7. 52

3.9 Average NDVI indices for the months March to August averaged over four years (2007–2011) from MODIS/MYD09CMG. 53

3.10 Average NO_2 VCDs from OMI for the months March to August averaged over four years (2007–2012). 54

3.11 Latitudinal averages of VCDs in 1×10^{15} molecules cm^{-2} over a selected part of Northern Africa (20° W to 35° E and 5 to 20° N) for the three instruments: OMI **(left)** GOME-2 **(middle)** and SCIAMACHY **(right)**. Each coloured line represents the latitudinal average over the region per month. Filled squares indicate the highest NO_2 VCDs per month. 55

3.12 Latitudinal averages of precipitation (TRMM/TMPA) and NDVI (MODIS) over a selected part of Northern Africa (20° W to 35° E and 5 to 20° N). Each coloured line represents the latitudinal average over the region per month. For the NDVI averages, all values less than -0.1 are screened as they mostly represent water areas. 56
3.13 Temporal evolution of several quantities around the day with the first rain event for the Sahel region after at least 60 days of drought for April/May/June (2007–2010). Grey shaded areas represent precipitation estimates from TMPA, CMORPH and PERSIANN. **(a)** Blended ESA-CCV soil moisture. **(b)** Water vapour total column densities from GOME-2. **(c)** Temperature at 1000 hPa from ECMWF Interim Analysis. **(d)** Relative and absolute humidity at 1000 hPa from ECMWF Interim Analysis. **(e)** NO_2 VCDs from SCIAMACHY, GOME-2 and OMI with standard mean error (SME). **(f)** HCHO VCDs from SCIAMACHY, GOME-2 and OMI with SME. 57
3.14 **(a)** ESA GLOBCOVER land cover classification for the Sahel downscaled to 0.25° x 0.25° resolution with the corresponding (official) identification number, short name and colour information for each class. **(b)** Spatial location and number of OMI observations for the reference case analysis (AMJ, 2007–2010). **(c)** Rain-triggered NO_2 enhancements from OMI for the Sahel region separated by the dominant land cover types. 59
3.15 **Left panel**: NO_2 VCDs from OMI around the first day of rainfall for different soil temperatures on Day0 for the Sahel region (based on the reference case settings). **Right panel**: daily time series of soil temperature (from 12UTC ECMWF data) for the Sahel region (0–20° W, 12–18° N) averaged for the years 2007, 2008, 2009 and 2010. 60
3.16 Absolute enhancements of NO_2 VCDs from OMI on Day0, i.e. the first day of precipitation after a prolonged drought akin to Fig. 3.3.d but for higher resolution (0.5°) and split up for cases where Day0 is in one of these months: March, April, May, June, July, August. Precipitation and NO_2 VCDs are for the years 2007–2011. 61
3.17 Daily time series for the Sahel region (0–30°W, 12–18°N) averaged for the years 2007, 2008, 2009 and 2010. The first row of each panel shows mean NO_2 VCDs from OMI in molecules cm^{-2} (black) and a clean ocean reference (grey, 130–150° W, 12–118° N). The second row shows the number of active fire counts in the Sahel from MODIS. The third row shows average precipitation from the TMPA/TRMM product in mm. The fourth row shows the number of lightning strikes detected by WWLLN. 62
3.18 Effect of lightning screening on the response of NO_2 VCDs around the first day of rainfall after a prolonged dry spell. **(a)** NO_2 VCDs for the Sahel region from SCIAMACHY, GOME-2 and OMI without lightning screening (dashed lines) and with lightning screening (solid lines). **(b)** The corresponding results for central Australia (15–30° W, 2–10° S). 63

3.19 Investigation of cloud effects on the retrieved NO_2 SCDs and VCDs. **(a)** Mean cloud fraction of the three satellite instruments for the reference case (cloud fraction <20%). **(b)** Mean cloud fraction of the three satellite instruments but considering only observations with cloud fraction > 20%. **(c)** NO_2 VCDs for the reference case. **(d)** NO_2 VCDs only considering observations with high cloud cover (cloud fraction > 20%). **(e)** NO_2 SCDs for the reference case. **(f)** NO_2 SCDs only considering observations with high cloud cover (cloud fraction > 20%). 65
3.20 Mean ECMWF wind vectors at three different pressure levels. At the surface, a strong south-westerly wind is blowing the 2 days before the first rain event in the Sahel region followed by northerly winds. At 600 hPa winds are constantly from the north-west. 66
3.21 Same as Fig. 3.13d, but filtered for **(a)** northerly and **(b)** southerly winds. The filter criterion is fulfilled, if the wind direction at 600, 850 and 1000 hPa is north or south, respectively. 66
3.22 **Left**: Average precipitation over 60 days following Day0 in the central pixel (red) and for the neighbouring 10 pixel buffer (blue). **Right**: % of pixels in a 10 pixel buffer around pixel *i* experiencing the first rain event after pixel *i*. 67
3.23 Analysis of NO_2 VCDs 60 days before and after the first day of rainfall in the April-May-June period for the Sahel region. **(a)** NO_2 VCDs from OMI, GOME-2 and SCIAMACHY. **(b)** Latitudinal-averaged NO_2 VCDs corresponding to the reference (for details see text). **(c)** Latitudinal-averaged NO_2 VCDs corresponding to the reference considering an additional buffer of 10 pixels around the actual-triggered pixel to avoid influence of enhanced NO_2 VCDs in the vicinity of the precipitation events. **(d)** Background corrected NO_2 VCDs: panel (a) - panel (b) **(e)** Background (with buffer) corrected NO_2 VCDs: panel (a) - panel (c) 69
3.24 Investigation of the effect of different periods of dry days following Day0. **(a)** Reference case analysis for OMI NO_2 VCDs filtered for time series experiencing 0, 3, 5, 10 and 20 days of drought after Day0. **(b)** Background time series of NO_2 VCDs without buffer screening as presented in Fig. 3.23b for the corresponding time series experiencing 0, 3, 5, 10 and 20 days of drought after Day0. **(c)** The corresponding background time series of NO_2 VCDs with buffer screening as presented in Fig. 3.23c. **(d)** Differences between panels (a) and (b). **(e)** Differences between panels (a) and (c). . . 71
3.25 **(a)** NO_2 VCDs from SCIAMACHY, GOME-2 and OMI for south-western Africa in September-October-November around the first day of rainfall in this period. Precipitation is represented by the grey shaded areas. **(b)** Results for central Australia for the complete years 2007–2010. 72

3.26 Reference case for different precipitation products as trigger. NO_2 VCDs are shown (akin to Fig. 3.13.e) from TRMM/TMPA (**A1**), CMORPH (**A2**) and PERSIANN (**A3**) around the first day of rainfall for different precipitation products as trigger for the precipitation threshold of 2 mm for the Sahel region. The left panels represent the full time series of 60 days before and after Day0, the right panels show a zoom-in for the 10 days before and after. 74
3.27 Different drought lengths for the reference case. NO_2 VCDs are shown from OMI (**B1**), GOME-2 (**B2**), SCIAMACHY (**B3**) around the first day of rainfall for different preceding drought periods for the Sahel region with a precipitation threshold of 2 mm. For better intercomparison, the latitudinal background correction with buffer as described in Section 3.4.2.8 is applied to each time series individually. The left panels represent the full time series of 60 days before and after Day0, the right panels show a zoom-in for the 10 days before and after. 75
3.28 Different precipitation thresholds on Day0 for the reference case. NO_2 VCDs are shown from OMI (**C1**), GOME-2 (**C2**), SCIAMACHY (**C3**) around the first day of rainfall for the Sahel region for a drought period of at least 60 days. The results are separated for different intervals of the precipitation threshold on Day0. A drought day is defined by precipitation < 0.1 mm per day. For better intercomparison, the latitudinal background correction with buffer as described in Section 3.4.2.8 is applied to each time series individually. The left panels represent the full time series of 60 days before and after Day0, the right panels show a zoom-in for the 10 days before and after. 76
3.29 Global Maps for other satellite instruments (60 days of drought, 2 mm precipitation threshold). Absolute differences in NO_2 VCDs compared to Days -10 to -2 from GOME-2 (**D1**) and SCIAMACHY (**D2**) on Day0 (first day of rainfall) are depicted which were computed similarly as for OMI in Fig. 3.3.d for OMI. The data was screened for significant changes and pixels containing less than 20 measurements on Day0 (or less than 50 measurements from Day-10 to Day-2). 77
3.30 Figures **E1** and **E2** depict the NO_2 enhancement on Day0 as in Fig. 3.3d, but based on CMORPH and PERSIANN data, respectively. While the absolute values differ for the Sahel, the final emission estimates for pulsed emissions are quite similar (see Table **E3**), as the choice of the precipitation data affects the background correction as well. 78

4.1 MODIS Aqua RGB image (Bands 1,4,3 from MYD09GA product) of Lake Chad on February 1st 2016. Country borders as well as main rivers feeding Lake Chad are highlighted. Lake Chad is divided into a northern and southern pool by the 'Great Barrier' which is highlighted with a grey bar. The approximate area of Lake Chad which is constantly filled with water throughout the year is encircled in blue. 86
4.2 Adapted from the historic Sahel precipitation index (doi:10.6069/H5MW2F2Q). The anomalies are with respect to 1900–2013 and calculated from 20 ° W to 10 ° E and from 10 ° N to 20 ° N. Sahel precipitation was above the long-term mean from 1915 through the late 1930s and during the 1950s-1960s, after which it was persistently below the long-term mean, with the largest negative anomalies in the early 1980s. 86
4.3 Area coverage in percent for each class of the land clover classification by Babamaaji and Lee (2014) for the Lake Chad region. 1975–1979: Mosaic Landsat-MSS land use/land cover map, 1991: Landsat-TM land use/land cover map, 2006: NigeriaSat-1 land use/land cover map. 87
4.4 Daily time series for the year 2007 of precipitation (TRMM/TMPA) and OMI NO_2 VCDs averaged over Lake Chad. 89
4.5 The evolution of the precipitation system on June 15th and 16th 2007 around Lake Chad. 90
4.6 Precipitation summed over the period from June 15th 13:30LT 2007 until June 16th 13:30LT 2007 91
4.7 ECMWF mean wind speeds for the time period from June 15th 18:00LT to June 16th 12:00LT at 900 hPa (left) and 650 hPa (right). 91
4.8 NO_2 VCDs as viewed by the OMI satellite instrument. Shown here are averages for the period from June 1st to 14^{14} 2007 **(a)** and daily observations for June 16th **(b)** June 15th **(c)** and June 17th **(d)**. On June 15th the Lake Chad region is captured by the largest OMI pixels at the far end of the swath. . . 93
4.9 OMI cloud fraction averaged from 1st to 14th July 2007 (left) and OMI cloud fraction for June 16th (right) 94
4.10 OMI NO_2 SCDs averaged from 1st to 14th July 2007 (left) and OMI NO_2 SCDs for June 16th (right) 95
4.11 Spatial occurrence of lightning strikes as detected by WWLLN. The panels thereby show the location of lightning strikes in different time windows: June 15th 13:30LT to 18:00LT **(a)** June 15th 18:00LT to June 16th 0:00LT **(b)** June 16th 0:00LT to 6:00LT **(c)** June 16th 6:00LT to 13:30LT **(d)** 96
4.12 Fire locations (black crosses) and image classification from the MODIS instruments on Terra **(a)** and Aqua **(b)** derived from the MOD/MYDA1 products for June 16th on a 1 by 1 km resolution. Note, some fires lie close to each other and therefore appear as bigger crosses. The local overpass of MODIS Terra is at 9:30LT and for MODIS Aqua at 13:30LT. The maximum fire radiative power (max FRP) for each grid pixel is given in **(c)**. 98

4.13 The left panels present days with high fire counts overlayed with the corresponding OMI NO_2 VCDs for this day: October 30th **(a)**, October 31st **(b)**, November 1st **(c)** and November 2nd **(d)**. Fire locations are from the MODIS instrument on Aqua (MYDA1 product). The maximum fire radiative power (max FRP) for each fire pixel of the particular day and for the area encircled in black in the map is provided in the right panels. 99

5.1 Left: Map depicting the elevation in the vicinity of the Nördlinger Ries based on data from NASA SRTM. Right: True colour (RGB) image from Landsat 8 on July 17th 2014 depicting the Nördlinger Ries. Dark green patches on the crater rim indicate forests and the yellow and brown patches within the Ries illustrate the large number of cultivated fields in the region. 105

5.2 Left: Agronomic yield potential of soils in Bavaria calculated and provided by the Federal Institute for Geosciences and Natural Resources. The highest index is found in the Nördlinger Ries with about 90 %. Right: NO_2 VCDs from the OMI satellite instrument averaged over the time period from January 1st 2010 to December 31st 2013. The approximate location of the Nördlinger Ries is highlighted with a black circle. High values of NO_2 VCDs ($> 5 \times 10^{15}$ molecules cm^{-2}) are observed over the cities of Stuttgart, Nuremburg and Munich whereas NO_2 VCDs in the Ries are comparatively low ($< 4 \times 10^{15}$ molecules cm^{-2}) 106

5.3 Street map of the Nördlinger Ries from ©OpenStreetMap data showing the main roads (orange lines) and cities in the vicinity. The largest city is Nördlingen in the centre of the Ries with a population of about 20.000. The border separating Baden-Württemberg (to the West) and Bavaria (to the East) is shown as a purple dashed line. 107

5.4 Climate diagram for the Nördlinger Ries in 2014 derived from temperature and precipitation data of the DWD weather station in Reimlingen/Ries. The average temperature is 9 °C and total precipitation per year is 750 mm; The altitude of the Reimlingen station is 435 m. 107

5.5 Measurement locations of the DOAS-type instruments at the castle and the barn station as well as the DWD weather stations and the LfU air quality monitoring station are indicated with a yellow star. Main viewing directions of the mini-MAX-DOAS instruments are indicated by the red lines (with a symbolic length of 10 km). The viewing direction of the LP-DOAS at the barn station is about the same as for the MAX-DOAS instrument (but has a fixed path length of 2.8 km). 109

5.6 mini MAX-DOAS instrument at the "castle station". A turning table for movements in the azimuth (covered by a circular shaped metal plate) was mounted underneath the mini MAX-DOAS August 14th 2014. 111

5.7 Location of the "barn station" (marked with a yellow star) where a mini-MAX-DOAS and Long-Path DOAS were installed. In the right panel, the city of Nördlingen is visible in the lower right corner. Image data from Bing Maps ©2016 - Microsoft Corporation. 111
5.8 Measurement set-up of the LP-DOAS at the barn station. Left: the reflector amidst crop fields. Right: the telescope next to the barn. 112
5.9 Air quality monitoring station in Öttingen, Göthestraße. Image in the centre by LfU, ©Bayerische Vermessungsverwaltung 2014; Right image from Bing Maps ©2016 - Microsoft Corporation. 113
5.10 Top: Locations of the weather stations (yellow stars) in-field around the barn station (red star). Image data from Bing Maps ©2016 - Microsoft Corporation. Note, that the top image is just for reference and the crops on the depicted fields do not represent the actual crops at that time. Bottom images show the weather stations which were installed in the field. Two identical stations were installed next to each other at the beginning of the study for evaluation purposes. The lower left image shows the barn station in the background. 114
5.11 **Top panels:** example for a typical DOAS fit for NO_2 at the barn station at an elevation angle of 1° on August 8th under clear-sky conditions at 12:07 local time. The optical densities of the fitted species (red) and the residuals (black) are displayed as a function of wavelength. **Bottom panels:** example for a typical DOAS fit for NO_2 at the castle station at an elevation angle of 1° on September 9th under clear-sky conditions at 12:15 local time. The optical densities of the fitted species (red) and the residuals (black) are displayed as a function of wavelength. 117
5.12 **Top panels:** example for a typical DOAS fit for HCHO at the barn station at an elevation angle of 1° on August 8th under clear-sky conditions at 12:07 local time. The optical densities of the fitted species (red) and the residuals (black) are displayed as a function of wavelength. **Bottom panels:** example for a typical DOAS fit for HCHO at the castle station at an elevation angle of 5° on July 24th under clear-sky conditions at 11:47 local time. The optical densities of the fitted species (red) and the residuals (black) are displayed as a function of wavelength. 119
5.13 **Top panels:** example for a typical DOAS fit for O_4 at the barn station at an elevation angle of 1° on August 8th under clear-sky conditions at 12:07 local time. The optical densities of the fitted species (red) and the measured residuals (black) are displayed as a function of wavelength. **Bottom panels:** example for a typical DOAS fit for O_4 at the castle station at an elevation angle of 1° on September 9th under clear-sky conditions at 12:15 local time. The optical densities of the fitted species (red) and the measured residuals (black) are displayed as a function of wavelength. 120

5.14 Quality analysis of the retrieved DSCDs of the trace gases for the mini MAX-DOAS instrument at the barn station. Plotted here are HCHO and NO_2 DSCDs [1×10^{15} molecules cm^{-2}] against the relative intensity offset [%], the RMS [optical density] and the SZA in degree. Additionally, the relative intensity offset is plotted against the SZA for the HCHO and NO_2 analyses. 122
5.15 Quality analysis of the retrieved DSCDs of the trace gases for the mini MAX-DOAS instrument at the castle station. Plotted here are HCHO and NO_2 DSCDs [1×10^{15} molecules cm^{-2}] against the relative intensity offset [%], the RMS (optical density) and the SZA in degree. Additionally, the relative intensity offset is plotted against the SZA for the HCHO and NO_2 analyses. 123
5.16 **Top panel:** Result of the cloud classification scheme for July 25th 2014 showing clear sky in the morning and evening and continuous cloud cover (and rain) in early afternoon. **Bottom panel:** Images from the webcam at the castle station at 9:00UTC, 12:00UTC and 17:00UTC 125
5.17 Top panel: climate diagram for the Nördlinger Ries in the year 2014. Bottom panel: average wind conditions (wind speed and direction) from June to November 2014 as observed by the in-field weather station with a 10-minute temporal resolution. 127
5.18 Evaluation of the simulated NO_2 and HCHO DSCDs from the profile retrieval. Left panels show the correlation between the simulated and measured DSCDs for the mini-MAX-DOAS instruments at the barn (first and third row) and castle station (second and forth row). The right panels show the absolute difference between the simulated and measured DSCDs for both trace gases and stations. 129
5.19 Average atmospheric profiles for HCHO, NO_2 and aerosol extinction (AE) deduced from the mini MAX-DOAS instruments at the barn (red lines) and castle station (blue lines) using the PriAM retrieval method. A priori profiles for each species are shown in black. The VMRs at each altitude were averaged over the period from August to September 2014. 130
5.20 Correlation study between the NO_2 VCDs derived from the mini MAX-DOAS instruments and NO_2 VCDs from the OMI satellite instrument. Left panel: correlation study for the castle station showing good agreement (R^2 0.93) with OMI observations. Right panel: the correlation study for the barn station also shows good agreement with OMI observations (R^2 0.97), but only based on 6 data points. 131

5.21 Top panels: NO_2 and HCHO DSCDs [1×10^{16} molecules cm^{-2}] of the azimuth scanning mode from the mini MAX-DOAS at the castle station grouped for different months. Shown are NO_2 DSCDs at 1° elevation at 8 defined azimuth directions: 247°, 267°, 287°, 307°, 327°, 347° and 7°. Error bars represent the standard error of the mean. Lower panel: Map of average NO_2 DSCDs (black line in the upper graph) for different azimuth positions. Different coloured lines represent the NO_2 DSCD whereby the length of the line is for illustrative purposes set to 15 km. The city of Nördlingen is marked in blue. 132
5.22 Diurnal cycle of NO_2 VMRs as observed by the two mini MAX-DOAS instruments (at the barn and castle station), the LP-DOAS and the air quality monitoring station from the LfU during the working week (left panel) and on weekends (right panel) in August and September 2014. . . . 133
5.23 Diurnal cycle of HCHO VMRs from the four instruments during the working week (left panel) and on weekends (right panel) in August and September 2014. 134
5.24 Weekly cycle of NO_2 and HCHO VMRs from the four instruments during the working week (left panel) and on weekends (right panel) in August and September 2014. 135
5.25 Monthly averages of NO_2 VMRs (top panel) and HCHO VMRs (bottom panel) from the four instruments for each month in the year 2014. 136
5.26 Upper panels: near-surface NO_2 and HCHO VMRs from the mini MAX-DOAS at the barn (red) and castle (blue) stations and from the LP-DOAS (green) separated for different sky conditions. Lower panels: Air temperature and global radiation (from the in-field weather station at the barn station) during different sky conditions. 138
5.27 Near-surface NO_2 and HCHO VMRs from the 4 instruments (mini MAX-DOAS instruments at the barn and castle station, LP-DOAS and LfU air quality monitoring station) filtered for low wind conditions (< 1 m s^{-1}) and windy conditions (> 1 m s^{-1}). 140
5.28 Correlation matrix of the environmental parameters chosen in Section 5.6.8 whereby the colour and size of each point represents the correlation coefficient. 141
5.29 Detailed correlation matrix of the environmental parameters chosen in Section 5.6.8. The diagonal panels illustrate the distribution of each variable. The lower left panels (below the diagonal) show the bivariate scatter plots. The upper right panels (above the diagonal) show the correlation coefficient including the level of significance:: p-values(0, 0.001, 0.01, 0.05, 0.1, 1) correspond to the symbols(“***”, “**”, “*”, “.”, “ ”). 146

5.30 Time series of several environmental parameters, trace gases and aerosols during the measurement campaign in 2014. First row: soil moisture data from the in-field weather stations and the DWD calculated soil parameters. Second row: hourly precipitation sums derived from the DWD Radolan precipitation product. Third row: near-surface NO_2 VMRs derived from the mini MAX-DOAS instruments, the LP-DOAS and the LfU station (daily midday averages, 8–14UTC). Fourth row: near-surface HCHO VMRs derived from the mini MAX-DOAS instruments and the LP-DOAS (daily midday averages). Fifth row: near-surface AEs derived from the mini MAX-DOAS instruments and $PM_{2.5}$ from the LfU station (daily midday averages). Sixth row: soil and air temperature from the weather stations in-field as well as calculated soil temperature from the DWD station (both daily midday averages). 149
5.31 Zoom-in of the time series presented in Fig. 5.30 centered around April 27^{th} for precipitation (from DWD Radolan), soil moisture (DWD and in-field weather station), near-surface NO_2 VMRs (mini MAX-DOAS at the castle station and LfU air quality monitoring station) as well as HCHO VMRs (mini MAX-DOAS at the castle). Both panels show a selected time period after the first intense precipitation (leading to a steep increase in soil moisture) after several days of no precipitation. 151
5.32 Analysis for April 28^{th} 2014. First row: the cloud classification indicates an almost complete coverage of continuous clouds over the day. Second row: Near-surface NO_2 VMRs for the mini MAX-DOAS at the castle station and the LfU air quality monitoring station. Fourth and sixth row: near-surface wind speed and direction derived from the DWD weather station in Harburg and ECMWF. Sixth row: NO_2 profiles during the day show that most NO_2 is located close to the surface. 152
5.33 Same as Fig. 5.31 but centered around June 29^{th}. 154
5.34 Analysis for July 2^{nd} 2014. First row: the cloud classification indicates an almost complete coverage of continuous clouds over the day (except in the evening). Second row: Near-surface NO_2 VMRs for the mini MAX-DOAS at the castle station and the LfU air quality monitoring station. Third row: NO_2 profiles during the day show that most NO_2 is located close to the surface. Fourth and sixth row: near-surface wind speed and direction derived from the own in-field weather station, DWD weather station in Harburg and ECMWF. 155
5.35 Schematic overview of the measurement stations at the castle and barn in the circular-shaped Nördlinger Ries. In Section 5.7, only observations at relatively low wind speeds ($< 1\,m\,s^{-1}$) from north-westerly direction (307° to 347°) are considered. The approximate distance an air mass travels through the Ries until it passes the measurements station (from this wind direction) is indicated in the Figure. 156

List of Tables

1.1 Overview of the main study region and research approach per chapter. . . 3

5.1 Instruments and their operational time during the measurement campaign 2014. Abbreviations for the operating institutes: Max Planck Institute for Chemistry (MPIC), Institute of Environmental Physics, University of Heidelberg (IUP), Landesamt für Umwelt (LfU), Deutscher Wetterdienst (DWD). 108

5.2 Settings used for the DOAS retrieval of O_4, NO_2 and HCHO. *solar I_0 correction following Aliwell et al. (2002): 1×10^{17} molecules cm^{-2} for NO_2 and 1×10^{20} molecules cm^{-2} for O_3, **NO_2 at 220K was orthogonalized to NO_2 at 294K. 116

5.3 Thresholds used for the data quality screening of the trace gas DSCDs. The columns '%' state the % of data which is screened by the corresponding threshold. 121

5.4 Multiple regression analysis of near-surface NO_2 VMRs from the four instruments against several environmental parameters. The independent variables as well as their selection process are explained in Section 5.6.8. . 144

5.5 Multiple regression analysis of near-surface HCHO VMRs from the four instruments against several environmental parameters. The independent variables as well as their selection process are explained in Section 5.6.8. . 145

5.6 Average NO_2 VCDs (partial column from 0–600 m) [molecules cm^{-2}] derived from the two MAX-DOAS instruments under low wind speeds ($< 1\,m\,s^{-1}$) from north-westerly direction (307 to 347°) and partitioned for working week days and Sundays for the period from June to September. A distinction is made for observations taken during clear and cloudy sky. . . 157

B.1 Summary statistics for the independent variables for the castle NO_2 analysis 175

B.2 Summary statistics for the independent variables for the barn NO_2 analysis 176

B.3 Summary statistics for the independent variables for the LP-DOAS NO_2 analysis 176

B.4 Summary statistics for the independent variables for the LfU station NO_2 analysis 177

B.5 Summary statistics for the independent variables for the castle HCHO analysis 177

B.6 Summary statistics for the independent variables for the barn HCHO analysis 178

B.7 Summary statistics for the independent variables for the LP-DOAS HCHO analysis 178

B.8 Multiple regression analysis of near-surface NO_2 VMRs from the four instruments against several environmental parameters. In this analysis, the NO_2 data is shifted backwards by one day. The independent variables as well as their selection process are explained in Section 5.6.8. 179

B.9 Multiple regression analysis of near-surface NO_2 VMRs from the four instruments against several environmental parameters. In this analysis, the NO_2 data is shifted forwards by one day. The independent variables as well as their selection process are explained in Section 5.6.8. 180
B.10 Multiple regression analysis of near-surface HCHO VMRs from the three instruments against several environmental parameters. In this analysis, the HCHO data is shifted backwards by one day. The independent variables as well as their selection process are explained in Section 5.6.8. 181
B.11 Multiple regression analysis of near-surface HCHO VMRs from the three instruments against several environmental parameters. In this analysis, the HCHO data is shifted forwards by one day. The independent variables as well as their selection process are explained in Section 5.6.8. 182